THE MECHANISMS OF DRYING OF SINGLE DROPLETS

By

Hassan Hadi Ali

A Thesis Submitted to

The University of Aston in Birmingham

for the Degree of

Doctor of Philosophy

Department of Chemical Engineering
University of Aston in Birmingham

August 1985

DEDICATED

To The Memory Of My Father

And to My Wife Who I Love

THE UNIVERSITY OF ASTON IN BIRMINGHAM

"THE MECHANISMS OF DRYING OF SINGLE DROPLETS"

Hassan Hadi Ali PhD August 1985

SUMMARY

The literature relating to evaporation from single liquid drops and the drying of drops of solution/slurry has been reviewed. An investigation has been undertaken of the mass transfer and heat transfer rates from single drops either suspended from a rotating nozzle, or in free-flight, in specially-designed wind tunnels.The study covered pure liquid (water), solutions (e.g. sodium sulphate decahydrate, organic and inorganic products) and slurries of various organic products and a range of air temperature and velocities.

Revised correlations were obtained for mass and heat transfer coefficients, for evaporation from saturated surfaces,

$$Sh = 2.0 + \beta\left(\frac{T_a - T_d}{T_{amb}}\right)^n Re^{0.5}\, Sc^{0.33}$$

$$Nu = 2.0 + \phi\left(\frac{\lambda}{C_p \Delta T}\right)^m Re^{0.5}\, Pr^{0.33}$$

where for free-flight drops, $\beta = 0.617$, $\phi = 0.314$, $n = -0.01$, $m = 0.17$
and for rotated-suspended drops, $\beta = 0.501$, $\phi = 0.228$, $n = -0.03$, $m = 0.2$

Very good agreement was obtained between experimental overall mass transfer coefficients and those predicted from

$$\frac{1}{K_o} = \frac{1}{H_1 k_g} + \frac{1}{k_c}$$

where k_g was predicted from the above correlation and k_c, the controlling crust coefficient from,

$$k_c = \frac{D_v \varepsilon^{1.5}}{\psi}$$ for any of the eight materials studied.

A high resolution Scanning Electron Microscope was used to determine specific pore areas on collected dried crusts. Together with crust pressure drop measurements this facilitated estimation of porosity ε using a modified Kozeny equation.

Selected additives improved the drying rates through increased crust porosity. The optimum air temperature for an industrial spray tower was predictable from that allowing retention of uniform crusts on single droplets.

Limited studies, were made of particle-size distribution from a laboratory spray drier , using a Laser Particle Size Analyser. Drop size distributions in sprays from different nozzles and swirl chambers were also measured and correlated.

Key words: Mass Transfer Coefficient, Crust Thickness, Crust Porosity, Droplet Drying

ACKNOWLEDGEMENTS

The author wishes to express his gratitude to Professor G V Jeffreys and Dr C J Mumford for their dedicated supervision and encouragement throughout the course of this research programme, and for their helpful advice and moral support.

The author also wishes to thank the following persons:

Mr N Roberts and his staff in the Department of Chemical Engineering for their co-operation and advice;

The Department of Metallurgy, for use of their Scanning Electron Microscope;

Dr J P Fletcher and Mr A R Cooper, for their help and encouragement whilst I was in hospital in 1981. Mr A G Thompson and his medical team for their care and attention at the Royal Orthopaedic Hospital in Birmingham; The University of Aston Health Centre, for their help whilst I was ill.

My Mother, Sisters and Brothers, for their continual encouragement, financial support and moral help. My Children, for their understanding of our situation, their intelligence and their sacrifices and patience.

The University of Technology in Baghdad, for their initial financial support.

CONTENTS

LIST OF FIGURES

LIST OF TABLES

LIST OF PLATES

CHAPTER ONE

INTRODUCTION

The drying of solids is an operation of widespread importance in the chemical industry and in the processing of natural products. Indirect drying involves vaporisation of the liquid contained by the solid, followed by the removal of the vapour in a stream of air or other carrier gas. For this purpose the liquid, normally water, in the solid must travel from the interior out to the surface and this may involve a number of mechanisms. The basic requirement is the supply of the heat of vaporisation of the water and a sufficient flow of air for removal of the vapour. The energy requirement is large because of the latent heat of vaporisation. Thus, there is a wide variety of dryer designs, to cater for the specific solid, drying conditions and finished product specification. Economy of energy usage is however important with all designs (1).

The drying process for slurries or solutions dried as droplets is similar to that for wet bulk solids. Characteristically the rate of drying tends to be constant whilst the surface remains saturated, referred to as the constant rate period, followed by a period, or periods, in which the rate falls off with time. The latter arises because moisture must travel to the surface, generally by diffusion through pores in the formed crust. However, movement of liquid in a solid 'crust' may be caused by various forces and possible mechanisms discussed in the literature are;

1. Liquid diffusion due to difference in moisture concentrations.
2. Liquid movement due to capillary forces.
3. Vapour diffusion in partly air-filled pores, due to differences in partial pressures.
4. Liquid or vapour flow due to differences in total pressure, generated by external pressure, capillary movement, shrinkage, or high temperature inside the moist material.

Spray drying involves the transformation of a feed of solution, or slurry, into particulate dried-product by the removal of moisture in a single operation. In practice feed can be either a solution, suspension or paste depending on the upstream process. The feed is atomised to provide a large surface area, and the spray is contacted with a gaseous drying medium. A process of simultaneous heat and mass transfer occurs between the droplets and the hot gas streams. The dried product is then

recovered in a series of separation stages.

Either of two systems are used to recover the product from co-current flow spray dryers. One arrangement involves separation of dried product at the base of the drying chamber. During operation, the majority of product falls to the base of the chamber, while a small fraction passes out entrained in the air and is recovered in a cyclone. Hence this system involves primary product discharge and a secondary product discharge. The second arrangement involves total recovery of dried products in the separation cyclone equipment (2).

A desirable commercial product is generally one which is dust-free, contains no large agglomerates and evenly -dried (i.e. without any fraction degraded due to excessive temperature or residence time). The manner in which spray contacts the drying air is an important factor in spray dryer design, since this affects dried product properties by influencing droplet behaviour during drying. The gas flow may be cocurrent flow in which feed and air pass through the dryer in the same direction. This arrangement is widely used for products where rapid crust formation is desirable and the products are heat-sensitive. Alternatively, the spray can be contacted with air in countercurrent flow or mixed flow. Drop sizes are generally in the range 10 to 1000 μm (2).

The process of spray drying finds extensive use when it is able to meet the dried product specification most desirable for subsequent processing or direct consumer usage e.g. a dust-free product for easy dispensing or dissolution. The process is characterised by its flexibility in meeting product requirements. Applications have arisen in all major industries ranging from production under the most stringent of conditions in food and pharmaceutical manufacture to bulk chemicals.

The atomisation stage in spray drying produces a dispersion of droplets having a high surface-to-mass ratio. With correct drier design and operation the dried product that results from moisture evaporation from the spray can be arranged, within limits, to possess the desired particle size distribution through control of the atomisation variables. The ideal requirements of an atomiser is to produce a homogeneous spray.

In practice however, sprays are not homogeneous; therefore there is a distribution of drop sizes and velocities in the drying chamber. This variation of drop size and residence time clearly has a fundamental influence on drying efficiency.

Drying involves combined heat and mass transfer. Upon contact between an atomised droplet and drying air, heat is transferred by convection from the air to the droplet; the vaporised moisture is transferred into the air by convection through the boundary layer surrounding each droplet. As indicated earlier, atomised droplets should ideally be equi-sized to produce a product which is equi-dried and containing no fines or agglomerates unless they are required. A wide droplet size distribution can result in failure to dry the larger particles, wall deposits due to impingement of undried particles, and/or in decomposition or overcuring of the smaller particles and poor thermal efficiency. Hence the importance of control of the particle size and size-distribution in spray drying is reflected in both the actual drying process and in the end product itself.

In summary, the spray drying process is one in which a liquid is finely dispersed in a gas, usually with a nozzle or a rotary atomiser. At the outlet of the nozzle or atomiser a liquid film, or a series of jets, are formed which disintegrate into small droplets. Once the droplets contact hot gas evaporation commences; at some stage a skin or crust forms which acts to resist mass transfer i.e. evaporation from the droplet surface is generally controlled by the thickness and porosity of the crust. As a particle dries, the crust increases in thickness resulting in an increase in the resistance to heat and mass transfer. This invariably increases the core temperature causing a reduction in the partial pressure and temperature driving force. The transfer process is therefore highly complex and difficult to model mathematically. Furthermore following crust formation, fracture, shrinkage or inflation may occur; these further complicate the modelling of heat and mass transfer and, of course, affect the final form.

Because of the complexities, spray drying of solutions or slurries in pilot scale equipment yields limited information regarding drying mechanisms and scale-up appears to be largely empirical. Therefore, evaporation from single drops of pure liquid and the drying of single drops has received some attention. The experimental

methods have involved suspension of drops >1mm to < 10 mm on filaments or nozzles or their retention in 'free-flight', by adjustment of the gas velocity, or for drops less than 10μm using an electrostatic field. However, a great deal remains to be done in this area with experimentation covering the complcte range of conditions likely to be encountered in spray drying. The aim of single drop investigations is to develop a method of predicting the drying rates of drops and to obtain fundamental information on the phenomena occurring during the drying process.

The present study was therefore initiated to further the understanding of the mechanisms involved in the drying of drops containing solids with the objective of improving the design of spray dryers and the quality of dried-products. The experimental investigation covered the evaporation of pure water droplets, the drying of solutions of organic and inorganic drops, and the drying of slurry drops of organic commercial products.

Experimentation involved two different methods of drop retention during drying:

(i) Drops suspended from a rotating nozzle in a horizontal wind-tunnel and hence drying as a hemisphere.

(ii) Drops of 1 to 7 mm held in free-flight in a vertical wind-tunnel resulting in a spheroid-based shape.

In addition some pilot-scale spray atomisation and spray drying studies were performed. The single drop results for both heat and mass transfer were correlated by modified, conventional methods and the pilot studies are discussed to assist scale-up procedures which are not product-specific.

Together with on-going work in the areas of spray-atomisation and characterisation of gas flow patterns in a large-scale tower, tlie progress reported should assist in strengthening the scientific base for spray-drying operations.

CHAPTER TWO

INTERPHASE MASS TRANSFER FUNDAMENTALS

When a concentration gradient exists within a fluid, or across a phase boundary, mass transfer will occur to reduce this gradient. Hence, when a liquid droplet evaporates into a still gas, vapour is transferred from the surface to the bulk of the gas as a result of the concentration gradient (3); the process continues until either all the liquid has evaporated, or the gas is saturated and the concentration gradient reduced to zero. Fick (4) in 1885 deduced by analogy with heat transfer that the rate of diffusion of component A in a mixture of two components, A and B, is directly proportional to the concentration gradient.

$$N_{(A)} = - D_{AB} \frac{dC_A}{dy} \qquad (2.1)$$

Equation (2.1) is often referred to as Fick's Law of Diffusion. When the fluid flow is turbulent, eddy diffusion takes place in addition to molecular diffusion and the overall rate of diffusion will increase. Vaccarezza et al (5) used Fick's Law to predict internal moisture distributions during the drying of sugar beet root dried at 81^{o}C in a vertical duct. No significant internal temperature gradients were determined in sugar beet root during drying, but the material temperature was found to be time-dependent. Moisture diffusivity was strongly affected by material temperatures. At the beginning of drying the material temperature increased rapidly towards the air temperature; when 90% of the initial moisture had been evaporated the difference between the material and air temperature became negligible. Plots of moisture change versus time gave a straight line indicating that Fick's Law with a constant diffusion coefficient was obeyed. However, application of Fick's Law was only useful for correlation of temperature and moisture change of sugar beet root during the first falling-rate period of drying.

2.1 MECHANISMS OF INTERPHASE MASS TRANSFER

In most of the important applications of mass transfer e.g. drying, distillation, liquid-liquid extraction, etc. material is transferred across a phase boundary. Since no material accumulates at the interface, the rate of transfer on each side must be equal and therefore the concentration gradients automatically adjust themselves so that they are proportional to the resistance to transfer in the particular phase.

The mass transfer rate between two fluid phases will depend upon,

a) the physical properties of the two phases,

b) the concentration difference,

c) the interfacial area, and

d) the degree of turbulence.

Mass transfer equipment is therefore generally designed to give the largest area of contact between the phases achieved without introducing unfavourable flow behaviour.

When a drop is introduced into a drying chamber the evaporation initially takes place from its free (i.e. saturated) surface. Resistance to mass transfer is then only in the gas film around the drop and the rate of vapour diffusion in the surrounding media depends on the concentration driving force between water vapour in the drying media and water vapour around the drop. Diffusivity of vapour is inversely proportional to the pressure and varies with the absolute temperature to the 1.5 power (6). Table 2.1 shows diffusivities for a number of vapours and gases in air at 25°C and 1 atm.

Table 2.1 Diffusion Coefficient of Gases and Vapours in Air (6).

Substance	Diffusivity $cm^2.s^{-1}$
Ammonia	0.236
Carbon Dioxide	0.164
Water	0.256
Ethyl Ether	0.093
Acetic Acid	0.133
Benzene	0.088

In drying the resistances generally comprise that limiting moisture diffusion in the solid and that restraining water vapour convection in the gas phase. The process involves diffusion of liquid or vapour through the solid to the surface, where evaporation takes place, followed by diffusion of the vapour into the drying medium, usually air. A relatively

stagnant air film on the solid surface represents a resistance to the passage of vapour from the surface into the air. The sum of the surface resistance to vapour diffusion and the internal resistance to liquid or vapour diffusion through the solid constitutes the total resistance to transfer of moisture from the droplets to the drying medium. The gas phase resistance is a function of the degree of turbulence, as in all conventional fluid mass transfer processes. The mechanisms proposed to describe the mass transfer across a phase boundary are discussed in the following sub-sections 2.2.1 to 2.2.4.

2.2 THEORETICAL MODELS

The phenomena associated with interphase transfer are complex, and a number of simplified models have therefore been proposed to describe it. The earliest attempt to explain the mechanism of mass transfer across an interface is the Whitman Two-Film Theory (7). This assumes that the resistance to transfer in each phase can be regarded as lying in a thin film close to the interface. In 1935, Higbie (8) suggested that the transfer process is largely attributable to fresh material being brought by eddies to the interface, where a process of unsteady-state transfer takes place for a fixed period at the freshly-exposed, surface. Danckwerts (9) modified this theory by considering the material brought to the surface to remain there for a varying period of time. Toor and Marchello (10) subsequently proposed a more general theory, the Film -Penetration Theory, and showed that each of the earlier theories is a particular limiting case of their own.

2.2.1 Two-Film Theory

In 1923, Whitman (7) attempted to describe the mechanism of mass transfer at the interface between two fluids. The turbulence in the two phases was assumed to die out near the interface such that a laminar layer exists in each of the two fluids. The total resistance to transfer was considered to lie within these thin, laminar layers on either side of the interface, in which transfer occurs by purely molecular diffusion, and it was suggested that the film resistances were additive. The concentration gradient is linear close to the interface and gradually becomes less at greater distances as shown by the full lines ABC and DEF in Figure 2.1.

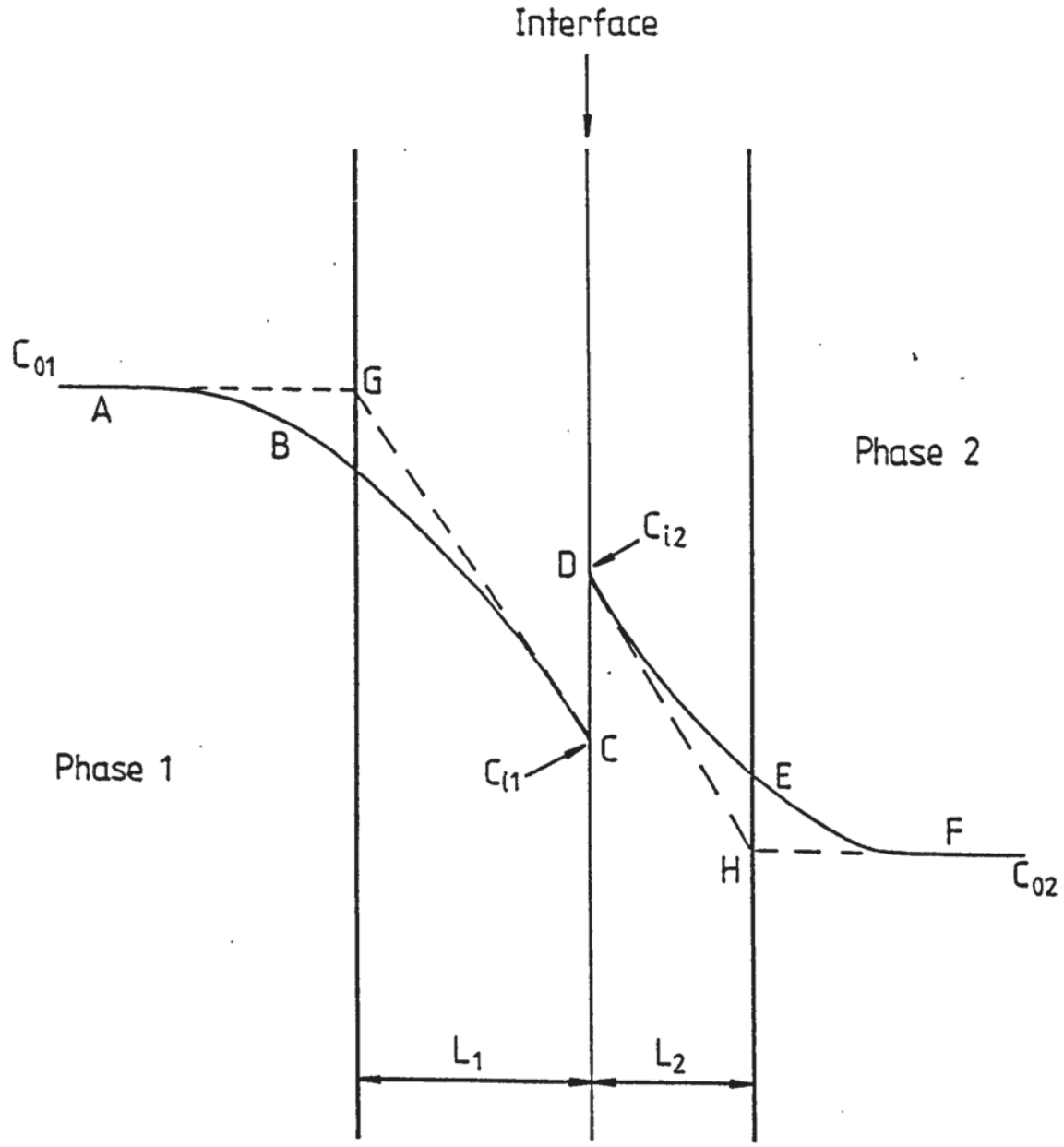

Figure 2.1 Two-Film Theory
Representation of Concentration Gradients.

The basis of the theory is the assumption that the zones in which the resistance to transfer lie can be replaced by two hypothetical layers L1 and L2, on either side of the interface, in which the transfer is entirely by molecular diffusion. The concentration gradients within L1 and L2 are linear and zero outside them. Equilibrium is assumed to exist at the interface. The mass transfer is treated as a steady-state process, thus limiting the theory to the case where the time taken to establish the concentration gradients is very small compared with the time of transfer, or where the capacity of the films is negligible. The model predicts that the overall mass transfer coefficient is directly proportional to the diffusivity D_v.

2.2.2 Penetration Theory

The work of Higbie (8) laid the basis of the Penetration Theory for unsteady-state mass transfer. This is based on the assumption that eddies in the bulk fluid bring discrete elements to the interface where they are exposed to the second phase for a definite interval of time, after which the surface elements are re-mixed with the bulk fluid. It is assumed that equilibrium is immediately attained by the surface layer and that a process of unsteady-state molecular diffusion then occurs and that the elements are remixed with the bulk fluid after a fixed period of time. The existence of velocity gradients within the fluids is ignored, i.e. the fluid at all depths is assumed to be moving at the same rate as the interface. By solving the unsteady state equation Higbie showed that the mass transfer coefficient is proportional to $(D_v)^{0.5}$.

Danckwerts (9) modified the Penetration Theory by suggesting the surface as being replaced continuously by fresh fluid in a random way. On the assumption that the rate of production of fresh surface S_f, is independent of the age of the element, he showed that the mass transfer coefficient is proportional to $(D_v.S_f)^{0.5}$.

2.2.3 Film-Penetration Theory

The Film-Penetration model, presented by Toor and Marchello (10) incorporates some of the principles of both the Two-film Theory and the Penetration Theory. Mass transfer is considered to occur as an unsteady-state process with resistance to transfer residing within a laminar film at the interface, as in the Two-Film Theory.

Surface renewal is assumed to occur at intervals due to eddy currents in the bulk fluid. Toor and Marchello's analysis showed that for a short exposure time, mass transfer across a boundary can be modelled by the Penetration Theory. For prolonged periods of exposure, when steady-state conditions arise, the Two-Film Theory is applicable.

2.2.4 Boundary Layer Theory

Boundary layer theory is applicable to the prediction of mass and heat transfer coefficients for spherical droplets. When a fluid flows over a solid surface, a velocity gradient is set up in the boundary layer. If there is a difference in temperature between the surface and the fluid, heat transfer will take place. If a concentration gradient exists mass transfer will take place simultaneously. The equations of motion, continuity and energy can be solved approximately to obtain the velocity, concentration and temperature profiles in a thin layer at the interface. Frossling (11) applied this theory to evaporating liquid drops of nitrobenzene, aniline and water of radius 0.1 to 0.9 mm in air flow of velocity 0.2 to 7 $m.sec^{-1}$. The mass transfer coefficient was found to be proportional to $(D_v)^n$, where n = 0.348 i.e. approximately 1/3rd.

2.3 MASS TRANSFER COEFFICIENTS

On the basis of the theories discussed above, the rate of mass transfer is directly proportional to the driving force, expressed as a molar concentration difference between the interface and the bulk phase, thus:

$$N_A = k_1 (C_i - C_b) \qquad (2.2)$$

where N_A = mass transfer rate per unit area

k_1 = mass transfer coefficient, and

C_i, C_b = molar concentration of the diffusing species in the interface and the bulk phase respectively.

When mass transfer occurs across a phase boundary (3) without accumulation at the interface, the mass transfer rate on each side of the phase boundary can be equated:

$$N_A = k_1 (C_{b1} - C_{i1}) = k_2 (C_{i2} - C_{b2}) \qquad (2.3)$$

If there is no resistance to transfer at the interface, C_{i1} and C_{i2} will be the corresponding values in the phase-equilibrium relationship. As the values of the concentration at the interface are generally unknown, the mass transfer coefficient is considered for the overall process:

$$N_A = k_1 (C_{b1} - C_{e1}) = k_2 (C_{e2} - C_{b2}) \qquad (2.4)$$

For a linear equilibrium relationship,

$$H_1 = \frac{C_{i1}}{C_{i2}} = \frac{C_{e1}}{C_{e2}} = \frac{C_{b1}}{C_{b2}} \qquad (2.5)$$

where H_1 is the proportionality constant, i.e. Henry's Constant.

From equations (2.3), (2.4) and (2.5) a relationship between the various transfer coefficeints could be expressed as:

$$\frac{1}{K_o} = \frac{1}{H_1 k_1} + \frac{1}{k_2} \qquad (2.6)$$

For the special case of the drying of droplets containing solids an additional crust resistance exists and this can be represented by the crust coefficient. The overall mass transfer coefficient therefore depends on both gas film and crust coefficients, neglecting any resistance at the interface.

To maximise the interfacial area in spray drying the feed is atomised to produce droplets generally of initial diameter in the range of 20 to 500μm (12). The particle size obtained in spray drying is affected by the mode of atomisation, the solids content of the feed and the drying conditions (13). Fine atomisation increases the drying rate, but in practice, may also result in a significant quantity of fines <20μm in the finished dry product (2). These may either be removed in a subsequent separation stage and recycled, or be agglomerated in a second stage e.g. using a fluidised granulation process, or a small amount of liquid may be added to promote agglomeration to give a 'dust-free' product (14, 12). In any event fines represent inefficient operation and recycling/reprocessing may result in product degradation e.g. with dyestuffs.

2.4 PRACTICAL CONSIDERATION OF MASS TRANSFER

Spray dryer design clearly requires consideration of a combination of heat transfer, mass transfer and fluid dynamics. Colburn (15) developed a general method for correlating forced convective heat transfer data using the relationship:

$$St.Pr^{0.67} = 0.023\ Re^{-0.2} \qquad (2.7)$$

The above equation formed the basis of the analysis for the j-factor of Chilton and Colburn (16).

2.4.1 The j-Factor for Heat Transfer

For heat transfer by convection to a fluid flowing through a tube Chilton and Colburn (16) correlated their experimental results in the dimensionless form:

$$Nu = 0.023\ Re^{0.8}.Pr^{0.33} \qquad (2.8)$$

Division of both sides of equation (2.8) by the product Re.Pr gives the well-known correlation of j-factor for heat transfer, j_h

$$\frac{Nu}{Re.Pr} = St = 0.023\ Re^{-0.2}.\ Pr^{-0.67} \qquad (2.9)$$

or

$$St.Pr^{0.67} = j_h = 0.023\ Re^{-0.2} \qquad (2.10)$$

Chilton and Colburn found that the plot of j_h versus Re gave approximately the same curve as the friction chart for flow in tubes.

2.4.2 The j-Factor for Mass Transfer

By analogy to heat transfer under forced convective conditions, Chilton and Colburn (16, 17) deduced that the rate of mass tranfer to, or from, a surface could be correlated in the form of three dimensionless groups:

$$\frac{k_g d_p}{D_v} = f\,(Re.Sc) \qquad (2.11)$$

By a similar method as for heat transfer they developed the j-factor for mass transfer, j_d

$$j_d = \frac{k_g P_{gf} M_m}{G} \cdot Sc^{0.67} \qquad (2.12)$$

Several workers performed experiments to establish a relationship between j_h and j_d. Gilliland and Sherwood (18) vaporised a number of pure liquids including water, toluene, aniline and propylamyl and butyl alcohol into an air stream flowing upwards in a wetted-wall column. When plotted logarithmically as,

$$\frac{k_g P_{gf} M_m}{G} \text{ versus Re}$$

the data yielded straight lines. By introduction of the Schmidt group the points for all the liquids were brought onto the same line represented by,

$$\frac{k_g P_{gf} M_m}{G} \left(\frac{\mu}{\rho D_v} \right)^{0.56} = 0.023\ Re^{-0.17} \qquad (2.13)$$

The index of the Schmidt group, $(\mu/\rho D_v)$, was evidently significantly less than the index of 2/3 for the Prandtl group for heat transfer. However, Maisel and Sherwood (19) performed experimental work in which water was evaporated from flat plates into air; water from cylinders into carbon dioxide or helium; benzene or carbon tetrachloride from cylinders into air; and benzene from spheres into air and their results showed good agreement with equation (2.12). Sherwood and Pigford (20) have shown that if the data of Gilliland and Sherwood (18) and others (19, 21) were plotted with the Schmidt number raised to the power 2/3, a reasonably good correlation was obtained. They also established that values of both j_d and j_h were approximately equal to the corresponding friction factor $R_f/\rho U^2$.

Linton and Sherwood (22) measured the rates of solution of benzoic acid, cinnamic acid and β-napthol into water under turbulent flow and for the range $1000 < Sc < 3000$ the results confirmed the index of 2/3 for the Schmidt group in equation (2.12).

Corresponding values of the j-factors for heat and mass transfer have been found to be approximately equal. This was confirmed by Maisel and Sherwood (19). Hence values of the mass transfer coefficient can be estimated from the corresponding

values of the heat transfer coefficients or vice versa.

However, the application of j-factors has its limitations. Sherwood (21) investigated the relationship between mass transfer and friction in turbulent flow. He calculated the approximate value of the skin friction (viscous drag at the surface) by subtracting the form drag (additional drag caused by the eddies set up as a result of the fluid impinging on an obstruction) from the total drag force. Only after isolation of form drag from the total drag force was he able to obtain reasonable agreement between corresponding values of j_h, j_d and $R_f/\rho U^2$.

The applicability of the Chilton-Colburn analogy to spray drying is also restricted since when a droplet containing dissolved, or suspended, solids is being dried in a hot medium concentration occurs until at some point it no longer presents a free vapour-liquid interface to the air stream. Once a crust forms the j-factors for heat and mass transfer are no longer equivalent.

Audu and Jeffreys (23) in an investigation on drying of single drops of aqueous slurries, identified the difference in the paths for heat and mass transfer. Initially a free liquid interface exists between the gas stream and the solution being dried, and evaporation proceeds as for a pure liquid. However, when the drop is concentrated beyond saturation a crust starts to form and separate the gas and liquid interface. This produces a particle with a saturated solution core. Subsequently, drying takes place by heat conduction through the solid in the crust and evaporation 'ideally' via pores in the crust. Thus the paths of heat and mass transport are completely different and the Colburn analogy can no longer be applicable. This is confirmed by the cracks and ruptures observed in particles of many spray-dried products. With such particles the rate of drying is probably so intense that jets of steam issue from the pores. In the extreme the particle may be fragmented by a pressure explosion, resulting in undesirable fines.

The theory described above is valid for single droplets prior to crust formation, and where no inter-drop-interaction or impingement on walls occurs. In practice, however when drying drops of solutions or slurries:

i) Drop shapes are not absolutely spherical i.e. drop drying is sometimes

accompanied by deformation. Therefore the area is difficult to calculate.

(ii) Some agglomeration occurs, due either to natural impingement of wet particles or fine particles stuck on the surface of larger particles. Over-dried, mis-shapen material may also result from drying of solution after hitting the walls.

(iii) Other mechanisms of moisture movement (e.g. displacement by shrinkage release by 'explosions 'or blow-holes, drop collapse, etc.) occur depending on the product and drying conditions.

(iv) A homogeneous spray is not generated.

(v) Formation of a crust generally introduces a controlling resistance to mass transfer.

All these factors are discussed in subsequent Chapters.

CHAPTER THREE

DROPLET HEAT AND MASS TRANSFER PROCESSES

The evaporation of liquid droplets is a process involving simultaneous heat and mass transfer. The basis of the theory related to evaporation from droplets, motionless relative to an infinite and uniform gaseous medium, was laid by Maxwell (24). For a perfectly spherical droplet (24) with a vapour concentration at the surface C_s continuously saturated it was shown that,

$$- dm/d\theta = 4\pi r.D_v (C_s - C_\infty) \qquad (3.1)$$

From equation (3.1), a gas phase mass transfer coefficient can be defined under stagnant conditions as:

$$k_g = \frac{-dm/d\theta}{4\pi r^2 (C_s - C_\infty)} = \frac{D_v}{r} \qquad (3.2)$$

and the Sherwood number can thus be expressed as:

$$Sh_o = k_g.2r/D_v = 2 \qquad (3.3)$$

For a dynamic equilibrium the rate of heat transfer is equal to the product of the rate of mass transfer and the latent heat of vaporisation (λ). The rate of heat transfer from the saturated surface is,

$$\frac{dQ}{d\theta} = h_c A \ (T_a - T_s) = \frac{dm}{d\theta} \lambda \qquad (3.4)$$

Following the heat and mass transfer analogy (3) the Nusselt number can be expressed as,

$$Nu_o = h_c.2r/k = 2 \qquad (3.5)$$

Mass transfer rate increases with an increase in relative velocity between the droplet and the surrounding air due to the additional evaporation caused by the convection in the boundary layer around the droplet. To include the increase in evaporation rate due to droplet motion Frossling (11) deduced that the right-hand side of equation (3.3) should be multiplied by a wind factor, i.e.

$$Sh = 2 (1 + \beta \ Re^{1/2}.Sc^{1/3}) \qquad (3.6)$$

where $\beta = 0.276$

The validity of these equations has been confirmed by numerous authors and they are discussed further in Sections 3.1 and 3.2.

3.1 Evaporation From Single Droplets and Spheres

Conclusions drawn from studies on the evaporation of single drops, and the phenomena associated with the evaporation process, form the basis for understanding the evaporation mechanisms in spray drying. Thus fundamental data on factors influencing the rate of heat and mass transfer for droplets are important to the operation of spray drying.

Studies of the evaporation from drops involve,

a) Determination of rate of heat transfer to the drop surface.

b) Determination of rate of evaporation and mass transfer from the drop.

c) Determination of temperature and concentration at the drop surface during evaporation.

d) The effect on evaporation rate of the original drop temperature, heats of solution and crystallisation,and the way in which solid surfaces form.

For convenience the following literature review is divided into two sub-sections dealing with evaporation from single droplets (or spheres) under conditions of natural convection or forced convection respectively.

3.1.1 Under Natural Convection

Evaporation from the surface of a sphere of volatile material into a still atmosphere is a diffusion-controlled process. Rates of evaporation were first determined in 1882 by Sreznevsky (42). Experiments were conducted using a convex liquid meniscus at the upper end of a tube of 3mm diameter, and on drops of liquid placed on the flat top of vertical, cylindrical columns of 1.8 to 3.6 mm diameter. The rate of evaporation was determined by following the outline of the drop through a horizontal microscope. If the base of a spherical drop resting on a horizontal plane remains unchanged during evaporation, then the decrease in volume of the drop divided by its free surface equals half

the rate of fall of the summit of the drop. In fact, the volume (V) and free surface (S) of a spherical segment of height (h) and radius of base (r) are expressed by

$$V = \frac{\pi h}{6} (3r^2 + h^2) \qquad (3.7)$$

$$S = \pi (r^2 + h^2) \qquad (3.8)$$

Differentiation of (3.7) with respect to time gives,

$$\frac{dV}{d\theta} = \frac{\pi}{2} (r^2 + h^2) \frac{dh}{d\theta}$$

$$= \frac{S}{2} \frac{dh}{d\theta} \qquad (3.9)$$

Using this theorem, Sreznevsky determined the rates of evaporation of hemispherical droplets of water, benzene, ether and chloroform with varying columns (and hence droplet) radius and found the relationship,

$$r \frac{dh}{d\theta} = \text{Constant} \qquad (3.10)$$

Morse (43) studied the evaporation into still air of spheres of iodine resting on the pan of a microbalance. He confirmed that the rate of evaporation was porportional to the radii of the spheres. Morse's results were examined by Langmuir (44); the latter derived an equation similar to Maxwell, and hence calculated the diffusion coefficient for iodine diffusing into air at atmospheric pressure, and at 20°C.

Whytlaw-Gray et al (45) performed experiments in 1934 on drops of water, aniline, quinoline, methyl salicylate and p-cresol with radii of 1 to 2mm. They found that the surface of the drops decreased linearly with time as shown in Figure 3.1, although the volume decreased by a factor of almost a hundred. No further experiments were made on drops placed on a flat support; instead, droplets were supported on thin filaments. Measurements by this method were first made in 1927 by Topley and

Whytlaw-Gray (46) on spheres of iodine of radius lmm fused to a quartz fibre and suspended from a quartz spring-balance in a cylindrical vessel of radius 2 cm. The walls and bottom of the vessel were covered with a thin layer of potassium hydroxide to absorb the iodine vapour.

Houghton (47) measured the rate of evaporation of drops of water suspended from a glass fibre using a horizontal microscope with an ocular scale. The fibres were covered with a thin layer of paraffin to reduce the distortion and to prevent wetting up the fibre. Fibres of radii 1.25, 12.5, 42 and 125μm were used on which drops of radii 50 to 250, 150 to 600, 500 to 1000μm and > 1000μm respectively could be supported. No details were published regarding the dimensions of the experimental chamber. The drop temperature was not measured, it being assumed to equal the temperature of wet-bulb thermometer placed in the chamber.

In their thorough investigation Langstroth, Diehl and Winhold (48) measured optically the rates of evaporation of drops of water and of a number of organic liquids; e.g. n-butanol, n-propanol, toluene, ethylbenzene and aniline, of 1.4 mm diameter. The drops were suspended from glass fibres of 50 μm radius, or from copper-constantan thermocouples. Experiments were performed within spherical vessels of 15, 20, 31 and 43 mm diameter. The inside of the vessel was covered with a thin layer of active charcoal, or for water a mixture of charcoal and phosphorous pentoxide, to absorb the vapour. Radiation effects were accounted for but the heat flux through the glass fibre was ignored. No difference was detected in the slope of the predictable, straight lines of the plot of d_p^2 versus time for water droplets suspended from a fine thermocouple when 15, 20 and 31 mm diameter vessels were used. The slope was from 13% to 22% greater when a 43 mm diameter vessel was used; this increased evaporation rate was attributed to the occurrence in the large vessel of convective air currents which were inhibited in the smaller vessels by increased resistance to convection.

Ranz and Marshall (26) investigated the rate of evaporation of single droplets of pure liquids, i.e. water, benzene, and aniline, suspended from the end of a glass capillary and thermoelement, inside a special dryer. The study covered drop

diameters ranging from 0.06 to 0.11 cm and air temperatures up to 220°C. They correlated their experimental results by the expressions,

$$Nu_o = 2.0 + 0.6\ Pr^{0.33}\ Gr^{0.25} \qquad (3.11)$$

$$Sh_o = 2.0 + 0.6\ Sc^{0.33}\ Gr^{0.25} \qquad (3.12)$$

Mathers et al (49) were the first to solve the simultaneous heat and mass transfer equations numerically for natural convection. In their investigation experiments were conducted on internally-heated brass spheres coated with naphthalene. In separate experiments the temperature difference between the coated sphere and the air was varied in the range 0°C to 23°C; a limited number of experiments were also carried out at low temperatures in the range -40°C to -10°C using benzene as the sphere-coating, and at atmospheric pressure. They proposed,

$$Nu_o = 2.0 + 0.282\ (Gr.Pr)^{0.37} \qquad (3.13)$$

$$Sh_o = 2.0 + 0.282\ (Gr.Sc)^{0.37} \qquad (3.14)$$

for Gr.Pr (or Sc) < 100

and

$$Nu_o = 2.0 + 0.5\ (Gr.Pr)^{0.25} \qquad (3.15)$$

$$Sh_o = 2.0 + 0.5\ (Gr.Sc)^{0.25} \qquad (3.16)$$

for $10^2 <$ Gr.Pr (or Sc) $< 10^6$

Equations (3.13) and (3.15) represent the heat transfer process whilst equations (3.14) and (3.16) represent the mass transfer process.

Experiments on heat transfer from spheres involving natural convection were performed by Yüge (50). He studied the heat transfer from internally-heated, carbon-chrome steel or brass, spheres of different sizes in the range 1 to 6 mm diameter. The sphere was suspended from two sides by thermocouple wires. The empirical correlation derived for heat transfer by natural convection is,

$$Nu_o = 2.0 + 0.392\ Gr^{0.25} \qquad (3.17)$$

for $1 <$ Gr $< 10^5$

Experiments involving natural convection were also performed by

Steinberger and Treybal (51) using benzoic acid spheres immersed in a Dewar flask. The flask was filled with water and allowed to stand for 8 hrs on a thick rubber pad to damp fluid circulations. A benzoic acid sphere was gently lowered into the stagnant fluid, a Lucite cover being used to support the sphere and a thermometer. The next day the sphere was carefully removed from the flask and the solution was mixed and titrated for benzoic acid content. The data were correlated separately according to the boundary layer becoming turbulent for $(Gr.Sc) < 10^8$

$$Sh_o = 2 + 0.569\ (Gr.Sc)^{0.25} \qquad (3.18)$$

and for $(Gr.Sc) > 10^8$,

$$Sh_o = 2.0 + 0.0254\ (Gr.Sc)^{0.33}(Sc)^{0.244} \qquad (3.19)$$

However, only three data points were available for establishing equation (3.19) so that the accuracy attributed to the constant and exponents is questionnable.

Using a quasi-steady vaporisation model developed earlier (52), Frazier and Chang (53) fitted the experimental results of Hoffman and Gauvin (54) for 0.4 to 1.4 mm drops of water, methanol, cumene, pentane or benzene at surrounding temperatures from 100°C to 550°C. For low temperatures, where the influence of radiation was small, the evaporation rate could be expressed as,

$$\dot{m}' = \dot{m}'_o\ (1 + f\ (Gr.Pr)) \qquad (3.20)$$

For the evaporation process under conditions including radiation effects

$$\frac{dm}{d\theta} = \dot{m} = \dot{m}_o\ \left(1 + \frac{\dot{m}_o'}{m_o}\ f\ (Gr.Pr)\right) \qquad (3.21)$$

where $f\ (Gr.Pr) = A\ (Gr.Pr)^{1/n}$

$A = 0.15, n = 2; Gr < 4.22/Pr$

$A = 0.215, n = 4; 4.22/Pr < Gr < 10^5$

The evaporation of free drops can be studied by supporting charged droplets in a Millikan condenser. The droplet is introduced into the apparatus and the

potential across the condenser continuously varied such that the electrostatic and gravitational fields are balanced and the droplet remains stationary. However, the maximum size of droplet which can be studied by this method is limited to a few microns, since both the size of the drop and the strength of the field have upper limits. Woodlands and Macks (55) published results from measurements of the rate of evaporation of dibutyl tartrate drops of diameter 3.34 μm and dibutyl phthalate drops of diameter 2.5μm. Shereshefsky and Steckler (56) performed similar experiments with dibutyl phthalate drops of initial diameters 1.26 to 5.32 μm, Nestle (57) and Schafer (58) with drops of mercury, and Gudris and Kulikova (59) with drops of water. The above research demonstrated that the Millikan condenser provided less accurate results than the method of suspended droplets; however it does enable droplets as small as ~1 to 6 μm to be studied.

3.1.2 Under Forced Convection

The results of greatest practical importance are those for the evaporation of droplets moving relative to a gaseous medium under the influence of gravity and/or inertia since this is the situation in spray dryers. Pritchard and Biswas (60) have provided a theoretical review on mass transfer from drops in forced convection. Most measurements of the rate of evaporation of droplets were made on fixed drops ventilated by a stream of gas.

The first measurements of rates of evaporation in a gas stream were made by Majama and Togino (6l). Individual drops of organic liquids or water, of 0.2 mm diameter, were placed on a horizontal glass fibre of radius 2.5μm in an air current of velocity up to 18ms^{-1}. The rate of change of diameter squared was found to be constant.

The most accurate measurements of the rate of evaporation of drops suspended in an air current were those of Frossling (ll) whose extremely-careful investigation served as a model for all subsequent work in this field. The experiments were carried out at 20°C using drops of water, aniline or nitrobenzene and spheres of naphthalene with initial diameters in the range 0.2 to 1.8 mm suspended in a wind tunnel. The drops of organic compounds were suspended from glass fibres of diameter 20 to

200μm or from a Constantan-Manganin thermocouple for water drops; the air current was directed from below, and velocities were varied within the range 0.2 to 7 $m.s^{-1}$. Evaporation rates, determined by periodically photographing the drop, were correlated by equation 3.6.

Frossling observed a variation in the rate of evaporation over the surface of a sphere of naphthalene; the average rate of evaporation from the forward (exposed) face was approximately ten times greater than the rate from the rear side of the sphere. Boundary layer theory predicts that the rate of transfer should be a maximum on the front side of the drop (facing the oncoming air stream), decrease to a minimum value near the separation point and increase to another, but lower, maximum rate on the trailing face which experiences velocities in the reverse direction.

For free-falling droplets, Vyrubov (62) studied the rate of evaporation of 2mm diameter water drops falling in a vertical tube 1 m long, down which heated air at 40°C to 100°C was passed at $1ms^{-1}$. The drops fell onto a weighing pan, so that their dimensions could be determined from the residual mass. The results were expressed in the form

$$Sh = 0.52\ Re^{0.5} \qquad (3.22)$$

at $100 < Re < 500$

Evaporation of water drops af 0°C to 40°C was studied by Kinzer and Gunn (63) using high-speed, still photography. Drops of diameter 10 to 140 μm dispersed from a capillary connected to the terminal of a battery became charged on breaking-away and allowed to fall freely through detector rings. For drops > 1 mm they used an 80 mm high,conical tube through which air was blown at a constant rate. A drop introduced into the tube assumed a definite position, where the weight of the drop equalled the hydrodynamic force, and as evaporation proceeded it moved up the tube. For the range of drop sizes 0.6 mm to 3.00 mm diameter, they obtained the same relationship as Frossling (equation 3.6)with a β value of 0.23 for $100 < Re < 1600$. At very small Re (less than 0.9) the wind factor was found to be unity, i.e. $\beta = 0$. On further increasing Re the wind factor rose; β increased to a value of 0.46 at $Re = 4$ and then gradually fell to the

above-mentioned value of 0.23 at Re = 100.

Johnston and Eade (64) measured the rate of evaporation of drops of dibutyl phthalate (0.4 mm to 0.7 mm in diameter) suspended from glass fibres, and of molten sulphur (0.8 to 1.0 mm diameter) on filaments of Wolframite, at 130°C to 190°C in a, 20 mm diameter, horizontal tube. They determined the time for complete evaporation of the drop as a function of its initial radius, and their results agreed favourably with theoretical predictions.

The fundamental experiments of Ranz and Marshall (26) in 1952 on pure liquid droplets confirmed Frossling's results. β was found accordingly to be equal to 0.3. In their work Ranz and Marshall (26) suspended individual drops of aniline, benzene or water from a glass capillary sealed to the delivery tube of a microburette at air tempertures up to 220°C. Liquid was supplied continuously through the burette at such a rate that the size of the drop remained constant. The rate of evaporation then equalled the rate of supply of liquid. The experimental data were presented in the following equations for heat and mass transfer respectively,

$$Nu = 2.0 + 0.6\, Re^{0.5}\, Pr^{0.33} \qquad (3.23)$$

and

$$Sh = 2.0 + 0.6\, Re^{0.5}\, Sc^{0.33} \qquad (3.24)$$

Equations (3.23) and (3.24) are the most widely-quoted for pure liquid droplets.

Hsu et al (65) used the same method as the previous workers, i.e. keeping the droplet diameter constant, and measured the rate of evaporation of 1.8 mm diameter drops of heptane at 37°C at Re values between 70 and 300. In this work great attention was paid to the influence of droplet shape on the rate of evaporation. The large size of the drops and the low surface tension of heptane, resulted in the drop shape deviating significantly from spherical, e.g. on fine capillaries (0.1 mm) the drops were pear-shaped and on wide capillaries (0.8 mm) truncated spheres. The results were correlated by,

$$Sh = 2\,(1 + 0.272\, Re^{0.5} Sc^{0.33})\,(1 + 1.147\,(1 - E))\,(1 - 0.0371\,(1 - d_v/d_h)) \qquad (3.25)$$

where $E = 6V/Ad_h$

Ingebo (66) determined the rate of evaporation of a number of single organic liquids at 20°C to 500°C from the surface of cork spheres of diameter 6.88 mm within an Re range of 1000 to 1600. The correlation proposed was,

$$Sh = 2.0 + 0.3\ (Re.Sc)^{0.6}\ (k/k_v)^{0.5} \qquad (3.26)$$

where k and k_v are the thermal conductivities of air and the diffusing vapours respectively. Maisel and Sherwood (19) measured the rate of evaporation of a liquid supplied continuously to a porous surface placed in a turbulent gas stream. Data on evaporation from flat surfaces were obtained in a duct 15 x 61 cm in cross-section; evaporation from spheres, cylinders and small discs was studied in a long, round duct of 10.2 cm i.d. The spheres were formed by binding sand with calcium silicate. Three thermocouples were tied to the surface of the sphere and the whole covered with absorbent cellulose tissue; a fourth thermocouple was located in the centre of the sphere. Water or benzene was fed from a burette via a hypodermic tube to the sphere. The rate of evaporation of benzene was found to be greater by a factor of 5 to 10 compared with water, which is predictable whatever the predominant mechanism of transfer within the sphere.

Garner and Grafton (141) measured the rate of dissolution of 1.27 cm diameter pressed-solid, benzoic acid spheres in a stream of water at room temperature. Dissolution was followed photographically using a cine camera, and the experimental results were correlated by the equation

$$Sh = 44 + 0.48\ Re^{0.5}\ Sc^{0.33} \qquad (3.27)$$

for $20 < Re < 1000$

This equation, although of similar form, differs from that of Frossling (11) and Ranz and Marshall (26). The difference is principally in the constant term due to the effect of natural convection. Later Garner and Suckling (68) used the same equipment and technique covering a range of 9.5 mm and 12.7 mm diameter spheres of adipic acid and 9.5, 12.7, 15.8 and 19.0 mm diameter spheres of benzoic acid. They correlated their results together with earlier work reviewed above, using the expression,

$$Sh = 2.0 + 0.95\ Re^{0.5}\ Sc^{0.33} \qquad (3.28)$$

for spheres with Reynolds numbers between 100 and 700.

Garner and Hoffman (69) studied the dissolution rate of organic acid spheres of 9.5 mm diameter in a water tunnel at 30°C for both upflow and downflow streams. They concluded that free convective effects did not disappear entirely until Re ~250 for the 9.5 mm spheres, compared with Re ~750 for 19.05 mm spheres in the previous work (70). At Reynolds numbers > 250, Garner and Keey (70) found that the overall mass transfer results tend towards the theoretical relationship

$$Sh = 0.94\ Re^{0.5}\ Sc^{0.33} \qquad (3.29)$$

for $200 < Re < 900$.

Simultaneous mass and heat transfer studies were performed by Evnochides and Thodos (71), using Celite spheres saturated with either water or nitrobenzene. Each sphere was supported horizontally, and rotated, just above the discharge-end of a 20 cm round duct. Sphere temperatures were measured by thermocouples connected to a potentiometer and, in order to determine the rate of evaporation, the porous spheres were periodically weighed. Following the same technique Pasternak and Gauvin (72) suspended a Celite sphere of known weight and moisture content from a hypodermic needle placed inside a 3.81 cm diameter, glass column through which air was passed under controlled conditions of temperature, humidity and velocity. For spheres of 5.59 to 11.63 mm diameter the results were correlated by,

$$Sh = 0.692\ Re^{0.514}\ Sc^{0.33} \qquad (3.30)$$

This expression was later confirmed (73) by results for radioactive Celite spheres saturated with acetone accelerated freely in a downward co-current air stream with velocities in the range 12.19 to 21.33 ms^{-1} at a constant air temperature of 210°C. Accurate particle velocity was determined using a radioactive tracer technique.

In a recent study by Bowman et al (74), a theoretical analysis of the influence of internal circulation on the mass transfer rate from spherical fluid particles, it was postulated that internal circulation affects the external flow pattern, thereby decreasing the resistance to transfer in the external fluid. This was illustrated by the work of Ward et al (75). Rates of mass transfer for four liquid-liquid systems were measured; from water drops into cyclohexanol and from drops of cyclohexanol, isobutanol or o-toluidine into

water. Their results demonstrated a four to six fold enhancement of mass transfer over that for a non-circulating drop.

From their study on cast benzoic acid spheres, Steinberger and Treybal (51) proposed a correlation of the data based on the additivity of the natural and forced convection processes. They proposed,

$$Sh = Sh_o + 0.347\ (Re.Sc^{0.5})^{0.62} \qquad (3.31)$$

with Sh_o, defined by equations (3.18) and (3.19), representing the natural convection contribution. Upward flowing streams of water and aqueous-propylene glycol were used to contact single spheres of 12.7, 19.1 and 25.4 mm cast benzoic acid. The above correlation demonstrated good agreement with the experimental results of eleven different authors' heat and mass transfer data from either gas or liquid streams.

Spheres of naphthalene, benzoic acid and camphor of 2.38 to 19.05 mm diameter wre freely-suspended in an air stream moving at a high velocity through rotameter tubes, and their evaporation was studied by Jones and Smith (76). Although it was observed that the particle spun and had an erratic motion both axially and radially, no difference in the mass transfer coefficient was detected compared to that for fixed particles. This could be due to the fact that when the sphere is spinning one side is stationary relative to the gas whilst the other side meets the flow at twice its linear velocity. A relationship was proposed which takes into account the Reynolds number of the gas, Re_g.

For the laminar region,

$$Sh - 2 = 25\ (Re.Sc.Re_g^{0.5})^{0.33} \qquad (3.32)$$

and for the turbulent region,

$$Sh - 2 = 0.055\ (Re.Sc.Re_g^{0.5})^{0.5} \qquad (3.33)$$

Theoretical approaches to the problem of estimating mass transfer from single spheres were reviewed by Kinard et al (77). They considered separately the forced convection effects in front of, and behind, the separation zone of the boundary layer. Coefficients were evaluated from selected data of Ranz and Marshall (26), Garner and Suckling (68) and Steinberger and Treybal (51) for mass transfer due to forced convection.

An additional term was added to account for transfer in the wake and the proposed correlation is,

$$Sh = 2.0 + Sh_o + 0.45\ Re.^{0.5}\ Sc^{0.33} + 0.00484\ Re.Sc^{0.33} \qquad (3.34)$$

Audu (23) applied a new method for drop suspension. Individual hemispherical drops of water were suspended from a nozzle which was slowly rotated in a horizontal wind tunnel. The correlation derived for ambient conditions was,

$$Sh = 2.0 + 0.473\ Re.^{0.5}\ Sc.^{0.33} \qquad (3.35)$$

Several workers (78, 79, 80) have studied the shape, oscillation and internal circulation of drops either falling-freely or freely-suspended in a gas. Garner and Kendrick (81) investigated mass transfer to suspended drops of water or glycol and amine in a gas stream. Gas from a centrifugal fan was expanded through a horizontal duct to a settling chamber. The gas left the chamber through a suction-flare and passed through a contraction section preceding the working section. Drops were observed to oscillate in three different ways.

a) Prolate-oblate oscillation;

b) Oscillations about axes 90° apart in the horizontal plane; or

c) Eccentric rotation about the vertical axis whilst the horizontal axes remained constant.

The only studies of single free-falling drops containing solids were made by Lihou (82) who used the wind-tunnel built by Kendrick (142) and also used by Finlay (79) and Jarvis (80) but with some modifications. (As described in Chapter 6, a further modification of this design was used in the present studies). Lihou (84, 85, 82) confined most of his study to the shape, oscillation and terminal velocity of drops containing 25% to 45% talc, 56% ballotini or 39% to 70% silica particles. The equations proposed to represent the shape of a deformed liquid droplet were;

$$\left(\frac{Z}{B_2}\right)^2 + \left(\frac{\overline{W}}{A_2}\right)^2 = 1 - \left(\frac{L_2}{Z}\right)^2 \qquad (3.36)$$

$$\frac{Z}{B^2_3} + \left(\frac{\bar{W}}{A_3}\right)^2 = 1 - \frac{L^2_3}{Z} \qquad (3.37)$$

where A, B and L = numerical parameters

Z = distance in vertical direction

$\bar{W}$ = distance in horizontal direction

Results for the evaporation of iso-butanol from 2-ethyl-hexane diol 1:3 and the absorption of CO_2 into water and diol, were correlated by expressing the fractional approach to equilibrium as a function of the dimensionless group $D_v\theta/r^2_e$. However, in the present study of free-flight drops the shape of the drop was regarded as a spheroid shape with a minor vertical axis and major horizontal axes. (This was confirmed as discussed in Chapter 7 and illustrated in Figure 7.5). It is clear from Plate 9.14, showing a pure water drop, that the shape tends to be spherical with increasing residence time in the tunnel. Spheroidal drops were formed immediately after injection and the equivalent diameter was calculated as:

$$d_e = \frac{d_x + d_y + d_z}{3} \qquad (3.38)$$

where d_x = horizontal drop diameter in x-direction

d_z = horizontal drop diameter in z-direction

and d_y = vertical drop diameter in y-direction.

In the present work described in Section 7.3 for an undistorted, stable drop, the horizontal diameter in the x and z-directions had to be equal, therefore,

$$d_e = \frac{2d_h + d_v}{3} \qquad (3.39)$$

This equation was therefore used in the calculation of drop equivalent diameter and hence drop area (A_e).

Miura et al (86) used a similar apparatus to these workers (81, 79, 80, 82) and studied the rate of heat and mass transfer from floating droplets in an ascending air current. When a screen mesh was set in the centre of the wind tunnel a slow velocity

region was produced in the central part of the air stream surrounded by an annular region of high velocity. Droplets were floated in the middle of this inverted parabolic velocity profile. Distilled water droplets of 2.9 to 3.3 mm diameter were used at air temperatures of 53 or 75°C. The experimental data were well represented by Ranz and Marshall's equations (3.23), (3.24), for a droplet suspended from a fine filament.

Sandoval-Robles et al (87) recently studied mass transfer around a sphere under streamline conditions. A suspended brass sphere of 5, 7, 9 or 10 mm diameter was rotated at a constant velocity around a circular channel filled with motionless electrolytic solution, a relative approach flat velocity profile is then perfectly constant. They represented the experimental data by the correlations

$$Sh = 1.032\ Re^{0.385}\ Sc^{0.33},\ \text{for } 2 < Re < 20 \qquad (3.40)$$

$$Sh = 0.803\ Re^{0.474}\ Sc^{0.33},\ 20 < Re < 2000 \qquad (3.41)$$

and

$$Sh = 0.3\ Re^{0.593}\ Sc^{0.33},\ 2000 < Re < 23000 \qquad (3.42)$$

It is noticeable that their results showed a significant dependency on the Reynolds number.

Measurements of mass transfer rates from a single sphere have also been performed in a highly turbulent liquid. Sandoval-Robles et al (88) used a 94 mm diameter, vertical, column with turbulence generated by a polyethylene porous plate fixed at the bottom of the column: The mass transfer from the sphere was measured by using an electrochemical method. The data were correlated using,

$$Sh = 6.86\ Re^{0.559}\ f^{0.069} \qquad (3.43)$$

where f = the turbulence intensity.

However, at low f the data obtained in this work are in good agreement with that published by Sandoval-Robles et al (87).

Evaporation rates of submicron aerosol droplets have been measured by Davis et al (89) by using laser light-scattering from a single droplet to determine the droplet size. Charged droplets of 0.5 to 0.9 μm were suspended in an electric field in a pressure controlled, light-scattering cell. An argon laser was used to measure drop size during the evaporation of dioctyl phthalate into helium and nitrogen at 36°C. This technique, which

is relatively new, was claimed to be extremely accurate especially for submicron droplets.

Investigations of mass transfer from spehrical droplets was sometimes accompanied by studies of heat transfer to the particles. The transfer of heat from the surroundings through a gas to a falling particle takes place by convection and/or by radiation; however, for suspended droplets heat transfer also takes place by conduction through the suspension device. Kramers (90) used three steel spheres (ball bearings) with diameters of 12.6, 7.87 and 7.09 mm suspended individually by a pair of thin thermocouple wires inside a cylindrical coil and heated by means of high frequency induction current. A vertical stream of air, water or oil flowed round the sphere in a 34 mm wide tube. The correlation, proposed was,

$$Nu = 2.0 + 1.3\,Pr^{0.15} + 0.66\,Pr^{0.31}\,Re^{0.5} \qquad (3.44)$$

for $0.7 < Pr < 400$ and Re up to about 10^5. Johnston, Pigford and Chapin (91) derived a formula for the heat transfer from spheres in a forced flow in the form of

$$Nu = 0.714\,(Pe)^{0.5} \qquad (3.45)$$

For low values of Re, however, their 'theoretical' curve deviates considerably from the experimental data. This may have been due to gradients at the surface of the spheres affecting the physical properties of the fluids. There was also formation of air bubbles on the sphere surface.

Tsubouchi and Sato (139) studied heat transfer between single particles and a fluid. They suspended thermistor spheres or 'beads', of 2.0 to 3.0 mm diameter in two types of wind tunnel: one was of the revolving-arm type with a speed range of 0.01 to 0.5 $m.s^{-1}$; the other of the Eiffel type, with a speed range of 1 to 20 $m.s^{-1}$. A current was passed through the thermistor and from current, voltage and resistance measurements the amount of heat dissipated and the temperature were obtained. The results were expressed as

$$Nu = 2.0 + 0.5\,Re^{0.5} \qquad (3.46)$$

for Re from 0.3 to 3000.

A further, extensive, investigation on heat transfer from spheres was that by Yuge (50). He suspended metal spheres in different wind tunnels and compared the effects of cross,

parallel and counter-flows. Test spheres of < 6mm diameter were heated in an electric furnace outside the wind tunnel and then brought mechanically into the flow stream; larger spheres (6 to 60 mm) were heated internally. The results of this study were represented by the fomulae

$$Nu = 2.0 + 0.493\ Re^{0.5} \qquad (3.47)$$

for $10 < Re < 1.8 \times 10^3$

and

$$Nu = 2.0 + 0.3\ Re^{0.5664} \qquad (3.48)$$

for $1.8 \times 10^3 < Re < 1.5 \times 10^5$

Rowe et al (92) reviewed published data on heat and mass transfer to spheres mainly in the range $10 < Re < 10^4$. New experiments were performed in which heat transfer was measured in air and in water using internally-heated, copper spheres of 12.7 and 38.1 mm diameter. Mass transfer was measured by observing the rate of dissolution of 12.7 and 38.1 mm size spheres of benzoic acid in water and the sublimation of 15.87 and 38.1 mm size spheres of naphthalene in air. The results were assessed, together with those of others, and described by:

For air, $Nu\ (or\ Sh) = 2 + 0.69\ Re^{0.5} Pr^{0.33} (or\ Sc^{0.33})$ (3.49)

For water, $Nu\ (or\ Sh) = 2 + 0.79\ Re^{0.5} Pr^{0.33} (or\ Sc^{0.33})$ (3.50)

Adams and Pinder (52) studied heat transfer coefficients during the evaporation of liquid drops. A dilatometric method was combined with a cine-photographic technique to obtain an average heat transfer coefficient for the evaporation of droplets of isopentane and cyclohexane in a continuous phase of glycerine-water solution. A series of runs was made with drops containing different size air bubbles. A drop was injected into the lower part of the column and as evaporation occurred the increase in volume of the air bubble was measured by a dilatometric tube. For all data the best fit was given by the equation:

$$Nu = 7550\ Pr^{-0.75} (\mu_c/\mu_c - \mu_d)^{4.3}\ B_o^{0.33} \qquad (3.51)$$

The evaporation and subsequent drying of the atomised droplets in a spray dryer involved simultaneous considerations of heat and mass transfer.

3.2 Evaporation from Single Droplets at Elevated Temperatures

When a drop evaporates, heat is transferred to the surface where it is used to transform the liquid into vapour which in turn is transferred away from the surface by diffusion. There is, of necessity, a temperature gradient from the surroundings to the surface and a concentration gradient from the surface to the surroundings. When the surroundings are at a relatively high temperature, heat transfer resulting from both mass transfer and by radiation should be taken into account.

Ranz (93), in his study on the evaporation of a drop of liquid in high temperature surroundings, showed that the flow of cold vapour to the surroundings during evaporation requires a considerable amount of the heat conducted inwards to be used to warm the vapour moving outwards. Hence only a small fraction of the heat entering the film surrounding the drop reached the liquid, the remainder being absorbed by the cold vapour in its radial flow from the drop.

Droplet evaporation at high air temperatures, i.e.> 150°C was observed by Marshall (94). He represented heat and mass flow around an evaporating drop diagrammatically and developed a differential equation to describe the differential heat balance over a spherical shell through which heat is passing inwards toward the drop whilst mass is passing outwards. Solution of this differential equation gave an expression for the temperature T as a function of distance x, through the gas film surrounding the evaporating drop.

$$\frac{T - T_s}{T_a - T_s} = \frac{e^{-E/x} - e^{-E/r_1}}{e^{-E/r_2} - e^{-E/r_1}} \qquad (3.52)$$

where $E = mC_{pv}/4\pi k_v$

r_1 is the radius of the evaporating droplet

r_2 is the outer radius of the gas film.

An obvious simplification was to neglect any variation in the thermal conductivity and heat capacity of the gas film caused by temperature and concentration gradients. Differentiating equation (3.52) at the drop surface yielded the following expression for the Nusselt

number,

$$Nu = \frac{2E/r_1}{e^{E(1/r_1 - 1/r_2)} - 1} \qquad (3.53)$$

Ranz (93) discussed a similar expression but included the effects of radiation.

An experimental study of the rate of evaporation of single, stationary droplets of water, methanol, cumene, pentane and benzene within an electrically-heated stainless steel sphere containing superheated vapour was performed by Hoffman and Gauvin (54). Drop diameters ranged from 0.4 to 1.4 mm and temperature from 100°C to 550°C; the drop was retained on a 70μm glass filament and the evaporation rates were recorded photographically. Figure 3.2 illustrates some of the results for water droplets at various high temperatures. The evaporation rate of stationary droplets in high temperature surroundings was found not to be governed by the rate of heat transfer by natural convection but to depend on the transfer number B, where $B = C_p\Delta T/\lambda$. Their results were expressed by the correlation:

$$Nu = \frac{3.2B^{0.97}Pr^{0.33}}{B'} \qquad (3.54)$$

B' is the Spalding transfer number (radiation included) = $C_p\Delta T/(\lambda - q/m)$

Pei and Gauvin's (95) experimental investigation involved measurement of the rate of evaporation of three different liquids, water, benzene, and methanol from stationary porous, hollow spheres 6.35 to 12.7mm diameter, at 204°C to 537°C. The main components of the experimental equipment used were similar to those of Hoffman and Gauvin. The experimental results were satisfactorily correlated by the expression

$$(Nu/Re^{0.5})\,(B'/Pr^{0.33}) = 3.32\,(Gr/Re^2)^{0.007} \qquad (3.55)$$

The stainless steel sphere (54, 95) was subsequently modified by Pei et al (96) to provide a stream of superheated steam at 150°C to 750°C with Reynolds numbers ranging from 5.5 to 510. They found that the contributions of forced and natural convection were non-additive and that the transition from one to the other was gradual. The natural convection effect was concluded to be negligible when $Gr/Re^2 < 0.2$,

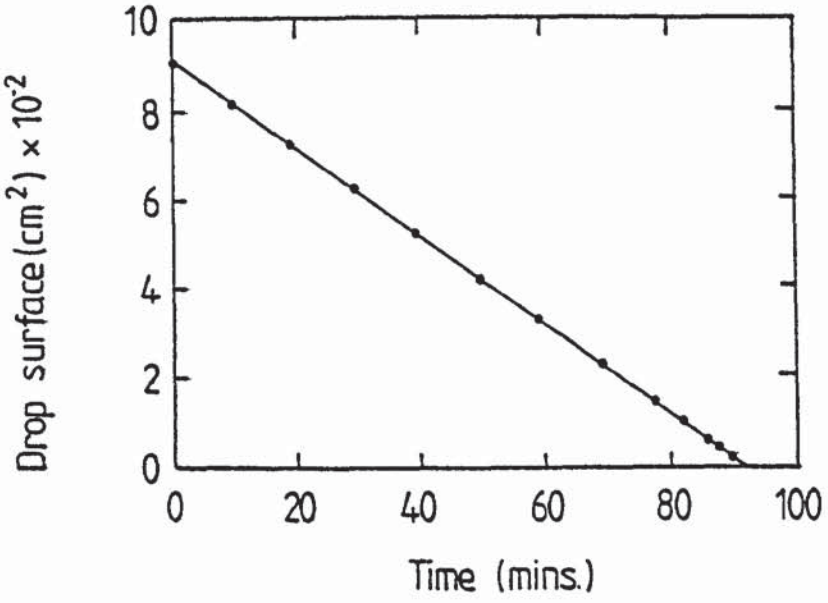

Figure 3·1 Evaporation of drops of water placed on the pan microbalance (Whytlaw-Gray, 45)

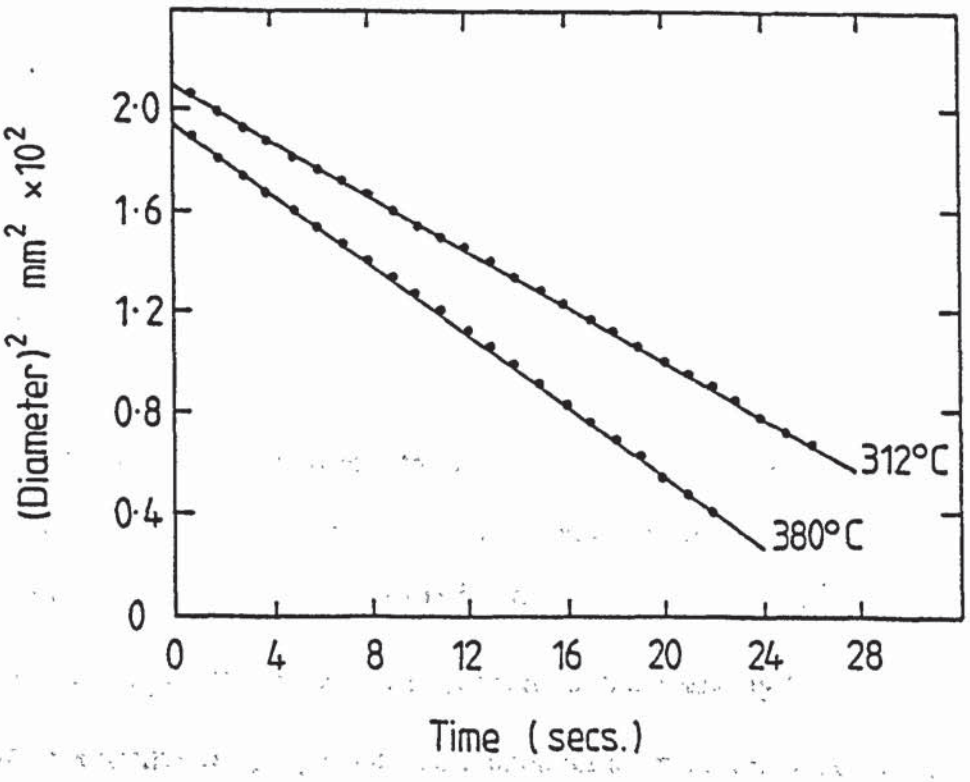

Figure 3·2 Measured variation of (diameter)^2 with time, for water droplets at high temperatures (reference 54)

whereas for values of $Gr/Re^2 >$ 10 forced convection had little influence.

Rates of evaporation have been correlated for drops of pure liquids evaporating in streams of high temperature air. Downing (97) studied drops of acetone, benzene, n-hexane and water, each of the order of 1 mm diameter and suspended in a dry air stream at 27 to 340°C with an Re range of 24 to 325. The experimental data were correlated by,

$$Nu = MN (\ln(1+B)/B) (2.0 + 0.6 Pr^{0.33} Re^{0.5}) \qquad (3.56)$$

and

$$Sh = M (2.0 + 0.6 Sc^{0.33} Re^{0.5}) \qquad (3.57)$$

where $M = 1 - 0.4 (1 - T_s / T_g)$

$$N = 1 - 0.4 (1 - \ln (1 + B)/B)$$

In this study the average film temperature T_f, was defined as

$$(T_f - T_s)/(T_g - T_s) = 0.6$$

and the average physical and transport properties were calulated at T_f.

An experimental method for the study of rapid vaporisation of liquid droplets in a high temperature gas stream is described by Frazier and Hellier (98). A stream of 440µm diameter Freon 113 droplets passed through a 669°C air jet and a photographic record of the vaporisation process was made using a Graflex camera. The mass transfer coefficient was concluded to be higher by a factor of 4 than the value obtained by Ranz and Marshall. To test this conclusion Crosby and Stewart (99) recalculated the previous results using a correction for the net flow through the interface based on the film theory and found a much smaller deviation of 33% between predicted and observed values.

Evaporation of water drops into superheated steam and air was investigated by Toei et al (100). The experimental data were correlated by,

$$Sh (P_{bm}/P_t)^{-0.20} = 2.0 + 0.65 Re^{0.5} Sc^{0.33} \qquad (3.58)$$

where P_{bm} is the average partial pressure in the boundary layer.

This correlation ratio is similar to the equivalent correction for temperature in the vapour film used by Downing. Lee and Ryley (101) suspended water droplets of between 230

and 1130μm on a 50μm glass fibre in a horizontal test section. The apparatus provided for air or superheated steam, in the Reynolds number range 64 to 250, as the gaseous media and evaporation rates were followed optically. The correlation equation was found to be similar to that of (26) with a coefficient of 0.74. In their analysis radiation effects were ignored.

The evaporation of water drops in superheated steam and in air at velocities of 1.6 to 2.1 ms^{-1} was studied by Trommelen and Crosby (27). An individual drop was suspended from a 76μm thermocouple and changes in the weight and temperature were measured as evaporation proceeded at different temperatures. Evaporation was found to take place more slowly in superheated steam than in air, but this difference decreased at higher temperatures. The results of this study support the findings of Toei et al and confirm that the accepted correlation for heat transfer coefficients applicable for evaporation of small drops of pure liquid in air is also valid for evaporation in a superheated vapour. Their analysis accounted for the increased rate of heat transfer to the drops, (beyond that due to convection) resulting from both conduction along the supporting thermocouple and direct radiation.

Matlosz et al (102) investigated experimentally and analytically the evaporation of n-hexane droplets in a nitrogen and argon gas environment at 286°C. The objective of the experimental research was to record the temperature and size of liquid droplets evaporating in high pressure, high temperature surroundings of 6.8 to 102 atm and 275°C. Comparison of theoretical predictions for the droplet temperature - time and radius-time histories with the experimental measurements indicated that, at the higher pressures, molecular mass transport may not be the controlling mechanism for the evaporation process. At low (6.8 atm) pressure the effective mass diffusion coefficient was in good agreement with the calculated molecular mass diffusion coefficient. However, the effective mass diffusion coefficient was > 6 times greater than the calculated molecular mass diffusion coefficient at 102 atm.

At elevated temperature, i.e. > 46°C Audu (103) introduced a temperature correction and correlated experimental data by,

$$Sh = 2.0 + 0.44\left(\frac{T_g - T_s}{T_{amb}}\right)^{-0.008} Re^{0.5}Sc^{0.33} \qquad (3.59)$$

A mathematical model of a single droplet evaporating in a high pressure, high temperature gaseous environment was recently proposed by Kadota and Hiroyasu (104). The calculations cover the unsteady and steady-state stages of droplet evaporation considering the effects of natural convection, non-ideal behaviour, and effects of high mass transfer rate on the temperature and concentration profiles and boundary layer thickness. The evaporation of n-heptane, ethanol, benzene and water droplets in high pressure, high temperature gaseous environments were found to be in a good agreement with the model (105).

To summarise, different techniques of drop suspension have been used, covering extensive ranges of drop size, temperature and gas velocity. The drops were studied whilst suspended in different ways; i.e.,

1) A stationary-drop suspended on a glass filament or thermocouple; under these conditions evaporation is not uniform from the drop surface. A higher evaporation rate occurs from the drop side facing the direction of air flow than in the wake.
2) A drop retained and suspended by means of an electric field. Such studies are limited to droplets of diameter < 10μm.
3) A drop retained and suspended freely in a rising air stream. This technique has been used mainly for evaporation from a pure liquid or for gas absorption by a liquid drop. Drying studies using this technique are very limited; therefore a rotated-suspended drop technique and free-flight drop equipment were developed in the present study (Chapter 6) for evaporation and drying studies.

The majority of previous heat transfer measurements were made in air whilst the majority of mass transfer experiments were with water. The results of all workers support the Ranz and Marshall Equation albeit with differing constants. However, the effect of circulation within a drop, drop oscillation and turbulence which are known to have a significant effect on heat and mass transfer rates have not been investigated thoroughly.

CHAPTER FOUR

DRYING OF DROPS CONTAINING SUSPENDED AND/OR DISSOLVED SOLIDS

Numerous investigators have studied evaporation from pure liquid drops which is less complex than the drying of drops containing dissolved and suspended solids. The presence of dissolved, or in certain circumstances to a lesser degree suspended, solids decreases the vapour pressure of the liquid at the drop surface; the vapour pressure driving force for mass transfer is thus reduced resulting in a reduction in the drying rate. When an evaporating droplet contains a solid either in suspension or solution, its surface temperature will be higher than the thermodynamic wet-bulb temperature for water. The drying characteristics feature the formation of solid material as a crust at the droplet surface, and thus differs from evaporation involving pure liquid droplets, since there is an additional resistance to moisture transfer into the surrounding media. Furthermore with some solutions a film or membrane may be formed which reduces the evaporation rate significantly. (This was observed for example with drops of organic pigment solution as discussed in Chapter 9).

In general, the effect of the presence of a solid is to increase the time to remove the required moisture compared with a drop of pure liquid. However, there are negligible vapour pressure lowering effects in droplets containing only insoluble solids.

Initially a drop introduced into a heated gas stream at some temperature below the corresponding wet-bulb temperature must first be raised in temperature by forced convective heat transfer. The rate of heat transfer is calculated from,

$$\frac{dQ}{d\theta} = UA_h\Delta T_m \qquad (4.1)$$

where A_h = heat transfer area

ΔT_m = logarithmic mean temperature difference

U = overall heat transfer coefficient.

Now,

$$\frac{1}{U} = \frac{1}{h_{gas}} + \frac{1}{h_{liquid}} \qquad (4.2)$$

but, for all practical purposes the gas film coefficient h_{gas} is controlling.

Hence, $$\frac{1}{U} \simeq \frac{1}{h_{gas}} \qquad (4.3)$$

and can be predicted from published correlations,

$$Nu = 0.023\, Re^{0.8}\, P_r^{n} \qquad (4.4)$$

where n has a value of 0.4 for heating. When the drop temperature reaches the wet-bulb temperature of the gas the drying proceeds initially at a constant rate.

Several workers (25, 26, 27) have shown that for many drying operations with various solids the first period of drying is characterised by evaporation from a free liquid surface, termed the 'constant rate' period. This phenomenon is also present with single drops. The moisture content at the end of this period is the 'critical moisture content', a solid phase has appeared, and the droplet is covered with a solid crust. As the crust grows, its resistance becomes predominant and the evaporation rate decreases. This period is termed the 'falling rate' period.

The general drying characteristics are illustrated by Figures 4.1 and 4.2. AB, represents the commencement of drying immediately the droplet contacts the drying gas. In phase BC drying proceeds at constant rate; the droplet surface is maintained saturated by adequate migration of moisture from within the droplet to the surface. At point C, the critical point is reached and moisture within the droplet can no longer maintain surface saturation. During the drying period between points C and D of Figure 4.2, the 'first falling-rate period', the surface becomes progressively depleted in liquid because the rate of liquid movement to the surface is slower than the rate of mass transfer from the surface. During the final phase DE, resistance to mass transfer is wholly in the solid layer. Evaporation continues at a decreasing rate until the droplet acquires a moisture content in equilibrium with the surrounding air.

4.1 Mechanisms of Moisture Movement Through Porous Media

Drying requires the transfer of moisture within the drop and its evaporation from the surface into the surrounding medium (28). There are three general theories for interpretation of moisture distribution and rate of moisture migration in

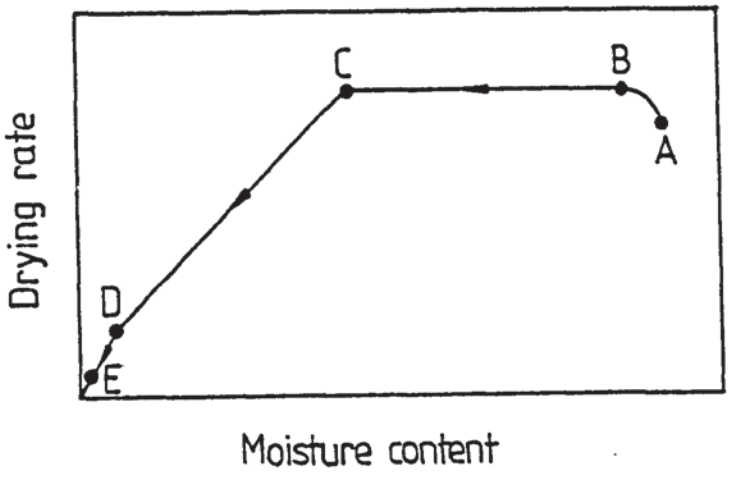

Figure 4·1 Drying rate curve

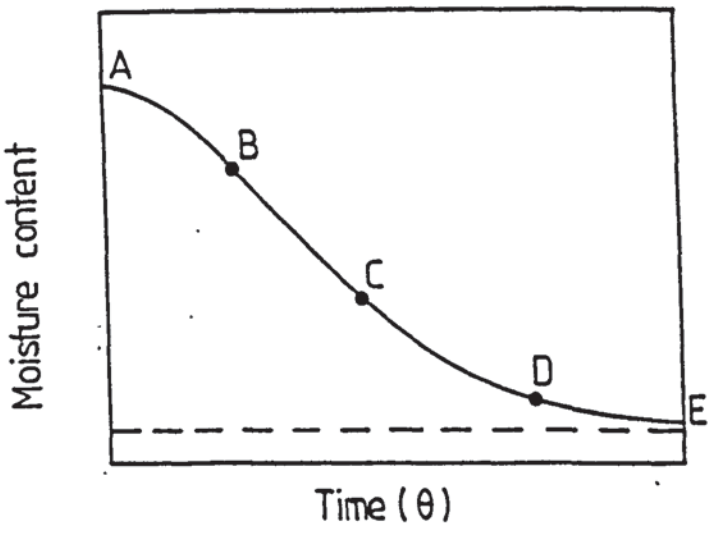

Figure 4·2 Drying curve

	Units
Moisture content	kg liquid / kg dry solid
Drying rate	Weight of moisture removed per unit area per unit time.

porous media; diffusion theory, capillary flow theory and evaporation-condensation theory. To be valid, each theory has specific requirements and the major factors that decide the mode of liquid movement through porous media are the nature of the liquid, the structure of the solid, the concentration of liquid and the temperature of the surrounding gas.

4.1.1 Diffusion Theory

The movement of moisture by diffusion was explicitly proposed as the principal flow mechanism by Lewis (29), and Newman (30). Sherwood (31) based his analysis on diffusion theory and suggested that moisture can either be transferred as a liquid from the interior through the pores to the solid surface followed by evaporation of the liquid at the surface, or by vaporisation of the liquid at a plane beneath the surface followed by diffusion of water vapour through the pores to the surface and thence out into the surrounding gas. The limitation of this theory is that for porous substances flow is caused by capillarity rather than diffusion. Difficulties also arise in solving the diffusion equation for cases where shrinkage occurs, or where the diffusivities are variable.

4.1.2 Capillary Flow Theory

The basic fundamentals of capillary flow theory were first laid down by Buckingham (32) who introduced the concept of capillary potential instead of a concentration potential. Hougen et al (33) discussed the conditions under which capillary and diffusional flow might be expected in solid drying. This theory was subsequently supported by Ceaglske and Hougen (34) with their work on the movement of moisture in sand. Sherwood and Comings (35, 36) considered moisture transfer in the drying of granular material to be caused by capillary movement, i.e. water evaporates from the small miniscuses exposed at the surface of the solids. Nevertheless, in the presence of an adequate temperature gradient, the resulting vapour pressure gradient may overcome the capillary potential.

4.1.3 Evaporation - Condensation Theory

It is assumed in the evaporation-condensation theory that moisture

migration takes place entirely in the gaseous phase via the pores. Gurr et al (37) and Kuzmak and Sereda (38) proved that when the system is subjected to a temperature gradient this assumption is correct, even at 'relatively high' pore saturation, presumably corresponding to crust formation i.e. approximately 70% moisture. Harmathy (39) developed a model based on this theory and successfully predicted the drying rates of porous material, e.g. clay brick. He presented a set of differential equations which yield on solution the moisture content, temperatures and pressure history of the system. Further work for different porous materials covering a range of porosity from low values (e.g. paper) to very high values (e.g. clay) would be needed to check the validity of the model.

4.2 Rate of Drying

In Sherwood's work (31, 40, 41) the drying process was shown in general to be divisible into a constant-rate and falling-rate period, as illustrated in Figures 4.1 and 4.2, the junction of these two periods being termed the 'critical point'. The falling-rate period was shown to frequently consist of two parts. In the period immediately following the critical point the rate of drying decreases; and in the last stage of the drying process the rate of diffusion of water through the solid controls the rate of drying.

4.2.1 Constant-Rate Period

During the constant rate period, evaporation is assumed to take place at the saturated surface of the material by diffusion of water vapour through a stationary film into the air stream (31). The rate of drying is thus limited by the rate of this diffusion process. Three important factors affecting the rate of drying in this period have been discussed by Sherwood (67) namely; radiation from the surroundings, air velocity, and the effect of adjoining dry surface from which heat may be supplied to the liquid contained by a very wet solid. Since the rate of drying during this period is controlled by the rate of water vapour diffusion through the surface air film, high air velocities cause turbulence in the air stream which tends to reduce the thickness of the air film on the surface of the liquid, and accelerate evaporation.

The rate of drying under these conditions is given by,

$$\frac{dw}{d\theta} = k_g A_m (p_s - p_w) = \frac{h_g A_h \Delta T}{\lambda} \qquad (4.5)$$

The rate of transfer depends on the velocity (v) of the air stream raised to a power 0.8, i.e. rate of transfer $\alpha\ v^{0.8}$

Hence,

$$\frac{dw}{d\theta} = \bar{k} A_m (p_s - p_w)\ v^{0.8} \qquad (4.6)$$

where A = area of interface

p_s = vapour pressure of water, and

p_w = partial pressure of water vapour in the air stream.

The rate of drying is thus determined by the values of h, ΔT and A. h will depend on the velocity, and direction of flow, of the air and it has been found that $h = 0.0128\ v^{0.8}$ (3) for parallel flow.

4.2.2 Falling-Rate Period

During the falling-rate period, the surface is no longer completely wetted, as would be expected since a crust or membrane forms during the drying of drops containing solids. Sherwood (40, 67) noted that this period was generally divisible into two secondary periods or zones, indentified as the zone of unsaturated surface drying and the zone where internal liquid diffusion controls.

Nissan et al (106, 107) investigated the drying of porous bodies during the falling-rate period and measured the temperature profile within the dried surface as well as the water distribution. During the zone of unsaturated surface drying, water diffuses to the surface as fast as it is evaporated and the resistance to the internal liquid diffusion may be considered small compared with the resistance to diffusion of vapour through the surface air film (108, 109). The rate of diffusion of water to the surface decreases so that a second critical point is reached beyond which the resistance to internal liquid diffusion is greater than the surface resistance to vapour removal. During this second zone of the falling-rate

period the rate of arrival of water at the surface is less than the rate at which evaporation can take place there; therefore the liquid near the surface tends to be depleted and the locus of evaporation recedes inwards.

Drying rates in the second period (25) showed considerable variation from particle to particle, dried consecutively under identical conditions. The movement of moisture when a pore opens or the crust fractures to admit air to the particle, is clearly related in part, to the structure of the crust. Since crust structure is somewhat random, drying rates in the second period are therefore very unpredictable.

4.3 Drying Of, and Evaporation From, Single Droplets Containing Dissolved and Suspended Solids

Ranz and Marshall's (26) study of the evaporation of pure liquid drops included some experiments on evaporation from droplets of ammonium nitrate and sodium chloride solutions and from droplets of suspensions of organic dye and reconstituted 'Klim' dried milk. For evaporation from drops containing soluble solids, it was assumed that during the period before crust or membrane formation evaporation proceeded as though the drop surface was saturated regardless of the average concentration within the drop. Results from ammonium nitrate and sodium chloride solutions confirmed this hypothesis but it was later challenged by Charlesworth and Marshall (25) who produced a rigorous mathematical model to predict the formation of the solid phase.

Duffie and Marshall (13) extended the study of evaporation from droplets as reported by Ranz and Marshall (26) from conditions of a suspended single drop evaporating in a constant temperature gas stream to conditions which simulated more-closely the conditions in a spray dryer. Their study covered a temperature range from 57°C to 130°C, and solids content range between 4% to 60% wt/wt. Work with thirteen different materials was performed in a 20.32 cm diameter and 6.1 m high co-current flow drier. The results were reported firstly based on a study of the bulk densities of the materials and the manner in which they varied with air temperature, feed temperature and

feed concentration. Secondly materials were classified according to the nature of their spray-dried products. From their observations, it is possible to postulate the factors contributing to the production of hollow particles. Hollow 'microspheres' arise due to the formation of films causing puffing, or ballooning, of the particle or due to the rate of evaporation exceeding the diffusion rate of solids back into the drop. Hence internal voids occur. A hollow particle may also be formed due to the capillary action of the shell on the drop surface drawing liquid and solids to the surface and creating subatmospheric pressures within the particle. The presence of entrained air in the feed may also contribute to the formation of a hollow particle.

Based upon observations of dried-particle structures these authors classified materials into: 'film forming' materials e.g. potassium nitrate, potassium sulphate and sodium chloride, 'crystalline' materials, e.g. sodium silicate, milk and gelatine, and intermediate material e.g. coffee extract and corn syrup. The interpretation of 'film forming' and 'crystalline' is however unclear since other work tends to contradict these observations. In every case, some hollow particles were found in these products although the mechanism for formation was different.

Charlesworth and Marshall (25) studied evaporation from single droplets of ten different aqueous solutions of inorganic salts and from droplets of coffee extract, sucrose, organic dye and whole fresh milk. The droplets to be dried were formed from a microburette, and suspended on a vertical glass filament of 340 μm diameter which was itself attached to another horizontal glass capillary tube connected to the tip of the burette. The deflection of the horizontal glass filament indicated the weight of the drop. The first sign of a solid phase was indicated by the formation of crystals at the bottom of the drop. As drying progressed more crystals appeared to form a surface crust which grew steadily up the side of the droplet. This mode of crust formation would not however be expected for a rotating drop or in a practical dryer, since some areas of the crust may redissolve and then reform.

Those authors presented a generalised description of the behaviour of the drying droplet, as shown in Figure 4.3. After crust formation the behaviour of the droplet

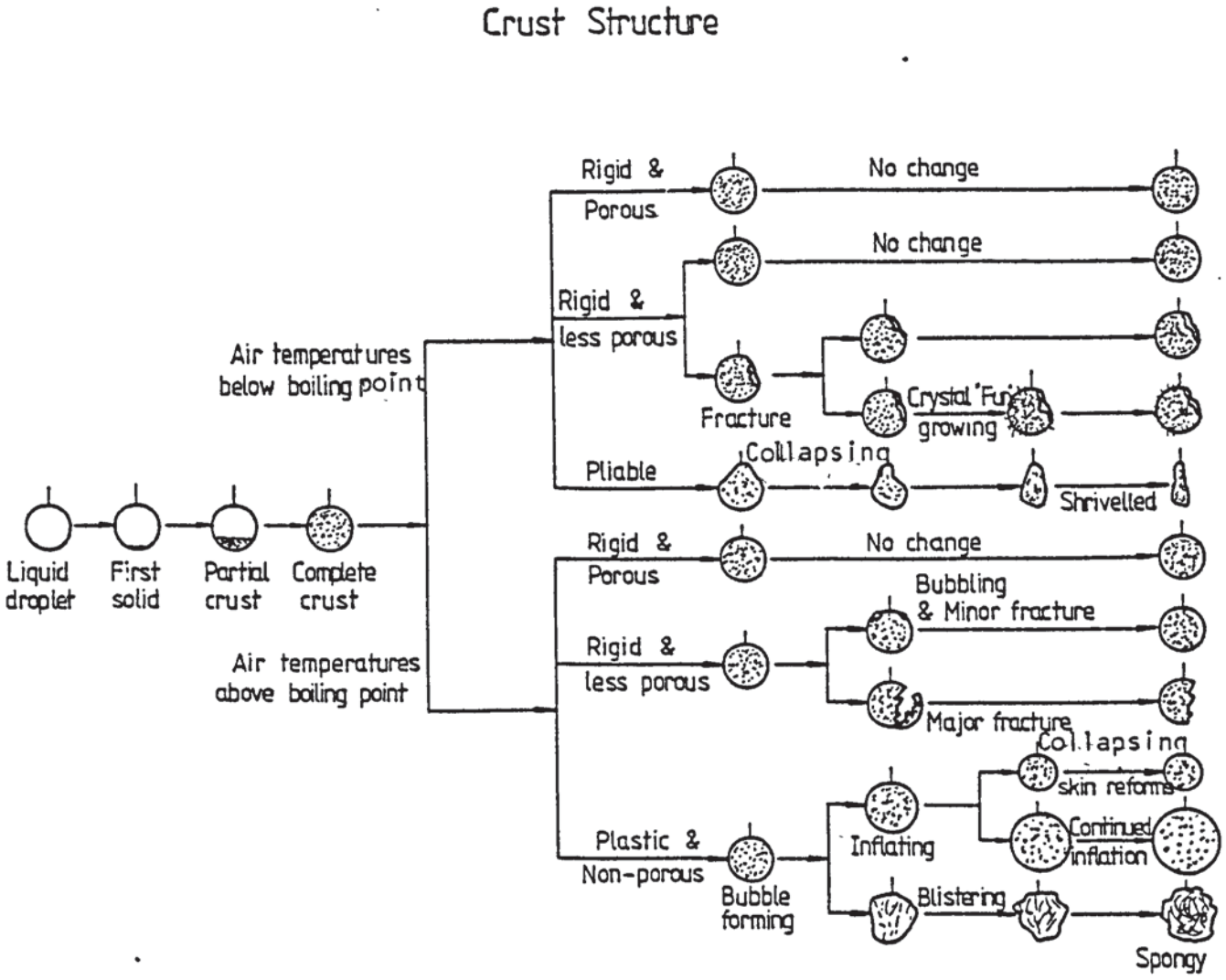

Figure 4·3 Appearance changes in drying droplets at air temperatures above and below the boiling point. (25)

was entirely controlled by the nature of the crust and whether the surrounding temperature was above or below the boiling point of the drop. The time for crust formation, θ_c was evaluated as,

$$\theta_c = \frac{(r_o^2/D_v) \ln (C_s/C_o)}{\phi_y^{\,2} + 2\gamma \ln (C_s/C_o)} \qquad (4.7)$$

Trommelen and Crosby (27) determined the loss in weight, and variation in temperature, as a function of time for single droplets of a number of aqueous solutions and suspensions of four food products and various inorganic salts drying in air and superheated steam. It was found that all materials dried more rapidly in air than in superheated steam with the exception of skimmed milk and sodium sulphate which dried considerably faster in steam. No major differences were observed between the final products for these two drying media except that some materials yielded denser particles in superheated steam than in air. This led to the conclusion that drying rates, and the structures, of dried material are product-specific. Given the mechanisms operating in the falling-rate period, discussed in Section 4.2.2. this is clearly correct. However, it would be expected that the structure of drops of a specific solid would depend upon drying parameters, e.g. air temperature.

Miura et al (110) studied the drying characteristics of stationary single drops of sodium sulphate solutions, skimmed milk and bentonite suspensions in air streams. They found that the equation for time of appearance of the crust proposed by Charlesworth and Marshall was reasonably accurate although the experimental values were generally 8 to 11% greater than the calculated values. To predict the crust thickness they proposed an equation based on a mass balance of solids in a droplet.

$$Y - 1 = \frac{1 - B^3}{3ZB^2 - 3Z^2B + Z^3} \qquad (4.8)$$

where $B = r/r_o$

$Y = C/C_o$

$Z = \psi/r_o$

Audu and Jeffreys (23) investigated the drying of single, suspended drops of sodium sulphate solutions and detergent slurries in a wind tunnel. They proposed a crust thickness ψ model, based on a mass balance of moisture in the surrounding air as,

$$\psi = R - \left(R^3 - \frac{3G}{2\pi C_o} (H_d - H_u) \Delta\theta \right)^{0.33} \qquad (4.9)$$

They also proposed a crust mass transfer coefficient k_c, expressed as,

$$k_c = \frac{D_v \varepsilon^{1.5}}{\psi} \qquad (4.10)$$

With the systems studied, the crust was found to provide 64.2% of the total resistance to mass transfer. However, some heat transfer occurred by conduction from the nozzle on which the drop was suspended and, in a surrounding temperature higher than ambient, a drop would have received a significant amount of heat by radiation. These two heat transfer sources to the drop were not considered in their study.

Wijlhuizen et al (lll) presented a theoretical calculation of the drying history of skimmed milk droplets under spray drying conditions. Concentration and temperature profiles were calculated for droplets containing no air bubble, the 'solid sphere', and for 'hollow spheres', i.e. droplets containing a central air bubble of known size. They concluded that the presence of entrapped air has a limited effect when the air outlet temperature is low, but increases with rising outlet temperature. When the outlet temperature is low, the droplet temperature remains well below the boiling point of the droplet liquid, internal evaporation is limited and a slight growth of the bubble radius occurs. This work was based on the experimental data of Van der Lijn (ll2) who introduced a concentration and temperature-dependent diffusion coefficient. The 'hollow sphere' model assumes an initial gas bubble of known size in a droplet and a uniform concentration profile. The resulting diffusion equations were solved to predict moisture concentrations and droplet temperatures during drying. A better fit for data for the earlier stages of drying would have been obtained if drying had progressed approximately

uniformly around the droplet sides.

An analytical model has been developed by Haertling (113) which is able to predict drying rates of clay bricks and burned clay. The model is based on the assumption that mass transfer within the material occurs simultaneously due to vapour diffusion and capilliary moisture movement. The calculated rates were found to be 21% higher than experimental data particularly at high air temperature, e.g. at 207°C and 247°C.

Esubiyi (114) included in his work drying of slurry drops of five different sources of Portland cement. He developed a mathematical model for estimating crust mass transfer coefficient, k_c, based on an assumed velocity of vapour discharge through the pores of the crust described by the Kozeny equation (3). The equation proposed for k_c was,

$$k_c = \frac{\varepsilon^3 \rho}{5(1-\varepsilon)^2 \mu s^2_b \psi} \qquad (4.11)$$

Sano and Kee (12) derived equations to describe the evaporation of moisture from a single spherical droplet containing colloidal material to yield a solid hollow particle. It is assumed that, once the equilibrium vapour pressure of the moisture inside the particle exceeds the pressure of the ambient air, the particle inflates and ruptures, forming a hollow sphere. After inflation and rupture, two limiting ways of deformation of a hollow particle were assumed:

i) the maximum radius does not change, but the void radius increases due to the moisture loss; or
ii) the void radius remains the same, while the outer radius shrinks.

The changes of moisture and temperature of a droplet with drying time were measured by similar techniques to Charlesworth and Marshall (25) for a drop of skimmed-milk suspended on a fine glass filament at temperatures of 100°C-150°C. They found that the outer radius shrinkage mechanism gave a more realistic approximation to their results. The inflated diameter of a particle was evaluated as the final diameter, obtained as the arithmetic mean of the breadth and length of the particle. Theoretical computations were

performed with an average inflation ratio of 0.88, and a ratio of 1.1 was used to fit the experimental data of Trommelen and Crosby (27) on drops of skimmed-milk at the same drying temperatures.

More recently Cheong (115) investigated the drying of drops of aqueous solutions of sodium sulphate decahydrate suspended on a suspension filament. A unique thermocouple was developed for the simultaneous measurement of evaporation rate and drop temperature during drying.This thermocouple consisted of a fine nickel wire of 50μm diameter inserted through a hollow glass filament of 0.18 to 0.2 mm diameter. A thin film of copper was deposited onto the outside of the filament, and a junction was made at the tip where about 0.5 mm of nickel wire was exposed. Three equations were derived which on simultaneous solution give the crust thickness, core temperature and weight of the drop as a function of time, viz.

$$\frac{dx}{d\theta} = \frac{b_1}{b_2x^2 + b_3x} \cdot \frac{p_g - p_c}{T_c} \qquad (4.12)$$

$$\frac{dT_c}{d\theta} = \frac{a_1/a_2}{a_2x^2 + a_3x} \cdot \frac{T_g - T_c}{x} + \frac{b_1/a_4}{b_2x^2 + b_3x} \frac{p_g - p_c}{T_c\, x} \qquad (4.13)$$

and,

$$\frac{dW}{d\theta} = -4\pi x^2 \rho_c \frac{b_1}{b_2x^2 + b_3x} \cdot \frac{p_g - p_c}{T_c} \qquad (4.14)$$

where,

$$a_1 = \frac{R^2 h_g k_c}{\rho_c x_w (\lambda - C_c)}$$

$$a_2 = k_c - Rh_g$$

$$a_3 = R^2 h_g$$

$$a_4 = \frac{C_p}{3\, x_w (\lambda - C_c)}$$

$$b_1 = \frac{R^2 D_v M_w k_g}{\rho_c x_w R_c}$$

$$b_2 = D_v - Rk_g$$

and

$$b_3 = R^2 k_g$$

The model gave good results for crust thickness prediction. Work on sodium sulphate decahydrate core temperature-prediction should have included a modification to account for the latent heat of fusion at 33°C. However, the model predicted the fall and rise of the core temperature at the transition point. After the transition point the model underestimated the core temperature by 20% because of the practical effect of cracks in the crust. After complete crust formation the model overestimated the drop weight; this was explained as being due to the loss of small fragments when the crust fractured, although significant crust fractures would not be expected during the earlier stages of solid formation.

4.4 Evaporation from Droplet Sprays

The evaporation characteristics of droplets within a spray differ from those of single droplets in that they are more complex. Although basic theory applies in both cases, there are added difficulties in defining a size distribution, the relative velocity between any droplet and its surrounding air, local temperature variation, droplet trajectory and the number of droplets present at any given time per given volume of drying air. Consideration must be given to size distribution during the evaporation of a spray. Many authors have prepared mathematical relationships to represent size distribution; the more common distributions and their mathematical definitions are given in Table 4.1 and have been extensively discussed by Masters (2) and Mugele and Evans (127).

4.4.1 Sprays of Pure Liquids

Probert (116) presented a theoretical analysis based upon a spray size distribution following the Rosin-Rammler (117) equation. Spray droplets were considered

to have no relative velocity and temperature driving force changes were assumed negligible during evaporation. It was predicted that the more homogenous the spray the faster evaporation proceeds to completion compared with one with a wider distribution but with the same mean diameter. This work was extended by Fledderman and Hanson (118) to cover spray evaporation under conditions of relative velocity, where the spray distribution was assumed to follow the Nukiyama-Tanasawa (119) equation, Table 4.1.

Table 4.1 Droplet Size Distribution Functions

Distribution	Form
Normal	$\frac{d(N)}{d(d_p)} = \frac{1}{S_N.(2\pi)^{0.5}} . \exp\left(\frac{(d_p - \bar{d}_p)^2}{2S^2_N}\right)$
Log-Normal	$\frac{d(N)}{d(d_p)} = \frac{1}{DS_G(2\pi)^{0.5}} \exp\left(- \frac{(\log d_p - \log d_{gm})^2}{2S^2_G}\right)$
Square Root Normal	$\frac{d(N)}{d(d_p)} = \frac{1}{2(2\pi d_p S_G)^{0.5}} \exp\left(- \frac{(d_p^{0.5} - d_{gm}^{0.5})2}{2S_G}\right)$
Upper Limit	$\frac{d(N)}{d(d_p)} = \frac{1}{d_p S_G(2\pi)^{0.5}} \exp\left(- \frac{\log((d_{max} - d_p)/d_{gm})^2}{2S^2_G}\right)$
Nukiyama-Tanasawa	$\frac{d(N)}{d(d_p)} = bd_p^2 \exp(-ad_p^f)$
Rosin-Rammler	$\bar{V}_d = 100 \exp(-(d_p/d_R)^f)$

A practical method of spray evaporation evaluation has been proposed by Marshall (94). The size distribution is divided into small size groups, the change of the average droplet diameter in each selected group can then be calculated over short time intervals. Although the method is only presented for drops of pure liquids, such, calculations are useful for illustrating the nature of the changes likely to occur in a dryer. It was deduced that for a range of pure liquids and temperatures up to 260°C evaporation was >90% completed in the first 1.5 seconds and that the air temperature had fallen to within 16°C of its outlet temperature during this period.

Manning and Gauvin (120) studied heat and mass transfer of water sprays in both cocurrent and countercurrent air flows. The progressive evaporation from the sprays was followed by measuring colorimetrically the increase in concentration of red dye and the droplet size distributions were determined on samples obtained by traversing the spray with an immersion cell containing Varsol. The equations proposed by Frossling (11) and by Ranz and Marshall (26) for stationary drops suspended in moving air streams were claimed to be generally applicable for correlating the Nusselt number but the scatter of the experimental data appears to be considerable. This may have arisen due to uncertainty in predicting relative velocities and droplet sizes in the vicinity of the atomising nozzle.

Bose and Pei (121) investigated the rate of evaporation of water sprays in a cocurrent-flow dryer of 152.4 mm internal diameter. The relative velocity between spray and air stream was found to be of significant importance in the determination of the rate of heat and mass transfer, which is indeed to be expected from the dependency of both Sherwood and Nusselt number on the Reynolds number. This is contrary to the study by Dlouhy and Gauvin (122) on spray dryers in which the effect of relative velocity between the droplets and the air was found to be negligible. However, their data were well correlated by Ranz and Marshall's correlation which takes account of relative velocities.

A computational study was presented by Dickinson and Marshall (123) to calculate the evaporation of sprays of pure liquid. The conditions of both negligible and significant relative velocity between sprays and air were studied. Mathematical equations

were developed for spray evaporation of non-uniform distributions. However the basic assumptions, of ideal conditions of constant droplet temperature and ideal flow, limit their usefulness.

Rates of evaporation from single water droplets surrounded by glass beads were measured, and the effects of drop and bead diameters and distance between the surface of the drop and the glass beads were investigated, by Miura et al (86). The following experimental equations were obtained,

$$b/d_g \leq Nu/Nu_R \text{ or } Sh/Sh_R = 0.71\,(b/d_g)^{0.25}\,(d_p/d_g)^{0.16} + 0.07 \qquad (4.15)$$

$$b/d_g > 2 \quad Nu/Nu_R \text{ or } Sh/Sh_R = 0.42\,(b/d_g)^{0.125} + 0.41 \qquad (4.16)$$

where b = distance between glass bead surface and water droplet surface.

A procedure for evaluating evaporation histories will rely on computer facilities, and the development of improved experimental techniques to study droplet and spray evaporation, e.g. possibly using the type of analyser described in Section 6.4.

4.4.2 Sprays of Solution or Slurry Droplets

The addition of a solute to a solvent lowers the surface tension considerably and hence affects the vapour pressure according to the equation,

$$-\Delta P = \frac{2\sigma_l}{r} \qquad (4.17)$$

From this 'Kelvin Equation' it is clear that the reduction in pressure due to surface tension is greater for small drops. For drops containing insoluble solids the surface tension is regarded as the same as for the pure liquid, i.e. the lowering of vapour pressure is negligible.

Both the degree of vapour pressure reduction due to the presence of solids and the resistance to moisture transfer will vary for drops throughout the size distribution. Spray evaporation analysis is therefore complex and investigations in this field have been limited.

Dlouhy and Gauvin (122) were among investigators to specifically study evaporation of sprays of calcium lignosulphonate solution in a cocurrent spray dryer of 203.2 mm diameter. They showed that the total spray evaporation time could be accurately predicted by employing a stepwise method of calculation proposed by Marshall (94). A step-by-step prediction procedure has been developed by Baltas and Gauvin (128) to predict the evaporation from a spray of sodium nitrate solution drops moving through the drying air. The predicted evaporation rates were however 3.5 times greater than the experimental values. Other results of computer calculations of local humidity and mass flow profiles showed a satisfactory agreement with experimental profiles.

Katta and Gauvin (129) proposed equations to predict the three-dimensional motion of droplets in a spray dryer based on a knowledge of the characteristics of the atomising device and of the gas flow patterns in the drying chamber. Experimental verification of this theoretical approach was obtained from a study of the drying of calcium lignosulfonate solutions in a 122 cm diameter, 183 cm high, circular cocurrent chamber with a conical bottom. Their model predicts trajectories of the droplets and the evaporation rate. The effect of nozzle position and the drying gas temperature on the capacity and efficiency of the spray dryer demonstrates the existence of an optimum nozzle position and gas temperature.

Spray drying of water, a sodium chloride solution, and a skimmed milk solution were studied experimentally by Miura et al (130, 140). A two fluid, pneumatic nozzle and a hollow cone pressure nozzle were used in this investigation. Sprays were dried in a square cocurrent drying chamber 36 x 36 x 294 cm, and the droplet size distributions were measured at four points in the dryer. In the computation, droplet size distribution was determined from the Nukiyama-Tanasawa equation, Table 4.1 and two sets of equations were used to investigate the heat and mass transfer. One set was the Ranz and Marshall equations for single droplets, i.e. equations 3.23 and 3.24 and the other set was equations 4.15 and 4.16 for a droplet in a spray cloud derived by Miura et al (86). It was shown that the latter set predicted their results more accurately than the former.

4.5 Temperature Within Evaporating Droplets

To estimate the evaporation times and evaporation rates for drops it is necessary to be able to specify, or estimate, the droplet surface-temperature in order to evaluate the temperature driving force. If a dynamic equilibrium is established between the rate of mass transfer and the rate of heat transfer, and if the heat transferred is essentially all consumed for evaporation, the drop surface temperature T_s can be estimated from the following equality,

$$\frac{T_g - T_s}{p_s - p_g} = \frac{k_g A_m \lambda}{h_g A_h} \qquad (4.18)$$

At the start of drying the temperature of a droplet solution will be only slightly above that of a water droplet evaporating under the same conditions. The extent of the difference is dependent on the relative lowering of the vapour pressure by the dissolved salt. When suspended solids are present, the surface temperature will initially approximate that for a pure liquid droplet. As evaporation continues and the surface layer of the drop becomes more concentrated, the drop temperature will rise slowly. However, once a crust is formed, the additional resistance to moisture diffusion will result in the core temperature rising above the saturation wet bulb temperature (26).

Williams and Schmitt (131) in their study of humidity measurements in the presence of soluble salts showed that heat of crystallisation, or solution, should be considered. For solutions of ammonium nitrate for example, the heat of crystallisation is approximately 20% of the latent heat of vaporisation. Hence equation 4.18 becomes,

$$\frac{T_g - T_s}{p_s - p_g} = \frac{k_g(\lambda - C_c)}{h_g} \qquad (4.19)$$

Droplet temperature histories were investigated by several workers (26, 25). The temperature of the drop was measured by embedding a thermo-element junction inside the drop and the readings were taken during the evaporation. Ranz and Marshall's (26) results for the drying of a drop containing 3.0×10^{-4} gm of ammonium nitrate

showed a gradual increase in drop temperatures due to the effect of heat of solution followed by a rapid rise when crystallisation occurred. No correction was included for conduction along the thermocouple wires.

Trommelen and Crosby (27) measured simultaneously the change in weight and temperature of an evaporating drop suspended at the junction of a Chromel-Constantan thermocouple which itself was affixed to the end of a glass filament which acted as a torsion balance. The results of their study showed that food products generally did not exhibit any constant temperature period, unlike clay slurry and inorganic salts. The rise in temperature was interrupted by one or more cycles of inflation, rupture or collapse which varied from one drop to another. Heat transfer through the suspension device to the drop was taken into account by (45, 97, 112). Sano and Keey (12) derived equations to predict the temperature of a spherical droplet containing colloidal material. The model was found to slightly underestimate the drop temperature especially at high air temperatures, i.e. > 150°C; this was probably due to their neglecting conduction along the thermocouples.

A unique method for simultaneous measurements of drop weight and core temperature for sodium sulphate decahydrate suspended on a thin film thermocouple was developed recently by Cheong (115). He observed an initial transient period in the core temperature history curve before equilibrium was established and the core temperature reduced to the wet bulb temperature. The core temperature then rose steadily as the resistance to heat and mass transfer increased with the crust thickness, then rose very sharply and reached the air temperature. However, this sudden rise in temperature was caused by the evaporation interface receding away from the themocouple junction, resulting in the dry crust temperature being measured.

From the above discussion, evaporation from pure liquids is evidently not such a complex process as from liquids containing solid. However, to overcome the complexity of studying evaporation from solutions in a real spray dryer it is useful to study the evaporation characteristics and residence times of droplets of liquids. It is also clear

that fundamental data for spray drying are obtainable from studies of single, suspended-drop drying and evaporation. In the present investigation an extensive study and observations were made of drops of pure liquids, slurries and solutions either suspended on a rotating nozzle or in free-flight in an air stream as described in Chapter 6.

CHAPTER FIVE

MATHEMATICAL MODELS FOR EVAPORATION FROM, AND DRYING OF, SINGLE DROPS

This Chapter reviews mathematical models developed by some investigators to characterise drying of single drops. Modifications of these models are proposed here

(a) To allow for the heat transferred by conduction via the rotating nozzle and by radiation from the surroundings, and

(b) To account for the area of a free-flight drop not corresponding to a spheroid.

5.1 Evaporation from Pure Liquid Drops

Figure 5.1 shows a hemispherical drop suspended on a nozzle, in a constant flow of air, having an initial humidity H_i and temperature T_i. Following moisture transfer the outlet air himidity is H_o and the temperature T_o. Audu (103) made the following assumptions in order to derive a mathematical model to express mass transfer rate and mass transfer coefficient;

(a) The drop radius was maintained constant (achieved in his experimentation by a controlled liquid feed);

(b) The air flowrate and inlet temperature were constant, and

(c) Air physical properties were constant over the temperature range studied.

5.1.1 Mass Transfer Rate

Suspended Drops

From a mass balance, over the suspended drop the amount of water evaporated per unit weight of air is,

$$H_o - H_i = \Delta H \qquad (5.1)$$

Thus the rate of evaporation, N_A, is the product of the dry air mass flow rate, G and ΔH:

$$N_A = \frac{G.\Delta H}{A_m} \qquad (5.2)$$

$$G = \frac{\bar{G}}{1 + H_i} \qquad (5.3)$$

In the present study of drying suspended drops, i.e. without replenishment, the area term, A, clearly did not remain constant. Therefore direct measurement of drop dimensions was necessary at increments of drying time.

Free-Flight Drops

For a free-flight drop the rate of mass transfer can be expressed as,

$$N_A = \frac{dm}{d\theta} \cdot \frac{1}{A_e} \qquad (5.4)$$

where $A_e = \pi d_e^2$ and $d_e = \frac{2d_h + d_v}{3}$

As explained in Section 3.1.2 and illustrated later in Section 9.6.2, the drops were not spherical and therefore an equivalent diameter must be defined. $\frac{dm}{d\theta}$ can be calculated from a plot of drop mass against time.

5.1.2 Mass Transfer Coefficient

The rate of mass transfer is proportional to the driving force and the constant of proportionality was denoted k. The driving force used is the humidity driving force, which at the drop temperature T_s is expressed as,

$$(\Delta H)_s = H_s - H_i \qquad (5.5)$$

Therefore the rate of mass transfer can be expressed mathematically as,

$$N_A = k_H (H_s - H_i) \qquad (5.6)$$

Equation (5.5) can be transformed to yield the pressure driving force ΔP by converting the humidities to pressure analogues. Thus

$$H = \frac{M_w}{M_a} \cdot \frac{p}{P - p} \qquad (5.7)$$

$$p = \frac{H \cdot P}{(M_w/M_a) + H} \qquad (5.8)$$

where p = partial pressure of water vapour

P = total pressure

H = humidity

M_a = molecular weight of air

M_w = molecular weight of water vapour.

According to Hinchley and Himus (132) the rate of evaporation is proportional to the pressure driving force:

$$N_A = k_p (p_s - p) \qquad (5.9)$$

The mass transfer coefficient is obtained from equation 5.9 after substituting for N_A from 5.2 and 5.4:

$$k_g = \frac{G.\Delta H}{A_m(p_s-p)} \qquad (5.10)$$

k_p has units of $gm.cm^{-2}.s^{-1}.atm^{-1}$.

Equation (5.10) can be modified to give,

$$k_g = \frac{G.\Delta H}{A_m(p_s-p)} \cdot \frac{R_c T_i}{M_w} \qquad (5.11)$$

This equation was first applied to suspended drops by Audu (103).The units of k_g in equation (5.11) are $cm.s^{-1}$ and it is the mass transfer coefficient.

In the new case of a free-flight drop the mass transfer coefficient can similarly be expressed as,

$$k_g = \frac{dm}{d\theta} \cdot \frac{1}{A_e} \cdot \frac{R_c T_i}{M_w(p_s-p)} \qquad (5.12)$$

5.1.3 Nusselt Number

To determine the experimental value of the Nusselt number, the following

assumptions were made by Cheong (115).

1. The temperature at the surface of the drop is equal to the wet bulb temperature and the drop has a constant density,
2. Temperature driving force remains constant, and the latent heat of vaporisation and thermal conductivity can be evaluated at the mean temperature between the drop and the air.

The rate of mass transfer from a spherical drop can be expressed as,

$$-\frac{dw}{d\theta} = \frac{dQ/d\theta}{\lambda} \qquad (5.13)$$

The heat transfer to the drop can be determined from,

$$\frac{dQ}{d\theta} = h_g A_h (\Delta T) \qquad (5.14)$$

The Nusselt number Nu is defined as,

$$Nu = \frac{h_g d_p}{k} \qquad (5.15)$$

Substituting equation (5.14) into (5.13) yields,

$$-\frac{dW}{d\theta} = \frac{h_g A_h (\Delta T)}{\lambda} \qquad (5.16)$$

This equation can be simply extended to the present study. Since the weight of a hemispherical drop,

$W = \pi d_p^3 \rho_d/12$ and for a spheroidal free-flight drop the weight $W = \pi d_e^3 \rho_d/6$, equation (5.16) becomes,

$$h_g = -\frac{\lambda \rho_d}{6\Delta T} \cdot \frac{1}{d^2_p} \cdot \frac{d(d_p^3)}{d\theta} \qquad (5.17)$$

where the surface area of a hemispherical drop = $1/2\ \pi d^2_p$ and for a spheroid droplet = πd^2_e.

In Cheong's work the drop was spherical in shape whilst in the present investigation the drop was either hemispherical or a spheroidal shape depending on the experimental method. However, substitution of equation (5.17) into (5.15) gives,

$$Nu = - \frac{\lambda \rho_d}{6k\Delta T} \cdot \frac{1}{d_p} \cdot \frac{d(d_p^3)}{d\theta} \qquad (5.18)$$

$$\text{Since } \frac{d(dp^3)}{d\theta} = \frac{3d_p}{2} \cdot \frac{d(d_p^2)}{d\theta}$$

Therefore,

$$Nu = - \frac{\lambda \rho_d}{4k\Delta T} \cdot \frac{d(d_p^2)}{d\theta} \qquad (5.19)$$

$d(d_p^2)/d\theta$ can be determined from a plot of d_p^2 versus θ.

5.1.4 Heat Transfer to the Drop by Radiation

In a wind tunnel, or in the real case inside a spray tower, a drop receives an amount of heat by radiation; therefore radiation effects may have to be taken into consideration.

The radiative heat transfer rate q_e, can be expressed as,

$$q_e = F_a A \sigma e (T_g^4 - T_s^4) \qquad (5.20)$$

The geometry factor F_a can be assumed to be unity since the drop is surrounded by the drying chamber.

5.1.5 Heat Transfer to the Drop Through The Nozzle-Suspension Device

Since any nozzle for drop suspension inside the working section will be exposed to the drying air some heat will be transferred from the nozzle to the drop by conduction. Cheong (115) derived a model for conductive heat transfer to the drop through a glass filament. In the present work the transfer took place via the material of the more substantial nozzle instead of the glass filament. Let the following

assumptions, previously made by Cheong, be valid:

(1) Heat is transferred to the nozzle from the surroundings by radiation and convection;

(2) The temperature around the nozzle is constant and equal to the dry air temperature;

(3) There is no radial temperature gradient;

(4) The length of the nozzle is much longer than the diameter; this will always be valid.

Under these assumptions and considering the filament as a cylinder of infinite length heat transferred through the glass filament could be expressed as (115)

$$q_f = \frac{\pi}{2}\left(\frac{k_t d_f^3}{5}\left(2\sigma e_g (T'_s{}^5 - T'_g{}^5) - 10\,\sigma\, e_g\, T'_g{}^4 (T'_s - T'_g) + 5\, h_f (T_s' - T_g')^2\right)\right)^{0.5} \quad (5.21)$$

In this investigation q_f is equivalent to q_n, d_f is equivalent to d_n and e_g is equivalent to e_n, therefore equation (5.21) may be written as,

$$q_n = \frac{\pi}{2}\left(\frac{k_t d^3_n}{5}\left(2\sigma e_n (T'_s{}^5 - T'_g{}^5) - 10\,\sigma\, e_n\, T_g{}^4 (T'_s - T'_g) + 5\, h_g (T'_s - T'_g)^2\right)\right)^{0.5} \quad (5.22)$$

5.2 Drops Containing Dissolved, and/or Suspended, Solids

Consider a hemispherical drop suspended from a nozzle as shown in Figure 5.2. Let the following assumptions be valid (after 103, 114),

(1) Once the crust is formed, the external radius R remains constant;

(2) The core temperature T_c is uniform throughout the core;

(3) Air flowrate, air temperature and other physical properties of the air are constant;

(4) Heat is transferred from the drying air to the crust by convection and it is transferred through the crust by conduction;

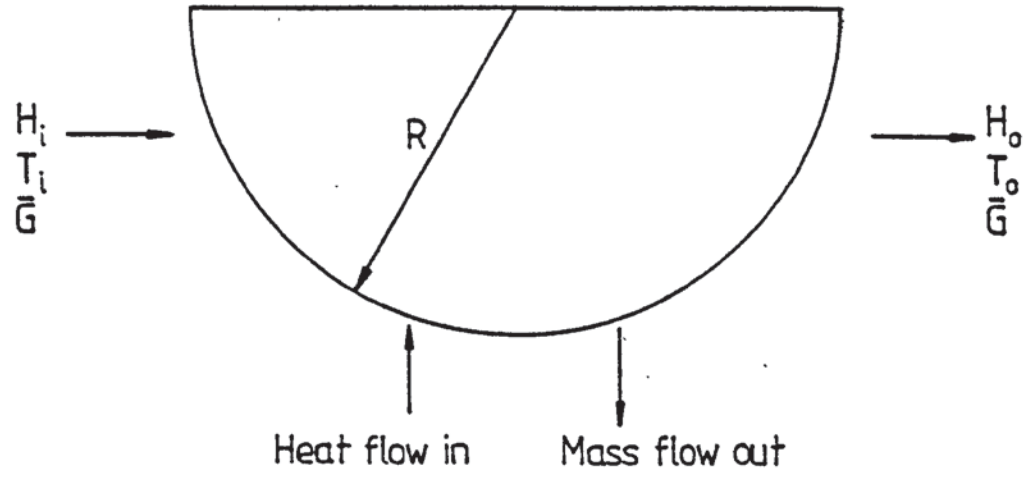

Figure 5·1 Suspended drop of pure liquid.

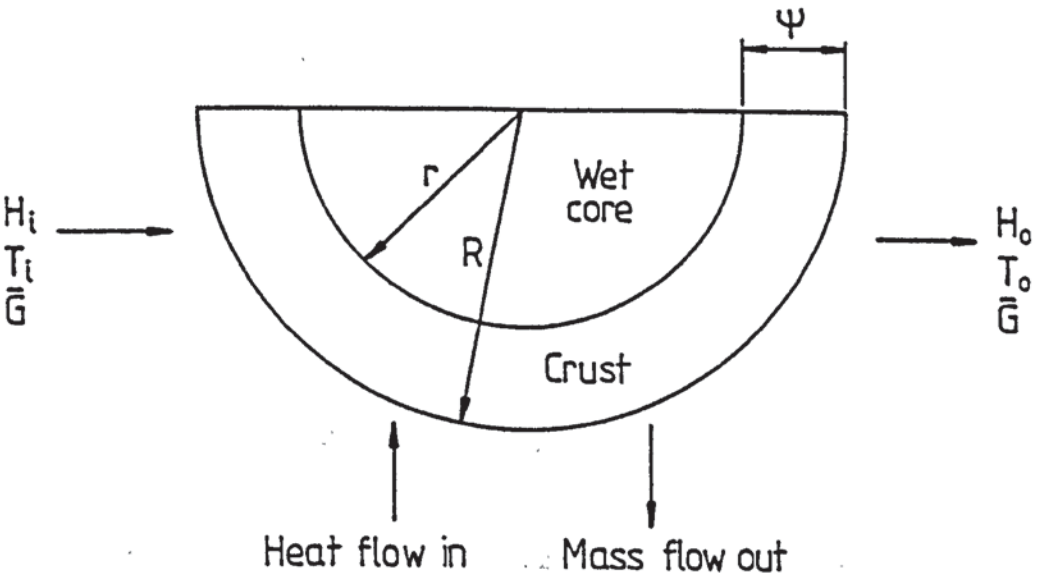

Figure 5·2 Suspended drop containing solids.

(5) There is a receding interface between the solution and the crust. As drying proceeds the crust grows inwards and the external radius of the drop remains constant. The internal radius is hence a function of time.

(6) The moisture is transferred from the evaporation interface by vapour diffusion through the pores.

(7) The core density remains constant during the evaporation process, i.e. as water evaporates at the interface, it precipitates an equivalent mass of solid as crust. This model which led in Cheong's work to equations 4.12 to 4.14 could not be tested in the present work since the suspended drop could not be weighed. In future it may be important to qualify assumption (7) e.g. to more closely relate deposited solid to evaporated vapour in the molecular formula. Also the model is restricted to conditions whilst there is still a wet core (since as described later hollow spheres generally result from extended drying).

5.2.1 Crust Thickness

The amount of moisture evaporated during time interval $\Delta\theta$, from a mass balance over the drop, is

$$\Delta W = G\,(H_d - H_u)\,\Delta\theta \qquad (5.23)$$

This is also equal to the quantity of water displaced in forming a crust of thickness (R - r). This is represented mathematically for a hemispherical drop as:

$$\Delta W = \frac{2}{3}\,\pi\,(R^3 - r^3)\,C_o \qquad (5.24)$$

By rearrangement of the above equation the crust thickness, ψ, becomes:

$$\psi = R - \left(R^3 - \frac{3}{2}\,\frac{G}{\pi C_o}\,(H_d - H_u)\,\Delta\theta\right)^{1/3} \qquad (5.25)$$

Equation (5.25), first developed by Audu (103), was used in this investigation, Section 9.2, for crust thickness prediction.

5.2.2 Mass Transfer Coefficient

The overall resistance to mass transfer of water vapour from the wet core to the air is composed of resistances to mass transfer through the crust and through the gas film surrounding the drop. Thus,

$$\frac{1}{K_o} = \frac{1}{k_g H_1} + \frac{1}{k_c} \qquad (5.26)$$

The air in the crust voids is saturated with water vapour, in the presence of liquid water. Hence the use of k_g from equation (5.11) is valid. The mass transfer coefficient of the crust is a function of the crust thickness, porosity and diffusivity of the water vapour and may be expressed mathematically by (23, 103),

$$k_c = \frac{D_v \varepsilon^{1.5}}{\psi} \qquad (5.27)$$

Thus equation (5.27) gives the mass transfer coefficient of the crust. This value of k_c can then be used in equation (5.26) to evaluate the overall theoretical mass transfer coefficient.

5.2.3 Crust Porosity

The rate of drying of drops containing dissolved or suspended solids would be expected to increase with increase in porosity, ε,. Porosity of the crust in this study was determined using a modified form of the Kozeny (3) equation - given below

$$\varepsilon = \left(\frac{5G.S_b^2.\nu}{2\pi d_c} \quad \frac{\psi}{\Delta P} \right)^{0.33} \qquad (5.28)$$

Audu (103) applied the above equation and calculated the porosity of detergent slurry drops. Subsequently Esubiyi (114) used the same formula in his investigation using drops of cement slurry. In the present investigation this modified equation was applied for crust porosity estimation of different drops of organic and inorganic solutions and slurries (Section 9.3).

CHAPTER SIX

EXPERIMENTAL INVESTIGATION

6.1 Introduction

Methods of predicting the evaporation and drying rates of single drops, and the phenomena associated with the evaporation process, are of importance in the analysis of chemical engineering operations involving dispersions in gases. They are particularly relevant to design calculations for spray dryers, to the correlation of fundamental information on the phenomena occurring during the drying process, and to closer simulation of conditions in the spray dryer. A wide distribution of drops of different sizes, which have different drying rates and residence times, are generated by atomisation in practical driers. Therefore, single drops have been studied (Sections 6.2 and 6.3). However, these drops have necessarily been of larger diameter (i.e. 1 mm to 8 mm) than the actual size in spray-drying i.e. 1μm to 1000 μm. This has proved necessary because it is difficult to support or retain single drops in this size range.

As discussed in Chapter 3 previous studies of the evaporation from single suspended-droplets and their drying behaviour were performed by Frossling (11), Charlesworth and Marshall (25) and Trommelen and Crosby (27) over a range of temperatures from 18°C to 400°C. These workers suspended drops of nitrobenzene, aniline, water, aqueous sodium sulphate, ammonium nitrate solution, copper sulphate solution, coffee extract and detergent drops, from fine glass filaments.

Evaporation from freely-falling drops was observed by Kendrick (142), using an apparatus in which a drop could be held stationary in space for long periods of time by means of an upward-flowing air stream at the terminal velocity of the drop, such that there was a hydrodynamic balance between gravity and the upward thrust due to air flow. Lihou (82, 84, 85) studied single drops falling in a gas stream and observed the effect of small amounts of various powders on the drop shape and terminal velocity. Finlay (79) and Jarvis (80) studied shape, oscillation and circulation, terminal velocity and rate of evaporation of freely-suspended liquid drops.

The present investigation is an extension of these studies. Drying characteristics and evaporation from free-flight drops was studied in addition to

suspended drops in order to compare the results and to evaluate their significance for spray drying. A limited number of experiments was also performed to study actual drop and particle size distributions using two different spray drying chambers. The droplet size distribution study involved the use of pressure nozzle and a coherent He/Ne laser to illuminate the droplets. Dried particles for study were produced from a rotary atomiser in a small-scale dryer and sized in a similar manner.

6.2 Horizontal Wind Tunnel for Suspended Drop Studies

6.2.1 Overall Experimental Arrangement

The experimental apparatus was a completely-modified, version of that used by Audu (103) and Esubiyi (114). The new design included the following improvements:

a) The wind tunnel and the working section were fabricated throughout with a circular cross-section, whereas the original design consisted of two sections of square cross section comprising the working section situated between two lengths of circular cross section. The modification was intended to eliminate eddies, and thus induce a uniform flow along the tunnel and working section, by avoiding any change in air flow path.

b) In the original design; upstream and downstream air humidities were measured using two sensors. Since no two sensors have the same sensitivity and calibration, in the new version the upstream and downstream humidities were measured by using one sensor only.

c) A secondary air-dryer was also added to obtain air of increased dryness and hence a higher humidity driving force between the saturated drop surface and the surrounding air.

d) Provision was made for direct drop temperature measurements via the newly-designed, nozzles. Only a hemispherical drop was suspended on

the nozzle, whilst in the original design the solution was continually introduced inside the nozzle and heat conducted from the nozzle to the liquid could therefore result in the initial drop temperature being higher than the ambient temperature.

The new nozzles were designed to be easily introduced into, or removed from, the working section. This enabled more accurate assessment to be made of drop drying time, i.e. the time of actual exposure in the working section. Moreover, due to the rapidity of nozzle introduction into the tunnel the initial drop temperature reading was essentially ambient temperature. All nozzles were made to accommodate thermocouples for improved drop temperature measurements. Previous designs (103, 114), required drop temperature measurement by the introduction of a thermocouple into the wind tunnel beneath the drop such that the junction of the thermocouple penetrated the drop. (With that arrangement hot air would tend to heat up the thermocouple which would then conduct heat into the drop. Moreover the thermocouple could deform the crust whilst the nozzle was rotating).

The flow system was designed to supply hot, dry air to the working section at a selected constant humidity and uniform temperature. The experimental apparatus for single suspended-drop studies is shown in the schematic diagram Figure 6.1, and in Plate 6.1. Essentially it consisted of an air reservoir, a Birlec air dryer, a secondary air dryer assembly, a metric rotameter type 18F, heating elements, a T-piece of brass material, and a Shaw Hygrometer.

Compressed air from the laboratory mains supply, at approximately 100 psi, was transferred via a reservoir, to dampen any fluctuations, and then into the Birlec air dryer. The pressure was then reduced to 1.5 bar via a valve (V4) and the air passed to the system via the secondary air dryer. The air flowrate was controlled by a gate valve at the inlet to the wind tunnel. The air was heated to any desired temperature in the range 21°C to 300°C using three, 1 kW electric heating elements. These were controlled by a rotary Regavolt Voltage regulator connected to the electrical

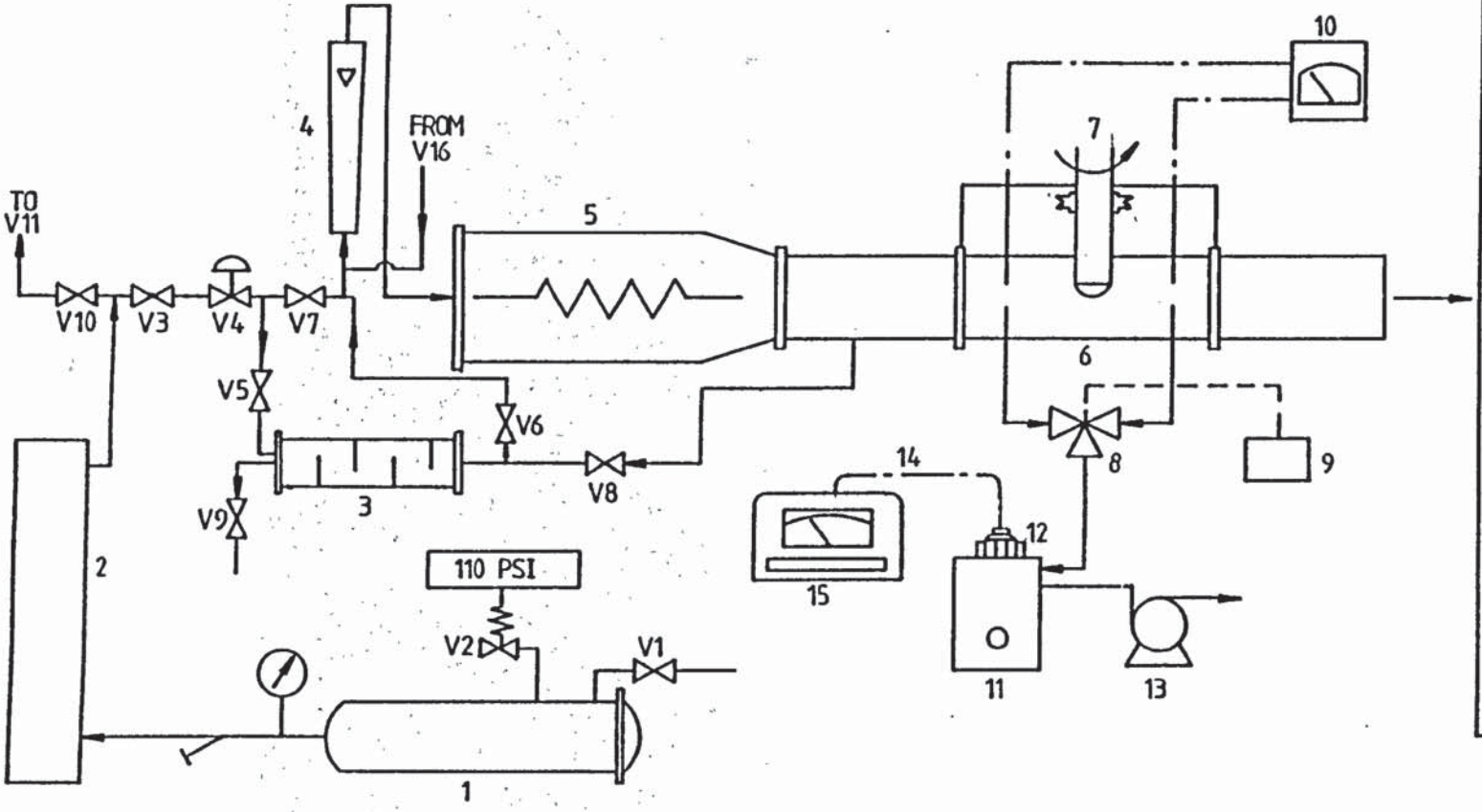

Item No.	Description
1	Air Reservoir
2	Birlec Air Dryer
3	Secondary Air Dryer
4	Rotameter
5	Air Heater
6	Working Section
7	Drop Suspension Device
8	Three-way Valve
9	Selector Switch
10	Temperature Recorder
11	Constant Temperature Unit
12	Sensor
13	Sample Pump
14	Coaxial Cable
15	Shaw-Hygrometer

Figure 6.1 Schematic Diagram of Suspended-Drop Experimental Apparatus.

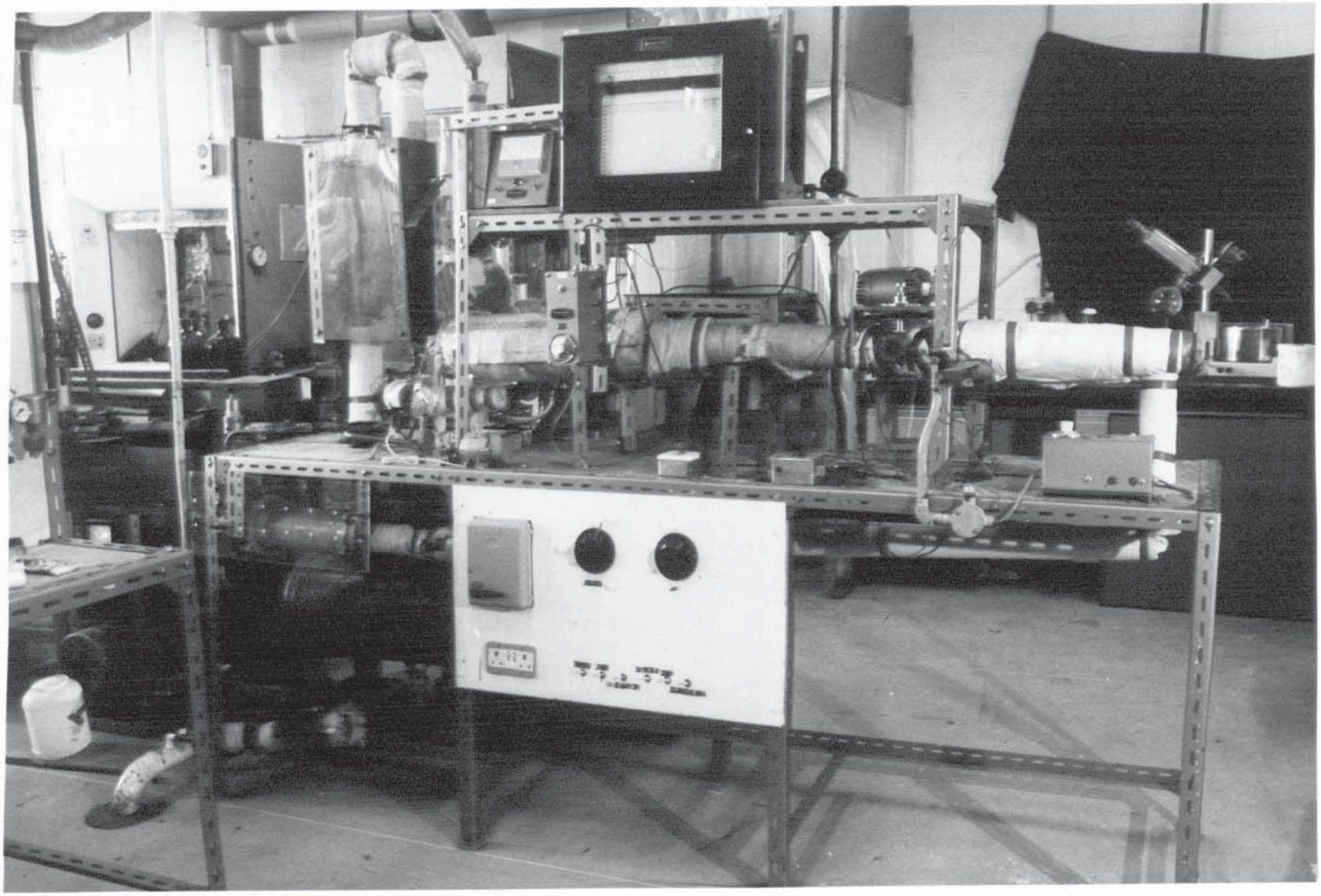

Plate 6.1 Horizontal Wind Tunnel - General Arrangement

supply.

As shown in the schematic diagram, Figure 6.2, superheated vapour, e.g. steam, could be used as the drying medium instead of dry air. For this purpose steam from the mains supply was piped into a reservoir through globe valve (V13). The pressure was then reduced and the steam super-heated by passage over the heater. The flowrate of the superheated steam into the tunnel was controlled by a globe valve and measured by the 18F rotameter. Condensate left via a steam trap with a maximum working pressure of 200 psi.

A - Air Reservoir

The air reservoir was constructed from a 30 cm diameter by 60 cm long, gas cylinder with a maximum working pressure of 100 psi. A 12.7 mm diameter Saunders diaphragm valve (V1) was provided on the inlet side; a pressure relief valve (V2) set at 110 psi was connected to the reservoir. The outlet pipe from the cylinder was coupled to a pressure indicator and a 12.7 mm diameter Spirax Sarco Strainer, and then to the Birlec Dehumidifiers.

B - Air Dryer

The air was dried by passage through a Birlec Dryer Type AB 30 containing granular Molecular Sieve and then through a packed column of self-indicating silica gel and a column of self-indicating aluminate silicate Molecular Sieve (Type 4A). The air dryer piping system and the secondary air drying assembly for regeneration are shown in Figure 6.3.

The Birlec air dryer was 1.05 m high and 190 mm wide. It was constructed from solid drawn steel tube with welded ends, with inlet and outlet side branches and a screw plug through which the adsorbent could be inserted or removed. An inner tube, with external longitudinal fins, contained the heating element. The vessel had a maximum working pressure of 100 psi.

The air from the Birlec dryer at 75 psi passed through a 12.7 mm Saunders diaphragm valve (V3) and then through a Spirax-Monnier type SR1 pressure

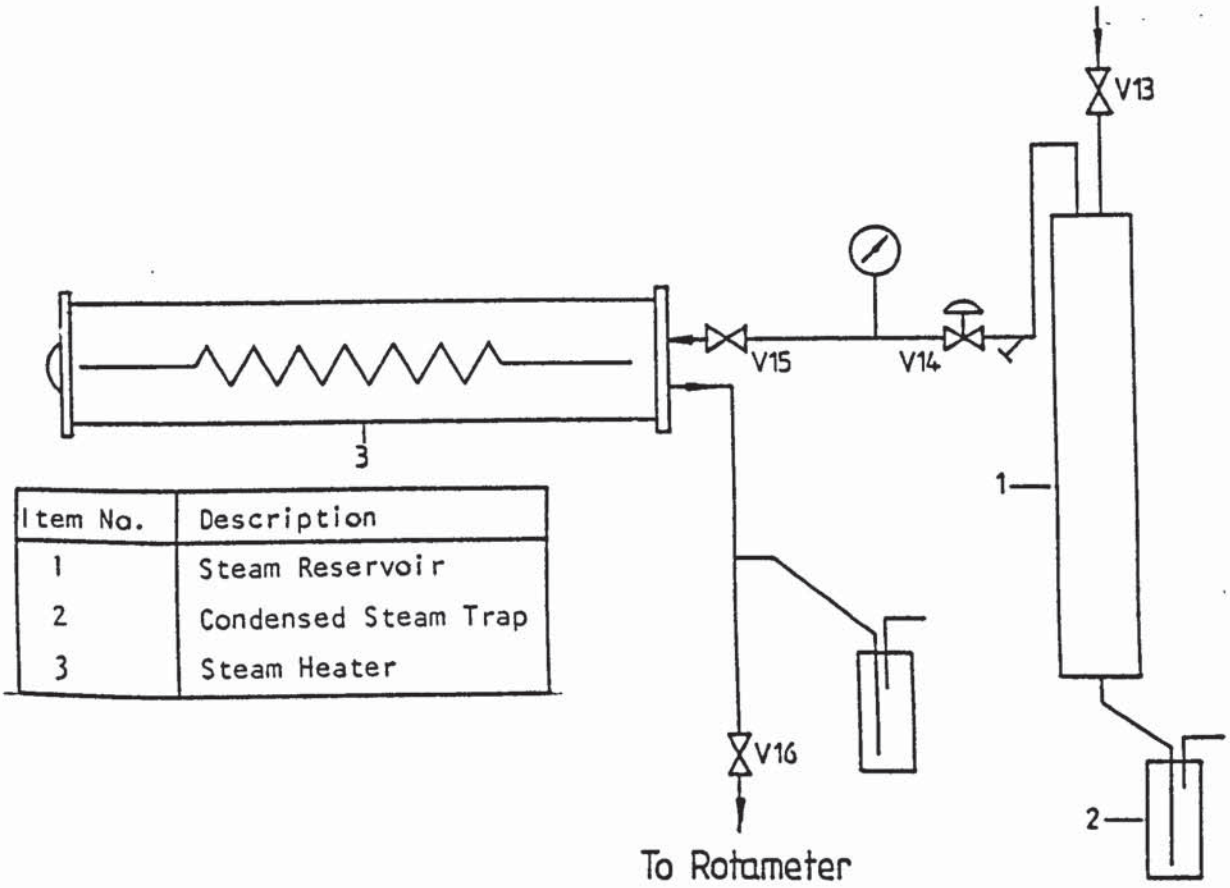

Item No.	Description
1	Steam Reservoir
2	Condensed Steam Trap
3	Steam Heater

Figure 6.2 Flow Diagram of Superheated Vapour Generation Apparatus.

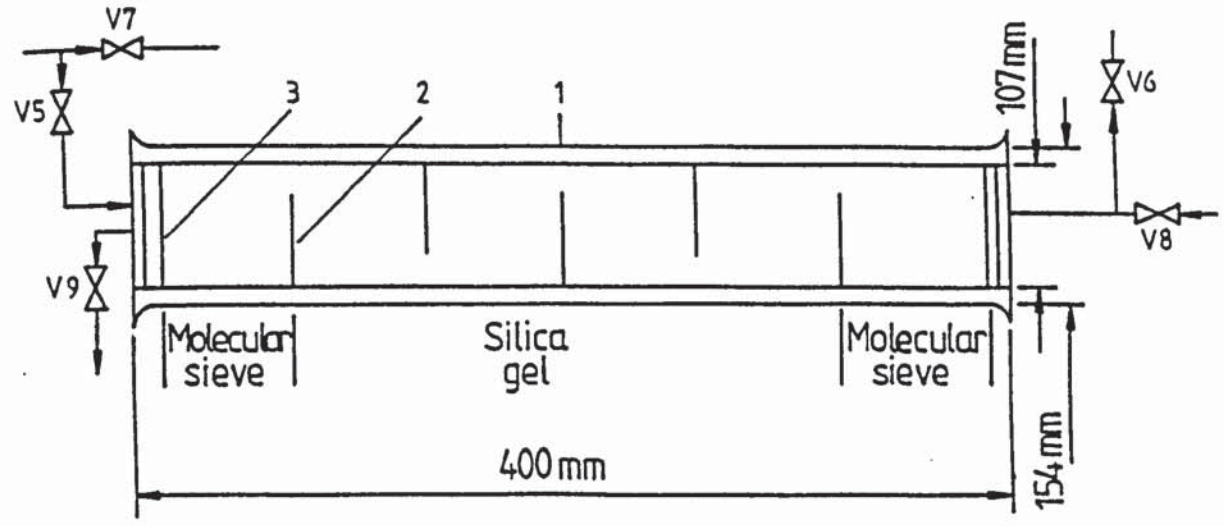

Item No.	Description
1	QVF Pipe Section
2	Baffle Plate
3	Wire Mesh

Figure 6.3 Secondary Air Drier Assembly.

reducing valve (V4) before entering the secondary air dryer. The secondary air dryer comprised a 400 mm long horizontal glass pipe section of 107 mm i.d. packed with silica-gel and molecular sieve. Five 'three-quarter' baffle plates were located evenly along the column to promote air redistribution. Dried air passed directly into the wind tunnel; the inlet and outlet moisture content of the air were measured using Shaw-Hygrometers.

Two layers of 5 mm mesh stainless steel, wire mesh were fitted at the ends of the column to prevent any particles from being carried downstream. Regeneration of the dessiccants, was performed by closing valves V5 and V6 and opening valves V7, V8 and V9.

C - Air Heater

The inlet air to the tunnel was controlled by means of 15 mm gate valve V6 and measured by means of an 18 F G.E.C. Elliott rotameter with a Duralumin float. The air was then heated by passage over three 1 kW, electric-bar heaters inside a 65 cm long copper tube of 8 cm o.d. at the end nearest to the rotameter and flanged; the other end of this jacket tapered to a 42 mm i.d. nozzle and flanged to a 50 cm long standard 42 mm i.d. mild steel tube. This was followed by the 'working-section' which ended in a 50 cm long standard 48 mm o.d. mild steel tube. A schematic diagram of the heater and the wind tunnel assembly is shown in Figure 6.4. The air temperature was controlled using a 6A, 90 ohm Cressal Torovolt voltage regulator connected to the electrical supply of the heater. This was capable of raising the air temperature from ambient to approximately 600°C.

Three layers of 30 mesh, stainless-steel wire mesh were spaced in series inside the mild steel tube at approximately 6 pipe diameters upstream from the working section. This ensured a uniform air temperature and produced a flat velocity profile. The velocity profiles were in fact measured using a pitot tube and an inclined manometer. A typical profile across the working section at the position of drop suspension is shown in Figure 7.2a.

The heater and all pipe work downstream were insulated with 25.5 mm

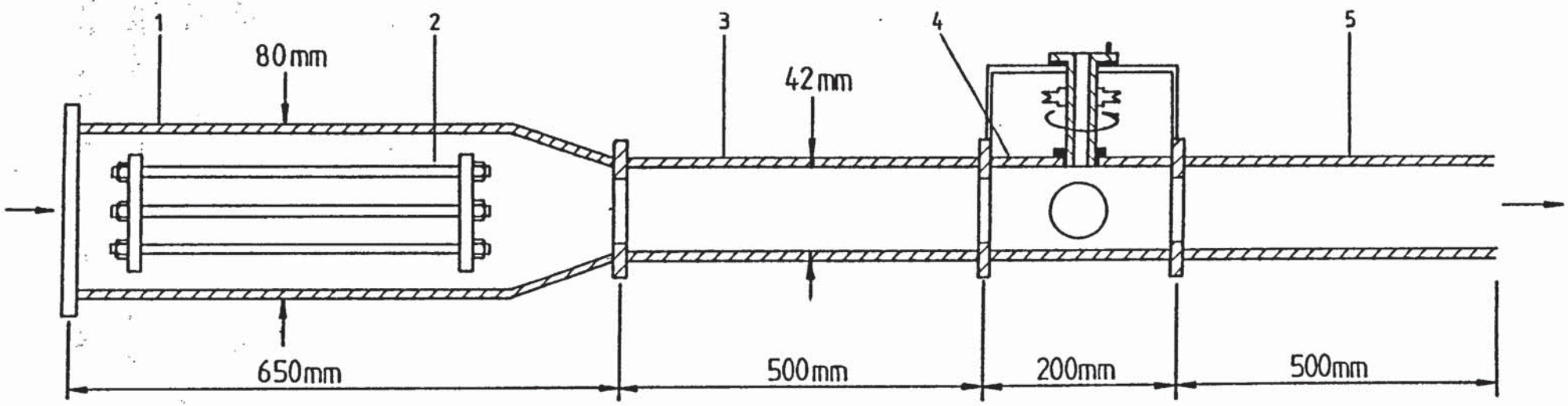

ItemNo.	Description	Materials
1	Heater Pipe	Copper
2	Heating Elements	Tungsten
3	Upstream Pipe	Mild Steel
4	Working Section	Brass
5	Downstream Pipe	Mild Steel

Figure 6.4 Air Heater and Wind Tunnel Assembly.

thick glass fibre insulation.

D - Working Section

The working section is shown in Figure 6.5 and Plate 6.2. It was fabricated from brass tube 20 cm long x 52 mm o.d. x 42 mm i.d. Two windows were located on opposite sides of the brass tube; each was flanged to hold an optical flat glass 6 mm thick and 40 mm diameter through which the suspended drop was photographed, or observed, with the required back lighting. The stainless steel housing of the drop suspension device was mounted at the top of the working section. The housing was constructed from 20 mm o.d. by 16 mm i.d. by 75 mm long stainless steel tube mounted at the top of the working section and sealed with polytetra-flouroethylene. The housing sat upon a metal frame 21 cm long x 8 cm wide x 7 cm high and bolted to the ends of the working section. A 70 mm V-shaped pulley served to drive the housing and hence the drop suspension device by means of a spigot on a metal ring at the top of the housing. The spigot was positioned in a hole in the metal ring of the nozzle, and the assembly was driven by a 50 Hz Parvalux electric mctor.

Air temperature was measured at points 50 mm upstream and 50 mm downstream of the drop by Nickel-Chromium/Nickel-Aluminium thermocouples connected via a manual selector unit to a Comark electric thermometer. Another thermocouple was installed inside the nozzle to measure the drop temperature directly as drying proceeded. Air humidities at points 50 mm upstream and downstream of the drop were measured with a Shaw-Hygrometer Unit.

6.2.2 Drop Suspension Device

The drop suspension unit is shown in Figure 6.6. It consisted of a metal plunger 145 mm long. Three were constructed of 4, 6 and 8 mm o.d. and an i.d. of 2.8 mm to enable the thermocouple for drop temperature measurement to be inserted. Three stainless steel tubes were constructed with inside diameters of 4, 6 and 8 mm respectively to accommodate each appropriate plunger. The stainless steel tube was 113 mm in length with an outer diameter of 16 mm at the top; the lower 20 mm end of the

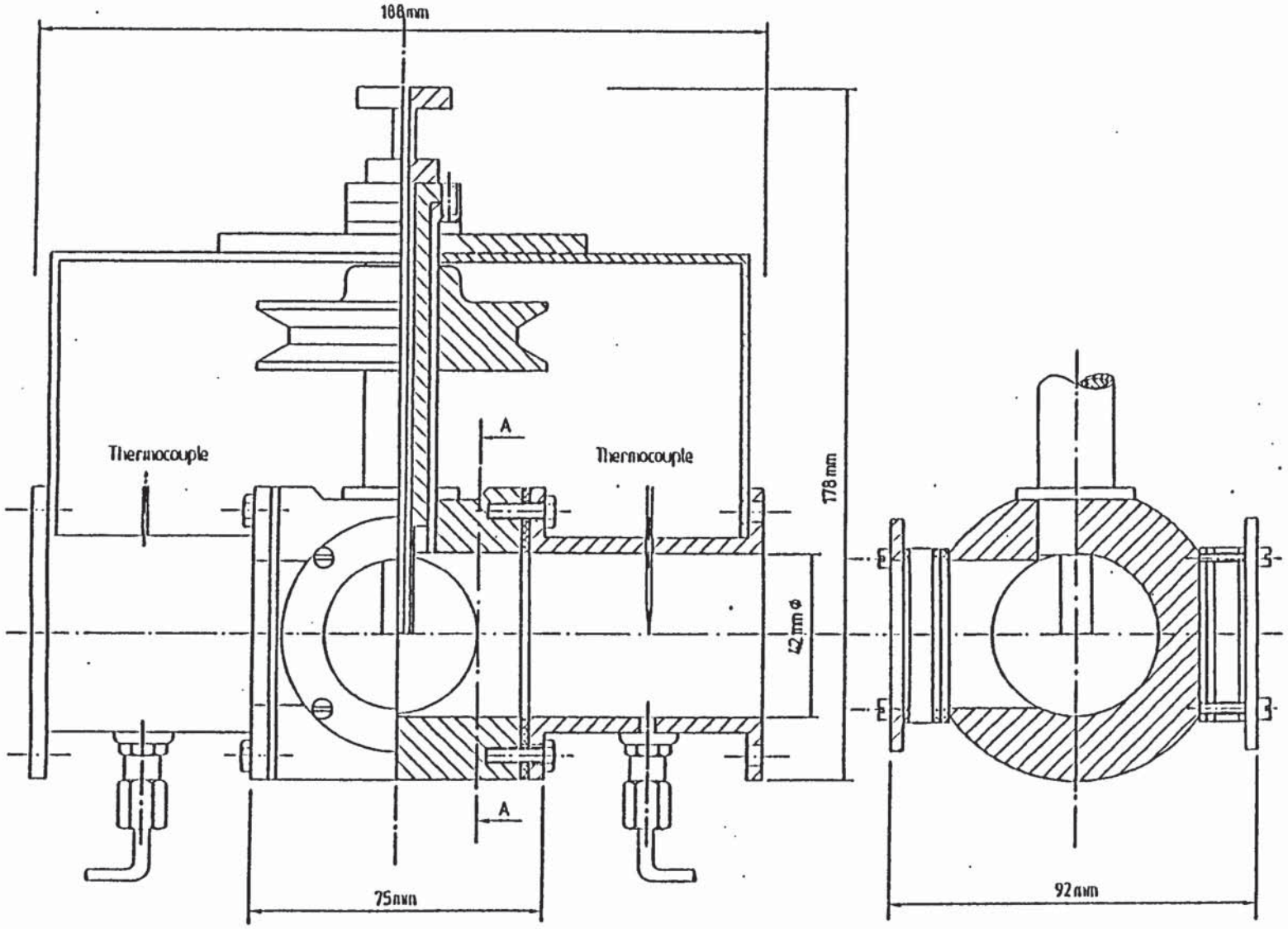

Figure 6·5 Working section of Suspended-drop experimental apparatus.

Item No.	Description
1	Thermocouple
2	Plunger
3	Stainless Steel Tube
4	Hole
5	Spigot
6	Ptfe Washer
7	70mm V-shaped Pulley
8	Stainless Steel Housing
9	Frame
10	Ptfe Disc
11	Ptfe O-ring
12	Working Section

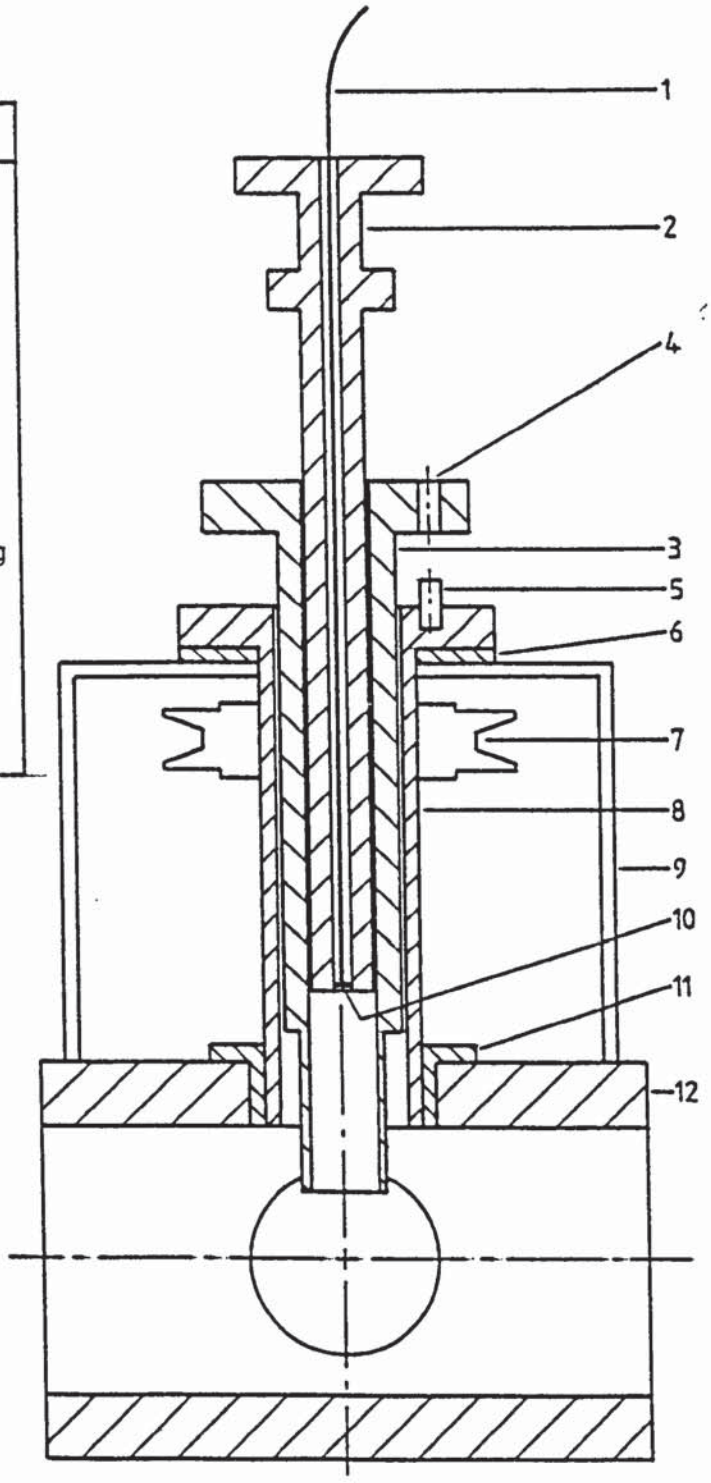

Figure 6.6 Drop-Suspension Device Assembly

tube was turned down to outer diameters of 7, 8 and 9 mm. This end fitted inside the working section. This reduction in the outer diameter of the lower end was intended to minimise the extraneous turbulence in air flow around the drop. A 32 mm o.d. ring was firmly secured to the top end of the tube; this ring contained a hole to accommodate the spigot.

The stainless steel tube and plunger assembly could be rotated by the electric motor with a maximum speed of 100 r.p.m. However, the speed actually used was only 15 r.p.m., since this was found to have no effect on the shape of the drop. The speed was controlled with a 27 ohm, 10A Cressal Torovolt resistor wired into the armature of the motor. A 35 mm V-shaped pulley connected to the motor shaft was coupled by a V-shaped belt to a 70 mm V-shaped pulley on the housing of the working section. The maximum speed of the drop rotater was hence half the speed of the motor due to the 1:2 pulley ratio.

6.2.3 Hygrometry Arrangements

The arrangement for humidity measurement consisted of a hygrometer, a moisture sensing element, a constant temperature unit, a sampling pump, coaxial cable, a three-way valve, and selector switch, as shown in Plate 6.3.

The principle of operation of the sensing elements was that the capacitance varied in direct proportion to the dewpoint of the gas. The probe of the sensor was protected from contamination by a sintered bronze filter. Once air flowed over this filter a dynamic equilibrium was set up between the liquid water contained in the pores and the water vapour pressure outside. Owing to the small size of the pores, large molecules could not enter and the sensor was hence specific to water vapour. The sensor estimated the capacitance of the gas and transmitted it via the coaxial cable to the dewpoint meter. The latter was scaled to read dew-points from -80°C to -20°C and 0-1000 parts per million of water vapour by volume.

The constant temperature unit maintained a constant temperature in the gas flowing to the sensing element. It also prevented condensation of the flowing gas on

the sensing element by maintaining the gas at a temperature well above its dewpoint. The unit consisted of a brass container into which the sensor was screwed. A dial switch mounted on the unit operated a sensitive thermostat which maintained a constant temperature in the range 0°C to 110°C and indicated by the dial switch. The sensor chamber was heated by a 30 W heater. This chamber was constructed from heavy brass and was chrome-plated, the inlet and outlet were of 3.2 mm o.d. copper piping. A constant flow of air through the unit was supplied from the working section by the sampling pump which delivered air at a rate of 0.5 dm^3/min.

6.3 Vertical Wind Tunnel for Free-Flight Drop Studies

6.3.1 Overall Arrangement

The experimental apparatus for free-flight drop experiments which followed the original design of Lihou (82) is illustrated diagrammatically in Figure 6.7 and shown in Plate 6.4. The wind tunnel consisted of a closed circuit of rectangular and circular ducting constructed of 10 gauge mild steel sheet.

Air from the 3-phase, 0.75 kW centrifugal fan (A) expanded through the horizontal tapered expansion duct (B) to a large cubical settling-chamber (C) containing two rows of five and three 1 kW electric bar heaters (D) respectively. To reduce the turbulent eddies, and to assist the 90° change in direction of the air flow, a fine mesh gauze (E) was placed at the exit of the settling-chamber. The suction flare (F) was designed in order to reduce the cross-section without re-introducing turbulence.

The smoothing section (G) contained four damping screens (H) to reduce turbulence and provide a gas stream with a uniform velocity. This damping section was followed by the smooth contraction (I) in which the parallel filaments of air were brought together and accelerated whilst further reducing the intensity of turbulence. A screen wire gauze (J), of 20 mesh, was inserted between the working section (K) and smooth contraction; this was shaped to produce an inverted, uniform velocity profile on the axis of the working section. The shape of the gauze and velocity profile it

Figure 6.7 Schematic Diagram of Free-Flight Drop Experimental Apparatus.

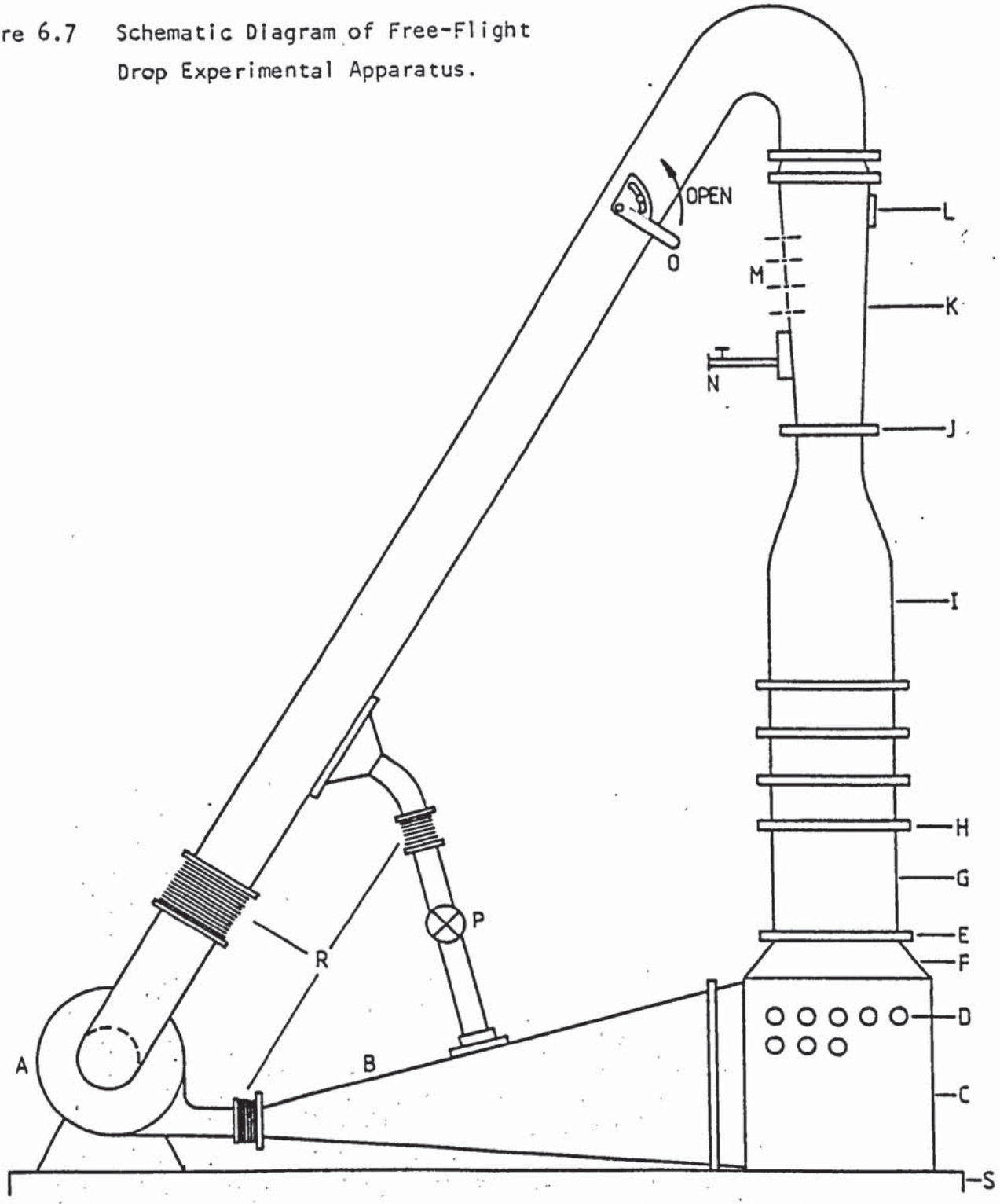

A	Fan	H	Damping Screens	N	Drop-Catching Unit
B	Expansion Duct	I	Smoothing Contraction	O	Control Valve
C	Settling Chamber	J	Wire Gauze	P	Butterfly Valve
D	Heater Elements	K	Working Section	R	Rubber Connections
E	Mesh Gauze	L	Tapped Hole for Drop Producing Unit	S	Stand
F	Suction Flare	M	Tapped Holes for Pitot Tube		
G	Smoothing Section				

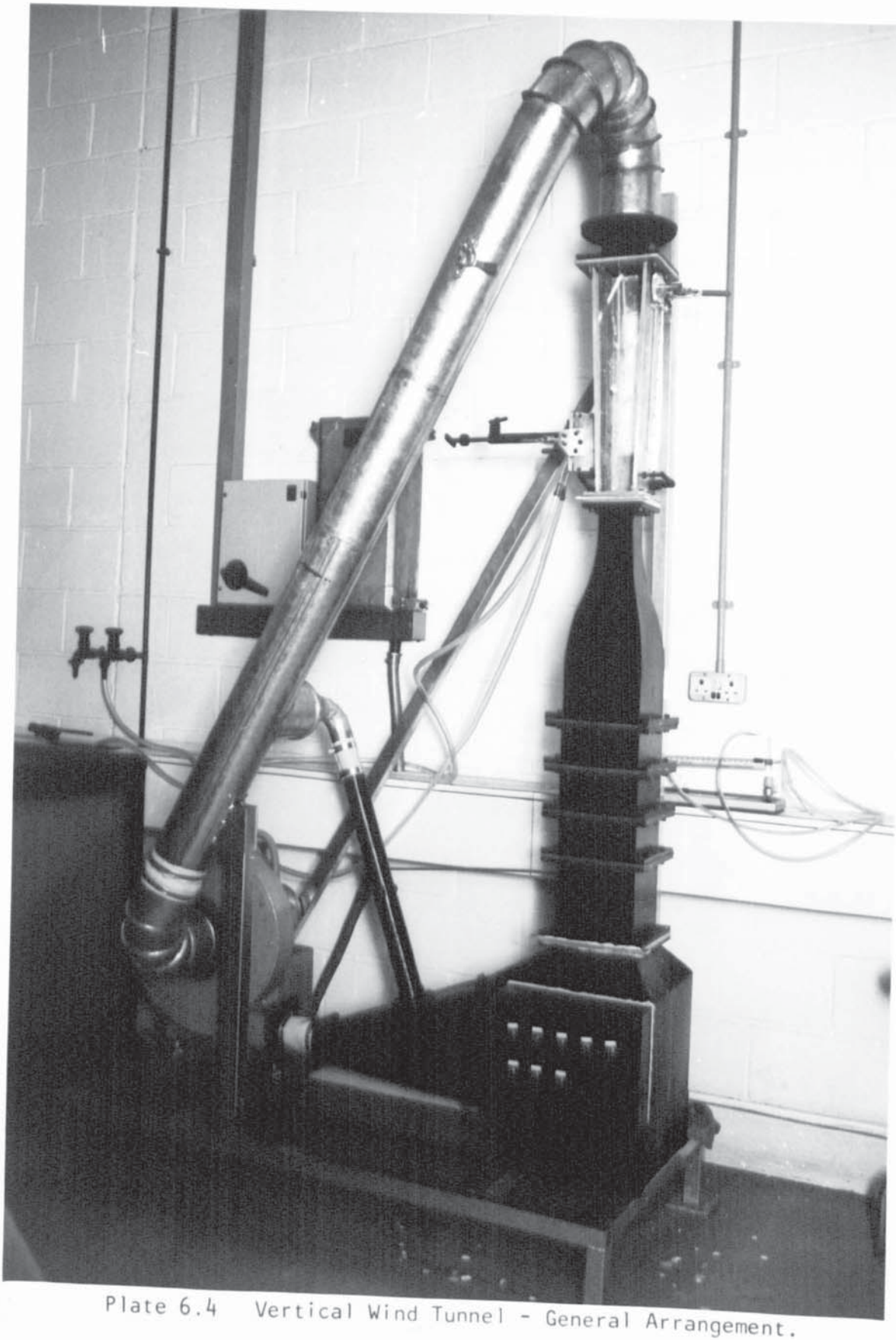

Plate 6.4 Vertical Wind Tunnel - General Arrangement.

produced are shown in Figure 7.3. The gauze was screwed to a removable frame to enable rapid access for cleaning.

The working section shown diagrammatically in Figure 6.8, and represented by Plate 6.5, diverged with a 3^{o} total angle giving an increased area downstream. The divergence provided a vertical velocity gradient such that the velocity decreased downstream. This enabled the drop to find its own level of stability. The front wall was of plate glass cemented into the other three walls of aluminium. Smaller glass windows were let into the right and rear side walls for illumination purposes. A 52 mm diameter circular hole (L) was cut through the top of the right-hand side wall through which the drop forming unit was introduced. Once the drop had formed in the column, the drop forming unit was removed and replaced by a flat aluminium circular plate with quick-relase clamp to seal the hole perfectly. Four, 6 mm diameter, holes (M) were drilled in the left-hand side wall at a spacing of 52 mm vertically to allow a pitot tube to be inserted into the working section. When not in use these holes were plugged with 6 mm removable bolts. The drop collection unit (N) was attached to the same side.

The air flowrate was controlled by a main valve (O), which was used to bring the drop to the required position in the working section. A butterfly valve (P) was used for delicate alterations of the flowrate.

6.3.2 Drop-forming Unit

A schematic diagram of the drop-forming unit is shown in Figure 6.9. The liquid, contained in a 10 cc plastic syringe (A), was injected via a hypodermic needle (B) and a glass nozzle (C). Nozzles with different diameters were used to obtain different drop sizes. The nozzles were mounted in a rubber bung (D); the end of the hypodermic needle was bent through 90^{o} and passed through the top of this bung and into the top end of the nozzle. To shield a drop from the air flow during formation the rubber bung was inserted into a short length of perspex tubing (E); its

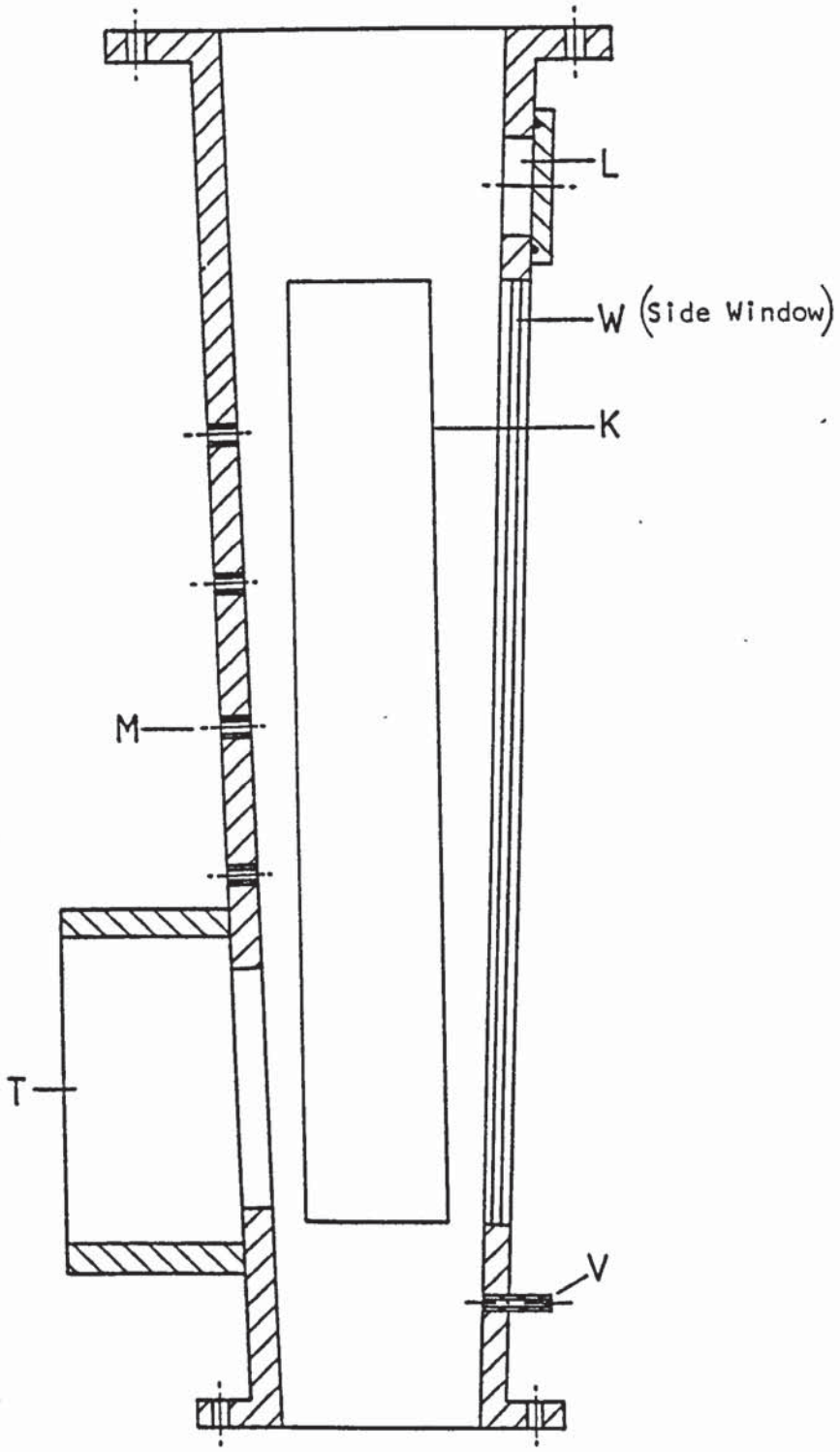

Item	Description
V	Standard Pressure Tapping
T	Housing for Drop-Catching Unit
K	Rear Window
L	Hole for Drop-Forming Unit
M	Pitot Tappings

Figure 6.8 Working Section of Free-Flight Drop Experimental Apparatus.

purpose was to prevent contact of the air stream with the drop prior to the moment of release. The drop detached from the nozzle under the action of gravity.

The unit was introduced into the air stream in the working section through the hole (L). Once the drop had been injected the unit was removed and the hole re-sealed.

6.3.3 Drop-Catching Unit

Drops were produced and stabilised in the working section one at a time i.e. each was caught and removed before the next one was injected. A special cup was designed to hold a small bottle for catching the drops so that they were removed rapidly from the air stream without further mass transfer during, or after, collection. This cup remained retracted through the wall of the working section except during collection.

A diagram of the unit is shown in Figure 6.10. It consisted of a hollow aluminium block (B), containing a 25 x 50 mm weighing bottle (A), which was supported on one side by a brass arm (C), and was spring-loaded to another square section metal support (D). The support was rigidly fixed to the detachable back (E) of a box fixed to the side of the working section by two quick-release clamps.

A cooling coil (F) of 2 mm o.d. stainless steel tube lined the recess in (B). Cooling water was passed through the coil via 4-5 mm o.d. rubber pressure tubing; this did not hinder the speed at which the block could be shot into the working section. With the column operating at 100°C the cooling coil was able to maintain the temperature of the cup at 25°C, this reduced any evaporation from a drop after collection.

Power for injection of the cup (B) was obtained by the action of spring (G) being released when desired by means of a trigger mechanism (H); this was also used to retain it in the retracted position.

Drops were caught in the cup when the spring was released. The aluminium block containing the weighing bottle was quickly introduced through the

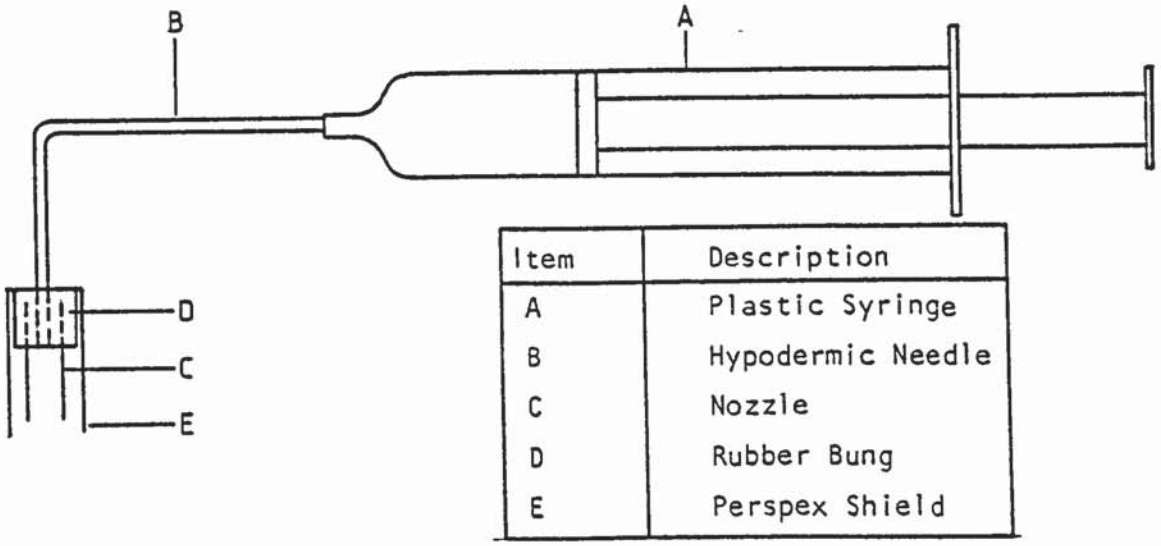

Item	Description
A	Plastic Syringe
B	Hypodermic Needle
C	Nozzle
D	Rubber Bung
E	Perspex Shield

Figure 6.9 Drop-Forming Unit.

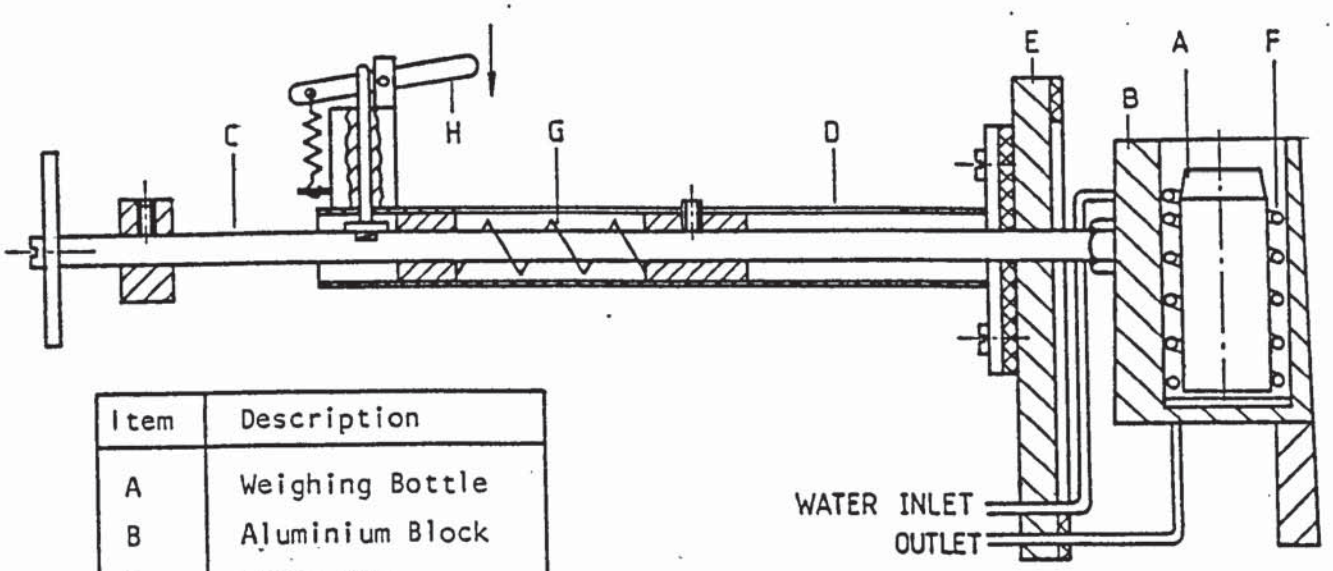

Item	Description
A	Weighing Bottle
B	Aluminium Block
C	Brass Arm
D	Metal Support
E	Detachable Back
F	Cooling Coil
G	Spring
H	Trigger Mechanism

Figure 6.10 Drop-Catching Unit

side-wall of the working section and beneath the drop, which then fell into the bottle because of the sudden decrease in air velocity in the region where the drop was supported. After drop capture, the whole unit was removed from the working section. It was found to be important to seal the bottle as quickly as possible in order to reduce further evaporation. The unit was then replaced in position and the spring recompressed for the next release.

6.3.4 Velocity Profile Modification by Screen Meshes

When a droplet was placed in an upward-moving air stream with a velocity equivalent to the terminal velocity of the droplet, it should, in theory, have been stably supported. In practice, the droplet did not float centrally but immediately after injection was thrown onto the wall of the working section.

A reduced velocity region was therefore produced in the central part of the air stream, by means of a screen mesh positioned in the entrance of the working section. With this arrangement, when the air velocity was adjusted to the terminal velocity, a drop inserted in this region floated until it was caught. Even if the droplet was moved in a radial direction by turbulence during the drying period, it was returned to the central region by the higher velocity flow. Any droplet inadvertently injected into the higher velocity region was carried away by the air stream. However, droplets in the slow velocity region always floated stably. Screen meshes of different shape, diameter and material were tested to find the best possible velocity profile for stable droplets. Figure 7.3 shows the velocity distribution in the working section at various positions above the screen, an air velocity profile, and the preferred screen gauze shape.

6.4 Pilot Scale Spray Driers

A Niro Spray drier, mobile minor, unit of the standard, open-cycle layout was used to produce dried particles. Air was drawn from the atmosphere, passed once through the drying chamber co-current with the sprayed drops and exhausted to

atmosphere. Dried particles were collected in the cyclone.

A larger perspex tower section was used to study spray size-distribution and spray cone angles.

6.4.1 Apparatus

Laboratory Spray Drier

The experimental spray drier for routine spray-drying tests is illustrated in Plate 6.6 and represented schematically in Figure 6.11a. It comprised a co-current air flow Niro spray dryer, with a rotary atomiser and a cyclone separator for dried-product removal. The drying chamber had an internal diameter of 0.8 m and was 0.6 m high. Feed was fed to the nozzle from a 3 litre container which rested on a vertical support above the pneumatic lid, lifting-device.

Transparent Tower

Plate 6.7 shows the perspex spray tower for drop atomisation studies. Figure 6.11b represents a schematic diagram of the equipment which comprised a 1.23 m diameter perspex tower, a centrifugal pressure nozzle, a Brook Crompton-Parkinson feed pump driven by a 3 kW motor and, a glass feed vessel. It was used in conjunction with the Malvern Laser Particle Size Analyser.

6.4.2 General Operating Procedure

Laboratory Spray Dryer

The air disperser and the rotary atomiser were located at the top of the Niro dryer chamber. (This co-current design is the most common in industrial operations). The feed liquid was fed to the atomiser under gravity and atomised into a fine spray of droplets. The spray was contacted with hot air entering the chamber through the top air disperser, positioned in the centre of the chamber roof and designed to create a swirling air flow directly around the vaned atomiser wheel. Removal of moisture from the droplets was accomplished rapidly (124) and, dry powder was drawn off with the air at the base of the chamber. Powder and air passed to a small

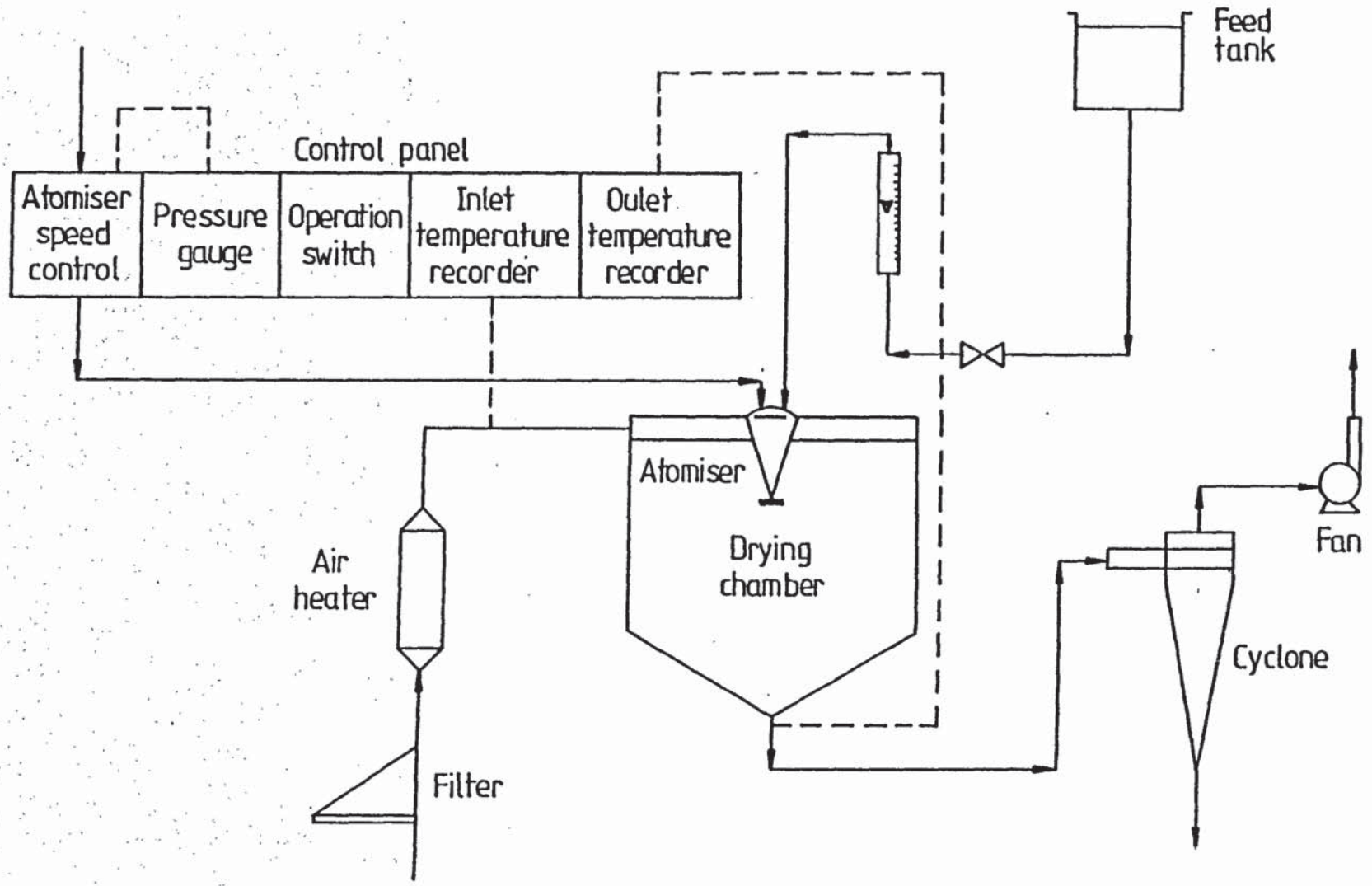

Figure 6·11a Diagram of spray drying unit

Niro-Atomiser

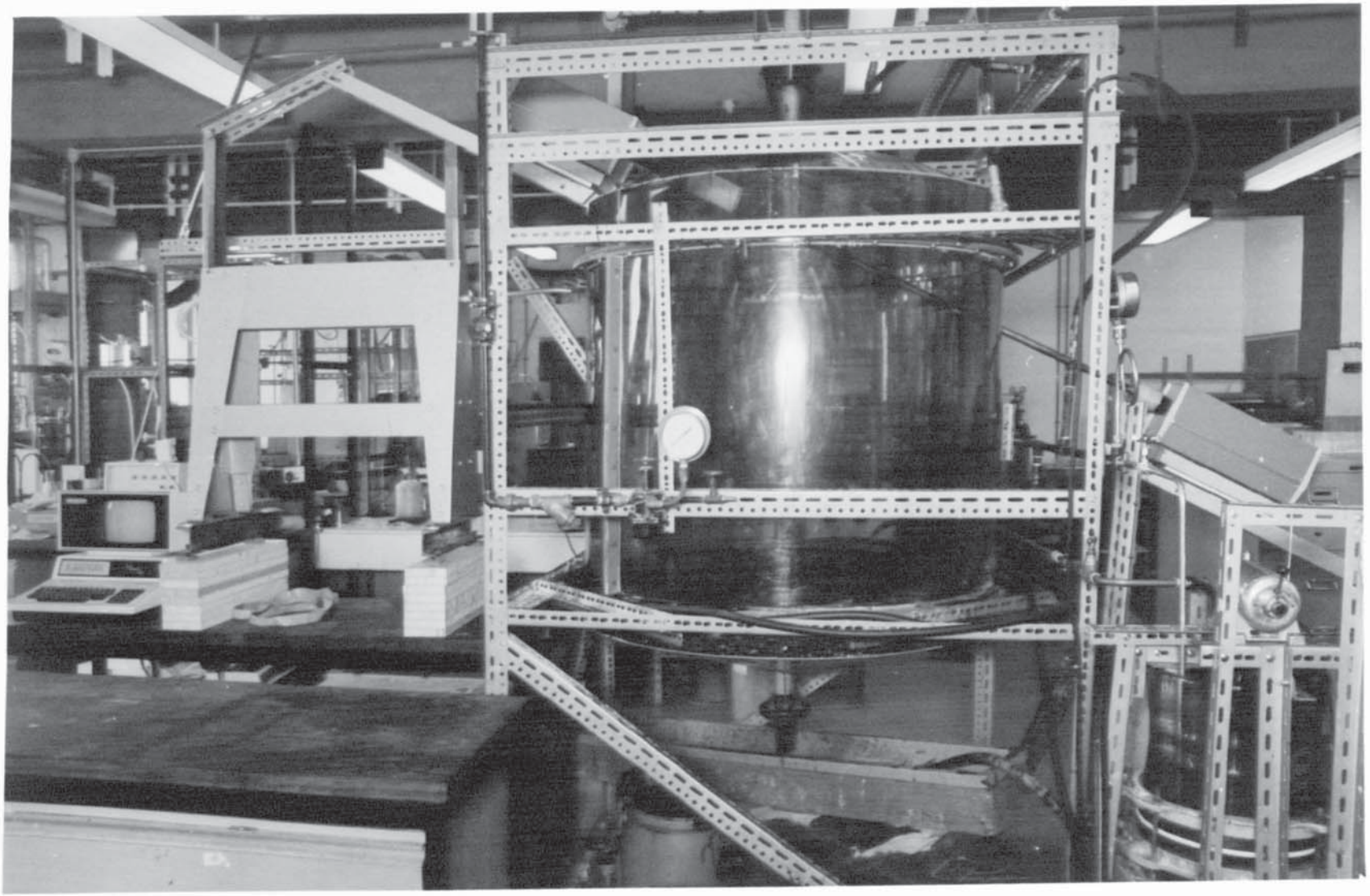

Plate 6.7 Perspex Spray Tower and Laser Particle Analyser (Malvern 2200 Particle Sizer).

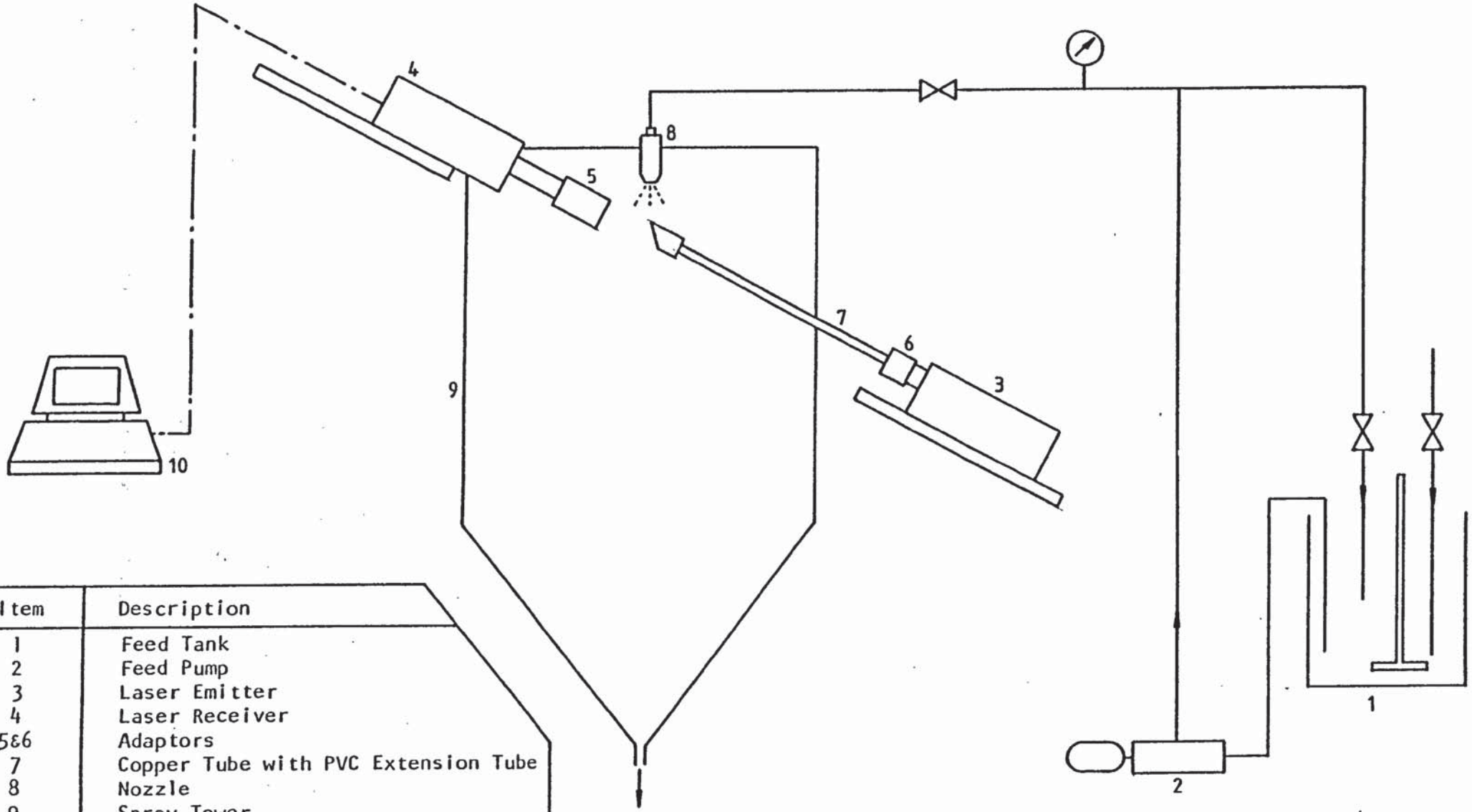

Item	Description
1	Feed Tank
2	Feed Pump
3	Laser Emitter
4	Laser Receiver
5&6	Adaptors
7	Copper Tube with PVC Extension Tube
8	Nozzle
9	Spray Tower
10	Microcomputer

Figure 6.11b Schematic Diagram of Perspex Spray Tower Experimental Apparatus.

cyclone where the powder was separated out and collected in an interchangeable glass jar. All the necessary controls and instrumentation were centrally located on the panel. The air flow was controlled by the damper situated at the right-hand side of the instrument panel.

Air and product left the chamber through a 50 mm diameter duct, connecting the chamber base to the cyclone. The chamber was fully insulated to minimise heat loss. Access into the chamber for cleaning was by lifting the chamber roof away from the chamber base using a built-in pneumatic system. Liquid dispersion was from a rotary type atomiser with a vaned wheel driven by an air turbine. The turbine was driven by compressed air at pressures adjustable from 1 $kg.cm^{-2}$ to 4.8 $kg.cm^{-2}$, thus enabling changes of wheel speed. The wheel incorporated 24 rectangular vanes of 6 mm x 3 mm.

Dried samples were collected in a glass jar placed beneath the cyclone. (To avoid dust inhalation during jar removal/replacement a 3M's dust mask was worn).

Drop Atomisation Studies

A limited amount of work was also carried out using the perspex spray tower. This involved droplet size distribution analysis using a Malvern Laser Particle Size Analyser. To study the droplet size distribution generated from the nozzle, the analyser was mounted across the 1.23 m diameter perspex tower. The receiver section of the analyser was mounted on an optical bench. The analyser was used with a 300 mm focal length lens fitted with a polypropylene adaptor to prevent spray settling on the lens. The laser emitter was located outside the tower and the laser beam protected from the spray with an 18 mm o.d. copper tube which extended into the tower and directly under the spray cone of the nozzle. A 200 mm long p.v.c. tube of 40 mm o.d. was mounted on the end of the copper tube such that the edge of the copper tube was shielded from direct impact by the spray. This prevented any slurry flowing down the tube and into the laser emitter. The positions of the emitter and receiver are shown in Figure 6.11b and Plate 6.7.

6.5 Ancilliary Apparatus

6.5.1 The Stereoscan Electron Microscope

The Stereoscan microscope was essentially a scanning electron microscope which produced three-dimensional photographs of the sample under observation. The specimen was scanned with a fine electron beam synchronised with the electron beam of a cathode ray tube. It had a wide magnification range, from 20 to 100,000 diameters, although the image began to blur above 20,000 diameters. This broad magnification range, together with the ease of changing magnification made it possible to zoom from a gross image of the object to an image showing fine details. Structural analysis of specimens of the crusts of the dried drops was achieved by this means.

6.5.2 Malvern Laser Particle Size Analyser

The Malvern Laser Partical Size Analyser consisted of He/Ne laser emitter and laser receiver and lenses.

Operating Procedure

When a beam of light falls on a spherical, or non-circular, droplet a diffraction pattern is formed whereby some of the light is deflected by an amount dependent upon the size of the droplet. If a suitable Fourier Transform lens placed in the light path between the droplets and the detector is placed at the focal point of the lens, then the light not diffracted by the droplet is brought to a point on the axis. Light which is not diffracted by the drop will be concentrated concentrically at some distance from the axis; this distance is a direct function of the droplet diameter. If a sample containing different droplet diameters is sampled in the beam, then a series of concentric light rings will be generated at various radii each being a function of a particular droplet size.

Application

In the Malvern Sizer light energy is extracted from the droplet diffraction pattern by a large scale solid state detector which consists of 31 concentric

semi-conductor photosensitive rings, surrounding a central quadrant, each ring being sensitive to one particular droplet diameter. The electrical output from the rings was scanned and amplified and the analysis of light energy distribution into particle size carried out in the associated computer. The Malvern 2200 Particle Sizer had a size range of 1 - 1800 microns (125).

6.5.3 Thermal Conductivity Experimental Apparatus

The thermal conductivity experimental apparatus specially-designed for this study was a modified form of Lee's Disc Apparatus (83). The arrangement is shown in Plate 6.8 and Figure 6.12. Essentially it consisted of three discs 1, 2 and 3 of good conducting metal, e.g. copper, an asbestos ring, a high vacuum pump, a D.C. voltmeter, a D. C. Ampere meter, a small electric heater, a Comark electric thermometer, and a Comark manual selector unit.

The discs were all of identical diameter, 139 mm, and 7 mm thick. Each disc was drilled from the side into the centre to take an Ni-Cr/Ni-Al thermocouple. The asbestos ring was 139 mm i.d. and 153 mm o.d. and 10 mm thick. Along the side of the ring was a 7 mm diameter hole into which was inserted a 6.4 mm o.d. copper tube, sealed by high temeprature cement. The copper tube was connected to a vacuum pump. The specimen was placed in between disc (1) and disc (2) and contained by the asbestos ring; the heater was placed between disc (2) and disc (3). These were all clamped firmly together. The heater was isolated from the surroundings and connected in series with an ammeter (range 0 - 5A) and voltmeter (range 0 - 100V). The apparatus was earthed and the assembly stood on a sheet of asbestos.

6.5.4. Apparatus for Pressure Drop Measurements Across Crust

The pressure drop across each dried crust was determined in the apparatus shown in Figure 6.13. The assembly consisted of two QVF tubes, a rotameter, a U-tube manometer and a crust support.

The test section consisted of two QVF glass tubes of 33 mm diameter and

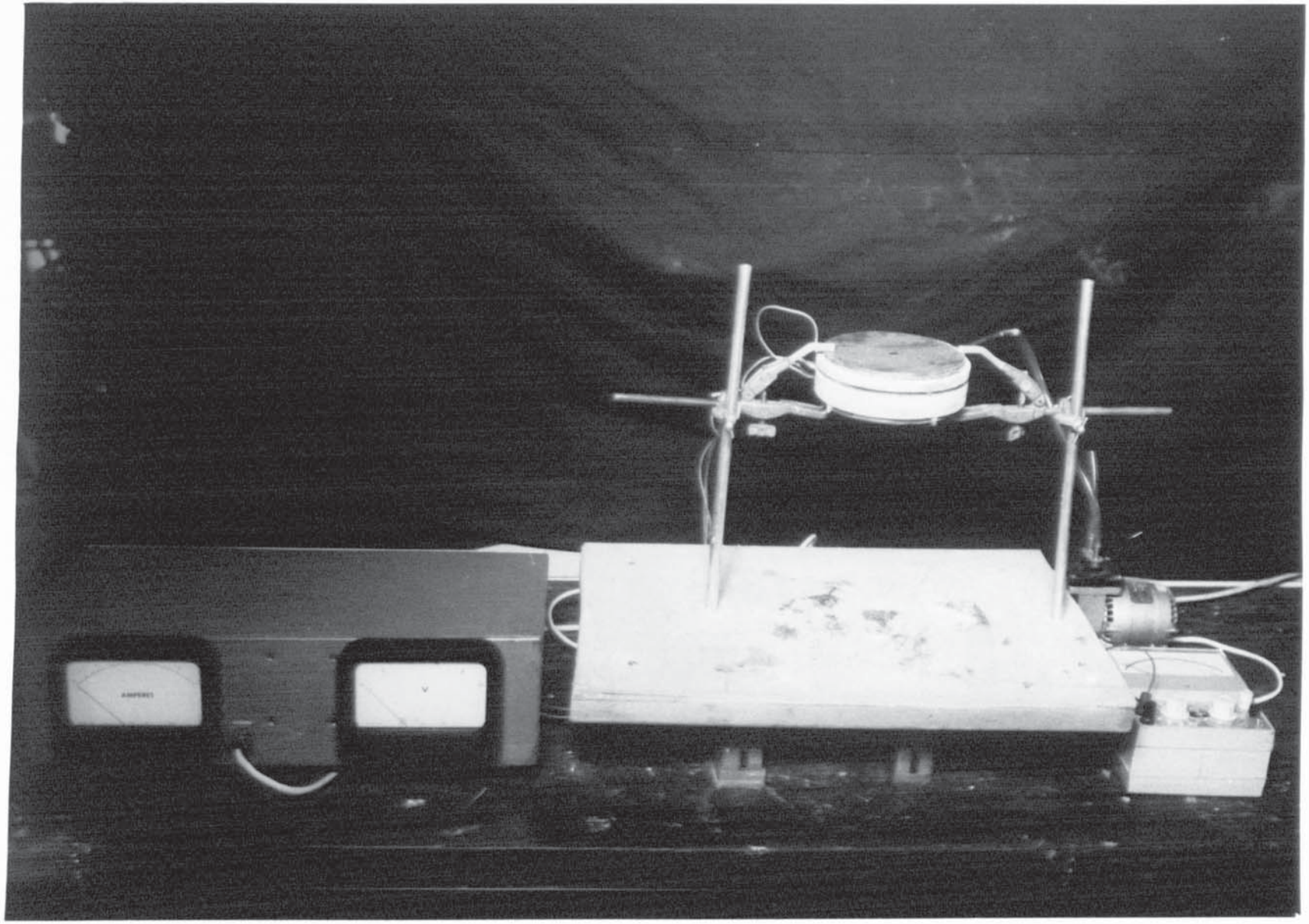

Plate 6.8 Thermal Conductivity Measurement Apparatus.

Item No.	Description
1	Metallic Discs
2	" "
3	" "
4	Heating Element
5	Asbestos Rings
6	" "
7	Box
8	Voltmeter
9	Ammeter
10	Vacuum Pump
11	Thermocouples
12	Temperature Recorder

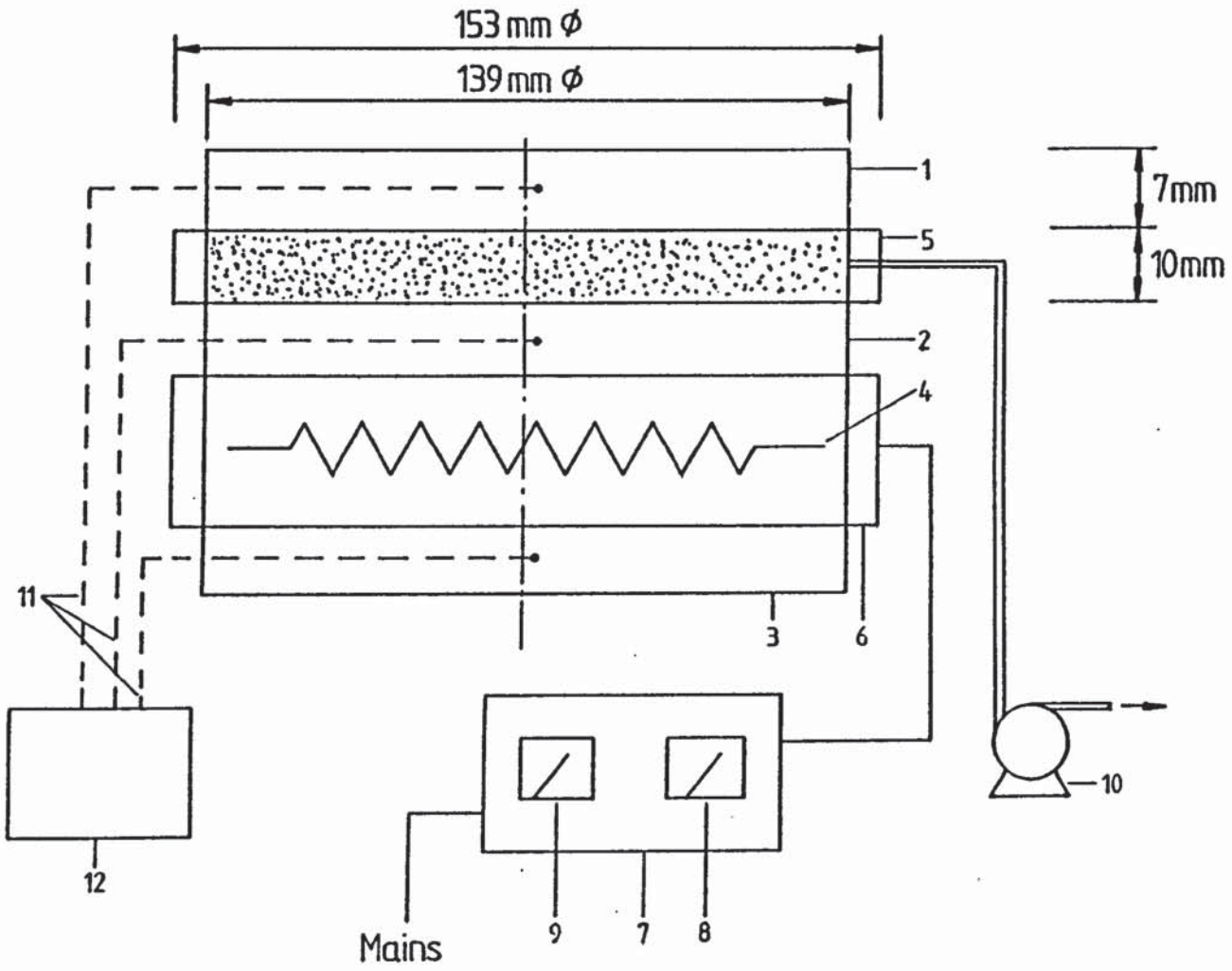

Figure 6.12 Schematic Diagram of Thermal Conductivity Apparatus Assembly.

Item	Description
1	Rotameter
2	U-tube Manometer
3	Industrial Glass Tube
4	" " "
5	Crust Support
6	Stainless Steel Tube
7	Crust

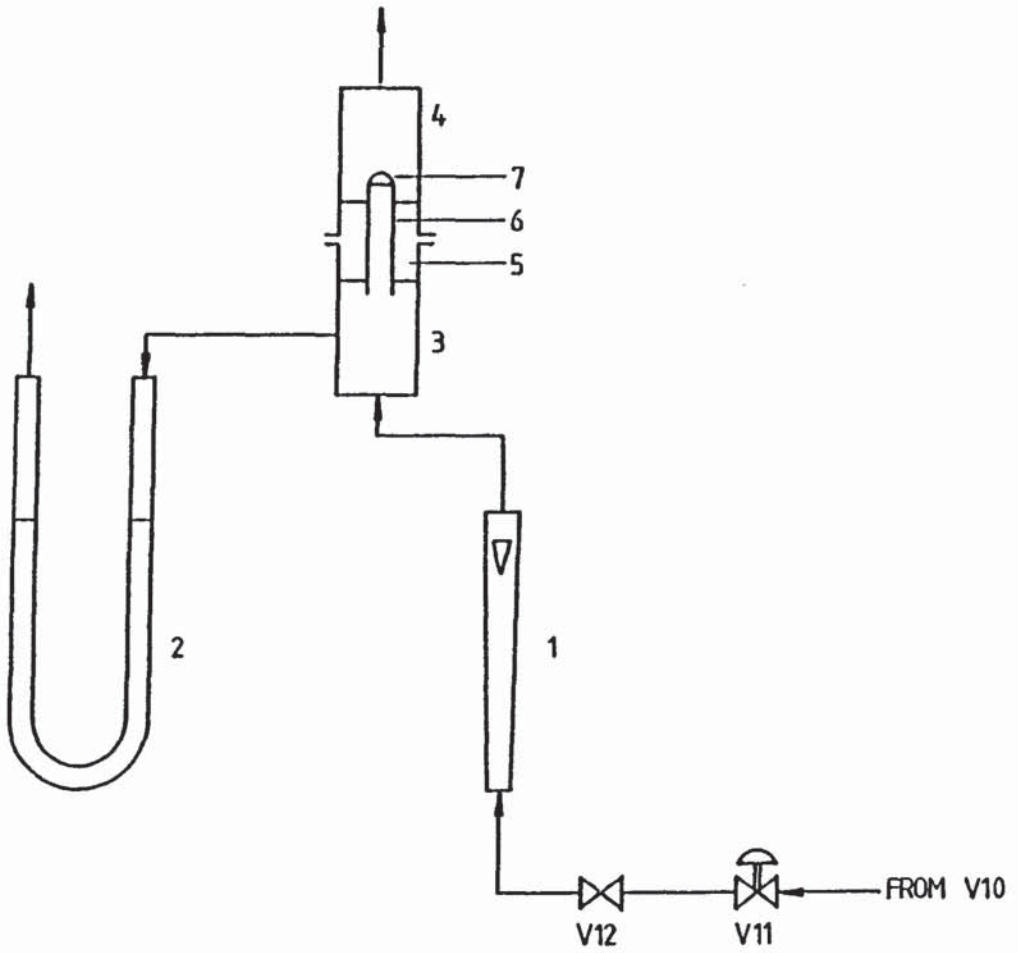

Figure 6.13 Schematic Diagram of Pressure-Drop Apparatus.

150 mm long respectively with side connections to the manometer. A crust support was mounted between them.

Dry air, from an air drier, passed through a Saunders diaphragm valve (V10), and was then reduced to atmospheric pressure by a 12.7 mm Spirax Sarco pressure reducing valve (V11) type BRV. The flowrate of inlet air was measured by a 7F metric rotameter and controlled with a 12.7 mm Saunders diaphragm valve (V12). The pressure drop across the crust was recorded by means of U-tube manometer.

CHAPTER SEVEN

EXPERIMENTAL PROCEDURES

7.1 Instrument Calibration For Rotating Drops

Air velocity, air temperature and air humidities were measured in each experiment. The calibration of the instruments used is discussed below.

7.1.1 Air Flowrate Measurement

The flowrate of air through the wind tunnel was measured by means of an 18F G.E.C. rotameter with a Duralumin float. The rotameter was calibrated against the flowrate of dry gas at ambient temperature measured with the aid of a Parkinson Gas meter placed in the outlet stream of the wind tunnel. Air velocity in the working section of the wind tunnel was then calculated for the different temperatures and corrected by using the appropriate air densities.

7.1.2 Hygrometry Measurements

Each sensor was supplied with its own calibration graph. Calibration was carried out over a dew-point temperature range -80/-20°C on the moisture meter. The calibration was checked by exposing the sensor to ambient conditions in the laboratory for five minutes; the value registered on the meter was noted and the relative humidity read from the supplied curve. This was compared to the relative humidity at the wet bulb and dry bulb temperatures. Good agreement was always obtained. A similar calibration check was made for the air flowing via the wind tunnel. Figure 7.1 shows a typical calibration curve for the Hygrometry Equipment.

7.2 Suspended Single Drop Experiments

The investigation was divided into two categories, the first a study of the rate of evaporation from water droplets at different temperatures and the second a major study of the drying of drops containing different dissolved, and suspended, solids under various conditions.

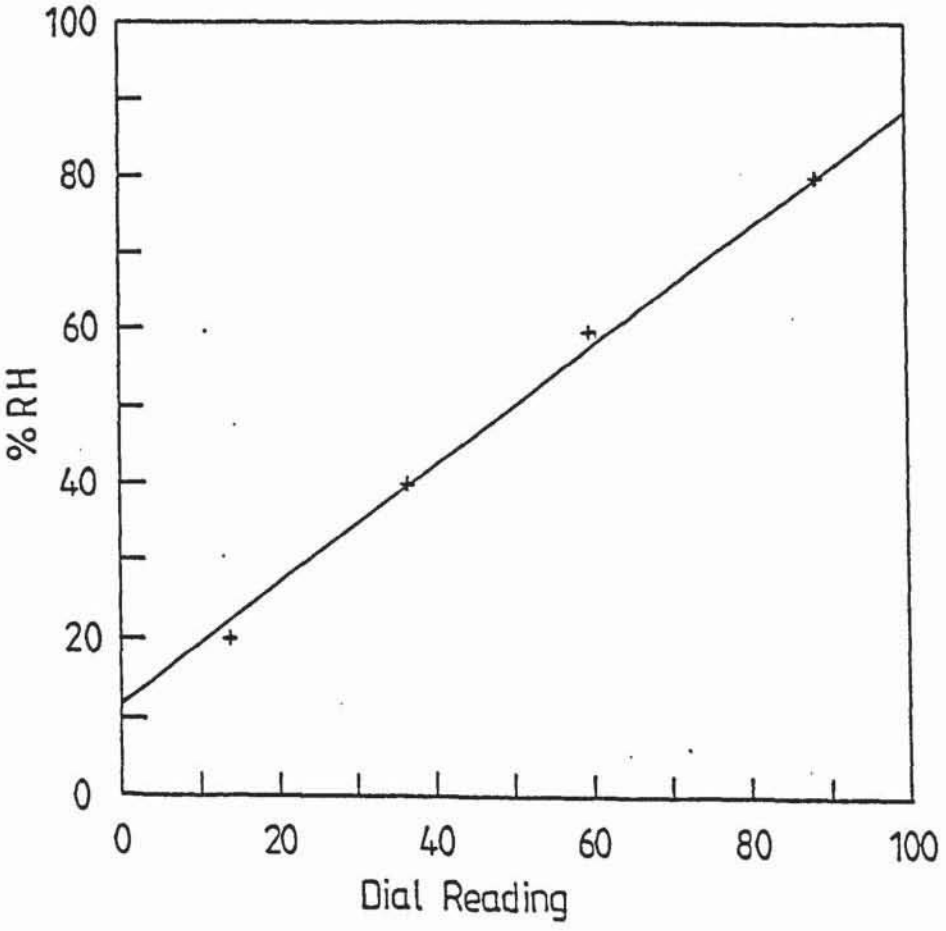

Figure 7·1 A typical Shaw Hygrometer calibration curve.

7.2.1 Water Drops

Dry air was passed through the wind tunnel and its velocity in the working-section controlled by adjusting the gate valve V6. The heater was switched on, and after steady state conditions had been obtained in the wind tunnel, the initial upstream and downstream humidities of the air were recorded on the Hygrometer. Air temperature in the working-section was recorded on the temperature recorder, and, when all readings had remained steady, a drop of distilled water was formed at the end of the drop suspension device. To ensure uniform evaporation from the drop, it was rotated by starting the motor driving the drop suspension device at a rate of 15 r.p.m. The drop size was measured with both a cathetometer, which also allowed visual observation of the drop, and from photographs taken with a 35 mm Chinon camera.

The air flowrate, temperature, and humidities upstream and downstream of the drop, and the drop diameter were recorded at incremental time intervals during each experiment, until the drop's hemispherical shape became distorted. This occurred when gravity could no longer sustain the drop's hemisphericity.

The wet bulb temperature was measured by means of a Ni-Cr/Ni-Al thermocouple with the thermojunction covered with a thin paper tissue saturated with distilled water.

7.2.2 Drops of Aqueous Sodium Sulphate Decahydrate

Solutions of sodium sulphate decahydrate were prepared by dissolving Analar quality sodium sulphate decahydrate (supplied by Fisons Scientific Apparatus Limited), in a fixed volume of distilled water. To measure evaporation rates, as in Section 7.2.1, a drop of solution of known solids content was suspended on the nozzle, placed in the working section, and rotated in the airflow at a steady 15 r.p.m. At fixed time intervals the upstream and downstream humidities were recorded together with the drop diameter measured wtih a cathetometer.

At the end of each run the crust formed by the drop was gently sliced off

onto a filter paper; this absorbed the excess solution in the hollow shell of the crust leaving a rigid hollow hemipsherical crust.

The crust to be photographed through S.E.M. was then glued onto an aluminium stud and kept inside a decanter to protect it from atmospheric humidity. On the following day the stud was placed in a vacuum chamber and a thin film of gold-palladium deposited onto it by a sputtering technique to maintain a constant electric potential over the crust. The coated specimen was then introduced into the specimen chamber of the Scanning Electron Microscope (S.E.M.) where it was scanned by a fine electron beam. A three-dimensional image of the specimen, up to a magnification of 5000, was displayed on the Visual Display Unit. Selected areas of the specimen could be photographed with a 35 mm camera attached to the S.E.M.

For experiments involving crust thickness measurements, or in order to study the internal and external crust structure, the above procedure was repeated after drying periods of 5, 10, 15, 20, 25 and 30 minutes. Each specimen was introduced into the chamber of the Stereoscan microscope for crust thickness observation and structural analysis. Microphotographs were obtained on 35 mm film for each specimen. A Zetron Optical Microscope with a 35 mm camera attached to it was mainly used for crust thickness measurements.

7.2.3. Drops of Aqueous Organic and Inorganic Chemicals

Two Organic Paste Formulations were used; A and B. Slurries of 12, 15 18% wt/wt solids contents for A and B were freshly prepared by admixture of water with the concentrated pastes.

Additive liquor was added to the feeds at the level of 13% for A and B, based on the actual weight of dry solids present in the paste. Runs were also performed in which the additive liquor was substituted with a similar percentage of saturated sodium chloride. Another two Organic Pigments A and B were also investigated using solutions of 22% wt/wt solids content.

Three solid Inorganic Powder Formulations C, D and E were also used. Aqueous solutions with solids content of 40, 50, 60 and 70% wt/wt were freshly-prepared by admixture of water with the solid.

Density was measured using a 50 ml specific gravity bottle. The viscosity of some samples was measured using a Ferranti Viscometer Model VL. Inlet air temperature was varied between 34°C and 300°C and air velocity between 0.7 - 2.1 ms^{-1}. As in Section 7.2.2 the evaporation rates were studied and Electron Microphotographs were taken of selected areas which highlighted the crust structure, fractures and holes.

7.2.4. Drop Temperature Profile Measurements

To study the temperature profile inside a drop, aqueous solutions of sodium sulphate decahydrate and inorganic solid C were prepared.

The apparatus was adjusted to give the required conditions of air temperatures and velocity. When steady state was achieved a drop of solution was suspended on the nozzle and placed in the working section and rotated. At fixed time increments the temperature inside the drop was recorded by projecting a Ni-Cr/Ni-Al thermocouple into the centre of the drop, The air temperature was varied between 20-100°C at a constant air velocity of approximately 1 ms^{-1}.

7.3 Free-Flight Drop Experiments

Free-flight drop experiments were divided into the following categories,

(1) Determination of the velocity profile of the gas stream in the working section.

(2) Study of the evaporation of water drops.

(3) Study of the drying of drops of aqueous sodium sulphate decahydrate and drops of aqueous organic and inorganic chemicals.

7.3.1 Measurement of Air Temperature Distribution and Velocity Profile in the Test Section.

The fan was switched on and the appropriate heaters, i.e. 1, 2 or 3, were turned on. (For practical purposes, with this apparatus, operation with no heating tended to give an air temperature 35°C, with one heater 68°C, two heaters 97°C, three heaters 125°C. Prolonged operation with four heaters was not practical e.g. trials to obtain an air temperature of 200°C caused electrical failure). Steady state was judged to have been reached when the temperature readings in the centre of the working section remained steady.

To measure air stream temperature distribution, a NI-Cr/Ni-Al thermocouple was inserted through side holes into the centre of the working section. Temperatures were recorded at different distances from the centre of the working section. The temperature field was found to be almost uniform within the test section. Figure 7.2b shows a typical air temperature distribution for different working temperatures at different heights above the screen.

The velocity of air in the working section was measured using a pitot tube and an inclined manometer. To conduct a velocity measurement the pitot tube was inserted into the working section, with the nose facing directly into the air stream. It was clamped so that the nose was at a fixed position within the test section. The differential pressure was read on the manometer. Various positions form the centre of the working section were selected for the pitot tube. Figure 7.3 shows the velocity distribution at various heights from the outlet of the screen mesh.

7.3.2 Evaporation of Water Drops

The fan was started and the required number of heaters, i.e. 1, 2 or 3 turned on for operation with any air temperature higher than ambient. The cooler around the collecting cup was only used for runs above 30°C.

The apparatus required about one and a half hours to reach a steady temperature. During this time the weighing bottles were carefully weighed, to two decimals (mg), using a Stanton analytical balance.

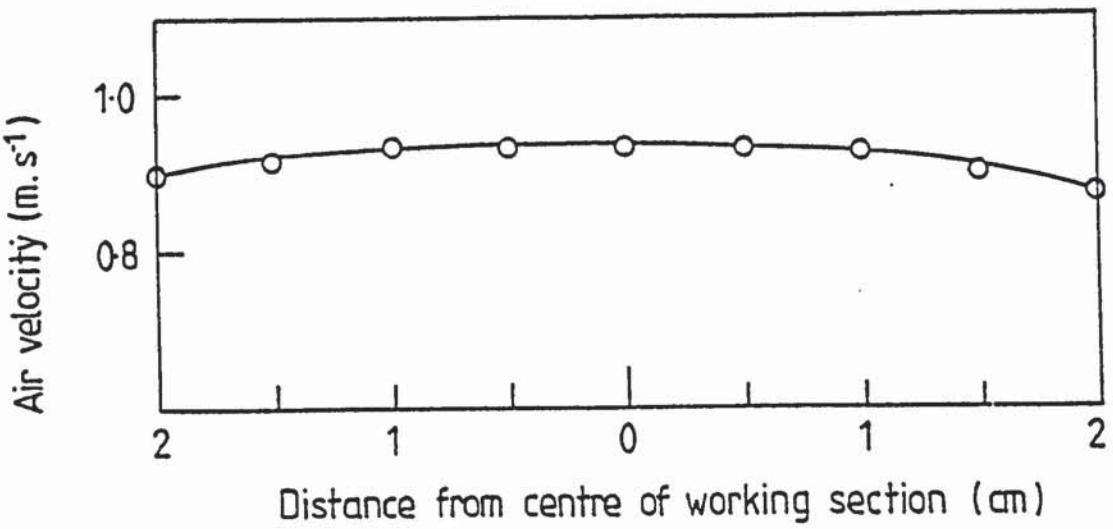

Figure 7·2a Velocity profile across the working section of horizontal wind tunnel.

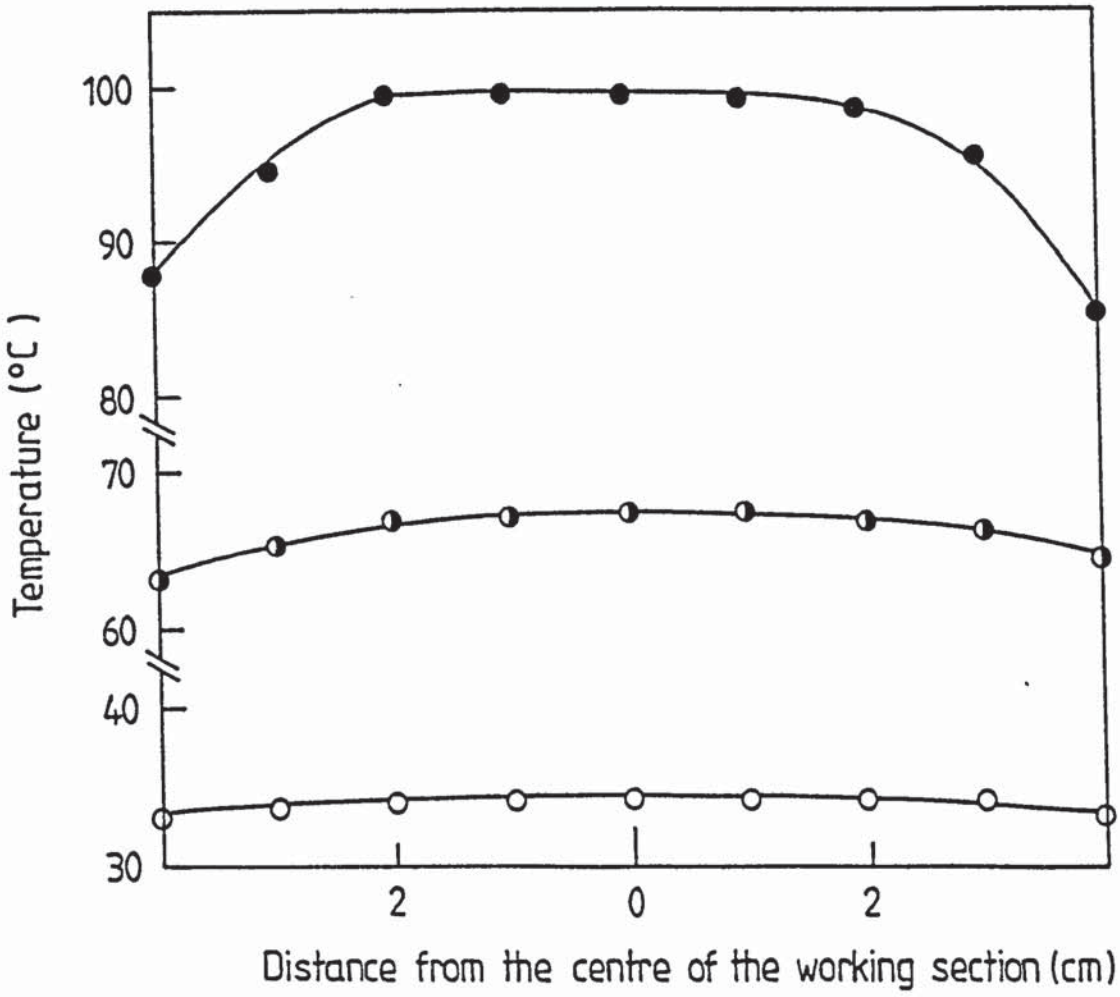

Figure 7·2b Temperature distribution of Air in the working section of the vertical wind tunnel at different working temperatures.

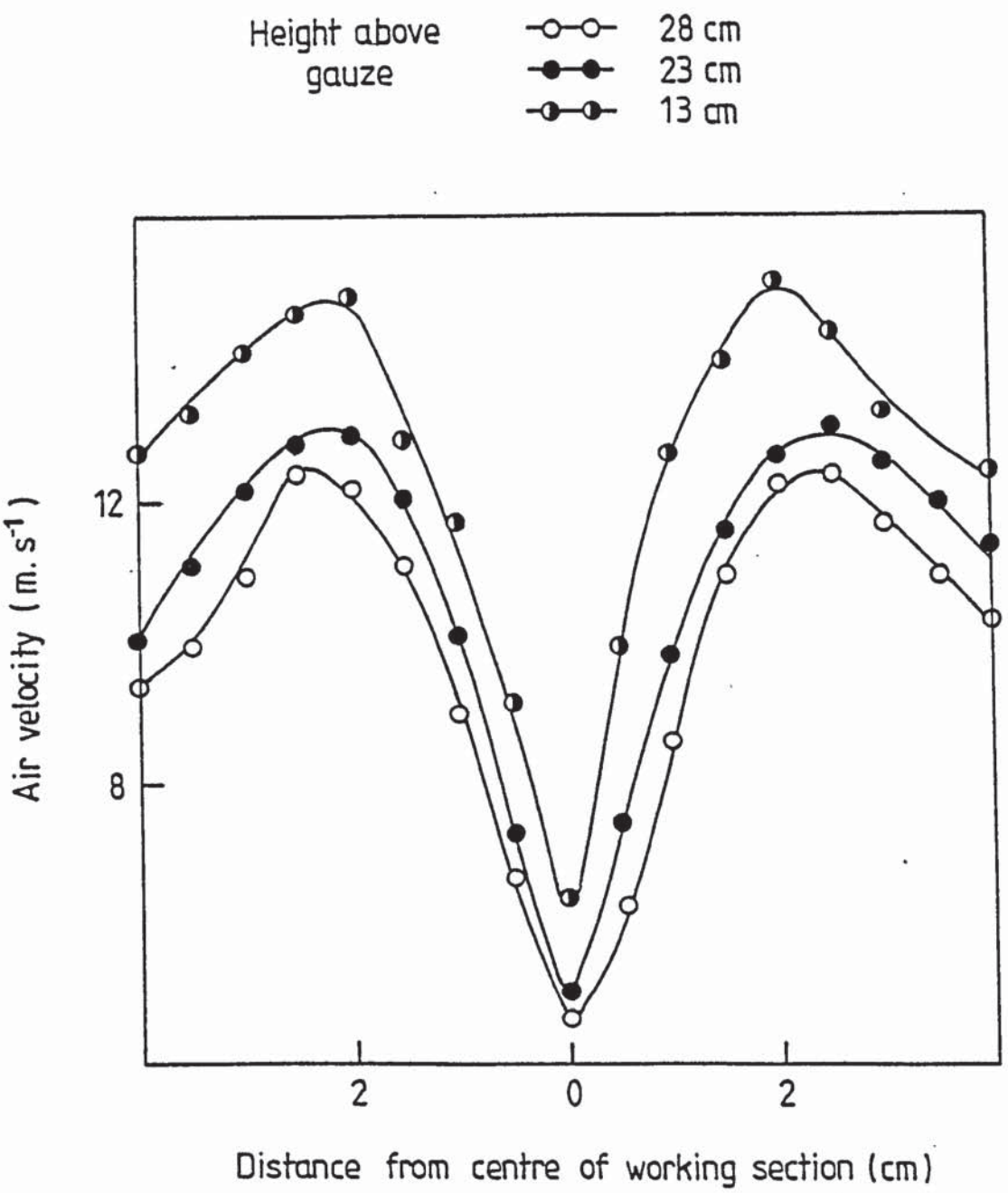

Figure 7·3 Velocity distribution and profile of Air in the working section of the vertical wind tunnel.

The rates of evaporation were determined by weighing successive equi-sized drops after varying intervals of time in the working section. When the apparatus was at a steady temperature a weighing bottle was placed in the collecting block and distilled water was transferred to the drop forming unit. A few drops were released from the nozzle to check that no air bubbles were included in the drops. The unit was then weighed, the hole (L, Figure 6.7) was uncovered, the nozzle was introduced into the working section and a single drop released. The nozzle was then withdrawn and the hole re-covered. The drop-forming unit was re-weighed, so that the drops initial weight could be determined by difference.

After a pre-determined period of time the drop was caught in the weighing bottle and the collection unit removed from the apparatus. The cover was placed on the weighing bottle, another bottle placed in the block and the collection unit again clamped into position. The period between pressing the trigger and placing the cover on the weighing bottle was in the region of six seconds. The bottle containing the collected drop was left in a desiccator before reweighing. The most stable position for drop collection was found to be 1 cm above the collection unit. If any drop hit the sides of the bottle instead of the bottom the results were rejected.

To measure drop diameter a drop was injected into the working section and its residence time measured with an accurate stop watch. A National Panasonic Video camera was used, with a Maxell, VHS 180 tape, to record the drop dimensions during drying.

Droplets were illuminated by a quartz iodine lamp, placed behind the glass window at the rear of the working section. Black stripes were sealed on the edges of the window to give a sharp definition of each droplet. In some cases some difficulty arose due to vertical movement of a drop in the test section, taking it out of the view of the video camera.

The video film was viewed on a TV screen. For each measurement the drop was stablised on the screen and the diameter measured by reference to a special transparent graticule shown in Figure 7.4. The droplets were not entirely spherical, but

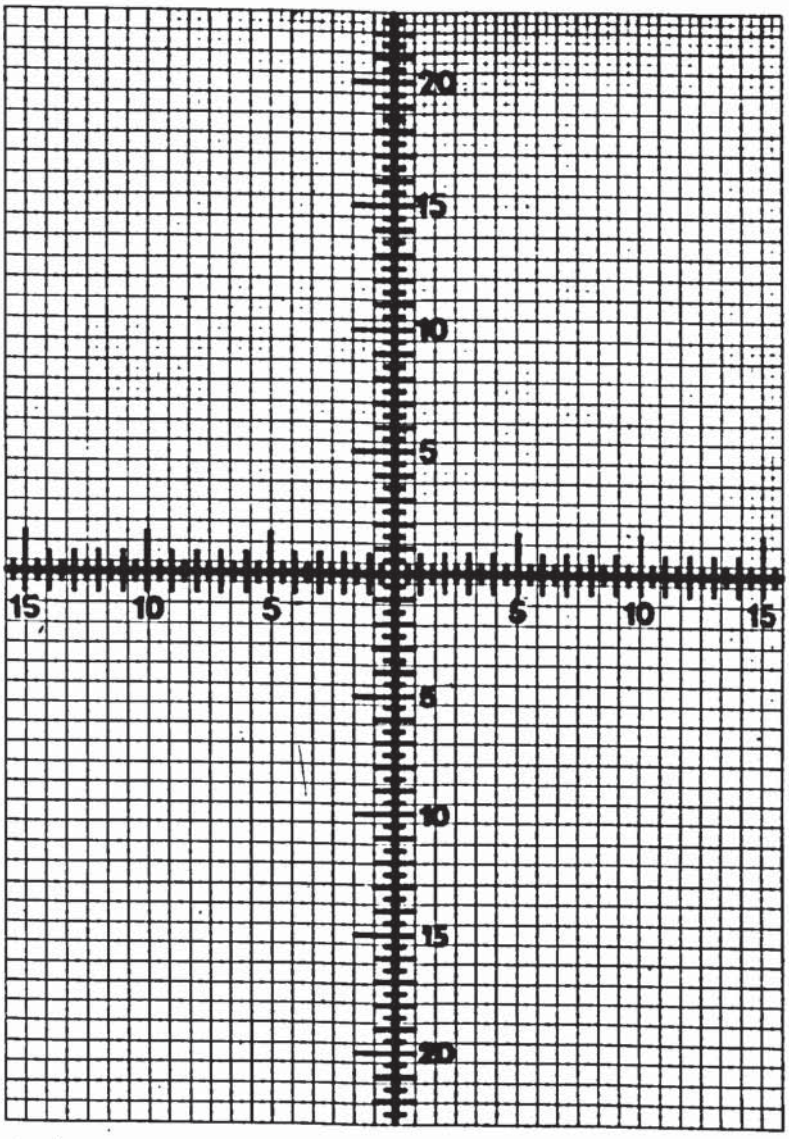

Figure 7·4 Transparent graticule for drop dimension measurements.

slightly flat-bottomed because of the upward motion of the air stream. Thus each droplet had major axes and minor axis and the mean was calculated by,

$$d_e = (2d_h + d_v)/3 \qquad (7.1)$$

Wet bulb temperature was measured by means of a Ni-Cr/Ni-Al thermocouple with the thermojunction covered with a thin paper tissue saturated with distilled water. The thermocouple was inserted into the air stream.

When a droplet was released from the nozzle into the tunnel its shape was not that of a sphere, but, by observation, spheroidal. In Figure 7.5 the spheroid ABCD has two sides; top side (ABC) and a lower one (CDA). The top half resembles a hemisphere whilst the underside is flattened due to the force of the air impinging on this face. As the residence time of the drop increases the lower part tends further towards sphericity. The spheroid has two identical diameters in the horizontal direction (x and z axes), and a third vertical diameter in y-direction comprising a major length OB and a minor length OD. As evaporation occurs from a drop OD icnreases due to the tendency of small drops to approach a spherical shape.

The transparent graticule shown in Figure 7.4 was placed on the TV-screen of the video to enable direct measurements to be taken for the drop diameters. From the geometry of the spheroid, Figure 7.5, for a stable non-distorted drop the horizontal axes (diameters, d_x and d_z) are equivalent while the vertical axis (dy) is always smaller due to the flattening as illustrated in Plate 9.14 and illustrated schematically in Figure 7.5. Thus to calculate the droplet area it was necessary to calculate the droplet equivalent diameter (d_e) and hence the equivalent mass transfer, or heat transfer, area (A_e). As mentioned in Chapter 3,

$$d_e = \frac{d_x + d_z + d_y}{3} = \frac{2d_x + d_y}{3} \qquad (7.2)$$

7.3.3 Drops of Aqueous Sodium Sulphate Decahydrate and Drops of Organic and Inorganic Chemicals

The required solutions of sodium sulphate decahydrate and organic and

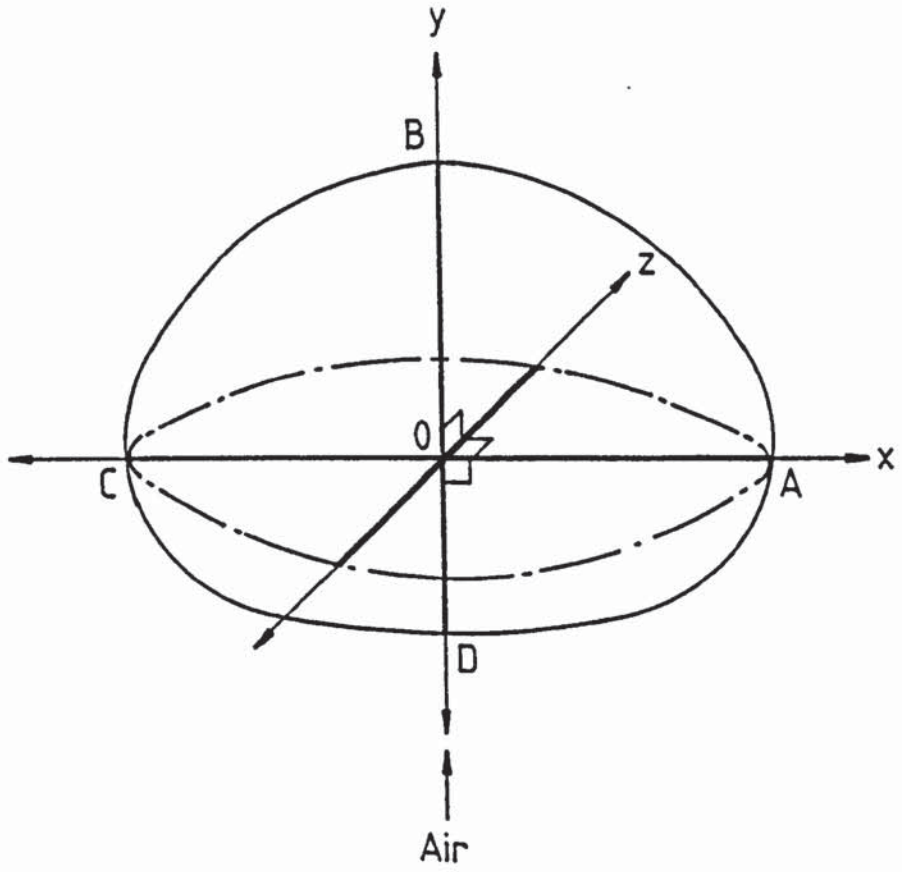

Figure 7·5 Schematic diagram of spheroid droplet geometry

AC = Drop diameter in horizontal direction (x and z axes)

DB = Drop diameter in the vertical direction (y axis)

inorganic chemicals were prepared. Drop evaporation rates were then studied at different air temperatures.

The procedure for evaporation rate and drop size measurements was similar to that for water drops as discussed in Section 7.3.2. However, once a crust had formed a drop started to bounce; this made drop collection difficult. It was also found that a dried drop could be broken when it hit the bottom of the weighing bottle; cotton wool was put into the weighing bottle to overcome this problem.

The procedure followed to study crust structure was as discussed earlier in Section 7.2.2.

7.4 Pressure Drop Test for Determining Porosity of Crust Experiments

Kozeny's (3, 126) technique, for correlating pressure drop and mean velocity for flow through a packed bed in terms of porosity and specific surface area of the bed, was adapted by Audu (103) to obtain an estimate of the crust porosity. Equation 5.28 shows the parameters which need to be known for porosity estimation.

The pressure drop test was performed in the apparatus described in Section 6.5.4. It involved passing dry air through valve V10; the pressure was reduced by pressure-reducing valve V12. Flowrate was controlled by valve V12 and measured by means of a 7F metric rotameter.

A crust from a solution of known solids content was formed in the horizontal wind tunnel after steady conditions of humidity driving-force had been achieved. The crust was mounted on a stainless steel tube and placed in the pressure drop apparatus. Dry air was passed through the crust and the pressure drop across it measured using the U-tube manometer.

A crust dried under identical conditions was glued onto an aluminium stud. In order to study crust structure, for the purpose of porosity determination, photomicrographs were then produced from the Scanning Electron Microscope using the procedure discussed in Section 7.2.2.

7.5 Thermal Conductivity Experiment

A supersaturated solution of sodium sulphate decahydrate was prepared. Additional sulphate was then added until a slurry was formed. This was then filtered and the filtrate washed with ethanol. The precipitate was placed in an oven at 65°C to dry slowly for two days. After complete dryness it was placed in the ring between discs 1 and 2. The whole assembly, shown in Figure 6.12, was adjusted and the vacuum pump switched on. The thermocouple wires were introduced into the holes in the discs. The Torovolt resistor was switched on and the current and voltage noted. Disc temperatures were recorded at various voltmeter and ammeter readings.

7.6 Spray Dryer Experiments

Drop Size Distribution

Solutions with the required solids contents were freshly-prepared by admixture of water with the solids. The viscosity of each sample was measured using a Ferranti Viscometer Model VL.,

To study the droplet size distribution the Laser emitter was switched on, the Laser beam focussed on the receiver, and the Malvern Particle Size Analyser switched on. The feed was then pumped to the nozzle using a 3-piston pump capable of delivering 1.73 m^3/h at a pressure of 50 bar. The volumetric throughput of the nozzle was determined by measuring the volume change in the cylindrical glass feed tank during the time of a run.

The cone angle of the spray was photographed with a Chinon 35 mm camera using front illumination from a Sunpack electronic flashgun.

Spray Drying

Spray drying tests were performed using the Niro Atomiser mobile spray drying, minor unit as shown in Plate 6.6. Feed solution was atomised by a pneumatically driven, vaned-wheel rotated at high speed. Hot air at a preset temperature entered the chamber around the atomised vaned wheel and flowed co-current with the spray. Dried product was subsequently separated from the exit air in a small cyclone.

Solutions of Inorganic Powder Formulation C with solids conent of 40%, 60% and70% wt/wt were used as feed and the inlet air temperature selected to give an outlet temperature between 110-130^{o}C. The heater controls on the drier were adjusted to the selected setting and 10 to 15 minutes were allowed for steady-state conditions to be reached. The air inlet and outlet temperatures were then recorded.

The atomiser was operated by opening the compressed air supply valve to give the requisite pressure, up to a maximum of 4.8 kg.cm^{-2}, as indicated on the gauge. Alternative air pressures of 4.4 kg.cm^{-2} and 2.2 kg.cm^{-2} (atomiser speed proportional to the air pressure) were also used.

CHAPTER EIGHT

PRESENTATION, AND DISCUSSION OF RESULTS-EVAPORATION OF PURE WATER DROPLETS

The experimental results for pure water drops are presented graphically and correlated according to whether the drop was suspended or in free-flight at ambient or at elevated air temperatures.

The mass transfer rates were calculated using equation 5.2 for suspended drops, and equation 5.4 for free-flight drops. Mass transfer coefficients were calculated from equations 5.11 and 5.12 for suspended and free-flight drops respectively.

The experimental Nusselt number was calculated for each incremental drop size during a run using equation 5.19. The instantaneous value of $d(d_p^2)/d\theta$ at each drop size was then obtained from a plot of d_p^2 against time, as shown in Figure 8.1.

Measurements were taken to one decimal place, resulting in a maximum experimental error of 5%.

8.1 Suspended Water Drops

The results confirmed that mass transfer rate, and hence the coefficient increases with rise in air temperature. The results are tabulated in Tables 8.1 - 8.4 and in Figures 8.2, 8.4, 8.6 and 8.8.

At ambient temperature the results were correlated according to the conventional equations, reviewed in Section 3.1.

$$Sh = 2 + \beta \ Re^{0.5} \ Sc^{0.33} \qquad (8.1)$$

$$Nu = 2 + \phi \ Re^{0.5} \ Pr^{0.33} \qquad (8.2)$$

A least squares technique described in Appendix A was used. The values of β and ϕ are shown in Tables 8.9 and 8.10 respectively.

The experimental modified Nusselt number was calculated using the new equation 5.19. The value of $d(d_p^2)/d\theta$ was obtained from the plot of d_p^2 against time. The results for the evaporation of suspended water drops within the temperature range 21°C - 120°C are summarised in Tables 8.5 - 8.8, and in Figures 8.3, 8.5, 8.7 and 8.9.

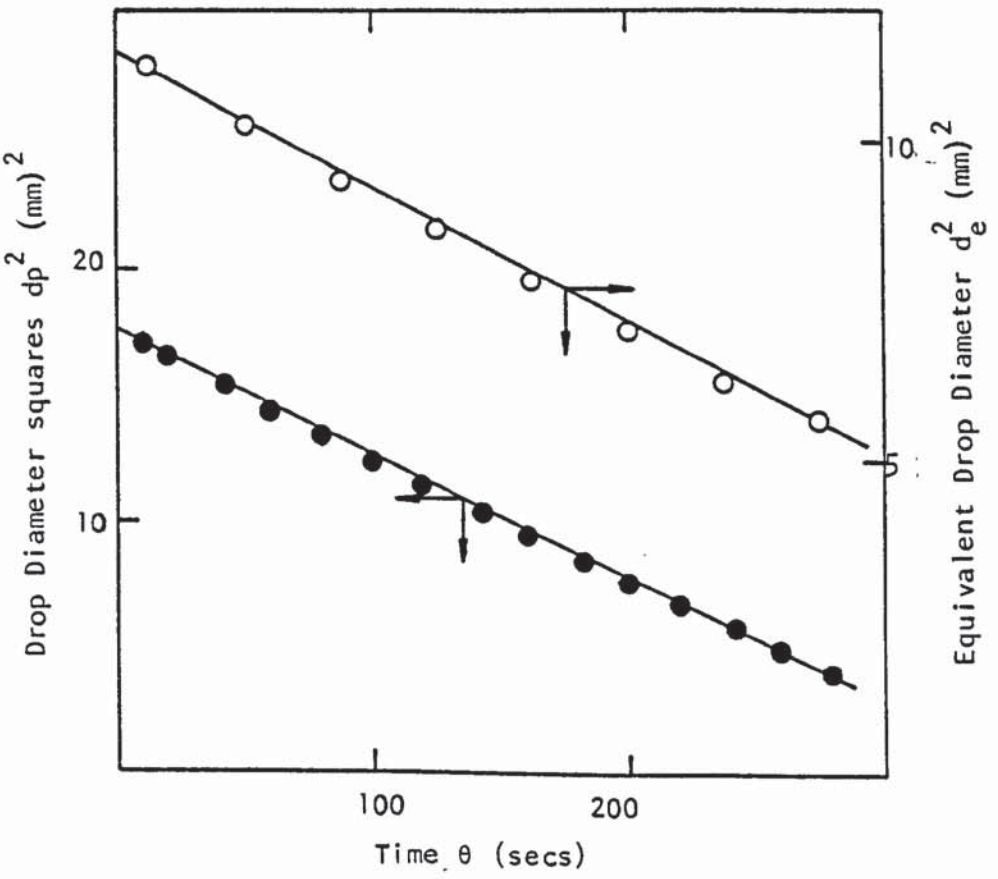

Figure 8.1 Evapoartion of Suspended and Free-Flight Drops of Water at Air Temperatures of 21°C and 35°C Respectively.

Suspended Drop

Free-Flight Drop

Table 8.1 Evaporation from Suspended Water Drops at 21°C

Drop Diameter $m \times 10^{-3}$	Mass Transfer Rate $kg.m^{-2}.s^{-1} \times 10^{-3}$	Mass Transfer Coefficient $m.s^{-1} \times 10^{-2}$	Sherwood Number Sh	Reynolds Number Re	$Re^{0.5}\ Sc^{0.33}$
2	2.5	6.2	5.0	36.6	5.1
	2.9	8.0	6.4	61.0	6.6
	3.2	8.3	6.7	99.1	8.4
	3.3	8.5	6.8	137.5	9.9
	3.5	9.3	7.4	180.1	11.4
	3.6	9.7	7.7	225.8	12.7
	4.1	10.0	8.0	274.6	14.1
5	0.9	2.9	5.8	54.9	6.3
	1.2	3.6	7.2	91.5	8.1
	1.4	4.1	8.3	148.7	10.3
	1.5	4.6	9.3	206.3	12.2
	1.6	4.8	9.7	270.2	13.9
	1.7	5.3	10.6	338.7	15.6
	1.9	5.6	11.2	411.9	17.2
8	0.6	2.0	6.5	73.3	7.2
	0.8	2.6	8.4	122.0	9.4
	1.0	3.0	9.7	198.3	11.9
	1.1	3.4	11.0	275.1	14.1
	1.3	3.6	11.5	360.3	16.1
	1.4	3.9	12.6	451.6	18.0
		4.2	13.5	549.2	19.9

Table 8.2 Evaporation From Suspended Water Drops at 50°C

Drop Diameter $m \times 10^{-3}$	Mass Transfer Rate $kg.m^{-2}.s^{-1} \times 10^{-3}$	Mass Transfer Coefficient $m.s^{-1} \times 10^{-2}$	Sherwood Number Sh	Reynolds Number Re	$Re^{0.5}\ Sc^{0.33}$
2	4.6	8.0	4.9	33.5	4.9
	5.5	8.2	5.0	55.9	6.4
	6.2	9.1	5.6	90.8	8.1
	6.5	9.6	5.9	125.7	9.6
	7.0	10.3	6.3	164.9	11.0
	7.3	10.8	6.6	206.8	12.3
	8.1	11.9	7.3	251.5	13.5
5	2.0	3.0	5.1	50.2	6.0
	2.5	3.7	6.4	83.9	7.8
	2.9	4.2	7.2	136.3	10.0
	3.2	4.7	8.0	188.6	11.7
	3.4	5.0	8.5	247.4	13.4
	3.7	5.5	9.3	310.2	15.1
	3.9	5.7	9.7	377.3	16.6
8	1.4	2.1	5.8	67.0	7.0
	1.8	2.7	7.3	111.9	9.0
	2.1	3.1	8.4	181.7	11.5
	2.3	3.4	9.4	251.5	13.6
	2.5	3.7	10.1	329.8	15.5
	2.7	4.0	10.8	413.6	17.4
	2.8	4.2	11.6	503.0	19.2

Table 8.3 Evaporation from Suspended Water Drops at 84°C

Drop Diameter $m \times 10^{-3}$	Mass Transfer Rate $kg.m^{-2}.s^{-1} \times 10^{-3}$	Mass Transfer Coefficient $m.s^{-1} \times 10^{-2}$	Sherwood Number Sh	Reynolds Number Re	$Re^{0.5} Sc^{0.33}$
2	4.6	8.3	4.7	30.0	4.7
	5.5	9.1	5.0	50.1	6.1
	6.0	9.9	5.4	81.5	7.8
	6.6	10.9	5.6	112.8	9.1
	6.8	11.3	6.2	148.0	10.5
	7.7	12.7	6.3	185.6	11.7
	8.1	13.4	7.0	225.7	12.9
5	2.0	3.4	4.8	45.1	5.8
	2.5	4.2	6.0	75.1	7.4
	2.9	4.9	6.9	122.1	9.5
	3.2	5.4	7.7	169.1	11.2
	3.4	5.6	7.9	221.8	12.8
	3.6	6.0	8.6	278.2	14.4
	3.8	6.4	9.0	338.3	15.8
8	1.4	2.4	5.4	60.1	6.7
	1.8	3.0	6.9	100.3	8.6
	2.1	3.5	7.9	163.0	11.0
	2.3	3.9	8.8	225.7	12.9
	2.5	4.1	9.4	296.0	14.8
	2.7	4.4	10.1	371.2	16.6
	2.8	4.7	10.8	451.5	18.3

Table 8.4 Evaporation From Suspended Water Drops at 120°C

Drop Diameter $m \times 10^{-3}$	Mass Transfer Rate $kg.m^{-2}.s^{-1} \times 10^{-3}$	Mass Transfer Coefficient $m.s^{-1} \times 10^{-2}$	Sherwood Number Sh	Reynolds Number Re	$Re^{0.5}\ Sc^{0.33}$
2	4.8	8.7	4.1	26.9	4.5
	5.7	10.3	4.9	44.9	5.8
	6.3	11.3	4.2	73.0	7.4
	6.9	12.4	5.2	101.1	8.7
	7.2	13.1	5.5	132.6	10.0
	7.7	13.9	5.8	166.3	11.2
	7.7	13.9	5.8	202.3	12.3
5	2.1	3.8	4.5	40.4	5.5
	2.6	4.7	5.7	67.4	7.1
	3.0	5.4	6.5	109.6	9.1
	3.3	6.0	7.2	151.7	10.7
	3.5	6.3	7.6	198.9	12.2
	3.9	7.0	8.4	249.5	13.7
	4.1	7.3	8.8	303.5	15.1
8	1.5	2.7	4.8	53.9	6.4
	1.9	3.4	6.0	89.9	8.2
	2.2	4.0	7.0	146.1	10.5
	2.5	4.4	7.8	202.3	12.4
	2.6	4.7	8.3	265.3	14.1
	2.9	5.1	8.9	332.7	15.8
	3.0	5.3	9.4	404.6	17.5

Table 8.5

Nusselt Number for Suspended Water Drops at 21°C

Time (Secs)	Nusselt Number Nu	Reynolds Number Re	$Re^{0.5}$ $Pr^{0.33}$
10	22.8	723.8	24.1
20	22.4	711.5	23.9
40	21.8	688.8	23.5
60	21.5	666.1	23.1
80	20.2	643.3	22.7
100	19.8	618.9	22.3
120	18.9	594.4	21.8
140	18.3	568.2	21.3
160	17.7	540.2	20.8
180	16.5	512.2	20.3
200	15.0	484.2	19.7
220	14.3	454.5	19.1
240	14.2	421.3	18.4
260	13.2	388.1	17.6
280	12.9	349.3	16.7

Table 8.6

Nusselt Number for Suspended Water Drops at 40°C

Time (Secs)	Nusselt Number Nu	Reynolds Number Re	$Re^{0.5}$ $Pr^{0.33}$
20	16.6	587.5	22.1
40	16.4	558.2	21.6
60	16.2	525.8	20.9
80	15.7	493.4	20.3
100	14.7	459.5	19.5
120	13.5	422.5	19.3
140	13.0	382.4	18.4
160	11.5	329.2	17.0
180	10.9	289.9	15.5

Table 8.7

Nusselt Number for Suspended Water Drops at 65°C

Time (Secs)	Nusselt Number Nu	Reynolds Number Re	$Re^{0.5}$ $Pr^{0.33}$
15	22.3	635.3	23.2
30	22.0	608.9	22.5
45	21.6	581.2	21.9
60	21.3	556.1	21.7
75	21.0	527.0	21.1
90	20.7	496.6	20.5
105	20.3	466.2	19.8
120	19.0	433.2	19.1
135	18.6	396.2	18.3
150	17.3	361.9	17.5
165	16.2	317.0	16.4
180	15.1	264.1	14.9

Table 8.8

Nusselt Number for Suspended Water Drops at 95°C

Time (Secs)	Nusselt Number Nu	Reynolds Number Re	$Re^{0.5}$ $Pr^{0.33}$
15	18.6	556.9	21.9
30	17.0	530.2	31.3
45	16.9	501.2	20.8
60	15.1	476.8	20.0
75	14.0	434.4	19.3
90	13.4	401.0	18.6
105	12.3	370.9	17.8
120	11.1	330.8	16.8
135	10.9	278.4	15.5
150	9.8	222.7	13.8

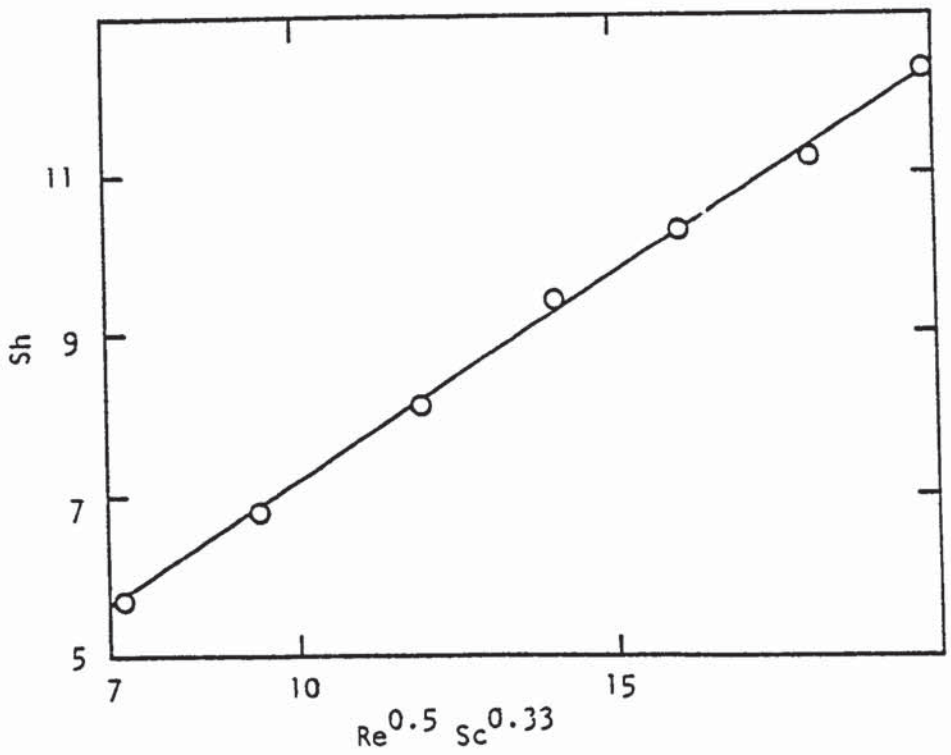

Figure 8.2 Plot of Sh Against $Re^{0.5}\ Sc^{0.33}$ for Suspended Water Drops at 21°C.

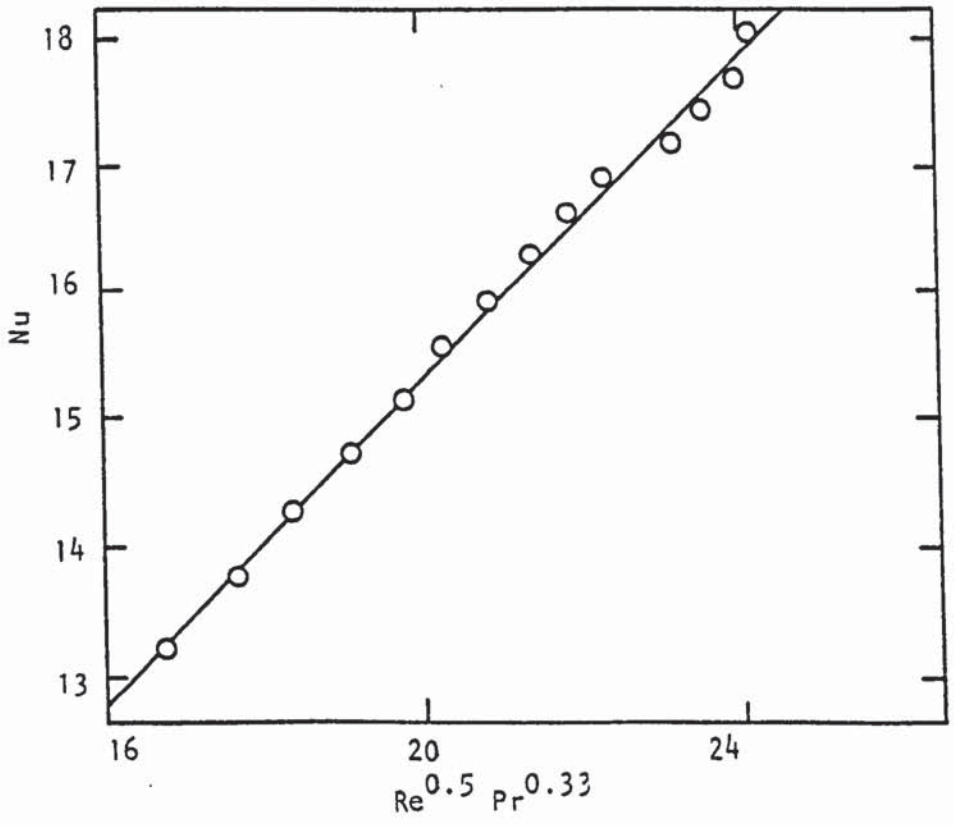

Figure 8.3 Plot of Nu Against $Re^{0.5}\ Pr^{0.33}$ for Suspended Water Drops at 21°C.

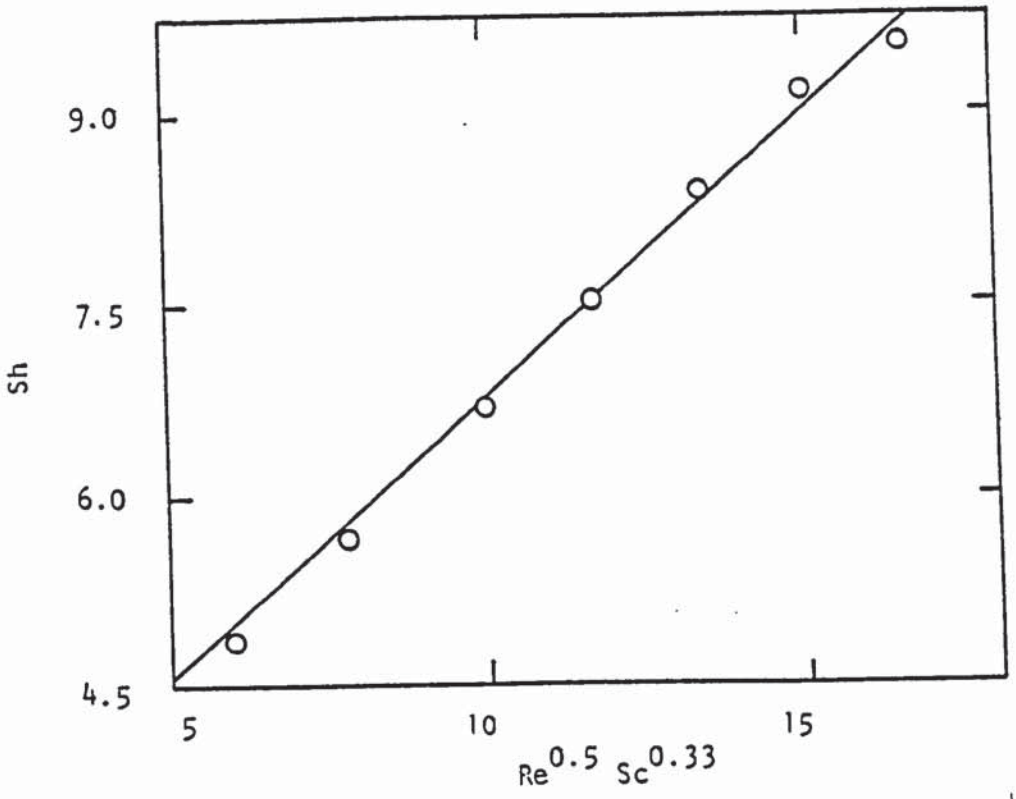

Figure 8.4 Plot of Sh Against $Re^{0.5}\ Sc^{0.33}$ for Suspended Water Drops at 50°C.

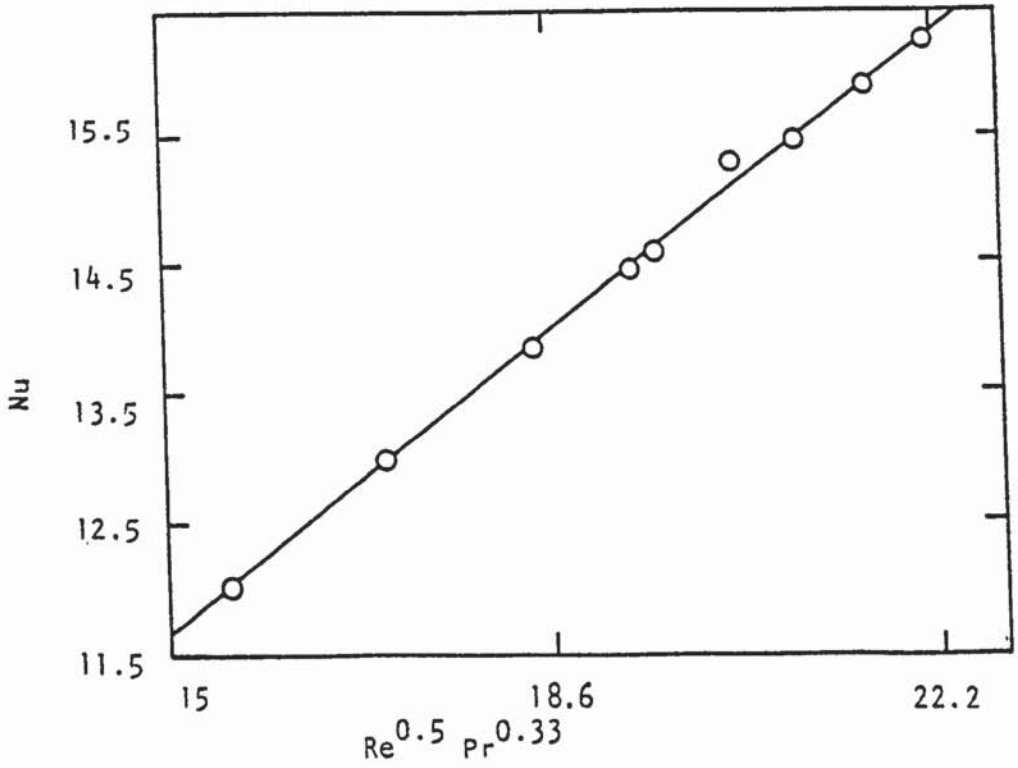

Figure 8.5 Plot of Nu Against $Re^{0.5}\ Pr^{0.33}$ for Suspended Water Drops at 40°C.

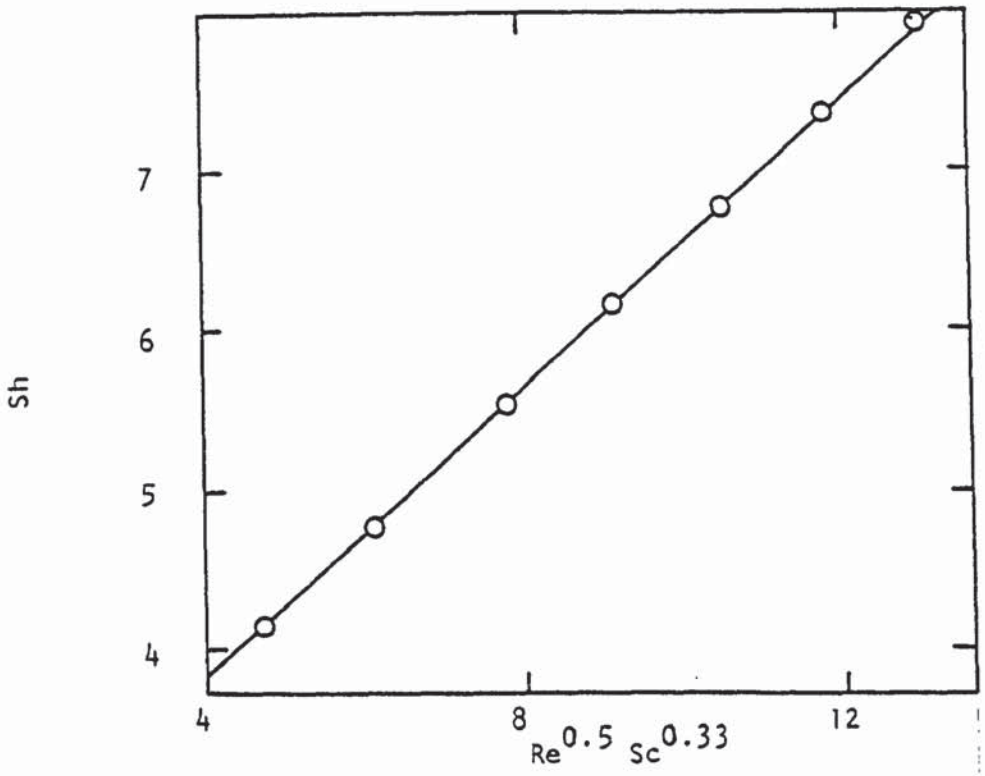

Figure 8.6 Plot of Sh Against $Re^{0.5}\ Sc^{0.33}$ for Suspended Water Drops at 84°C.

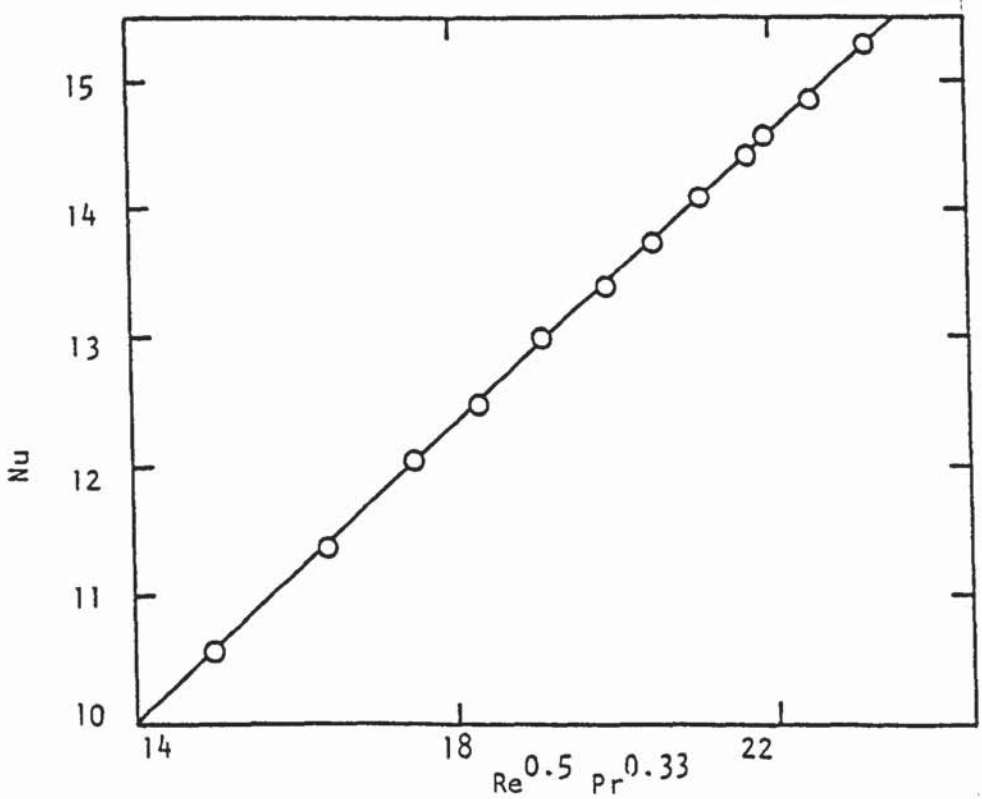

Figure 8.7 Plot of Nu Against $Re^{0.5}\ Pr^{0.33}$ for Suspended Water Drops at 65°C.

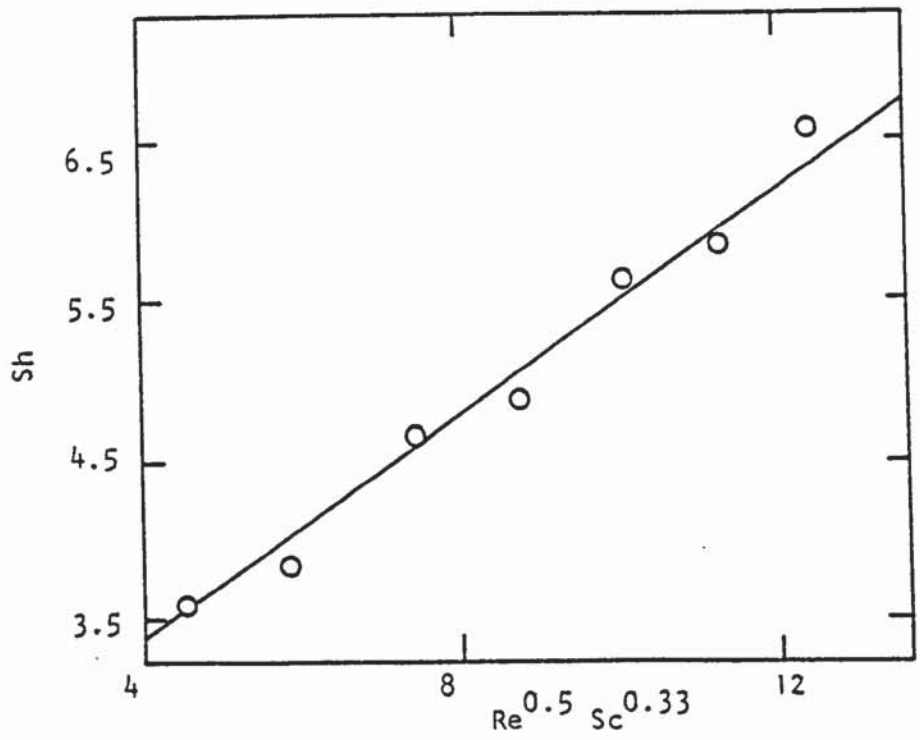

Figure 8.8 Plot of Sh Against $Re^{0.5}\ Sc^{0.33}$ for Suspended Water Drops at 120°C.

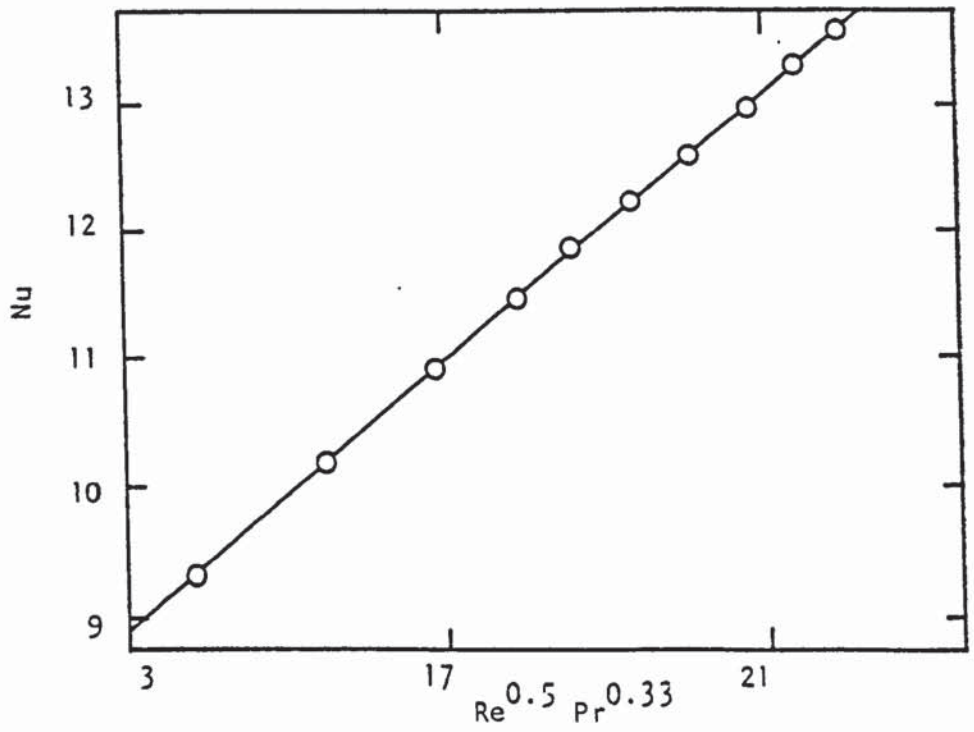

Figure 8.9 Plot of Nu Against $Re^{0.5}\ Pr^{0.33}$ for Suspended Water Drops at 95°C.

The values of β and ϕ appear to vary with air temperature within a range $0.374 \leq \beta \leq 0.516$ and $0.529 \leq \phi \leq 0.668$. The data can be correlated using the equation for Sherwood number proposed by Audu (103) and that proposed by Cheong (115) for Nusselt number.

$$Sh = 2.0 + \beta\left(\frac{T_a - T_s}{T_{amb}}\right)^n Re^{0.5} Sc^{0.33} \qquad (8.3)$$

$$Nu = 2.0 + \phi\,(1/B)^m\, Re^{0.5} Pr^{0.33} \qquad (8.4)$$

where $B = C_p \Delta T/\lambda$

A least squares technique, described in Appendix A was used to correlate the data according to the above equations. The resulting correlations were,

$$Sh = 2.0 + 0.501\left(\frac{T_a - T_s}{T_{amb}}\right)^{-0.03} Re^{0.5}\, Sc^{0.33} \qquad (8.5)$$

and

$$Nu = 2.0 + 0.228\left(\frac{1}{B}\right)^{0.2} Re^{0.5}\, Pr^{0.33} \qquad (8.6)$$

or for practical purposes,

$$Sh = 2.0 + 0.5\left(\frac{T_a - T_s}{T_{amb}}\right)^{-0.03} Re^{0.5}\, Sc^{0.33}$$

and

$$Nu = 2.0 + 0.23\left(\frac{1}{B}\right)^{0.2} Re^{0.5}\, Pr^{0.33}$$

Figures 8.22 and 8.23 are plots of Sh against $\left(\frac{T_a - T_s}{T_{amb}}\right)^{-0.03} Re^{0.5} Sc^{0.33}$ and

Nu against $\left(\frac{1}{B}\right)^{0.2}$ $Re^{0.5}$ $Pr^{0.33}$. The correlation coefficient for equation 8.5 was 0.97 and for equation 8.6, 0.98, indicating a very good fit.

8.2 Free-Flight Water Drops

Drops of pure liquid, water, were retained freely - suspended in the working - section by adjusting the upward flow of air. As described in Chapter 7, drop dimensions and residence time were followed by either photographic techniques or using a video camera. For photography, either still photographs were taken at different time intervals e.g. 30 s or high speed cine photography was used at 10,000 frame/sec. Video recording was the more convenient way to follow drop behaviour in the working section. The video tape was played back on a TV screen for drop dimension measurements.

The stability of the drop in the working section above the modified screen mesh increased for smaller initial drop sizes (< 2mm) i.e. larger drops tended to oscillate, accompanied by deformation outside the prolate/oblate profile. This behaviour died-out as the drop residence time increased i.e. with decrease in drop size. However pure liquid drops were more stable than drops containing solids; this difference is discussed in Chapter 9.

Results are listed in Tables 8.11 - 8.15 and in Figures 8.10 - 8.21. Mass transfer rates were calculated from equation 5.4, and mass transfer coefficients from equation 5.12. The value of $dm/d\theta$ was obtained from the plot of drop mass against time. As expected, mass transfer rates and coefficients increased with rise in air temperature. For example a six-fold increase in air temperature doubled the rate of mass transfer and increased the mass transfer coefficient by a factor of almost 1.5. A modified Nusselt number was calculated by using new equation 5.19. A least-square fitting technique, described in Appendix A, was used to determine the values of β and ϕ in equations 8.1 and 8.2 for different temperatures. The values of β and ϕ are presented in

Table 8.9 Values of β for Suspended Water Drops

Air Temperature °C	β
21	0.516
50	0.471
84	0.456
120	0.374

Table 8.10 Values of ϕ for Suspended Water Drops

Air Temperature °C	ϕ
21	0.668
30	0.650
40	0.644
50	0.600
65	0.572
80	0.553
95	0.529

Table 8.11 Values of β and ϕ for Free-Flight Water Drops

Air Temperature °C	β	ϕ
35	0.700	0.736
68	0.651	0.687
97	0.629	0.655
125	0.575	0.583

Table 8.12 Evaporation From Free-Flight Water Drops at 35°C

Mass Transfer Rate $kg.m^{-2}.s^{-1}x10^{-3}$	Mass Transfer Coefficient $m.s^{-1}$	Sherwood Number Sh	Nusselt Number Nu	Reynolds Number Re	$Re^{0.5}\ Sc^{0.33}$	$Re^{0.5}\ Pr^{0.33}$
1.2	0.1	25.7	26.7	1044.3	27.6	29.4
1.3	0.1	25.0	25.9	1018.7	27.3	29.1
1.4	0.2	17.7	22.8	981.9	26.8	28.5
1.5	0.2	17.3	20.4	936.6	26.1	27.9
2.3	0.3	17.4	19.6	874.4	25.2	26.9
2.5	0.3	16.7	18.6	807.5	24.3	25.9
2.6	0.3	16.5	16.4	535.3	19.7	21.1
2.7	0.3	16.3	15.6	504.7	19.2	20.5
2.7	0.4	16.0	13.7	457.0	18.2	19.5
2.8	0.4	14.8	10.6	425.3	17.6	18.8

Table 8.13 Evaporation From Free-Flight Water Drops at 68°C

Mass Transfer Rate $kg.m^{-2}.s^{-1}x10^{-3}$	Mass Transfer Coefficient $m.s^{-1}$	Sherwood Number Sh	Nusselt Number Nu	Reynolds Number Re	$Re^{0.5}\ Sc^{0.33}$	$Re^{0.5}\ Pr^{0.33}$
2.0	0.1	19.9	23.5	900.5	25.9	27.6
2.2	0.1	16.1	21.7	750.6	23.6	25.2
3.1	0.2	15.2	20.8	728.0	23.2	24.8
3.3	0.2	14.5	17.9	517.1	19.6	20.9
3.3	0.2	14.4	16.0	484.5	18.9	20.2
3.5	0.2	13.8	15.4	440.0	18.1	19.3
3.7	0.2	13.2	14.0	375.3	16.7	17.8
3.9	0.2	12.8	13.7	355.7	16.2	17.3
4.2	0.3	12.7	12.1	328.2	15.6	16.6
4.2	0.3	12.2	10.0	305.0	15.0	16.0

Table 8.14 Evaporation From Free-Flight Water Drops at 97°C

Mass Transfer Rate $kg.m^{-2}.s^{-1}x10^{-3}$	Mass Transfer Coefficient $m.s^{-1}$	Sherwood Number Sh	Nusselt Number Nu	Reynolds Number Re	$Re^{0.5}\ Sc^{0.33}$	$Re^{0.5}\ Pr^{0.33}$
2.1	0.1	18.8	21.3	750.0	23.7	25.4
2.4	0.1	17.7	19.6	647.5	22.0	23.6
4.0	0.2	17.0	18.7	600.5	21.2	22.7
5.1	0.2	16.5	16.9	534.1	20.0	21.4
5.3	0.3	15.6	14.5	458.7	18.6	19.8
6.0	0.3	14.7	14.0	421.2	17.8	19.0
6.0	0.3	13.8	13.8	387.4	17.0	18.2
6.7	0.3	12.2	12.2	333.1	15.8	16.9
7.4	0.4	11.2	11.5	296.1	14.9	15.9
8.0	0.4	10.9	9.8	243.6	13.5	14.5

Table 8.15 Evaporation From Free Flight Water Drops at 125°C

Mass Transfer Rate $kg.m^{-2}.s^{-1} \times 10^{-3}$	Mass Transfer Coefficient $m.s^{-1}$	Sherwood Number Sh	Nusselt Number Nu	Reynolds Number Re	$Re^{0.5}\ Sc^{0.33}$	$Re^{0.5}\ Pr$
2.5	0.1	17.5	19.0	662.6	22.4	24.1
2.9	0.1	16.1	17.6	614.1	21.6	23.2
3.5	0.2	15.1	16.8	557.3	20.6	22.1
4.7	0.2	13.8	14.9	485.6	19.2	20.6
5.5	0.3	12.5	13.1	450.6	18.5	19.8
6.2	0.3	11.7	12.7	406.4	17.6	18.8
7.9	0.4	11.3	11.3	275.6	16.9	18.1
9.2	0.5	10.2	10.6	347.9	16.3	17.4
10.2	0.5	9.2	9.0	258.7	14.0	15.0
11.8	0.6	8.3	8.9	210.2	12.6	13.5

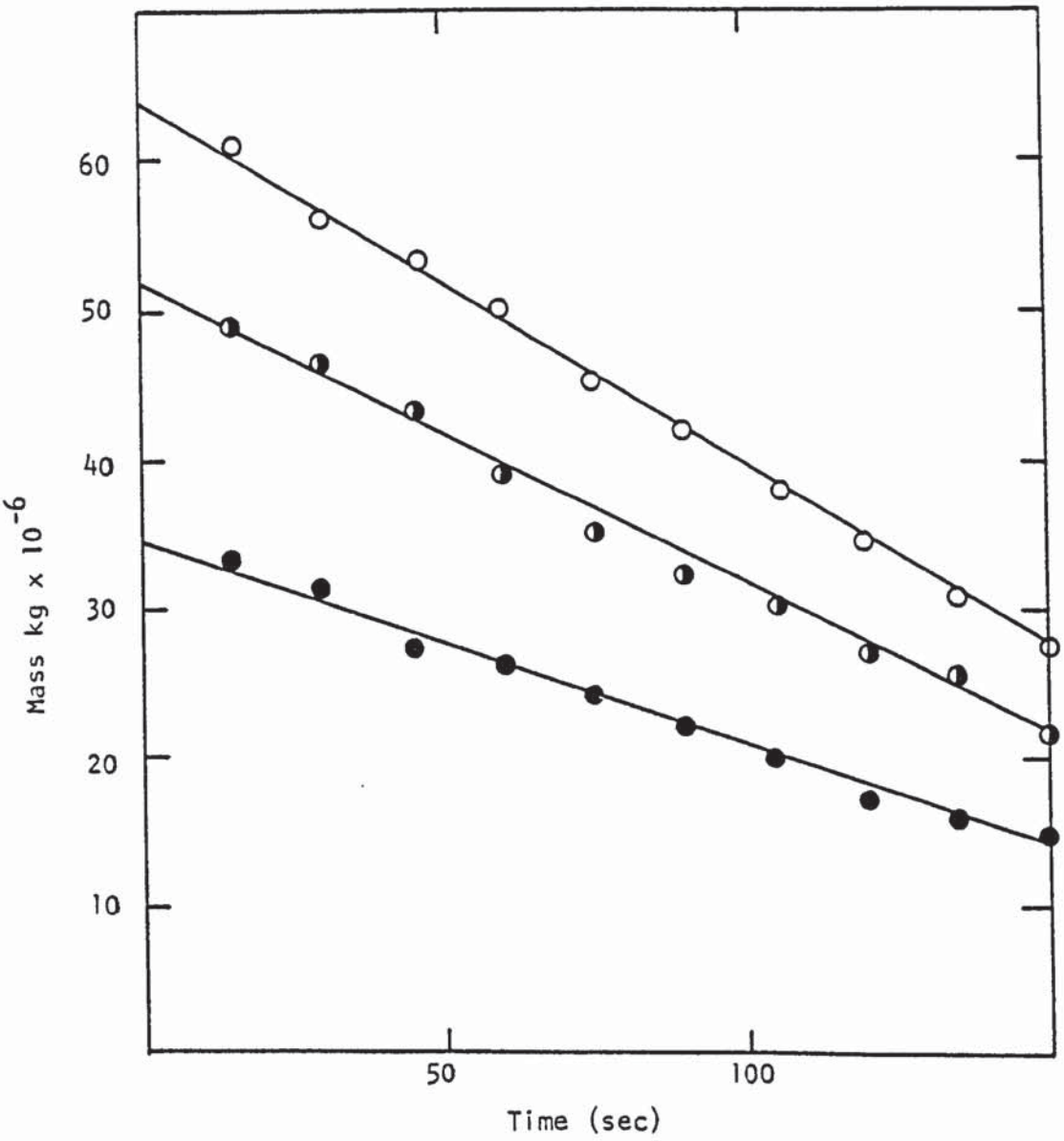

Figure 8.10 Drop Mass -v- Time for Free-Flight, Pure Water Drop at 125°C.

Nozzle Size
2.00 mm
3.00 mm
4.00 mm

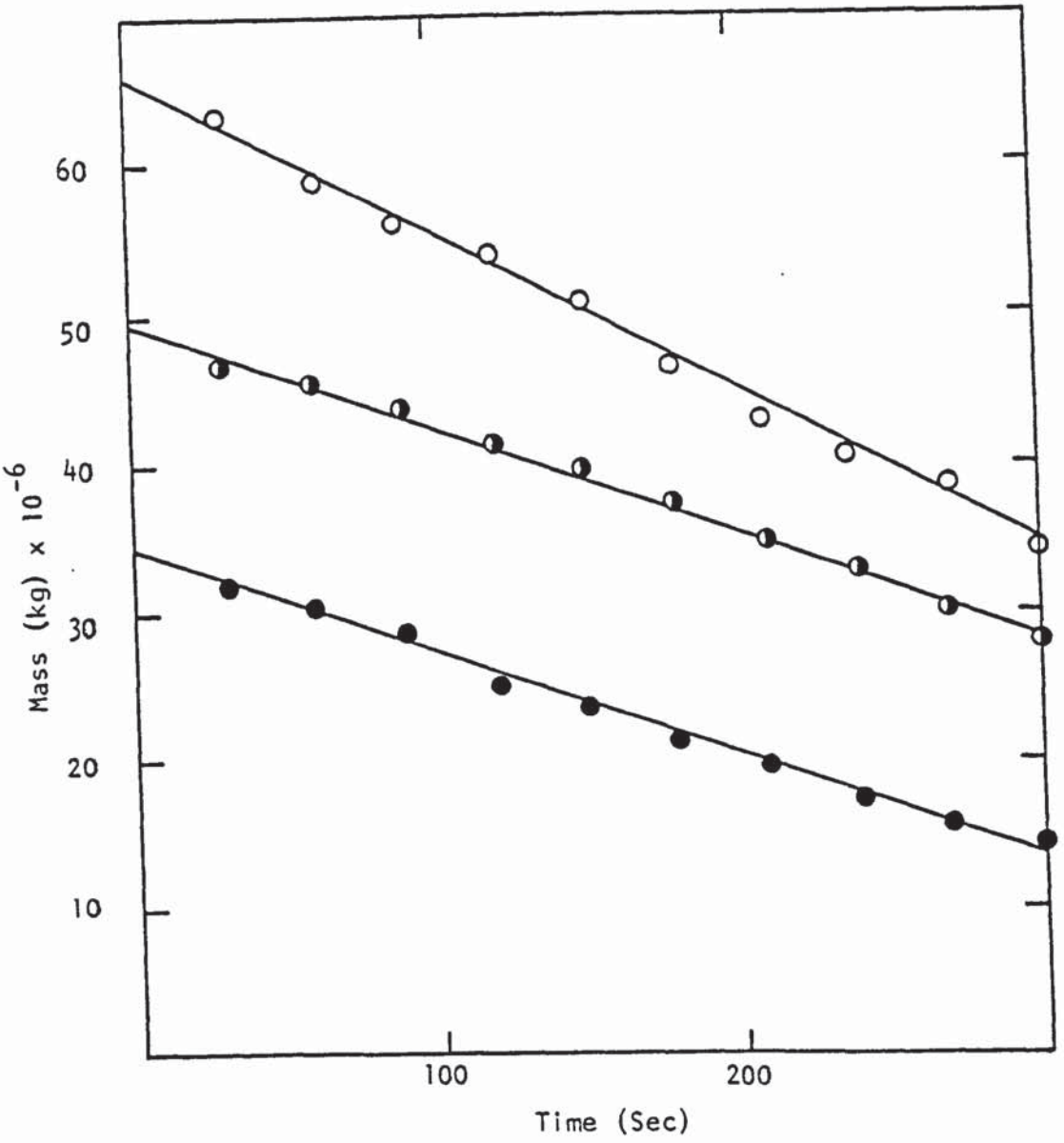

Figure 8.11 Drop Mass -v- Time for Free-Flight, Pure Water Drops at 97°C.

	Nozzle Size(mm)
●—●	2.00
◑—◑	3.00
○—○	4.00

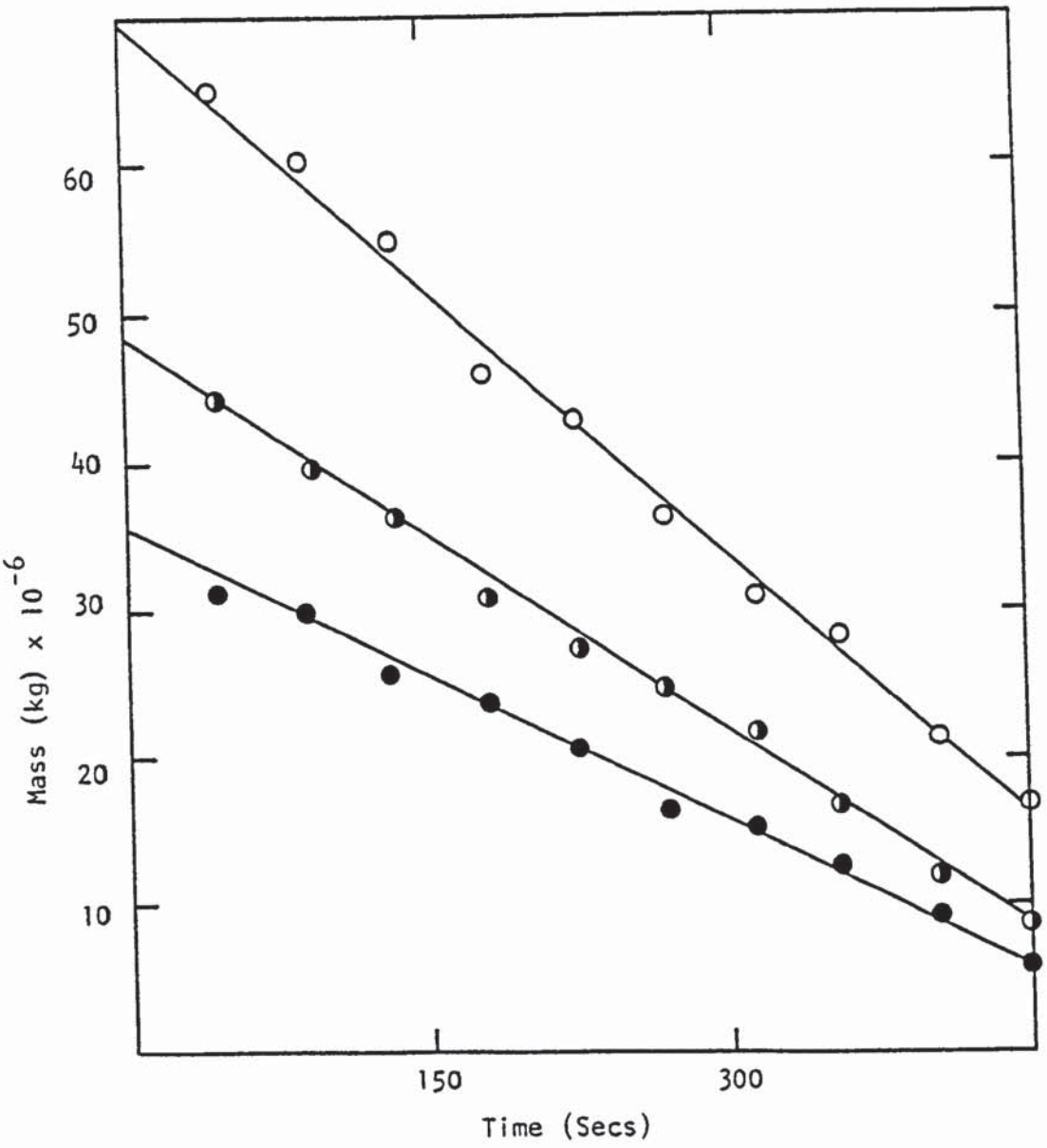

Figure 8.12 Drop Mass -v- Time for Free-Flight, Pure Water Drops at 68°C.

Nozzle Size (mm)
2.00
3.00
4.00

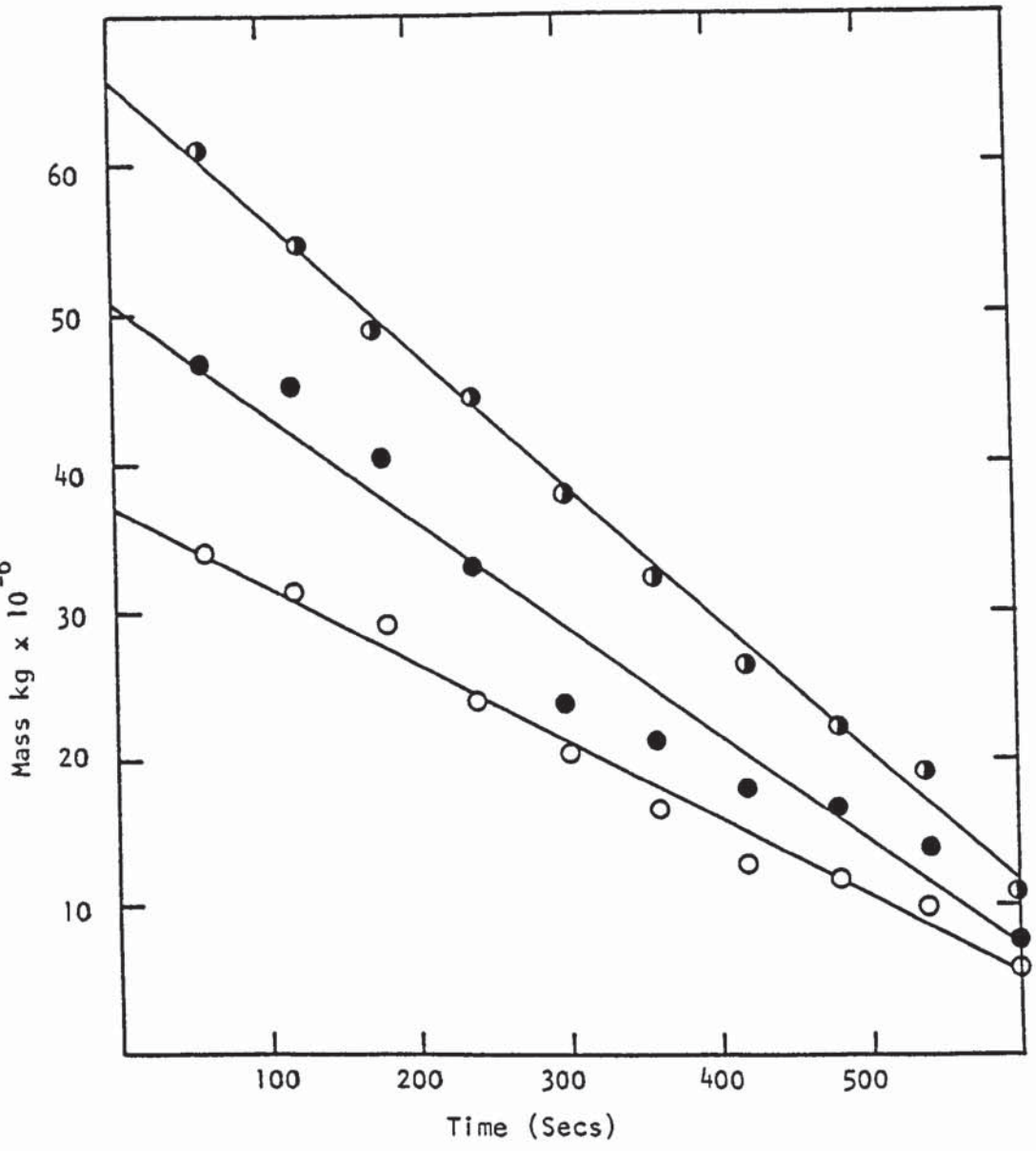

Figure 8.13 Drop Mass -v- Time for Free-Flight, Pure Water Drops at 35°C.

Nozzle Size (mm)
2.00
3.00
4.00

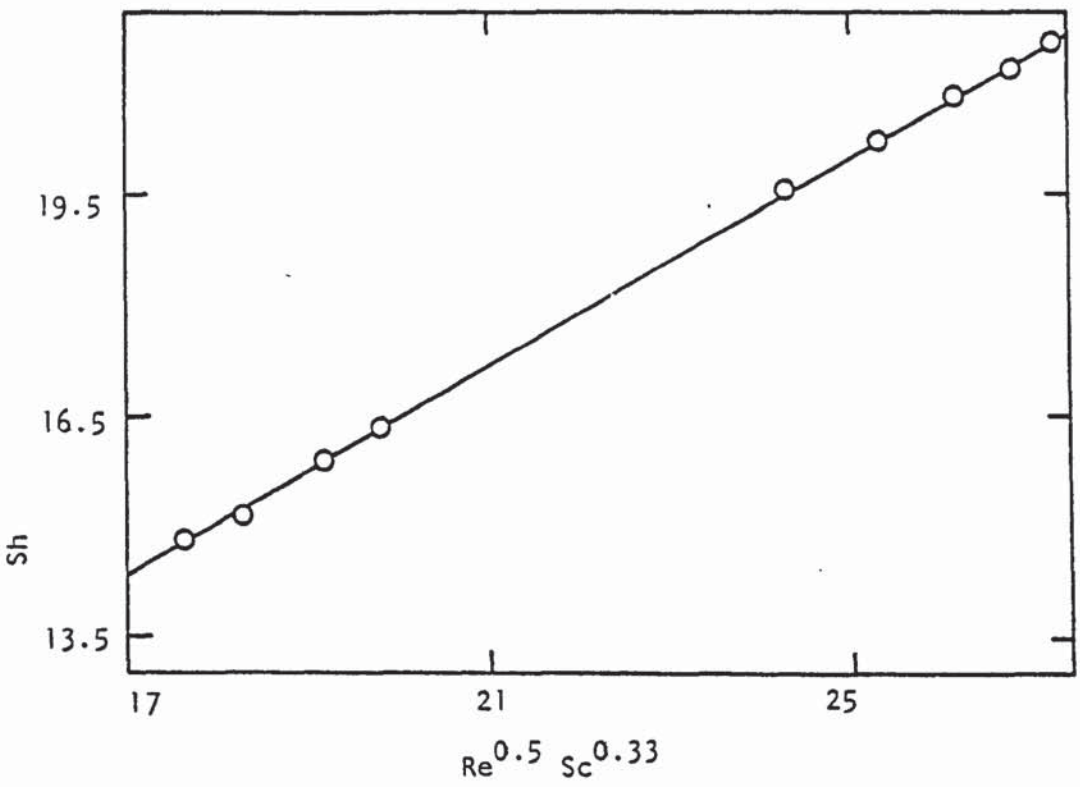

Figure 8.14 Plot of Sh Against $Re^{0.5}\ Sc^{0.33}$ for Free-Flight Pure Water Drops at 35°C.

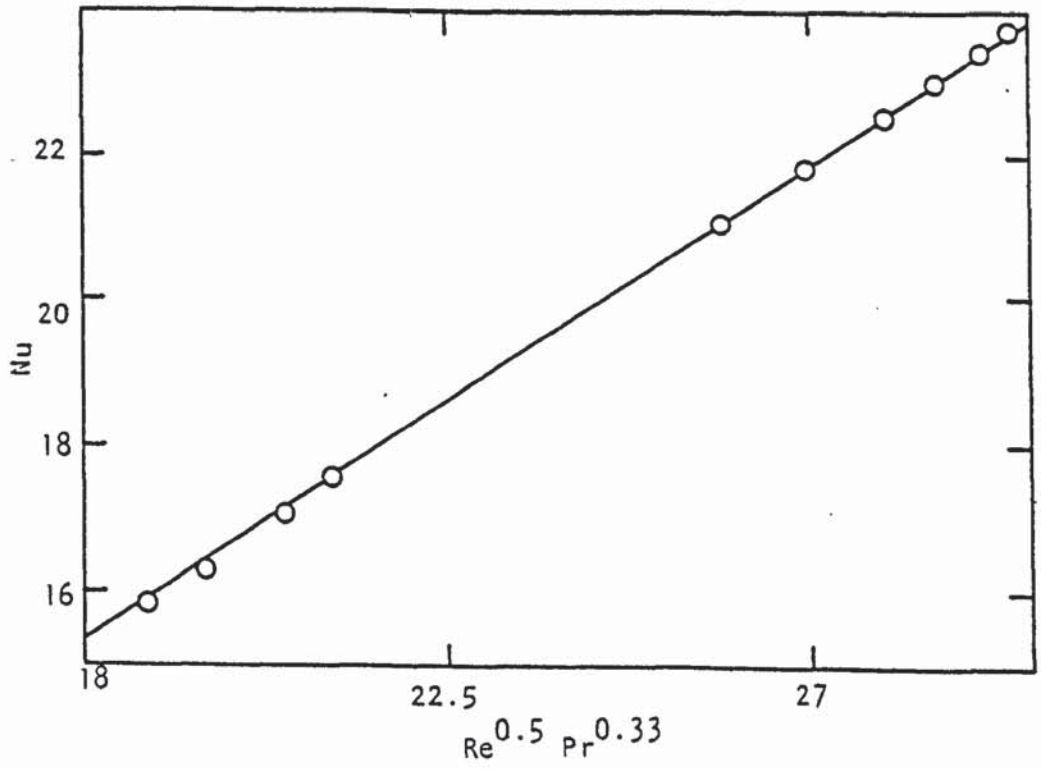

Figure 8.15 Plot of Nu Against $Re^{0.5}\ Pr^{0.33}$ for Free-Flight Pure Water Drops at 35°C.

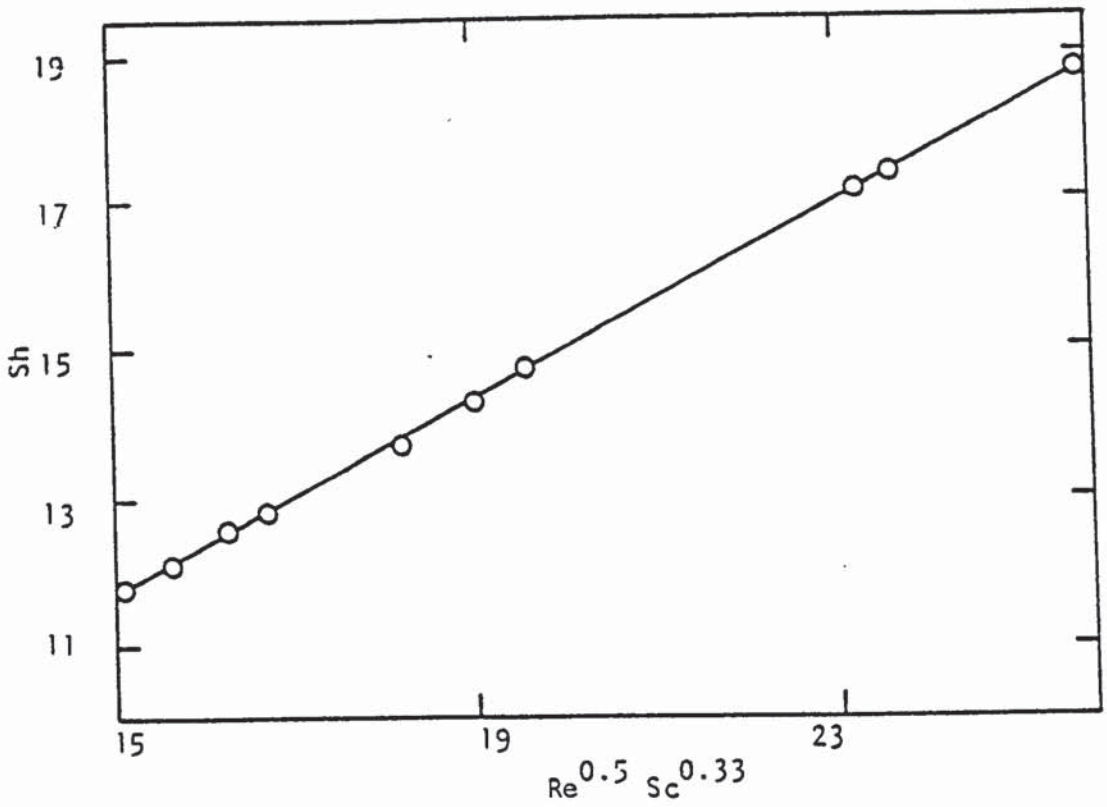

Figure 8.16 Plot of Sh Against $Re^{0.5}\ Sc^{0.33}$ for Free-Flight Water Drops at 68°C.

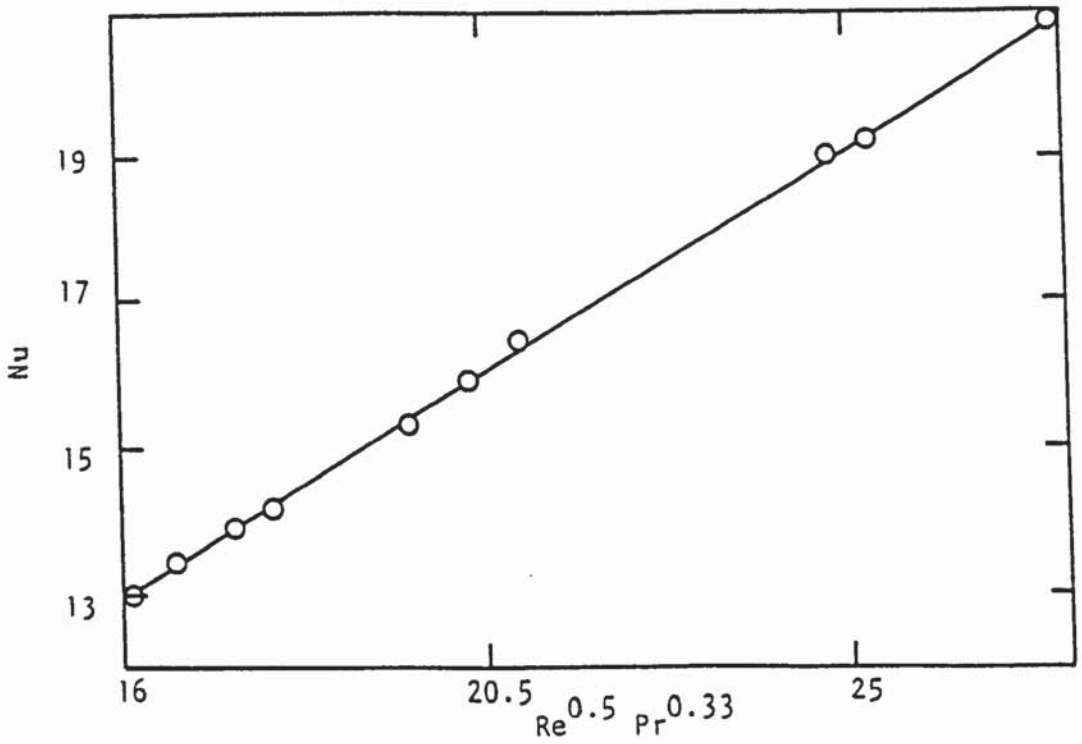

Figure 8.17 Plot of Nu Against $Re^{0.5}\ Pr^{0.33}$ for Free-Flight Water Drops at 68°C.

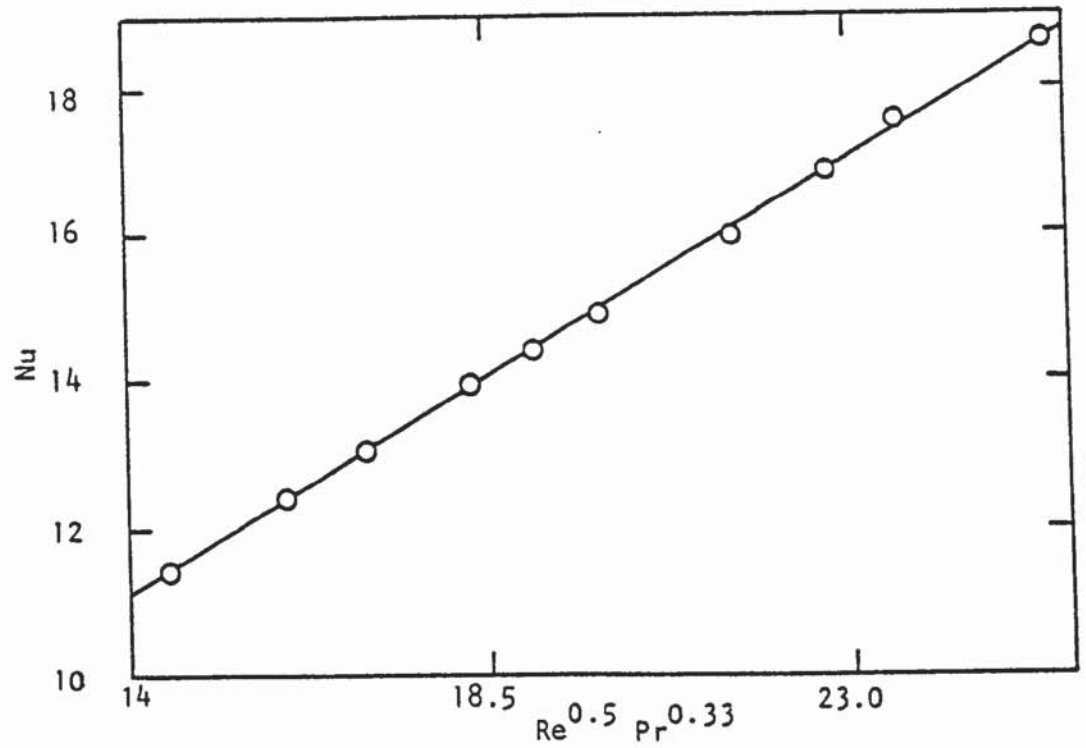

Figure 8.18 Plot of Nu Against $Re^{0.5}\ Pr^{0.33}$ for Free-Flight Water Drops at 97°C.

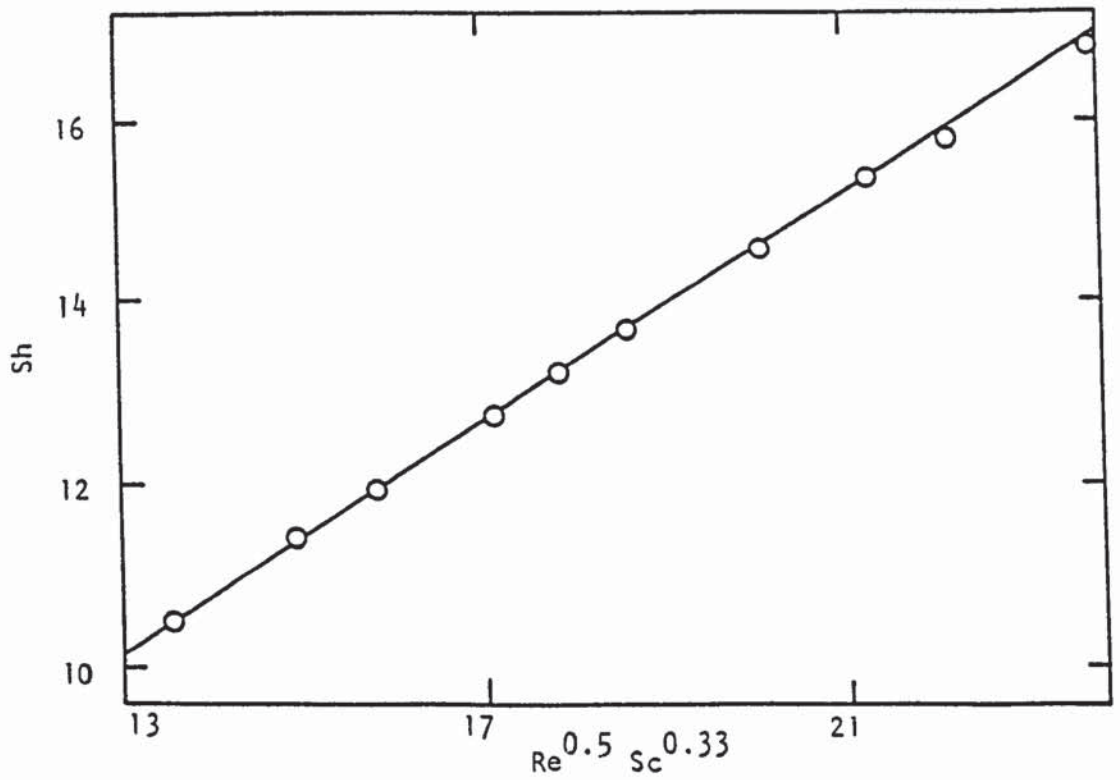

Figure 8.19 Plot of Sh Against $Re^{0.5}\ Sc^{0.33}$ for Free-Flight Water Drops at 97°C.

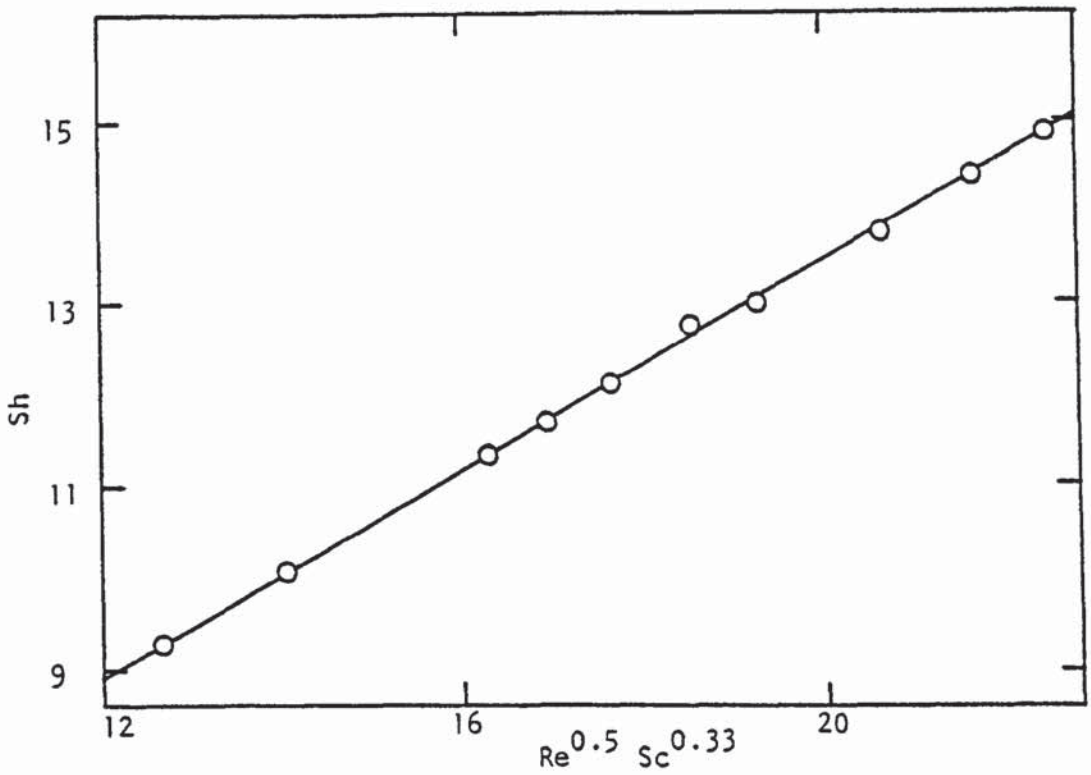

Figure 8.20 Plot of Sh Against $Re^{0.5}\ Sc^{0.33}$ for Free-Flight Water Drops at 125°C.

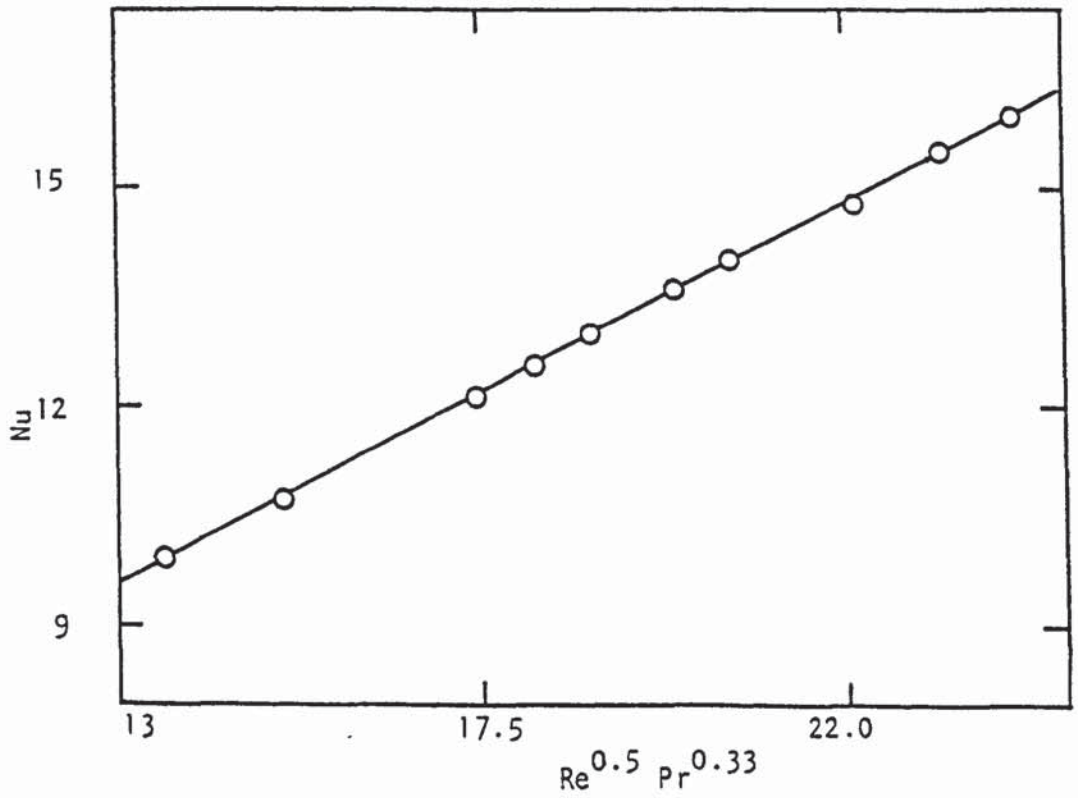

Figure 8.21 Plot of Nu Against $Re^{0.5}\ Pr^{0.33}$ for Free-Flight Water Drops at 125°C.

Table 8.11. In a similar way to that discussed in Section 8.1, two correlations were derived,

$$Sh = 2 + 0.617 \left(\frac{T_a - T_s}{T_{amb}} \right)^{-0.01} Re^{0.5} Sc^{0.33} \qquad (8.7)$$

and

$$Nu = 2 + 0.314 \left(\frac{1}{B} \right)^{0.17} Re^{0.5} Pr^{0.33} \qquad (8.8)$$

for practical purposes,

$$Sh = 2.0 + 0.62 \left(\frac{T_a - T_s}{T_{amb}} \right)^{-0.01} Re^{0.5} Sc^{0.33}$$

and

$$Nu = 2.0 + 0.3 \left(\frac{1}{B} \right)^{0.2} Re^{0.5} Pr^{0.33}$$

Figures 8.22 and 8.23 show plots of Sh against $\left(\frac{T_a - T_s}{T_{amb}} \right)^{-0.01} Re^{0.5} Pr^{0.33}$ and Nu against $(1/B)^{0.17} Re^{0.5} Pr^{0.33}$ respectively.

The coefficient for equation 8.7 was 0.98 and for equation 8.8, 0.98. The improved correlations represented by equations 8.5 and 8.6, and 8.7 and 8.8 respectively were subsequently used to predict k_g values in equation 5.26.

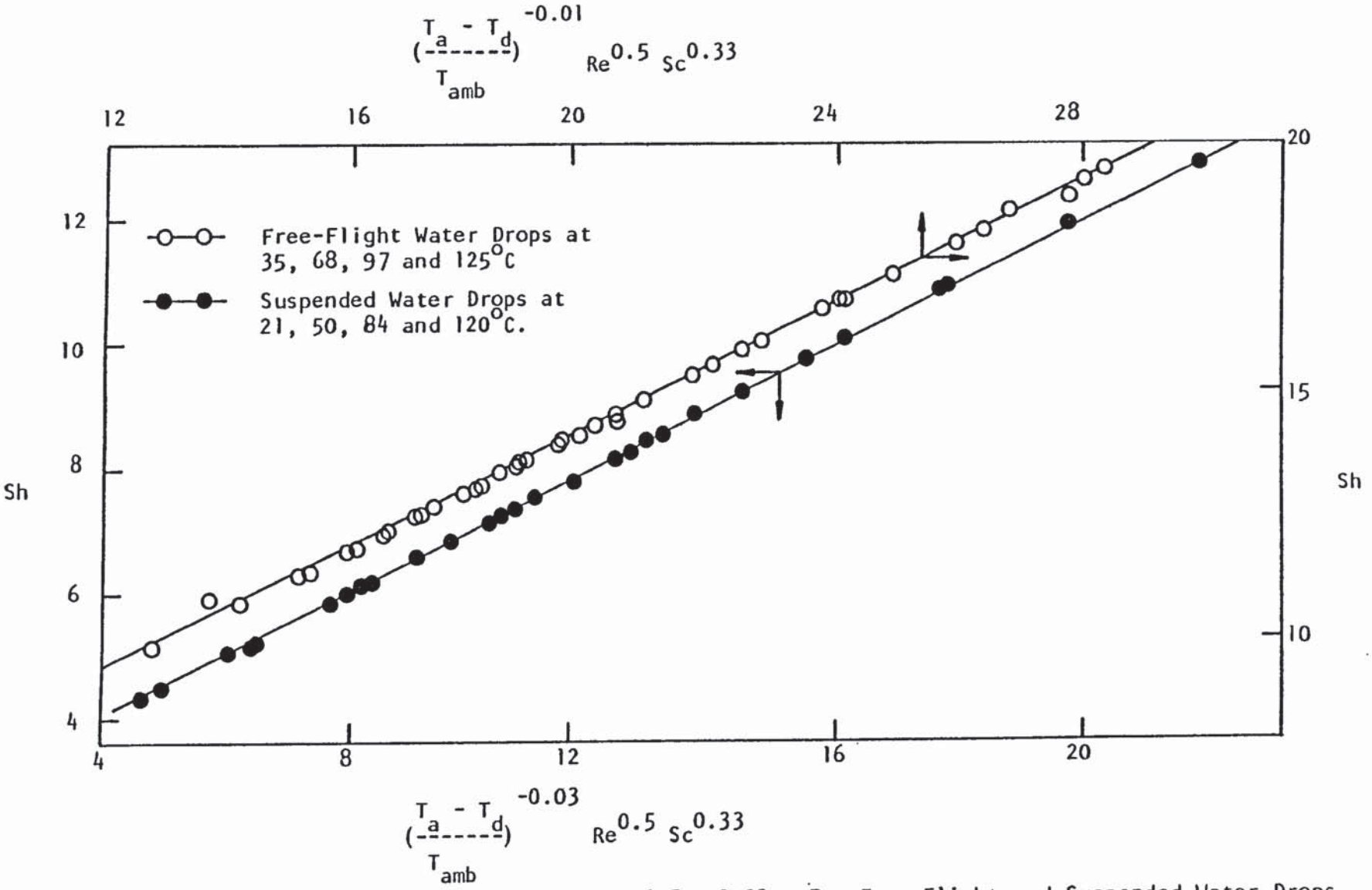

Figure 8.22 Plot of Sh Against $\left(\frac{T_a - T_d}{T_{amb}}\right)^n Re^{0.5} Sc^{0.33}$ For Free-Flight and Suspended Water Drops.

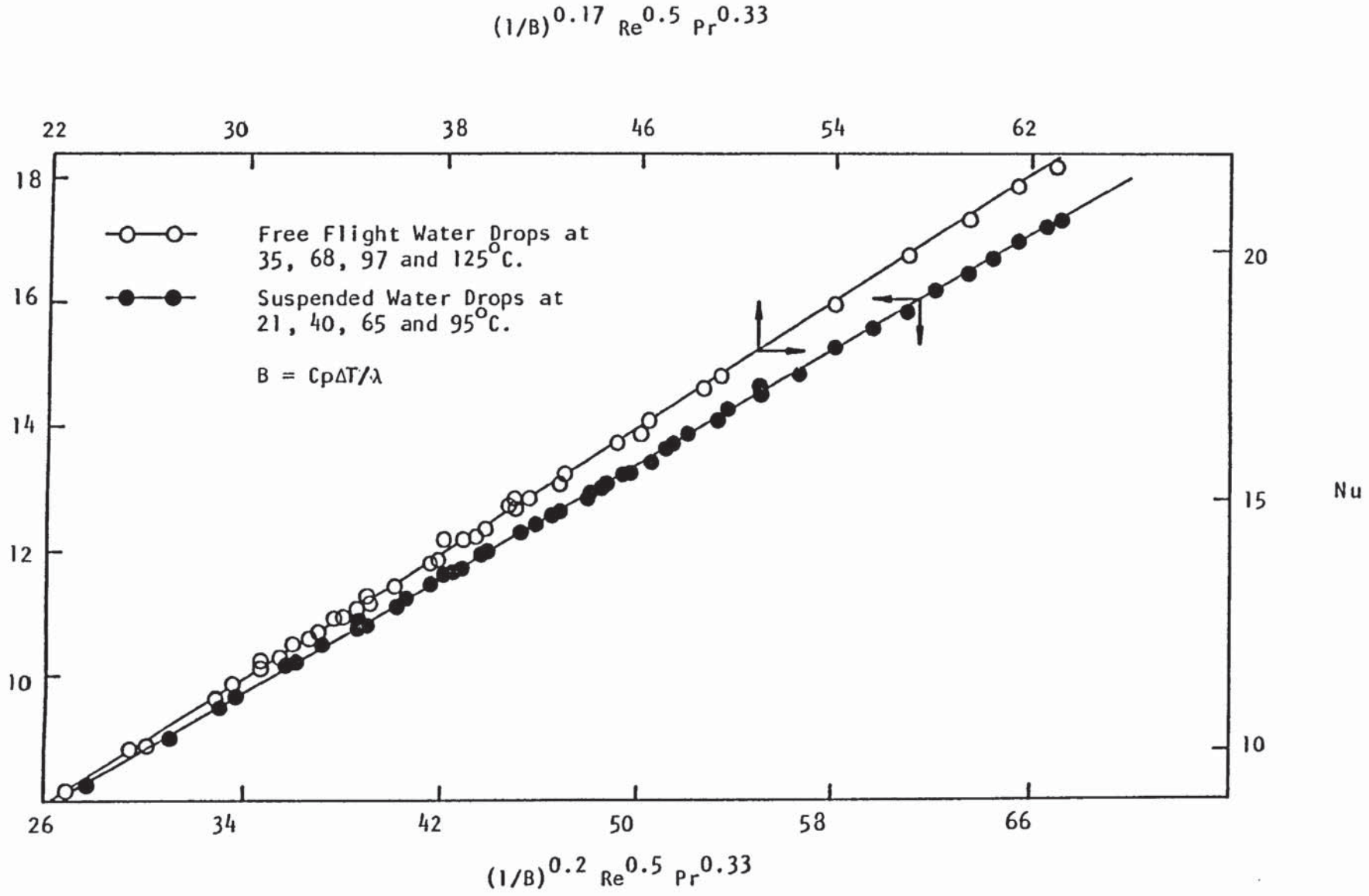

Figure 8.23 Plot of Nu Against $(1/B)^n\ Re^{0.5}\ Pr^{0.33}$ for Free-Flight and Suspended Water Drops.

CHAPTER NINE

PRESENTATION AND DISCUSSION OF RESULTS - DRYING OF DROPS CONTAINING DISSOLVED AND/OR SUSPENDED SOLIDS

Drops of different organic and inorganic materials were investigated, namely,

1. Drops of sodium sulphate decahydrate solution, containing up to 60% wt/wt solids. This material was selected since it has been described as forming a uniform, smooth crust (46, 55, 11). In the event it was indeed found to form smooth, crusts of even thickness which were crystalline and contained few cracks and pores.

2. Drops of two different organic paste slurries with solid content varied from 12% wt/wt to 18% wt/wt to assess how these differed from crystalline material, e.g. skin formation. The effect of additives upon drying rate and crust structure was also studied.

3. Two organic pigment solutions were also investigated, both to extend the range of materials and to compare the behaviour of solutions with slurries.

4. Solutions of three inorganic powders containing total solids in the range 25% wt/wt to 70% wt/wt.

Investigations were carried out by varying initial drop diameters and density and air velocity (and hence Reynolds number), air temperature, and nature of solid. The effect of additives was also studied.

9.1 Evaporation Rates

Plots of evaporation rate versus time after injection for droplets containing solids tend to show three periods (or stages). The first period is characterised by a sharp increase in evaporation rate whilst evaporation takes place from the free liquid surface of the drop. The drop temperature also decreases to the wet-bulb temperature but no crust is formed during this stage. The second stage is characterised by partial crust formation and the drop temperature starts to increase. Behaviour during this stage is specific for the material studied. For example it was found to be very short in the case of sodium sulphate decahydrate drops, since once this material reaches saturation the crust forms

quickly and hence the resistance to mass transfer is also increased. In the third stage there is a sharp decrease in evaporation rate because a crust has formed completely. Crust structure, thickness and porosity have a marked effect on the rate during this stage.

Evaporation rates were calculated from equation 5.2 and the corresponding crust mass transfer coefficient subsequently determined by applying equation 5.27. Theoretical crust thickness was predicted from equation 5.25 and the overall mass transfer coefficients from equation 5.26. Practical values of crust thickness were obtained from Stereoscan microphotographs or optical microscope photographs of which those shown in Section 9.6 are typical.

Air velocity, air temperature, the initial solids content, the nature of any additive, and the nature of the solid were the experimental variables. These effects were evaluated in terms of the evaporation rate, crust thickness, overall mass transfer coefficient, crust mass transfer coefficient, and crust porosity.

Data for sodium sulphate decahydrate are shown in Figure 9.1 at air temperatures of 100°C and 120°C, a constant initial concentration of 50% wt/wt solids, and an air velocity of 0.927 $m.s^{-1}$.

Evaporation rates from drops of an organic paste slurry at high air temperatures (200°C and 300°C) with the addition of 13% additive (sodium chloride solution or Dispersol) are shown in Figure 9.2. Figures 9.3 - 9.5 illustrate evaporation rates of drops of different solutions. All these curves, as mentioned above, show a linear increase in the evaporation rate consistent with evaporation from liquid drops until the drop wet-bulb temperature and a maximum evaporation rate were reached and the crust started to build-up combined with an increase in drop temperature. Once the crust was completed there was a sharp fall in the evaporation rate and then a steady, gradual fall to 'complete' drop dryness i.e. down to the bound moisture content. As expected, the higher the air temperature the greater the rate of evaporation and hence the shorter the time to 'complete' dryness.

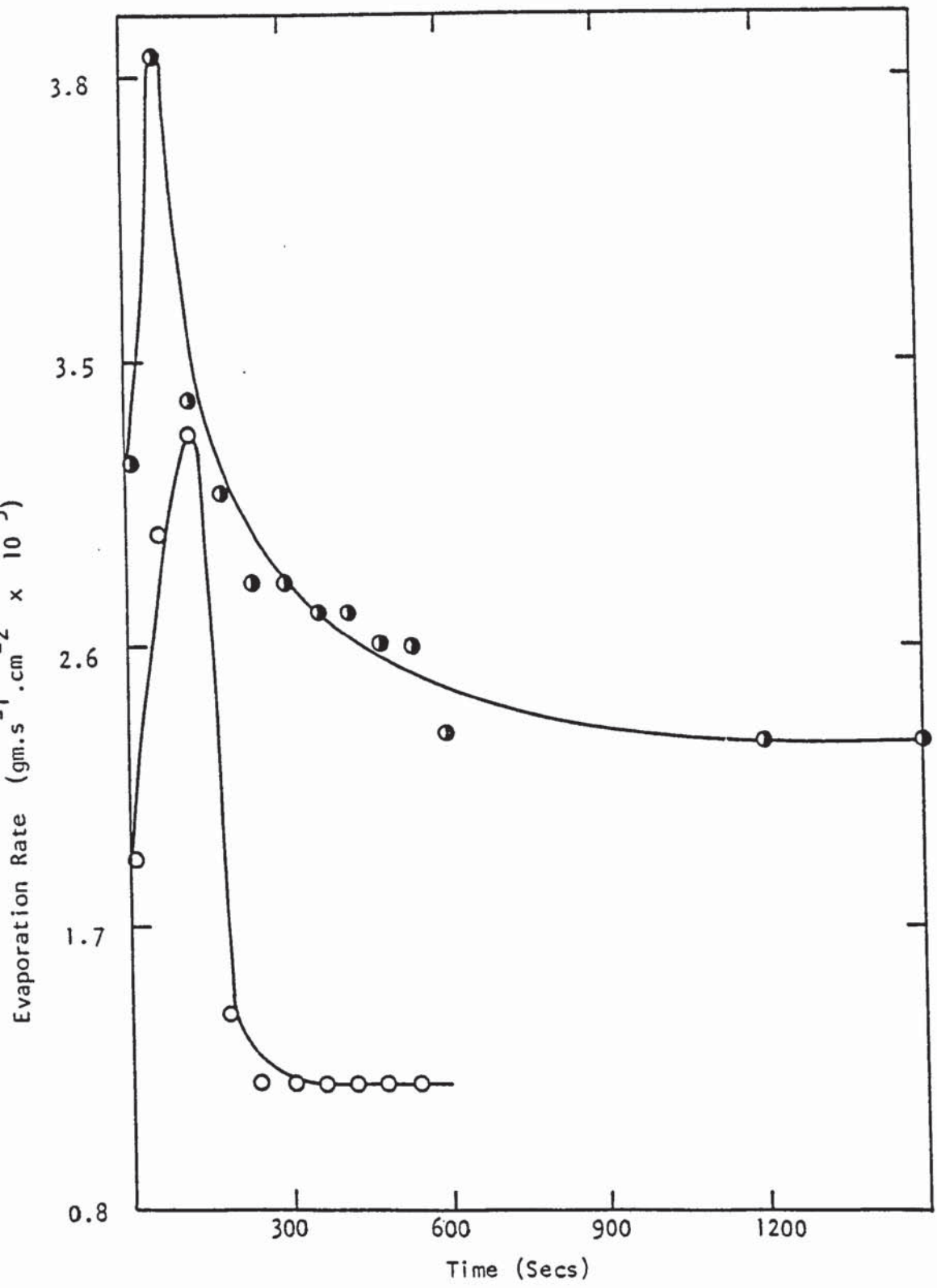

Figure 9.1 Effect of Air Temperature on the Evaporation Rates of Drops of Sodium Sulphate Decahydrate. Air Velocity of 0.927 ms^{-1}.

Air Temperature ^{o}C

—○—○— 100

—◑—◑— 120

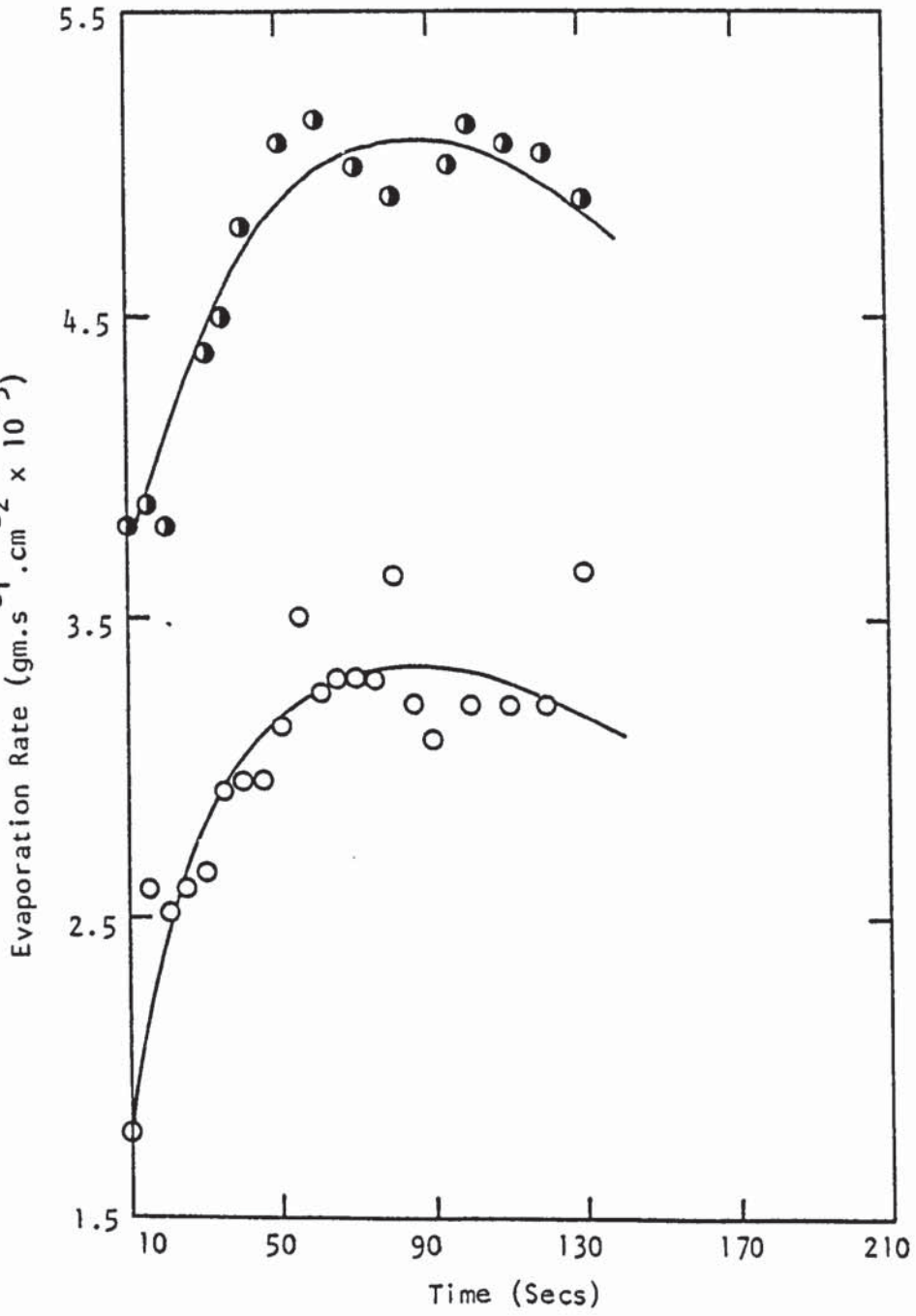

Figure 9.2 Effect of Air Temperature on the Evaporation Rates of Organic Paste Formulation A Slurry Drops of Initial Solids Contnet 12% wt/wt.

	Air Temperature °C	Dispersing Agent
—○—○—	200	13%
—◑—◑—	300	13%

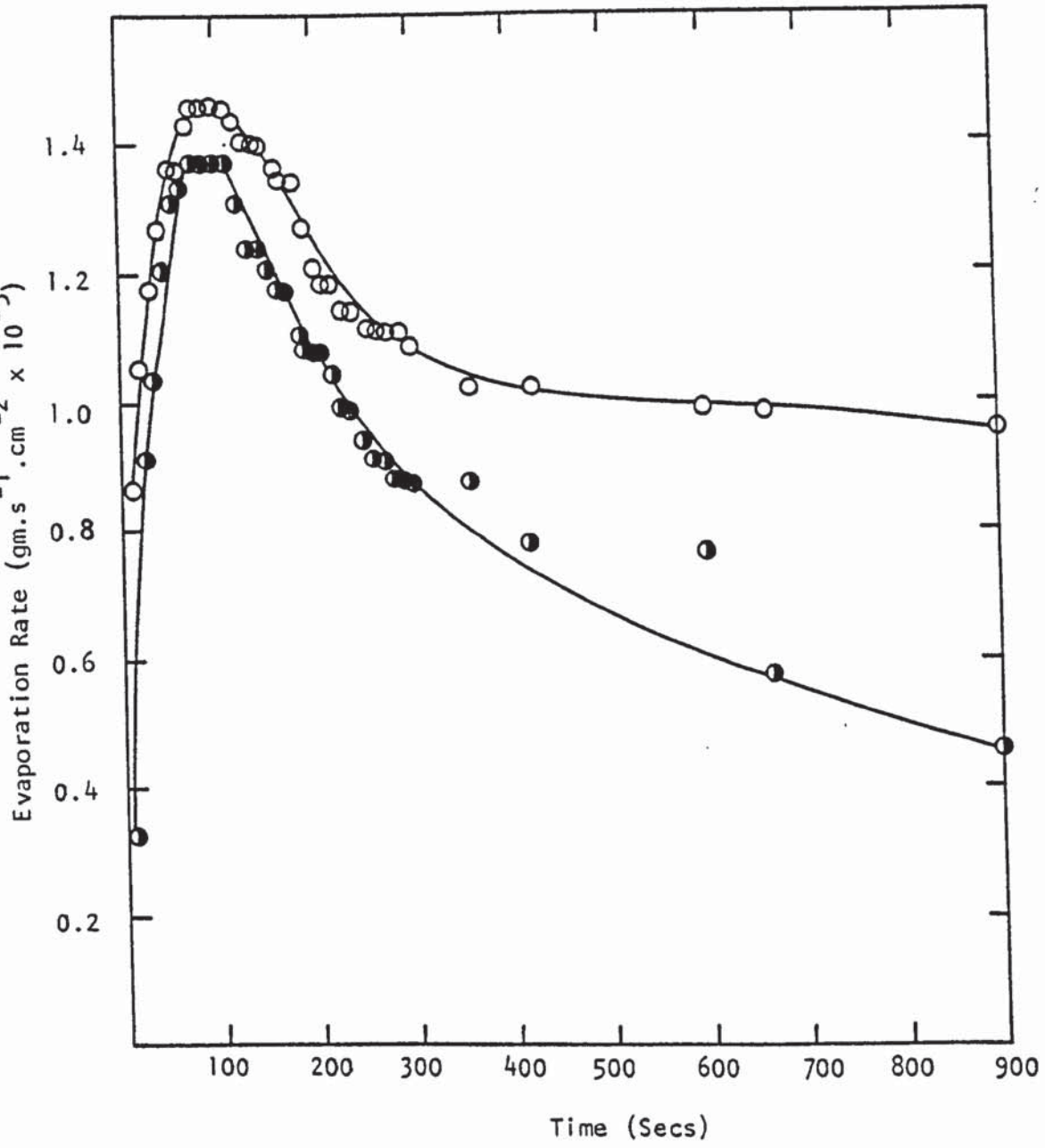

Figure 9.3 Evaporation Rates from 40% wt/wt Solutions of Inorganic Pow Formulation C at Air Temperatures of 110°C and 130°C.

Air Temperature °C

—○—○— 130°C

—◑—◑— 110°C

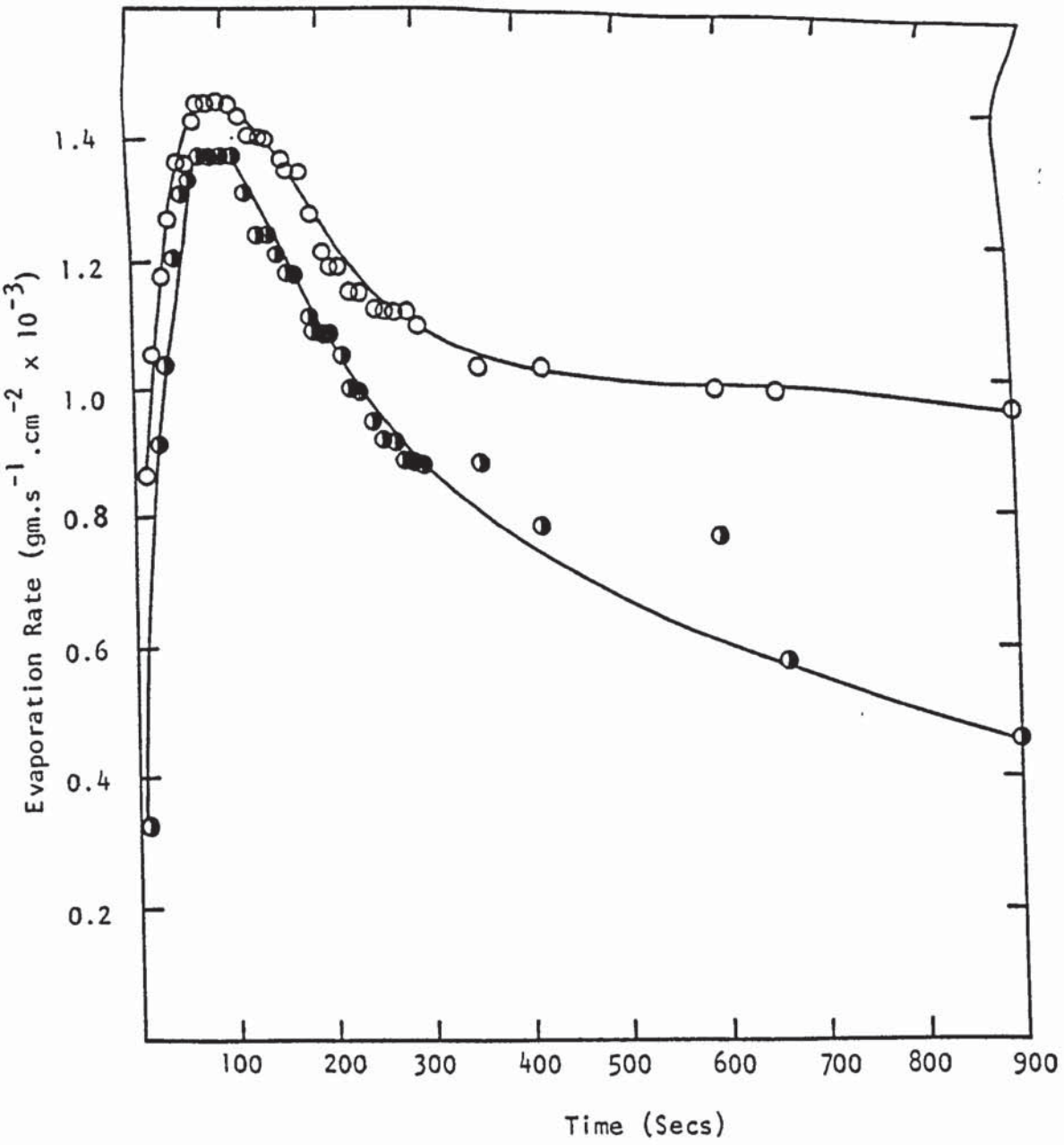

Figure 9.3 Evaporation Rates from 40% wt/wt Solutions of Inorganic Pow
Formulation C at Air Temperatures of 110°C and 130°C.

Air Temperature °C

—○—○— 130°C

—◑—◑— 110°C

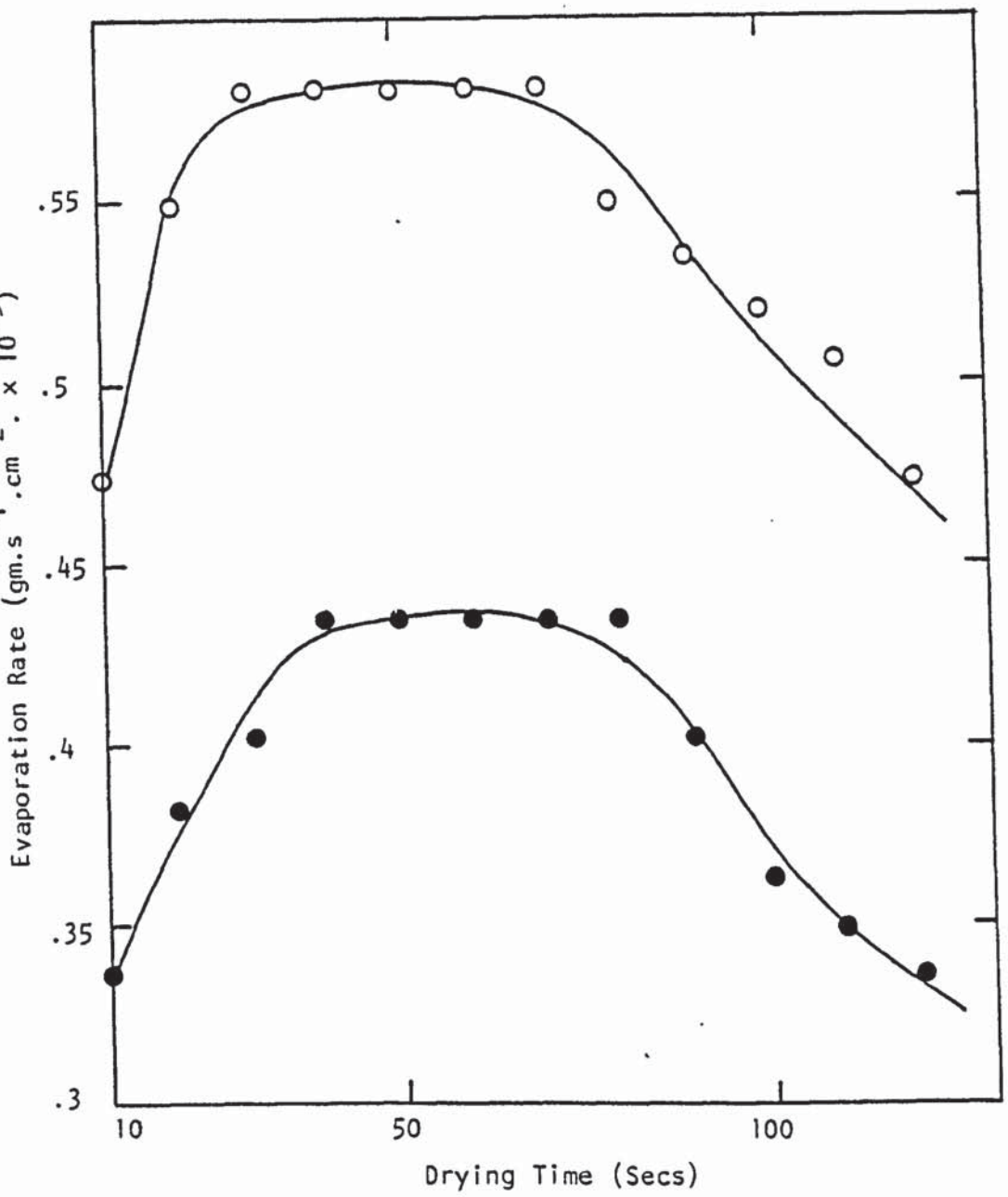

Figure 9.4 Evaporation Rates from 22% wt/wt Solutions of Organic Pigment A at Air Temperatures of 100°C and 135°C.

Air Temperature °C

●—● 100

○—○ 135

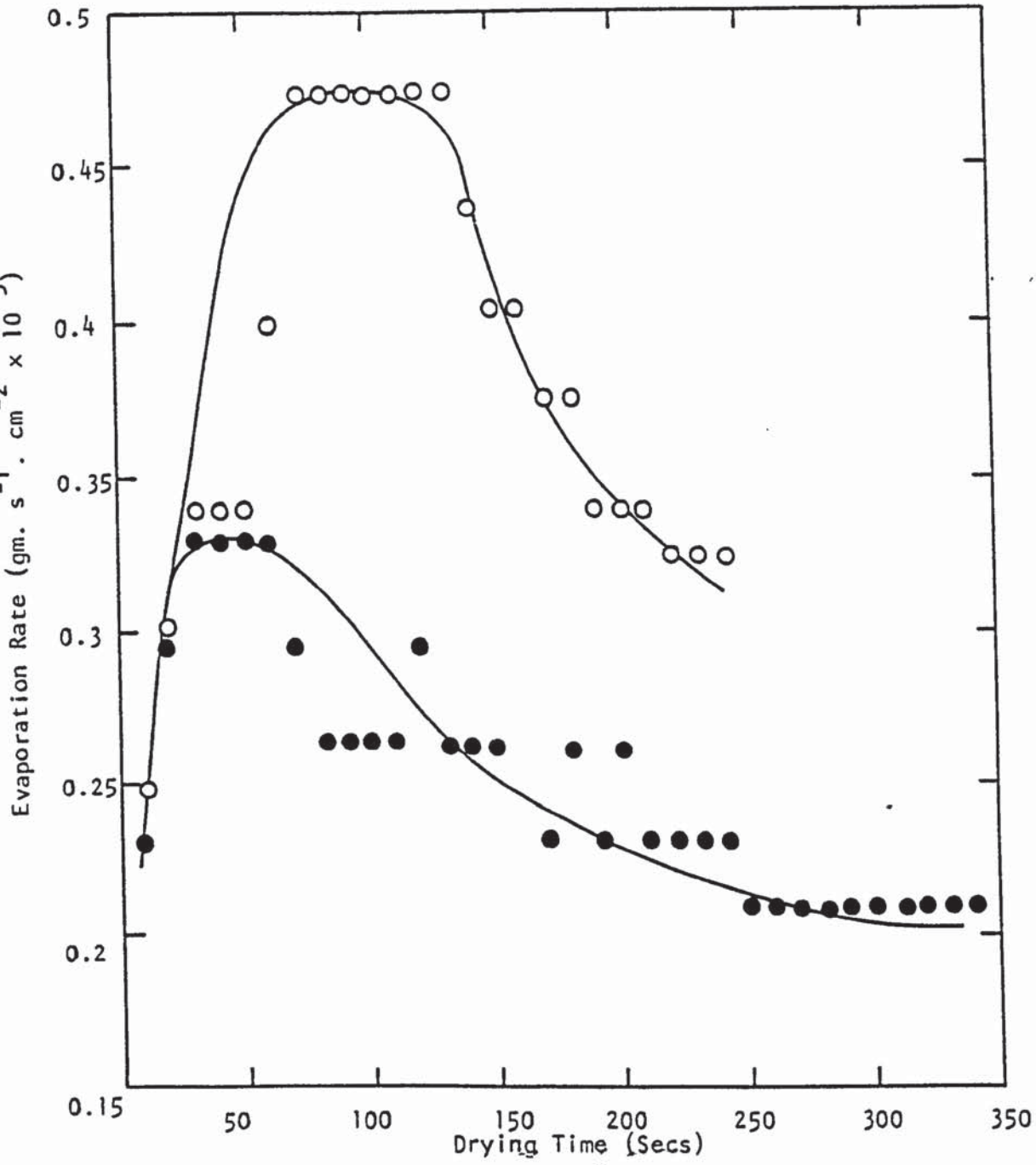

Figure 9.5 Evaporation Rate from Suspended Drops of Organic Pigment B at Air Temperatures 100°C and 135°C.

Air Temperatures °C

●—● 100

○—○ 135

Figure 9.6 represents two curves for evaporation rate from 50% sodium sulphate decahydrate at an air temperature of 100°C and air velocities of 0.18 ms^{-1} and 0.927 $m.s^{-1}$. Comparison of the rates during the initial period, when diffusion is from a saturated surface, shows that the rate at the higher air velocity was approximately three times greater. This is in good agreement with the increase predictable from equation 8.3. The maximum evaporation rates corresponding to the attainment of the wet-bulb temperature differ by a factor of 2.8 but then with crust formation there was a sharp decrease in rate. The steady-state drying rates, i.e. the horizontal portion of the curves, where the crust coefficient controls then differ by a factor of 1.2/0.48 = 2.5; the values of the coefficients were calculated as described later and summarised in Table 9.11.

At initial concentration ranges between 12 - 70 wt% solids the maximum evaporation rates for different drops of solutions and slurries, were as expected, found to be higher for drops of low initial solids content, i.e. the higher drop solids content the lower the evaporation rates. Figures 9.7 - 9.12 demonstrate this for the drying of drops of sodium sulphate decahydrate, inorganic powders and organic paste slurries respectively. Two effects may contribute to this,

(i) The lowering of the vapour pressure of water as solution concentration is increased;

and (ii) The attainment of the critical saturation point with concentrated solutions or slurries before the maximum temperature driving force ($T_a - T_{wb}$) is reached.

At corresponding solids contents, and air temperature and velocity, maximum evaporation rate was found to depend upon the nature of the solid. For example Figure 9.13 shows drying curves of two different slurry drops under identical conditions. Since reference to the original data (Tables C7 and C11) shows that the minimum drop temperatures attained were almost identical, the probable explanation for this difference is a variation in solubility and hence vapour-pressure depression.

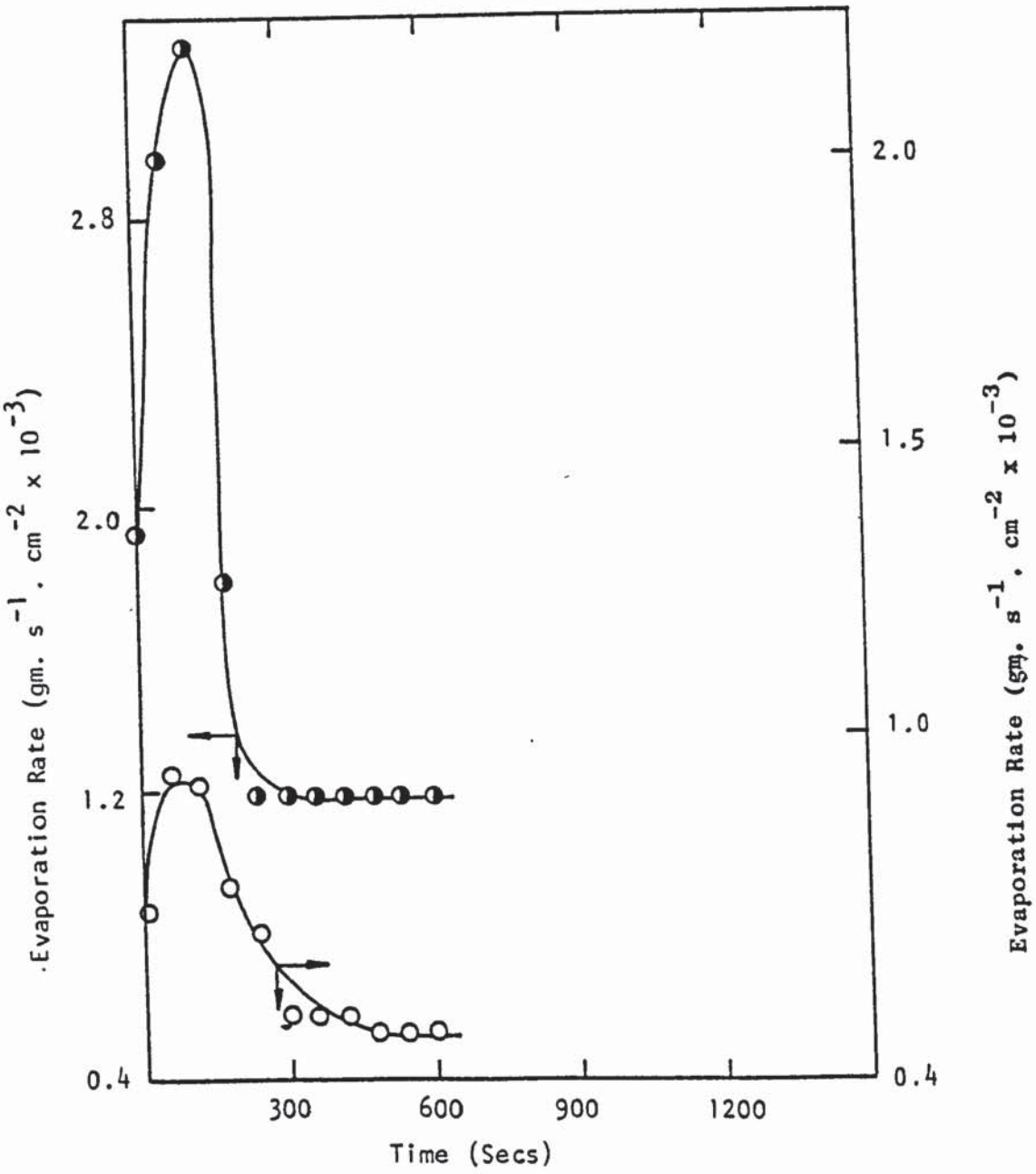

Figure 9.6 Effect of Air Velocity on the Evaporation Rates of Drops of Sodium Sulphate Decahydrate at Air Temperature 100°C.

	Air Velocity m.s^{-1}
—○—○—	0.18
—◑—◑—	0.927

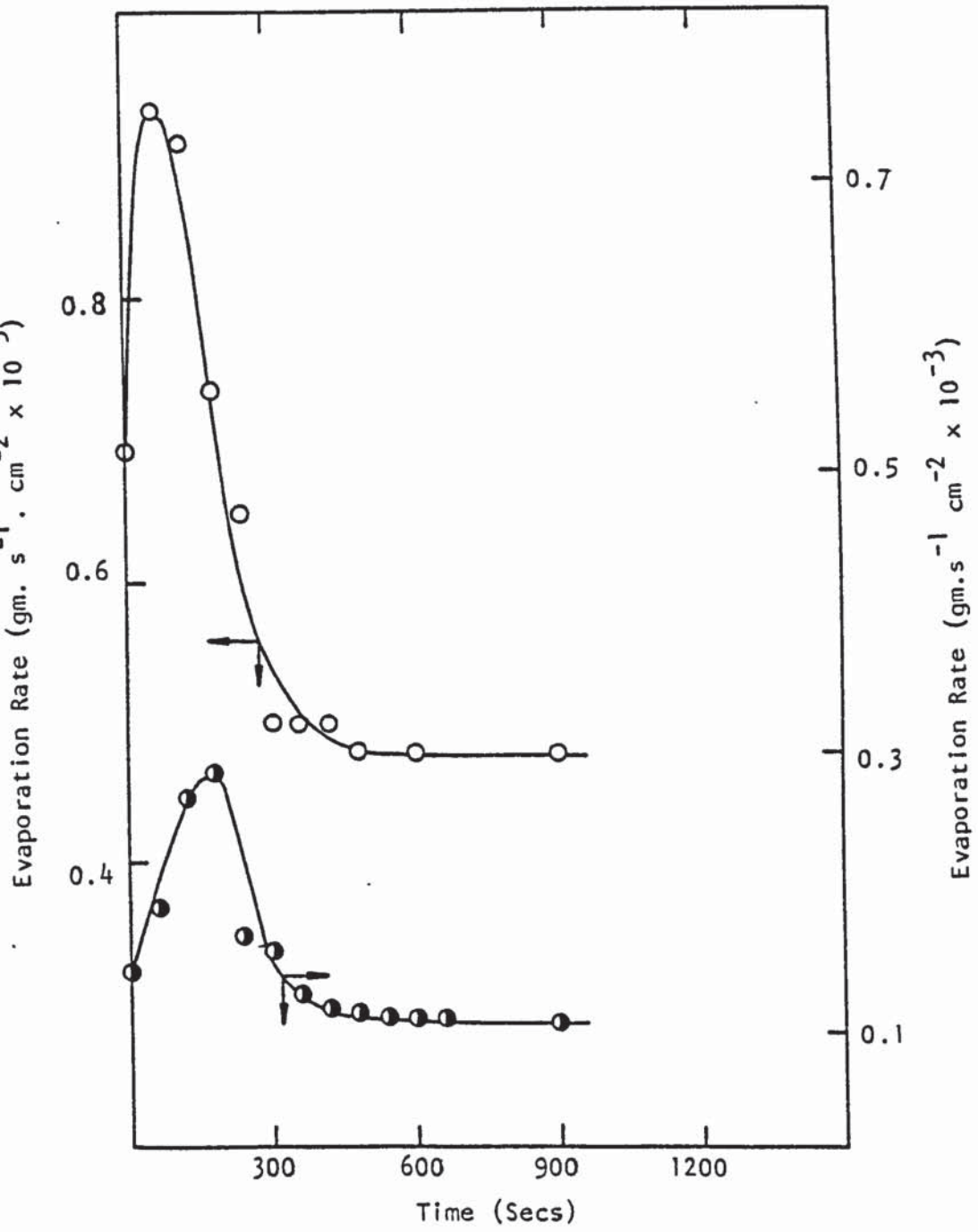

Figure 9.7 Evaporation Rates of 50% wt/wt Sodium Sulphate Decahydrate Drops at Air Velocity of 0.18 m.s^{-1}.

	Air Temperature ^{o}C	Drop Diameter m
—○—○—	100	4 x 10^{-3}
—◑—◑—	100	6 x 10^{-3}

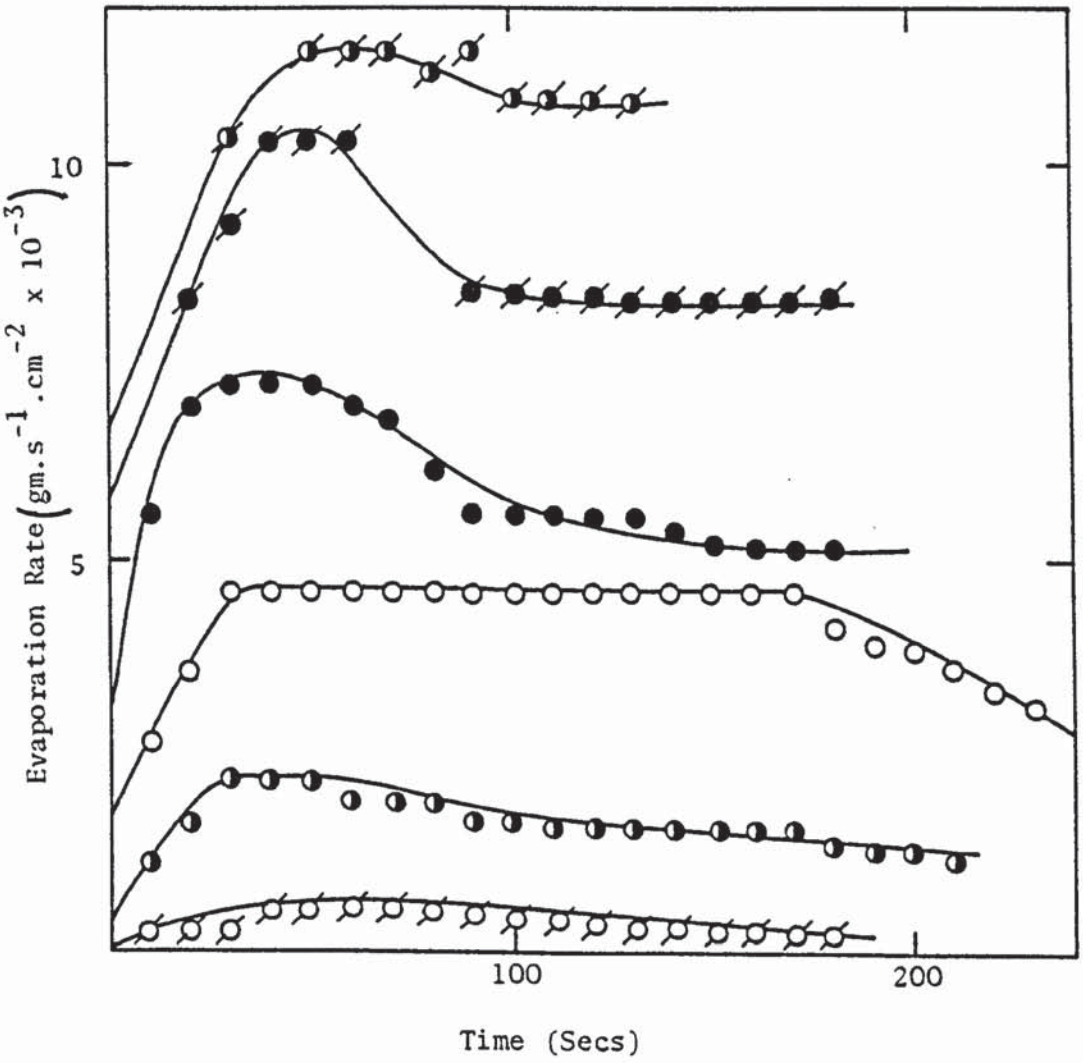

Figure 9.8 Evaporation Rates from 25% wt/wt Solution of Inorganic Powder Formulation E at Different Air Temperatures.

Air Temperature ^{o}C
34
64
130
165
200
93

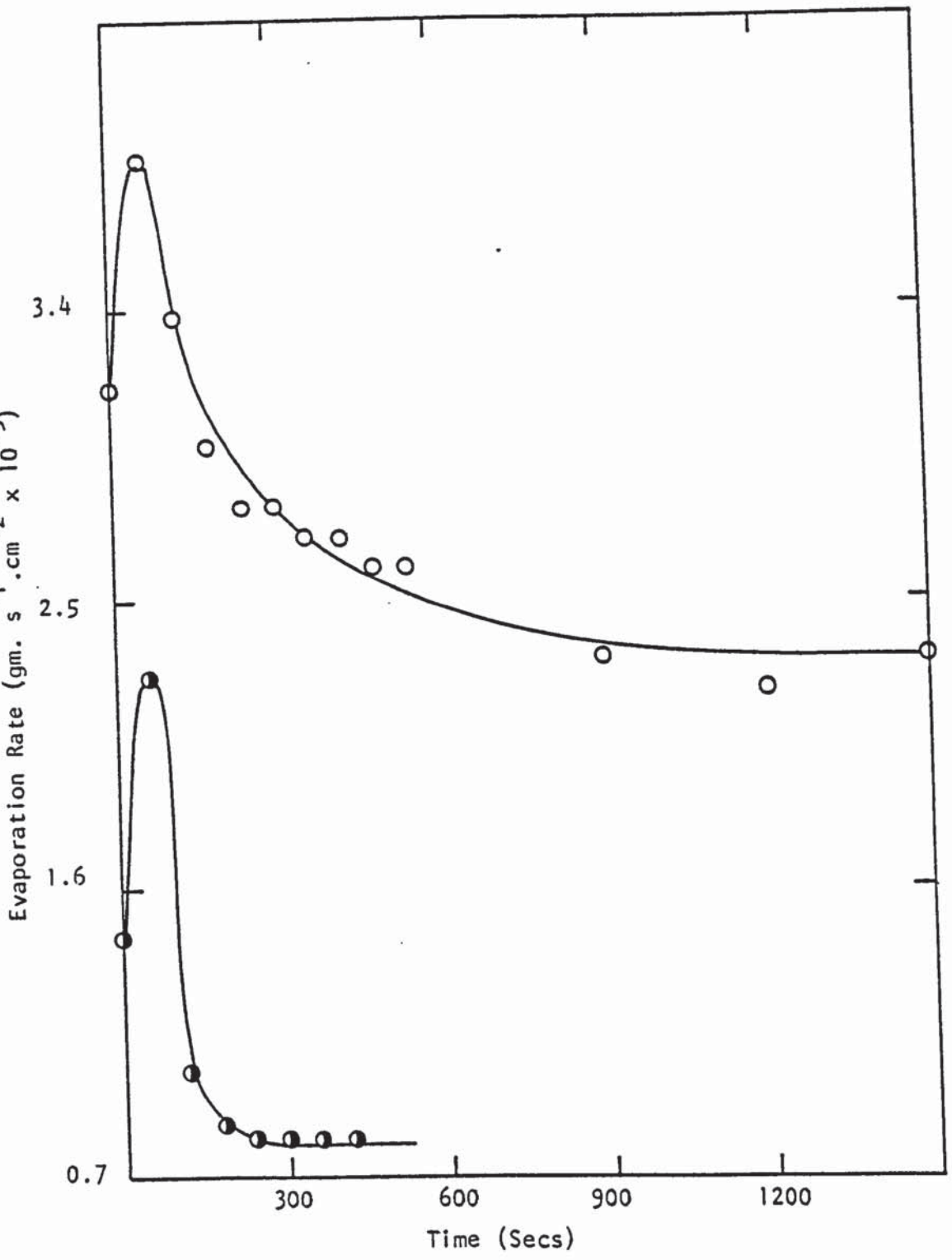

Figure 9.9 Effect of Solids Content on the Evaporation Rates of Sodium Sulphate Decahydrate Drops at Air Temperature of 120°C, 0.927 m.s^{-1} Air Velocity.

% Solids Content wt/wt	
-O-O-	50
-◑-◑-	60

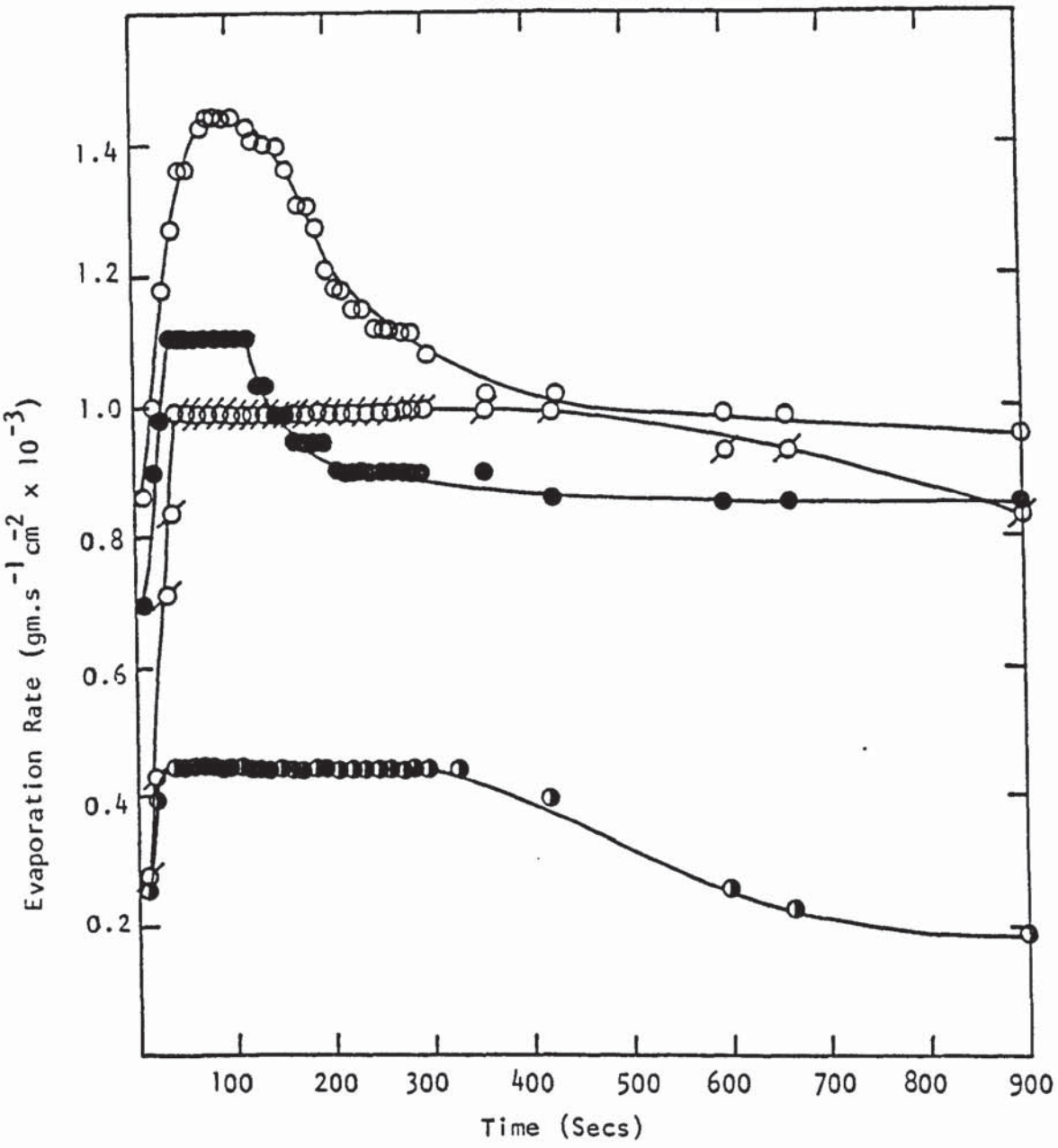

Figure 9.10 Evaporation Rates From Different Concentration Solutions at A Constant Air Temperature of 130°C of Inorganic Powder C.

Solids Content wt/wt

40%

50%

60%

70%

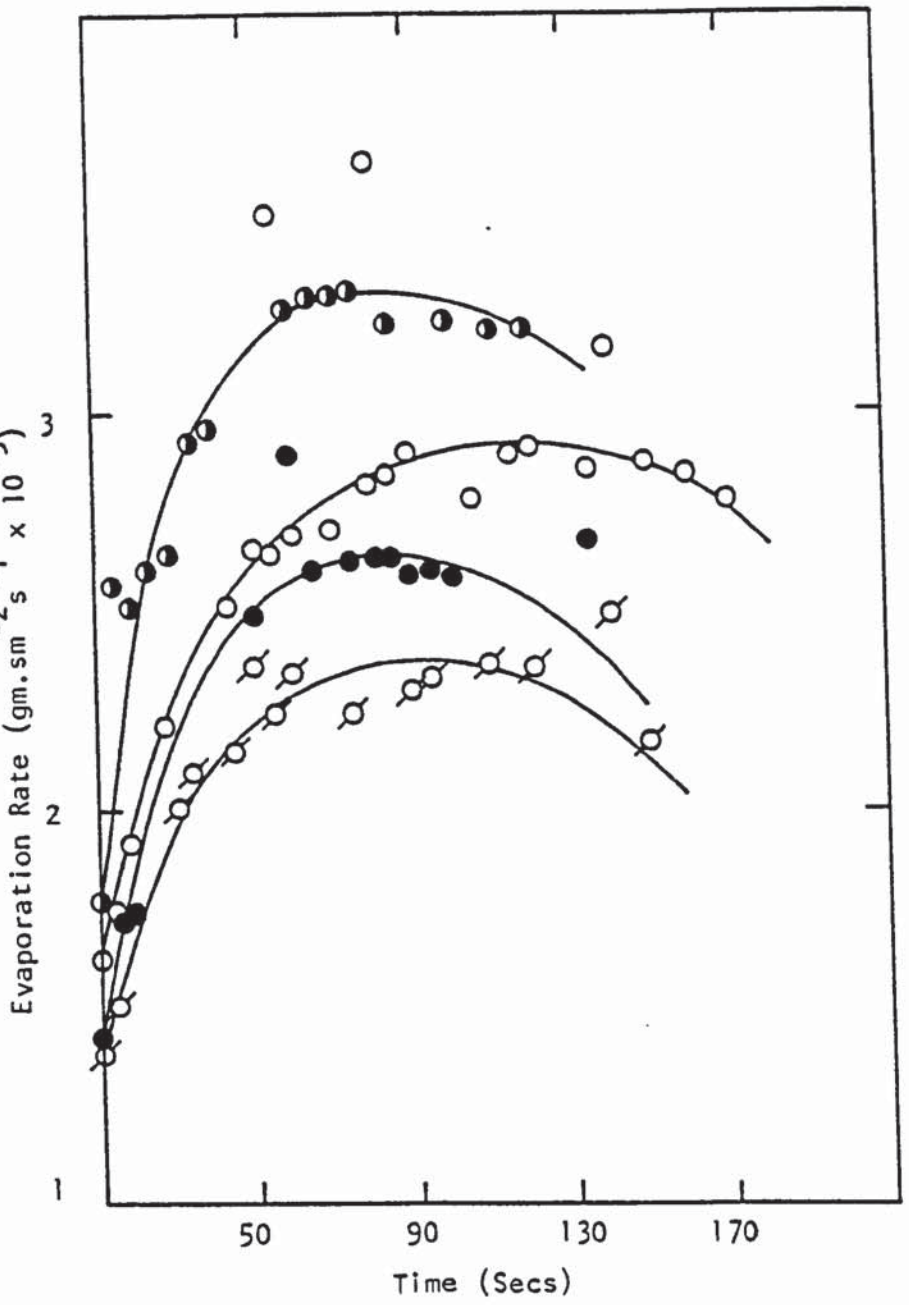

Figure 9.11 Effect of Solids Content on Evaporation Rates of Organic Paste Formulation A Slurry Drops at 200°C.

	Solids Content wt/wt	Dispersin Agent
⊖—⊖	12%	13% Dispersol
○—○	15%	13% NaCl Solution.
●—●	15%	13% Dispersol
⊘—⊘	18%	13% Dispersol

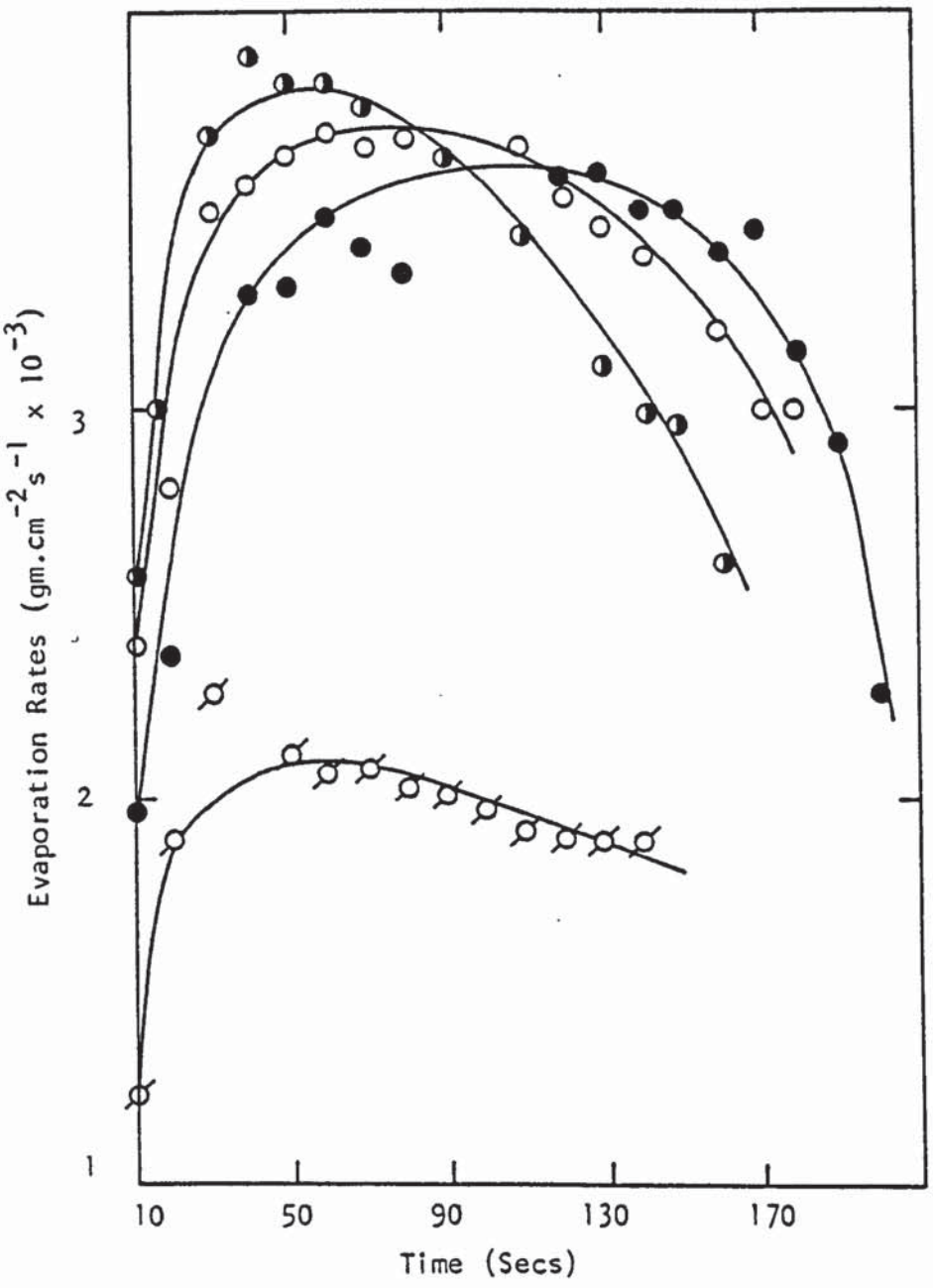

Figure 9.12 Effect of Solids Content on Evaporation Rates of Organic Paste Formulation B Slurry Drops at 200°C

Solids Content wt/wt	Disersing Agent
12%	13% Dispersol
15%	13% NaCl Solution
15%	13% Dispersol
18%	13% Dispersol

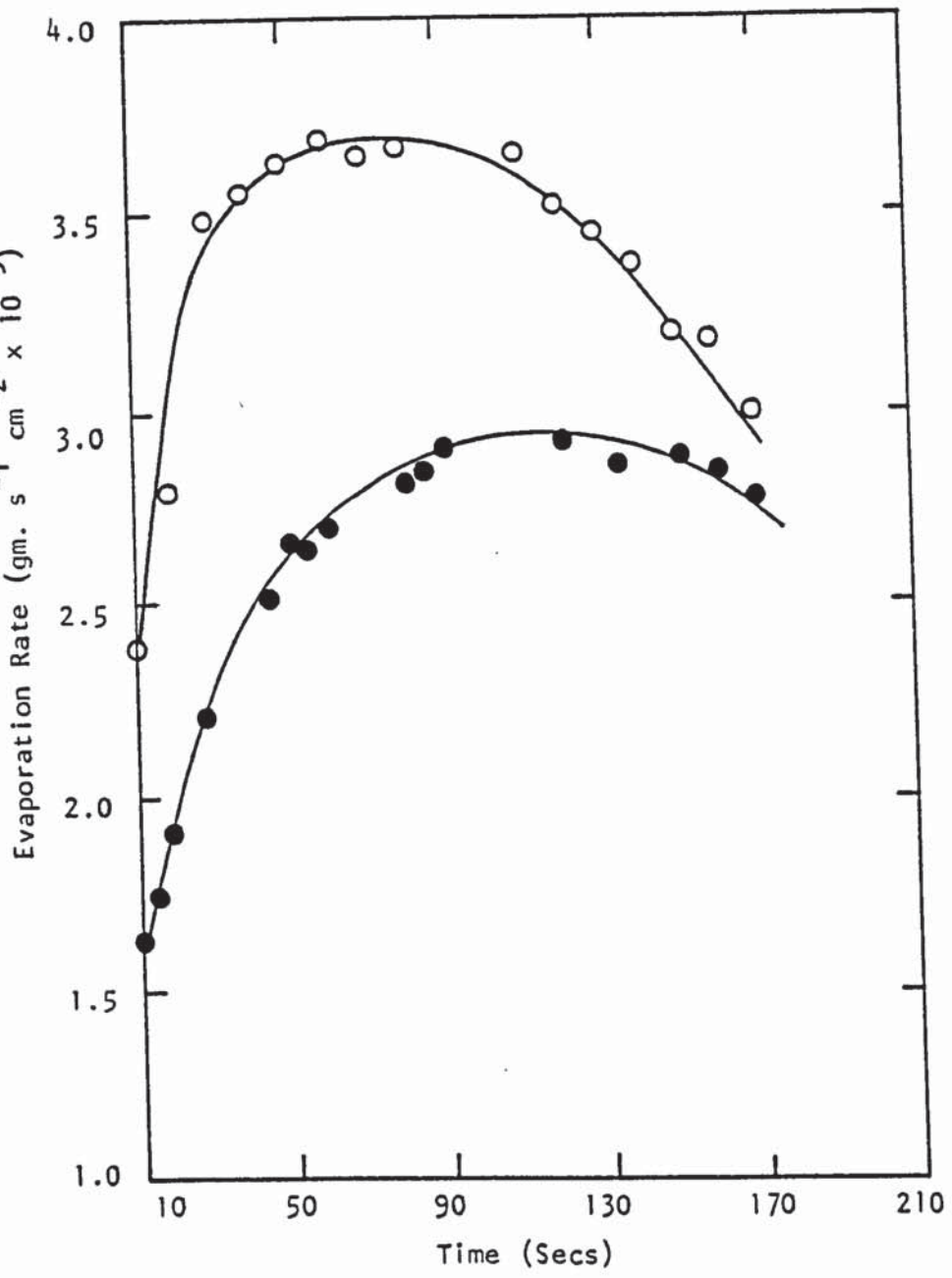

Figure 9.13 Effect of the Nature of the Solid on the Evaporation Rate of Organic Paste Slurry Drops.

	Solids Content wt/wt	Air Temperature °C
-○-○-	15% wt/wt Organic Paste B	200°C
-●-●-	15% wt/wt Organic Paste A	200°C

The presence of an additive had a pronounced effect on the evaporation rates. Figure 9.14 shows drying curves of drops of slurries when different kinds of additive were added. For a corresponding solids content and identical conditions the evaporation rate increased when the additive was present. The nature of the additive also affected the evaporation rate, for example a drop of Organic Paste Slurry Formulation A containing sodium chloride solution dried more rapidly, i.e. 40 seconds quicker, than a similar drop containing Dispersol at corresponding air velocity and temperature. Plate 9.8 confirms the change in crust structure for drops of slurry showing the effect of the additive, and its nature, on the crust. The enhancement of evaporation rate after crust formation, in these cases near the peaks, is explanable by the increase in pores as between (c) and (a) in this illustration. (The importance of crust porosity is discussed in Section 9.3).

Tables 9.1 - 9.5 represent the maximum evaporation rates and moisture contents after 10 seconds. On the assumption that at normal drop velocities about 10 seconds would elapse in an industrial drier before drops impinge on the walls, this type of calculation can predict the probability of excessive wall deposits. Thus, if 60% is the minimum amount of evaporation necessary to produce a drop which will not flatten and adhere, it can be deduced from (Tables 9.1 - 9.5) that sprays of Inorganic Powder Formulations E and D may tend to stick on the wall of the chamber. Sprays of Organic Paste Slurries A and B may behave similarly. Sprays of Inorganic Powder Fomulation C should not stick on the dryer chamber wall. Thus measurement of evaporation rates of single droplets as a function of drying conditions can yield fundamental information for optimising spray dryer design and operation.

9.2 Crust Thickness

The rate of increase in crust thickness was affected by the air temperature; the higher the air temperature the faster the crust grew as illustrated for sodium sulphate decahydrate in Figure 9.15. In general a 32% thicker crust was obtained with an increase in air temperature from 100°C to 120°C. Allowing for experimental errors in drop

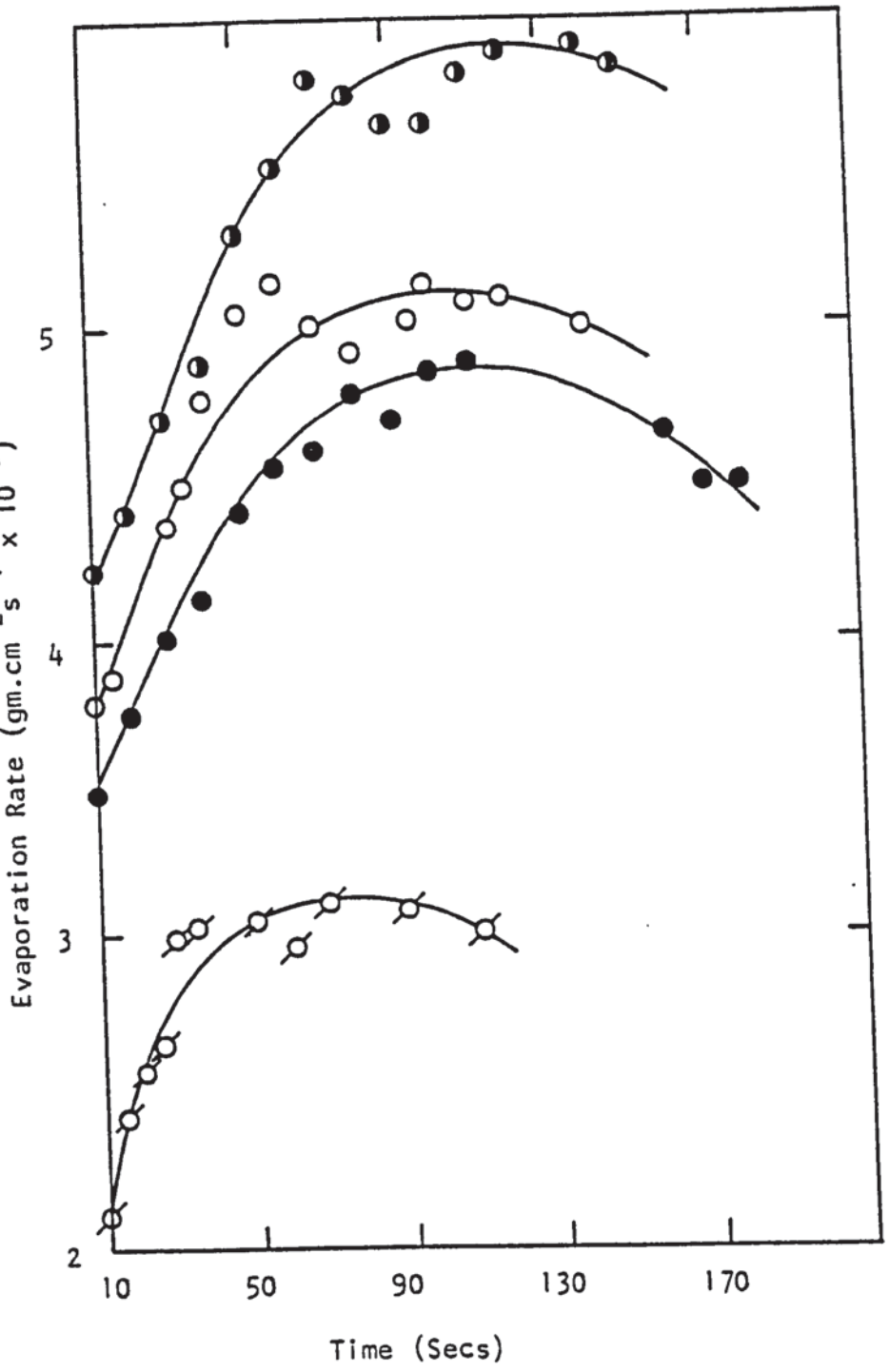

Figure 9.14 Effect of Additives on the Evaporation Rates of Organic Paste Formulation A Slurry Drops at 300°C.

	Solids Content wt/wt	Dispersing Agent
●—●	12%	13% NaCl Solution
○—○	12%	13% Dispersol
●—●	12%	---
⊗—⊗	18%	13% Dispersol

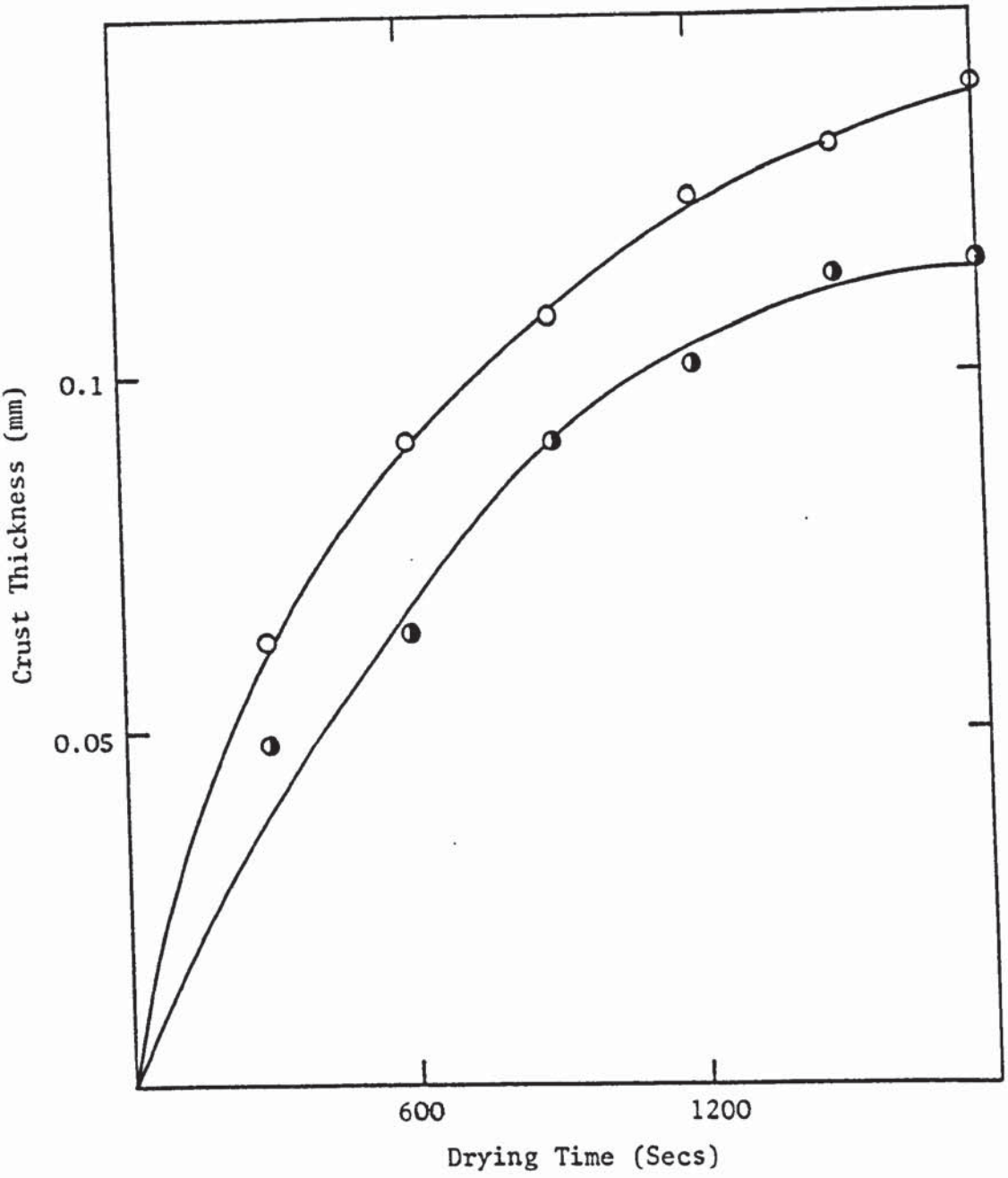

Figure 9.15 Effect of Air Temperature on Sodium Sulphate Decahydrate Crust Thickness.

Air Temperature ^{o}C

100

120

temperature measurements this is in agreement with the predictable increase in temperature driving force for heat transfer. The rate of crust growth also increased by 8% with an increase in air velocity from 0.6 $m.s^{-1}$ to 1.2$m.s^{-1}$, as shown in Figure 9.16. This confirms the relatively small resistance offered by the gas film once a crust is formed since, according to equation 8.3, k_g would differ by a factor of $\simeq (2)^{0.5} \simeq 1.4$ between these runs. Figure 9.17 shows a drying curve for sodium sulphate decahydrate when an increase in solids content from 50% wt/wt to 60% wt/wt resulted in an increase in crust thickness by 15%.

The equation 5.25 developed by Audu (103) was tested against all the experimental data listed in Appendix B, Tables B6 - B9, and the comparison is given in Table 9.6. One set of data are plotted in Figure 9.18. The theoretical prediction was generally too high by 14%; this may be because the model ignored heat transfer to the drop by radiation from the surroundings and by conduction through the nozzle. Hence, for an extension to this study, the model should contain an allowance for heat transfer to the drop in addition to convective heat transfer as outlined in Chapter 5.

However in a separate series of experiments with Organic Paste Formulation A 18% wt/wt solids content at air temperature of 200°C the phenomenon of an expanding drop was observed. The results are summarised in Table 9.7and Figure 9.17a. Clearly under these conditions at some point the crust thickness begins to decrease with time and Audu's model would not be applicable.

9.3 Crust Mass Transfer Coefficient and Porosity

Crust porosities were estimated using equation 5.28 and the data are summarised in Tables 9.8 - 9.10. As would be expected, crust porosity is affected by the nature of the solid forming the crust. As already mentioned, it was found that selected additives increased the porosity of the crust. Different additives had a different effect on crust porosity as shown in Plate 9.8.

The overall mass transfer coefficient following crust formation was obtained from equation 5.26. This coefficient increased only slightly with increase in air

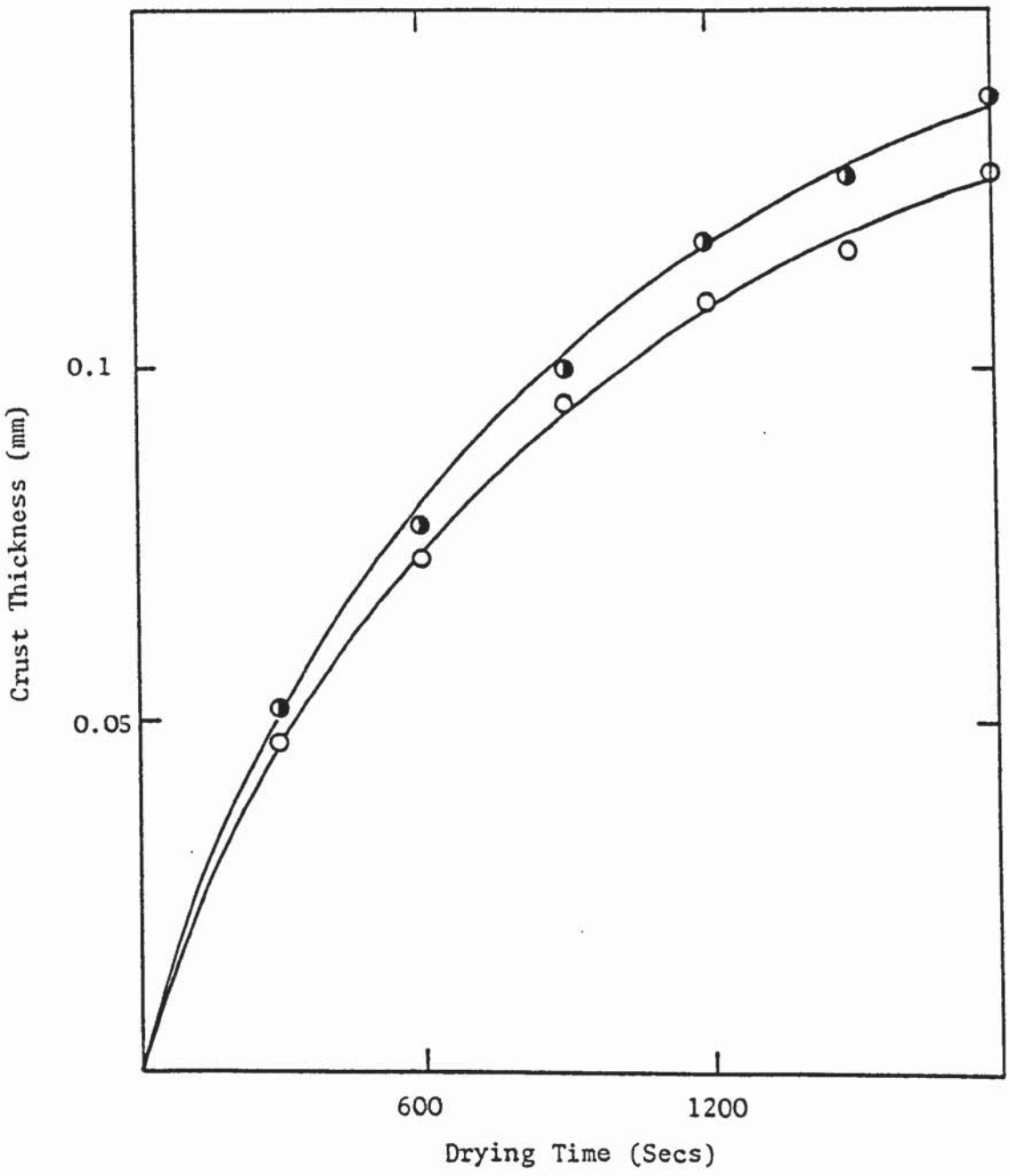

Figure 9.16 Effect of Air Velocity on Sodium Sulphate Decahydrate Crust Thickness.

Air Velocity $m.s^{-1}$

—○—○— 0.621

—◑—◑— 1.178

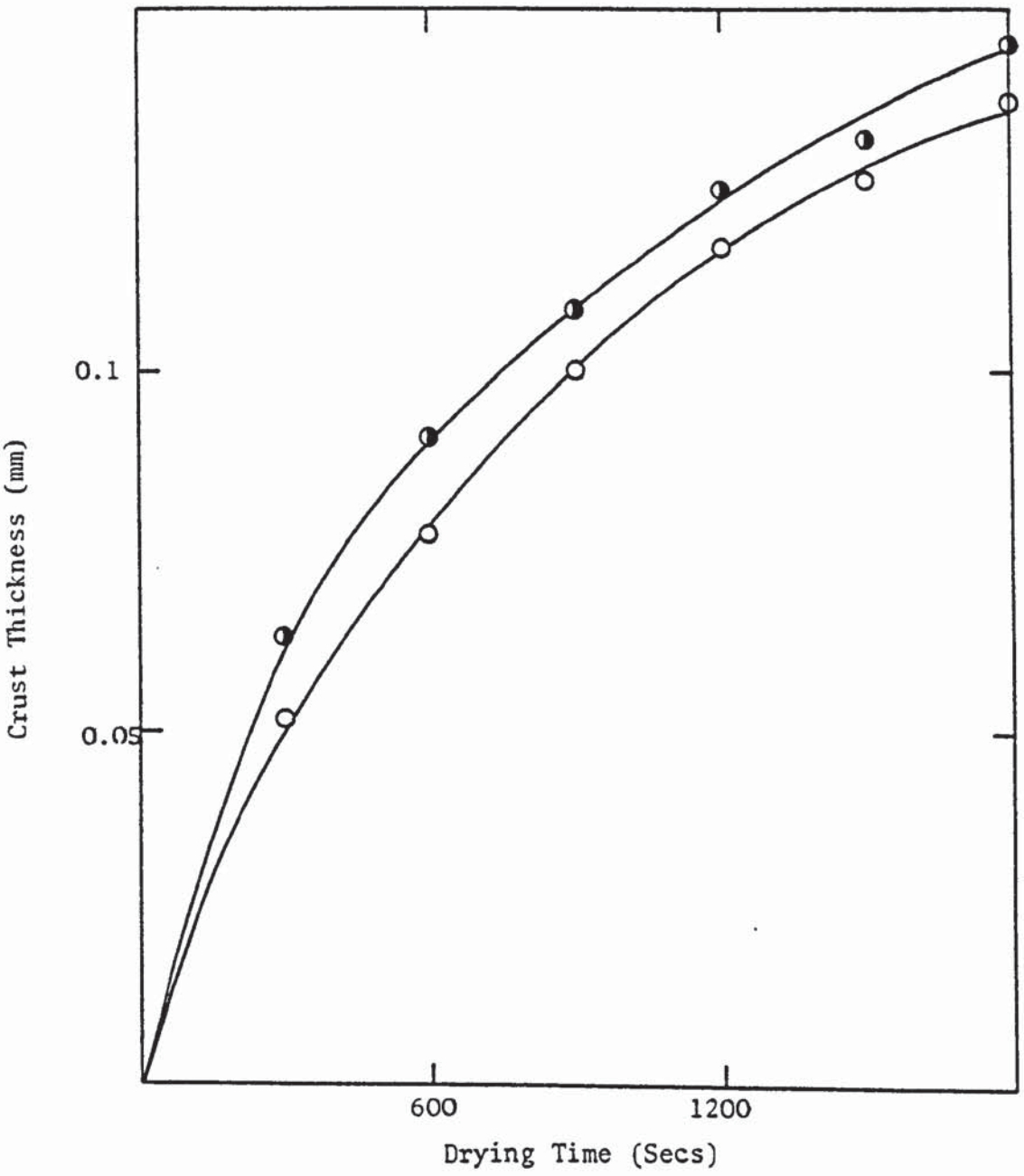

Figure 9.17 Effect of Moisture Content on Sodium Sulphate Decahydrate Crust Thickness.

Solution Solids Content wt/wt

50%

60%

Table 9.1

Maximum Evaporation Rates and Moisture Contents After 10 Seconds for Drops of Organic Paste A Slurries.

T_a = 200°C

% Solids Content wt/wt	Additive Solution %	Maximum Evaporation Rate $gm.s^{-1}.cm^{-2} \times 10^{-3}$	Corresponding Moisture Content After 10 Seconds
12	Dispersol	3.3	82.5%
15	Sodium Chloride	2.9	79.4%
15	Dispersol	2.6	80.2%
18	Dispersol	2.4	75.0%

Table 9.2

Maximum Evaporation Rates and Moisutre Contents After 10 Seconds for Drops of Organic Paste B Slurries.

T_a = 200°C

% Solids Content wt/wt	Additive Solution %	Maximum Evaporation Rate $gm.s^{-1}.cm^{-2} \times 10^{-3}$	Corresponding Moisture Content After 10 Seconds
12	Dispersol	3.8	67.6%
15	Sodium Chloride	3.7	64.1%
15	Dispersol	3.6	67.4%
18	Dispersol	2.1	65.7%

Table 9.3

Maximum Evaporation Rates and Moisture Contents After 10 Seconds for Inorganic Powder C Solutions.

% Solids Content wt/wt	T_a °C	Maximum Evaporation Rate $gm.s^{-1}.cm^{-2} \times 10^{-3}$	Corresponding Moisture Content After 10 Seconds
40	110	1.4	59.4%
40	130	1.5	59.1%
50	130	1.1	49.4%
60	130	1.0	39.6%
70	130	0.4	29.8%

Table 9.4

Maximum Evaporation Rates and Moisture Conents After 10 Seconds 25% wt/wt Solids Inorganic Powder D Solution.

T_a °C	Maximum Evaporation Rate $gm.s^{-1}.cm^{-2} \times 10^{-3}$	Corresponding Moisture Content After 10 Seconds
34	0.4	74.8%
64	3.0	73.9%
93	3.3	73.8%
130	5.6	73.0%
165	6.6	72.6%
200	11.5	70.5%

Table 9.5 Maximum Evaporation Rates and Moisture Contents After 10 Seconds 25% wt/wt Solids Inorganic Powder E Solution.

T_a °C	Maximum Evaporation Rate $gm.s^{-1}.cm^{-2} \times 10^{-3}$	Corresponding Moisture Content After 10 Seconds
34	0.6	74.7%
64	2.3	74.2%
93	4.1	73.5%
130	7.4	72.2%
165	10.4	70.9%
200	11.4	70.4%

Table 9.6 Comparison Between Measured and Calculated Crust Thickness of $Na_2SO_4.10H_2O$ Solution

ϕ Measured mm x 10^{-2}	ϕ Calculated mm x 10^{-2}
4.8	5.4
6.4	7.3
9.1	10.8
10.1	11.5
11.0	12.4
11.6	13.6
6.2	7.2
9.1	10.5
10.8	12.7
12.5	14.2
13.2	15.6
14.6	16.3
5.2	6.1
7.8	8.9
10.0	11.4
11.7	13.5
12.6	14.3
13.9	16.1
4.7	5.5
7.3	8.3
9.5	10.9
10.9	12.8
11.6	13.2
12.7	14.3

One set of data are plotted in Figure 9.18

Table 9.7

Crust Thickness Measurement for Slurry Droplet of 18% wt/wt Organic Paste Formulation A. T_a = 200°C

θ s	ϕ mm $10x^{-2}$
120	18.8
240	15.7
360	13.5
480	10.9
600	10.0
900	10.0

This data are plotted in Figure 9.17a

Table 9.8

Porosity Estimates for Organic Paste Formulation A Crusts

% Solids Content wt/wt	T_a °C	ε x 10^{-1}
18 + Dispersol	200	1.7
15 + Dispersol	200	1.9
15 + Sodium Chloride Solution	200	2.2
12 + Dispersol	200	2.5

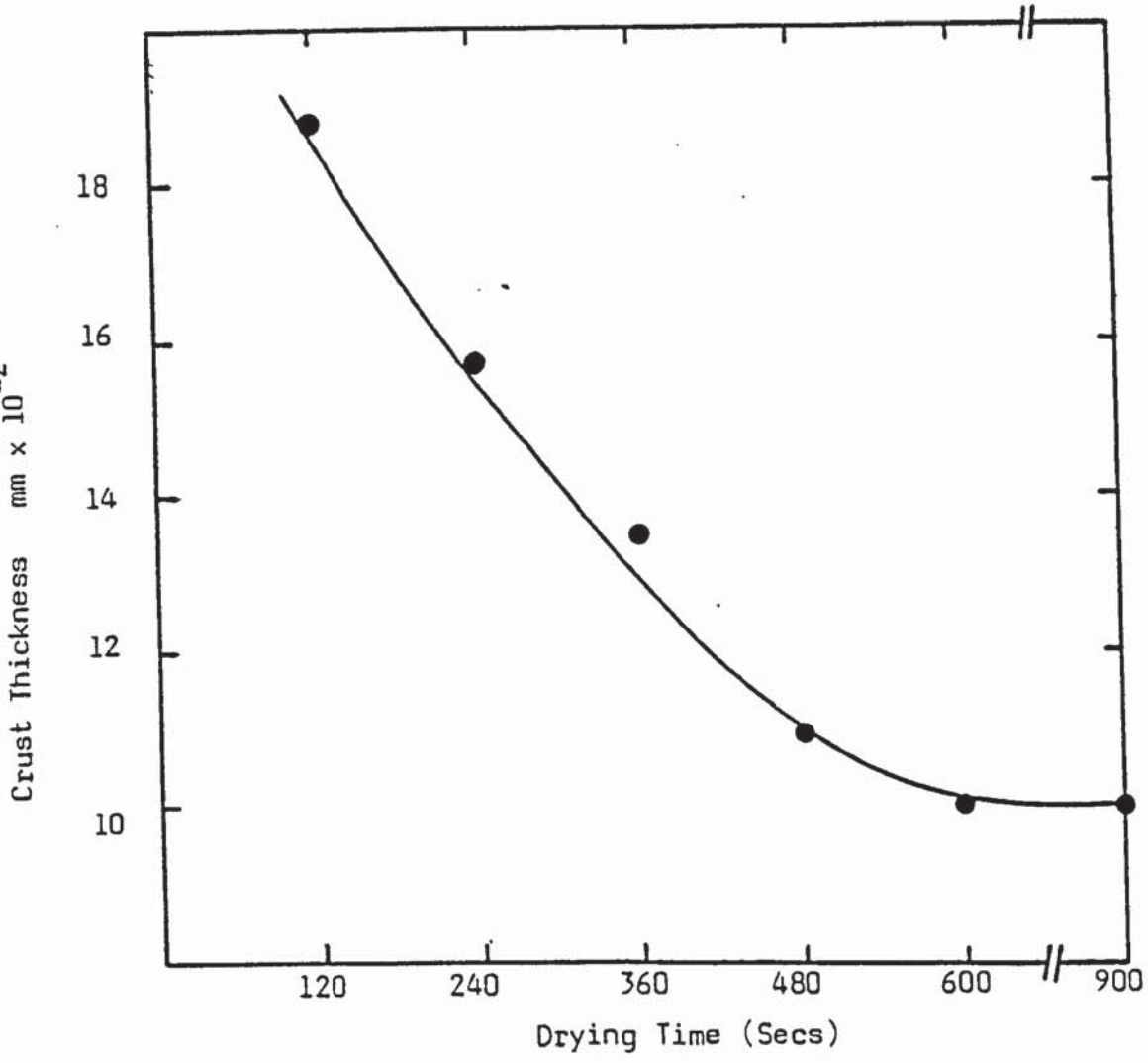

Figure 9.17a Plot of Crust Thickness -v- Time For Drop of 18% wt/wt Organic Paste Slurry Formulation A at T_a = 200°C.

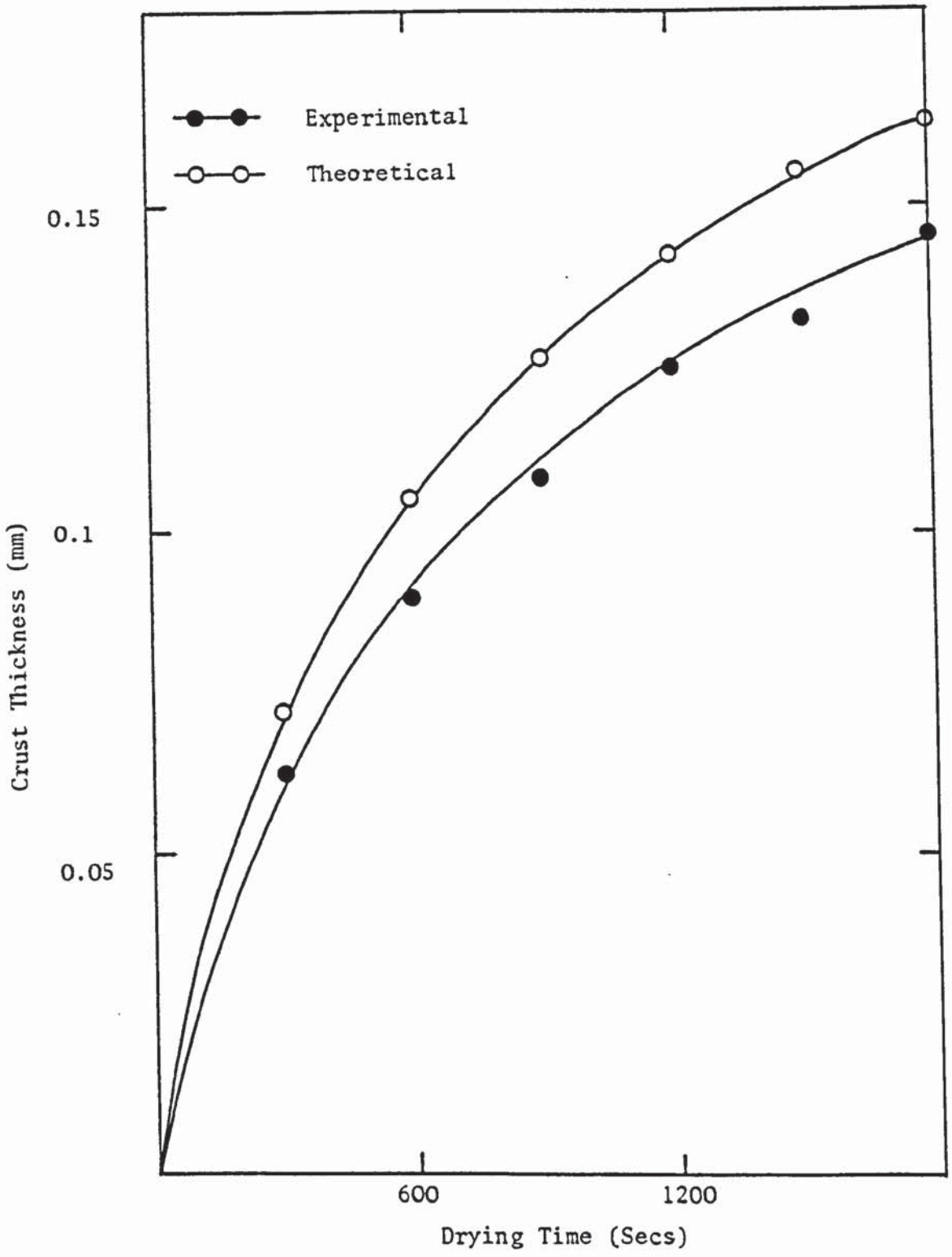

Figure 9.18 Comparison Between Measured and Calculated Crust Thickness.

Table 9.9

Porosity Estimates for Inorganic Powder Formulation C Crusts

% Solids Content wt/wt	T_a °C	ε
40	110	0.5
40	130	0.6
50	130	0.3
60	130	0.3

Table 9.10

Porosity Estimates for Sodium Sulphate Decahydrate Crusts

% Solids Content wt/wt	T_a °C	ε
50	20	0.2
60	20	0.1
50	60	0.2
60	60	0.2
50	100	0.3
60	100	0.2
50	120	0.3
60	120	0.3

velocity. As expected it decreased almost linearly with increase in crust thickness (Figure 9.19). Figure 9.20 shows the decrease of overall mass transfer with increase in drop diameter. Crust mass transfer coefficients for different crusts are tabulated in Table 9.11.

Experimental mass transfer coefficients were calculated from a modfiied form of equation 5.11;

$$K_E = \frac{G.\Delta H}{A} \cdot \frac{R_c}{M_w} \cdot \frac{Ti}{p_s - p}$$

where k_g was replaced by K_E, and

$A = 2\pi (R^2 - (R-\psi)^2)/\varepsilon$ is the area for mass transfer.

Theoretical mass transfer coefficients were estimated from equation 5.26 after substituting from equation 5.27 for the value of the crust coefficient k_c. Thus,

$$\frac{1}{K_T} = \frac{1}{k_g} + \frac{\psi}{D_v \varepsilon^{1.5}}$$

where K_T is the theoretical mass transfer coefficient; and k_g is the gas film mass transfer coefficient estimated from the proposed correlation for pure water drops, equation 8.5. Table 9.12 includes both the theoretical and experimental mass transfer coefficients for drops of solution and slurries of different materials.

Crust mass transfer coefficients were calculated from equation 5.27 for each specific material, of which 8 different materials were used for drying studies, porosity estimations and mass transfer coefficient. However, crust mass transfer coefficient was calculated only for three products, covering a range of temperatures from 100°C to 200°C and solids content between 12% to 60%. The other materials used were found to form either a non-hollow, impervious crust (and sometimes brittle), or a crust containing many cracks. Recovery of these types of crust for further study proved very difficult; thus it was not possible to calculate crust mass transfer coefficients. Table 9.11 shows values of k_c from equation 5.27 denoted by the sign (*) and values

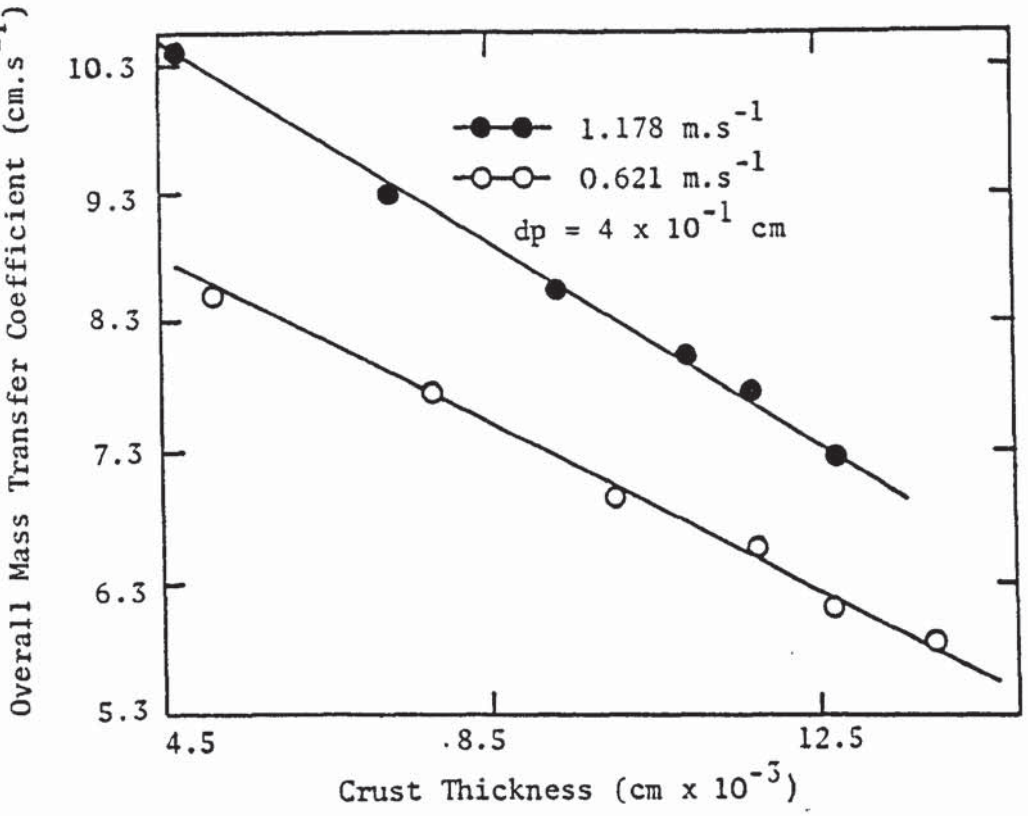

Figure 9.19 Plot of Overall Mass Transfer Coefficient Against Crust Thickness for 50% wt/wt Drops of Sodium Sulphate Decahydrate at 120°C.

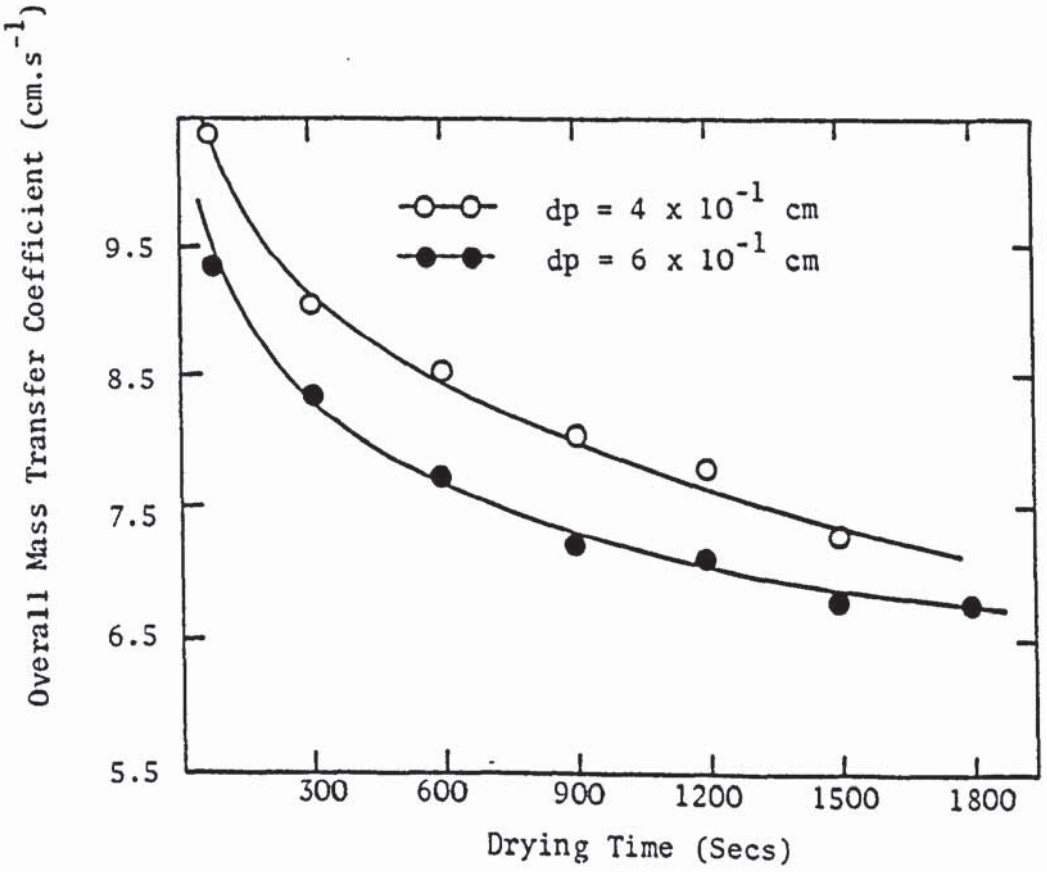

Figure 9.20 Plot of Overall Mass Transfer Coefficient Against Drying Time for 50% wt/wt Drops of Sodium Sulphate Decahydrate at 120°C and 1.178 m.s^{-1}.

Table 9.11

Values of Crust Mass Transfer Coefficient

Nature of Solids Forming Crust	% Solids Content wt/wt	T_a °C	k_c (*) cm.s^{-1}	k(**) cm.s^{-1}
Organic Paste B Formulation A	18 + Dispersol	200	4.1	5.9
	15 + Dispersol		5.8	5.8
	15 + Sodium Chloride		7.2	11.1
	12 + Dispersol		10.1	12.5
Inorganic Powder Formulation C	40	110	14.4	12.8
	40	130	16.3	12.7
	50	130	5.9	12.9
	60	130	4.5	13.3
Sodium Sulphate Decahydrate	50	100	6.9	6.2
	60	100	4.6	5.8
	50	120	6.5	4.3
	60	120	4.5	3,4

* = Predicted from Equation 5.27
** = Experimental

Table 9.12

Experimental and Theoretical Mass Transfer Coefficient

wt % Solids Content	K_E	K_T
18% Organic Paste Slurry A	2.3	2.2
15% Organic Paste Slurry A	2.2	2.6
15% Organic Paste Slurry A with Soduium Chloride	2.5	2.7
12% Organic Paste Slurry A	2.7	3.0
40% Inorganic Powder C Solution at 110°C	4.4	3.9
40% Inorganic Powder C Solution at 130°C	4.0	4.4
50% Inorganic Powder C Solution at 130°C	4.1	3.9
60% Inorganic Powder C Solution at 130°C	4.3	4.5
50% Sodium Sulphate Decahydrate Solution at 100°C	9.9	9.6
60% Sodium Sulphate Decahydrate Solution at 100°C	7.9	8.1
50% Sodium Sulphate Decahydrate Solution at 120°C	9.5	9.5
60% Sodium Sulphate Decahydrate Solution at 120°C	7.9	7.8

calculated from the overall mass transfer coefficient and the evaporation rates of each specific material denoted (**). Good agreement has been found except for 50% and 60% wt/wt solids content of Inorganic Powder Formulation C. This is explained by the formation of a crust characterised as shown in Plate 9.7 and 9.15 by cracks, fractures and an undulating crust. The first two features represent additional areas for vapour release and the latter causes a variation in pore area. Consideration of Figure 9.10 shows that the maximum evaporation for a 40% wt/wt solids content of this material was 1.5×10^{-3} $gm.s^{-1}.cm^{-2}$ whilst for 50% and 60% wt/wt solids content it was 1.1×10^{-3} and 1.0×10^{-3} $gm.s^{-1}.cm^{-2}$ respectively. This, and crust structure in the electron microphotographs, suggest that there is indeed a different crust formation at 50% compared with 60% wt/wt solids.

As evaporation from a drop proceeds a thin film starts to form followed by visible solid formation at some point; this solid deposition continues to form a complete crust. The crust structure depends on the nature of the solid content and the experimental conditions.

A unique observation was made during the drying of Organic Pigment B. This material formed a non-porous skin, or 'membrane' at an early stage i.e. after 8 seconds; this acted as an additional barrier to mass transfer so that the interior core remained 'wet' even for a drop left suspended on the nozzle for 1 hour. Hence in this case the overall mass transfer coefficient (equation 5.26) should contain a term to include for the resistance to mass transfer due to this primary film. Normally for drops that form only a crust, during the initial stage the gas film around the drop controls the mass transfer rate. Once the crust starts to form its resistance becomes controlling. However for the case when a skin forms the overall mass transfer coefficient prior to crust formation should include another term for skin mass transfer coefficient (k_s), thus,

$$\frac{1}{K_o} = \frac{1}{k_g} + \frac{1}{k_s} \qquad (9.1)$$

The overall mass transfer coefficient for such a drop once the crust formed reverts to equation 5.26.

$$\frac{1}{K_o} = \frac{1}{H_l k_g} + \frac{1}{k_c} \qquad (9.2)$$

since the outer surface is, by definition, solid and not a film.

The driving force for mass transfer once a crust is formed is the concentration gradient. At the earlier stage with a skin the driving force is the difference in vapour pressure just beneath the skin and outside. To increase the evaporation rate prior to crust formation in this specific case the following considerations might be applicable.

1. Additives may be used to affect the skin structure and give a porous membrane.
2. Increase the vapour pressure across the skin, this could be achieved by;
   (i) Use of air of reduced humidity
   (ii) Application of vacuum in conjunction with heat transfer by radiation, or with the feed initially heated then sprayed.
3. Application of micro-wave drying which might also induce turbulence within the drops.

In all cases with free-flight drops it was found that the underside face of the drop formed a solid crust whilst the topside remained initially in a liquid form, i.e. a combination of mass transfer mechanisms is involved, until a crust also covers the top face.

9.4 Film Resistance Prior to Crust Formation

At low temperatures transfer of moisture is by diffusion through the film, since the steady hemispherical profile (Plate 9.11) suggests that intermittent film rupture and reformation is not involved. The material (Organic Pigment B) which exhibited film formation also formed a crust with a smooth outer surface; this would be expected since the crust initially grows inwards from a smooth film. All other materials produced crusts

with a rough, or crystalline, outer surface.

The above phenomena, i.e. skin formation may be described by analogy to transport coefficients in membranes. Considering the transport of solvent A across a membrane the diffusional flux can be expressed as,

$$N_A = \frac{D_A}{x} (C_A - C_{Ax}) \qquad (9.3)$$

where D_A = diffusion coefficient.

x = membrane thickness.

The diffusion coefficient can be readily determined if values of N_A, C_{Ao}, C_{Ax} and x are available for a given process. Although the concentration of A on the surface of the membrane will be unknown this can be replaced by the partial pressure of A on either side of the membrane. Hence equation 9.3 becomes,

$$N_A = \frac{P_M}{x} (P_i - P_o) \qquad (9.4)$$

where P_M = permeability

p_i = partial pressure beneath the membrane

p_o = partial pressure outside the membrane

In the case of drying of droplets forming a skin p_i, prior to crust formation, will approximate to the vapour pressure at the wet-bulb temperature, albeit depressed as described in Chapter 4; p_o is the vapour pressure in the surrounding atmosphere at the known air temperature T_a; N_A can be measured experimentally. Hence P_M/x can be calculated and would represent the skin mass transfer coefficient.

In practical spray drying processes, materials that form films i.e. a 'skin' during drying tend to produce products that might stick together which is undesirable. Conversely particles which impinge on the chamber wall prior to 'dryness' may not

adhere due to them bouncing. On the other hand materials which do not form a skin during drying form non-sticking products but may adhere to the chamber wall on impingement.

Comparison of Figures 9.4 and 9.5, for which both pigments had the same initial solids-content, shows that the evaporation rate of Organic Pigment B prior to crust formation is 30% < Organic Pigment A at an identical air temperature. Hence from equation 9.1, the film represents 30% of the resistance to mass transfer prior to crust formation.

9.5 Drop Core Temperature Measurements

A series of observations were made on individual suspended drops of solutions and slurries of different chemicals covering a range of solids content (22 to 40%) and air temperature (34 to 220°C). Tables 9.13 to 9.16 represent visual and photographic observations of single suspended drops and the crust formed in a specific drying time. Core temperature measurements show that the history depends on the nature of the solid.

Figure 9.21 shows the core temperature history of sodium sulphate decahydrate drops at air temperatures of 20, 40, 60 and 79°C respectively with a constant air flow of 1 $ms.^{-1}$. At an air temperature of 20°C there was an initial transient period in the core temperature history curve before equilibrium was established and the core temperature reduced to the wet-bulb temperature. The core temperature then rose steadily as the resistance to heat and mass transfer increased with crust thickness. The core temperature histories at T_a = 40, 60 and 79°C were quite different to that at T_a = 20°C. At the higher air temperatures the core temperature rose gradually, followed by a period of nearly constant core temperature; the time for this period depends on the air temperature as shown in Figure 9.21. This phenomenon was caused by the fact that decahydrate crystals melt at 33°C, abosrbing heat in the process; the latent heat of fusion is + 2.39 kJ kg^{-1} (133, 134). The higher the air temperature the smaller this nearly -

Table 9.13 Observations of Single Suspended Droplets Behaviour-Organic Pigment A Solution 22% wt/wt.

T_a °C	Observations
100	Solid hemispherical crust formed, external appearance rough.
135	As above, but external crust appeared smooth.
160	The suspended drop tended to deform after about 240 seconds. Deformation increased and a protrusion formed from the side.
200	Drop deformation commenced at $<$180 seconds (i.e. earlier than at 160°C). Rough crust formed due to vigorous internal boiling and 'explosion'. This is illustrated in Plate 9.10.

Table 9.14 Observations of Single Suspended Droplets Behaviour-Organic Pigment B Solution 22% wt/wt.

T_a °C	θ s	Observations
100	2400	Drop formed a non-permeable skin initially which acted to resist mass transfer. Evaporation therefore very slow and extended drying-period required.
135	2400	Similar phenomena as at 100°C
165	900	Skin formation as above. Drop extended longitudinally as in Plate 9.11, before 'exploding'.
135	900	An aerated drop was suspended for comparison purposes. Expansion (Plate 9.12) was similar to a non-aerated drop at 165°C. Hemispherical dried crust obtained prior to final expansion and 'explosion'.

Table 9.15

Observation of Single Suspended Droplets - Inorganic Powder Formulation C Solution 40% wt/wt.

T_a °C	Observations
265	Drops fell-away from nozzle after 15 seconds, on average
250	Drops exhibited vigorous internal boiling. Most did not remain suspended for > 80 seconds. Some remained for > 120 seconds.
240) 230)	Similar observations to above but with suspension time < 106 seconds.
220	Drops remained suspended until completely dry. Solid hemispherical crusts recoverable by slicing from the nozzle. Vigorous boiling occurred within drops at < 180 seconds; crusts expansion then occurred due to internal pressure build up.

Table 9.16

Observations of Single Suspended Droplets - Solutions of Inorganic Powders D and E 25% wt/wt.

T_a °C	Observations
34	D drops produced uniform hemispherical crust when completely dry. E drops dried to irregular shaped particles. Similar observations were noticed at air temperature of 64°C.
93	D drops produced slightly deformed, hemispherical crust when dried, while Inorganic Powder E drops dried to uniform hemispherical crust.
130	Inorganic Powder D drops produced uniform hemispherical crusts when completely dry, and Inorganic Powder E drops produced deformed hemispherical crusts.
165	Drops of Inorganic Powder D produced deformed crusts with some longitudinal elongation. On complete dryness each drop had a small hole in its side through which pressure had been released; a hollow deformed, hemispherical crust resulted. At this temperature the other drops of Inorganic Powder E dried to uniform, porous hemispherical crusts.
200	Each drop of Inorganic Powder D formed a hemispheriecal crust with an elongated branch from the side; this 'blowing out' phenomena is illustrated in Plate 9.13. Inorganic Powder E drops exhibited internal boiling and did not therefore remain suspended.

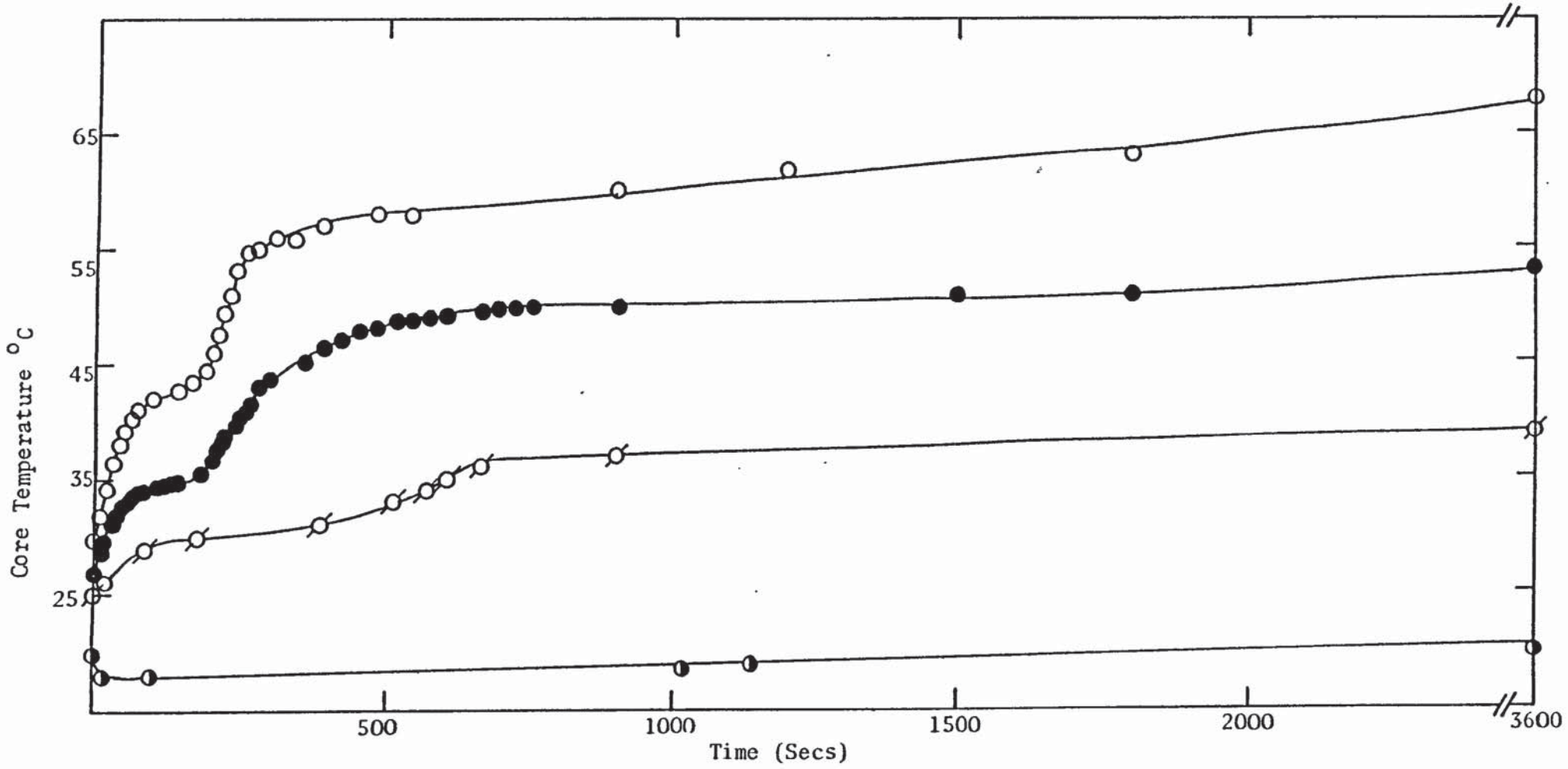

Figure 9.21 Core Temperature Profile of Sodium Sulphate Decahydrate Solution Drops

Air Temperature °C

20
40
60
79

constant core temperature period. Melting and recrystallisation occurs very rapidly and the crust starts to build-up; core temperatures then rose again. The general shape of the curves is in agreement with the data of Cheong (115) but the less-sophisticated, thermocouple technique did not detect the phase change so accurately.

Figure 9.22 illustrates core temperature histories for Inorganic Powder Solution C drops. At $T_a = 20^oC$ a similar core temperature history behaviour was found as for drops of sodium sulphate decahydrate. At $T_a = 40$, 61 and 79^oC a gradual increase in core temperature occurred due to crust growth and there was no constant core temperature period due to the absence of any melting process. This supports the theory regarding melting of sodium sulphate decahydrate crystals. A comparison of core temperature history for drops of decahydrate and Inorganic Powder Solution C is shown in Figure 9.23, for an air temperature of 79^oC.

9.6 Stereoscan Microphotographic, Optical Microphotographic, and Photographic Studies of Droplets and Crusts.

(The appropriate magnification of all electron microphotographs can be seen from the graticule reproduced in the left corner).

9.6.1 Suspended Drops

Experimental crust thickness measurements were carried out using an optical microscope or a Scanning Electron - microscope. Plate 9.1 illustrates microphotographs of a sodium sulphate decahydrate crust under optical (x 20) and scanning (x 50) microscopes. An optical microscope was used for the majority of crust thickness measurements.

Plate 9.2 illustrates a crust of sodium sulphate decahydrate dried from 50% wt/wt solids at $T_a = 60^oC$, and air velocities of 0.2 and 0.9 ms^{-1} respectively. At the lower velocity the crust was relatively smooth but at the higher air velocity the crust exhibited a distinct roughness and pores were present on the surface.

As described in Section 9.1 air temperatures had a greater effect on the

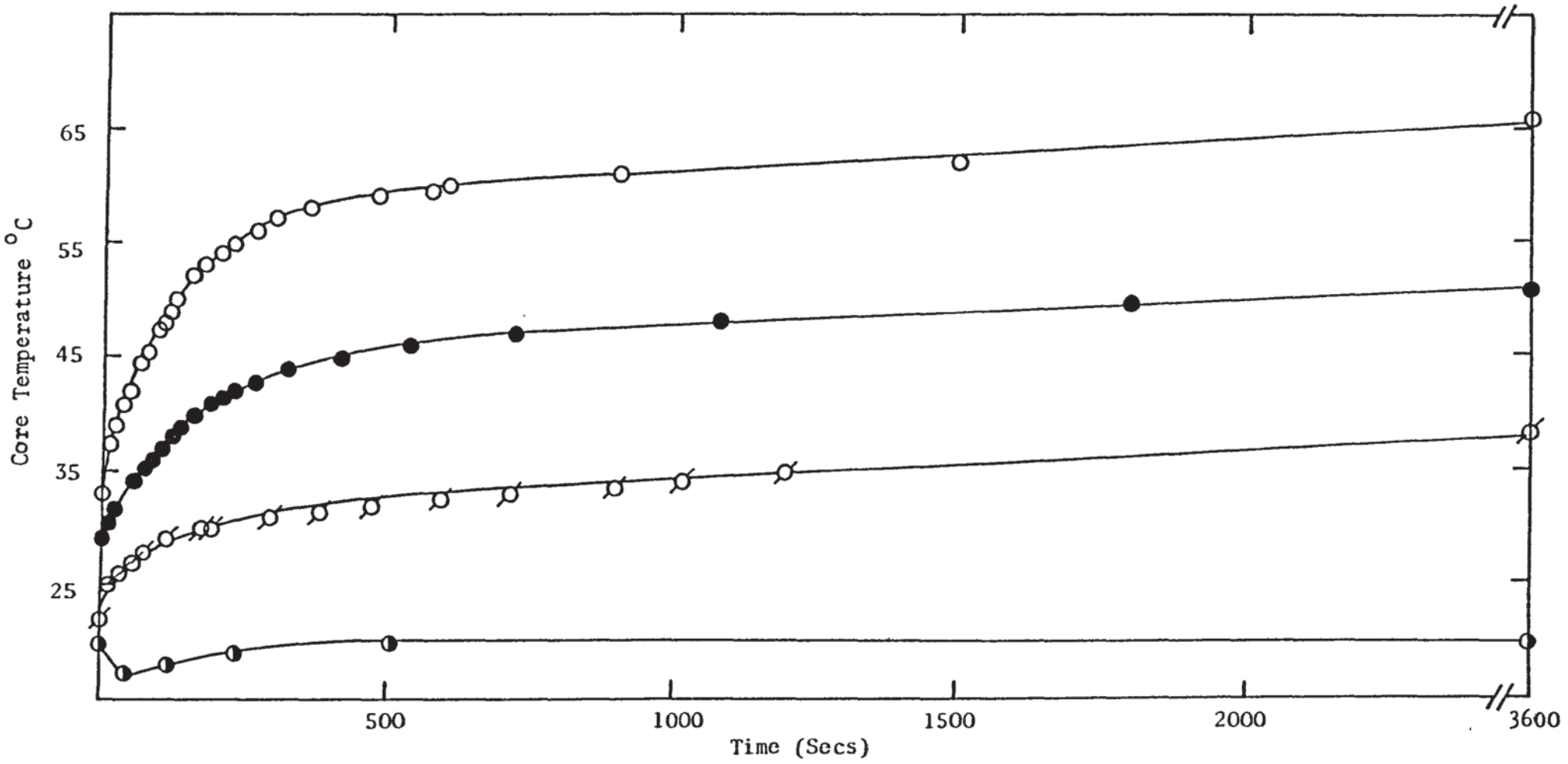

Figure 9.22 Core Temperature of Inorganic Powder Solution Drops

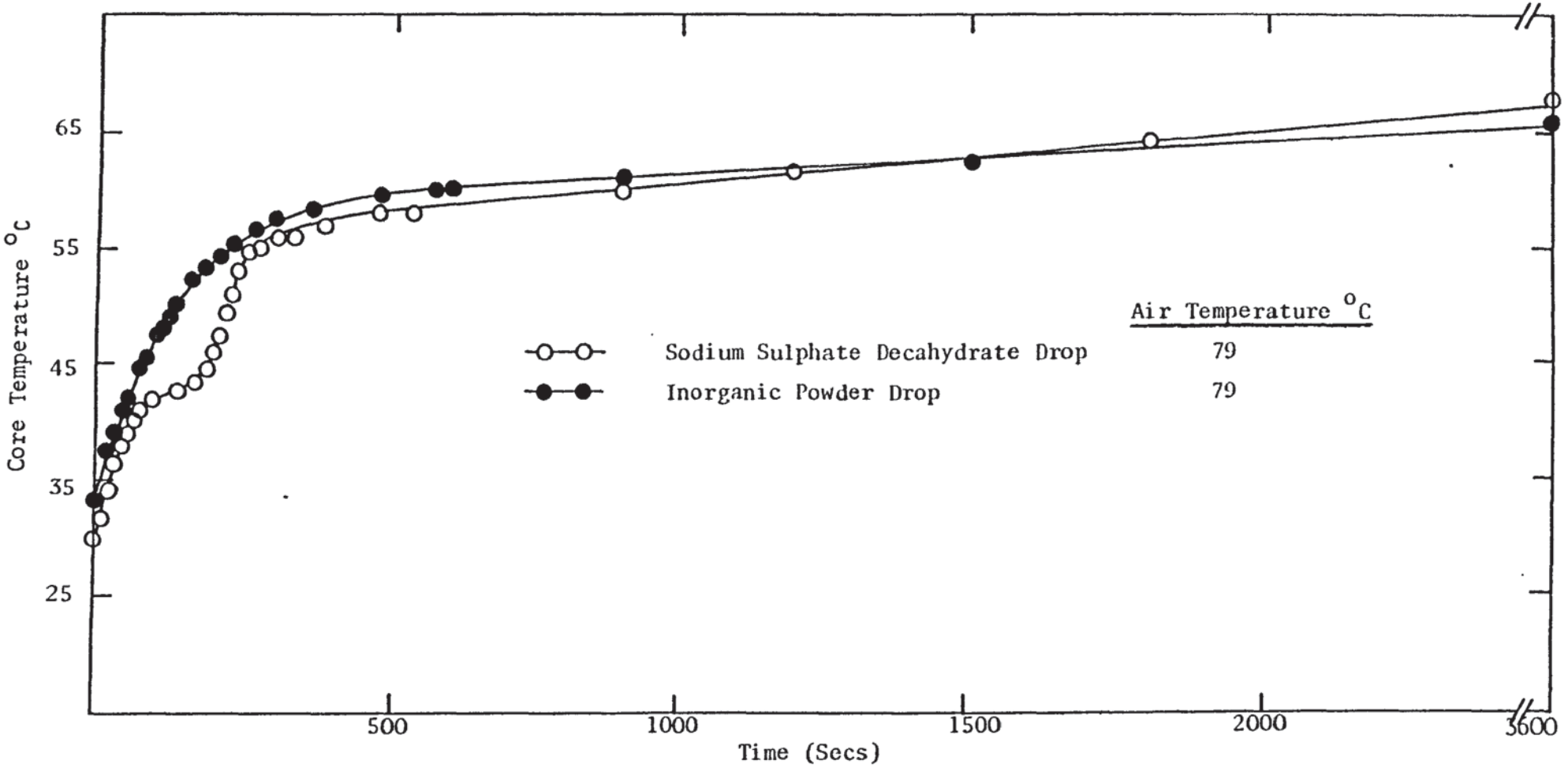

Figure 9.23 Drop Core Temperature Profile of Different Solids Nature Solution.

Plate 9.1

Sodium Sulphate Decahydrate Crust Thickness Measurements.

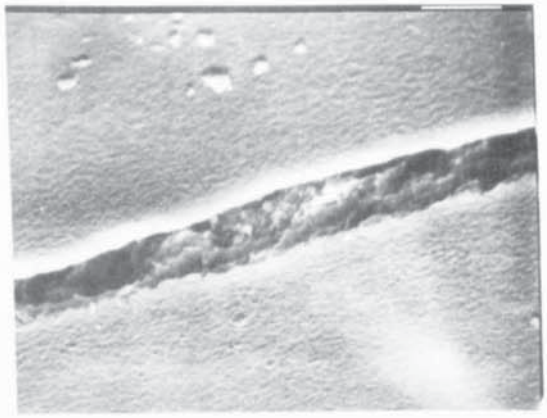

a. Scanning Electron Microscope

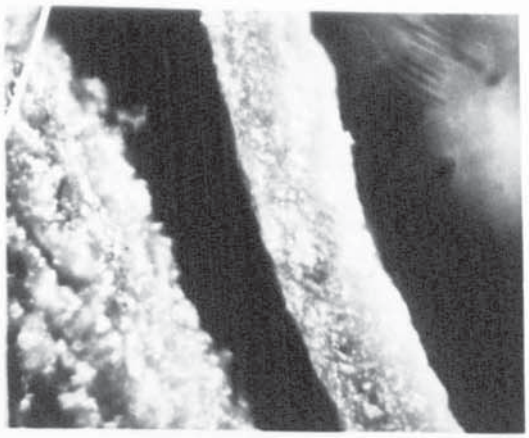

b. Optical Microscope

Plate 9.2

Electronmicrophotographs of Sodium Sulphate Decahydrate Crust Dried at Different Air Velocities

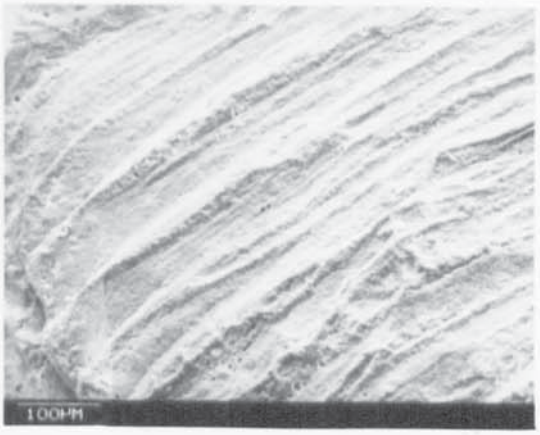

a. θ = 600s
v = 0.2 ms^{-1}

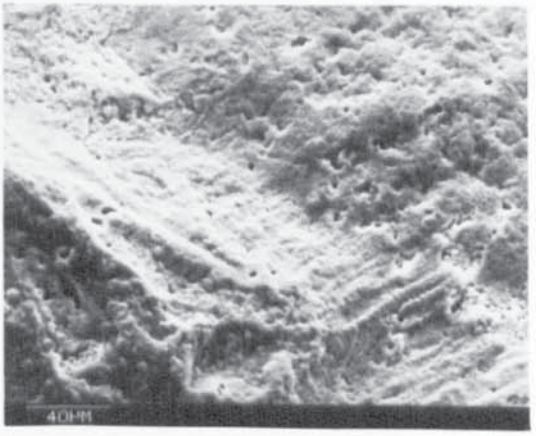

b. θ = 600s
v = 0.9 ms^{-1}

evaporation rate than the air flow rate. Electron microphotographs showed a wide range of crust structure, for example Plates 9.3 - 9.5 show crusts of different materials dried at air temperatures in the range 60°C to 200°C. These microphotographs illustrate how surface roughness tends to increase with air temperature, crystal formation (Plate 9.3b), and the increased appearance of cracks with increasing temperature. Such cracks may arise from internal pressure build-up which cannot be released via pores or 'case-hardening'.

Plate 9.6 represents the effect of the solid nature on the structure of the crust. The crust of Inorganic Powder Formulation E dried at 200°C was very porous, whilst that of Inorganic Powder D was rough with a major cracks. Other crusts shown in Plate 9.6c and d were very smooth with zig-zag cracks or many minor cracks.

The initials solid content was also found to affect crust structure and hence the rate of evaporation. Evaporation rates were reduced for drops containing a higher initial solid content. Plate 9.7 shows the surface of a crust dried from 60% wt/wt Inorganic Powder C; this was rough with an insignificant number of pores, whilst a crust from 70% wt/wt of the same material contained a few large holes. A hole just prior to blowing-up is shown in Plate 9.9; once such a hole was blown there was a sudden increase in the evaporation rate due to discharge of water vapour. This phenomena accounts for the higher points in Figures 9.11, 9.12 and 9.14.

Plate 9.8 shows the effect of additives on crust structure, and hence on the evaporation rate. As described in Section 9.1 the evaporation rate of a drop of Organic Paste A was lower than the same drop containing sodium chloride solution as additive. This observation is supported by the increase in porosity shown in Plate 9.8c and given in Table 9.8.

A series of photographs were taken of suspended drops of different products over a wide range of air temperatures. Plate 9.10 represents a drop of Organic Pigment A dried at 200°C. After a drying time of 140 seconds double protrusions started to form; this was a reproducible phenomenon under these conditions, and expansion of these double protrusions continued until, after nearly five minutes,

Plate 9.3

Electron Microphotographs of Sodium Sulphate Decahydrate Crusts Dried at Different Temperatures.
$v = 0.9\ ms^{-1}$

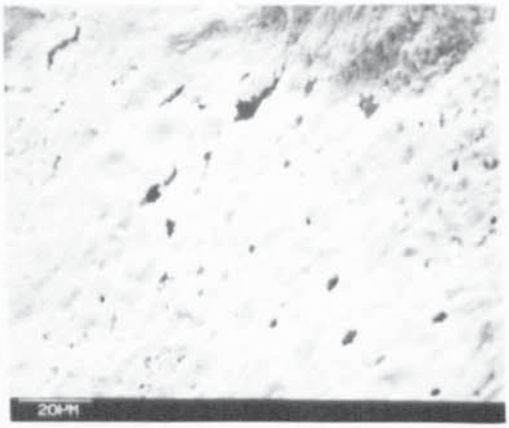

a. $T_a = 60^{\circ}C$
$\theta = 600s$

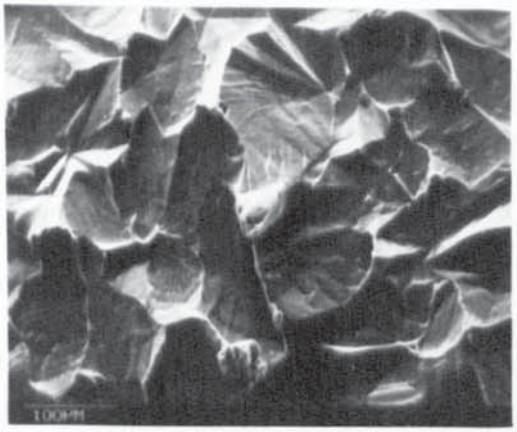

b. $T_a = 120^{\circ}C$
$\theta = 600s$

Plate 9.4

Electron Microphotographs of Inorganic Powder Formulation C Crusts Dried at Different Air Temperatures.

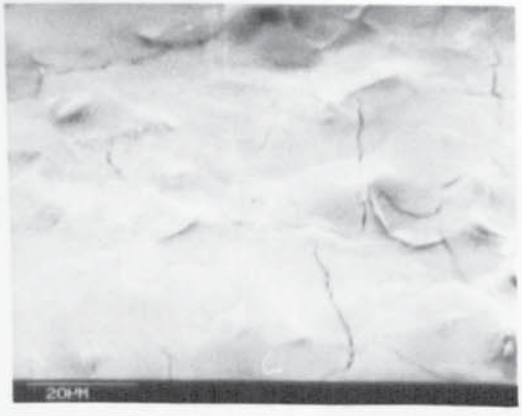

a. $T_a = 110^{\circ}C$
$\theta = 900s$

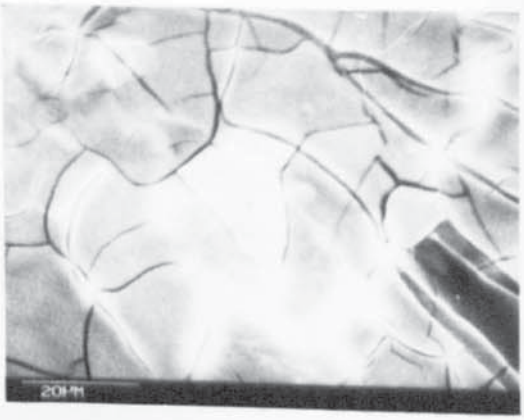

b. $T_a = 130^{\circ}C$
$\theta = 900s$

Plate 9.5

Electron Microphotographs Showing the Effect of Temperature on Internal and External Crust Structure of Drops of Inorganic Powder Formulation D.

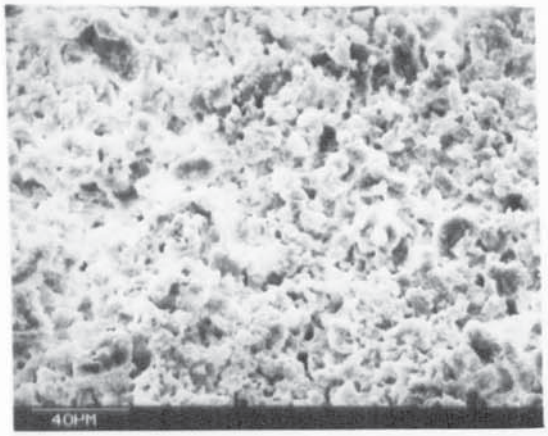

Internal
$T_a = 64^{o}C$

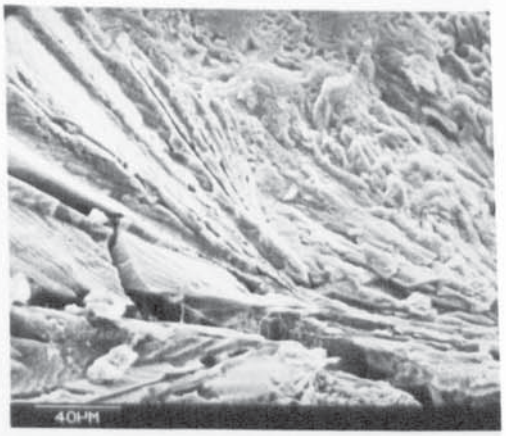

Internal
$T_a = 130^{o}C$

External
$T_a = 64^{o}C$

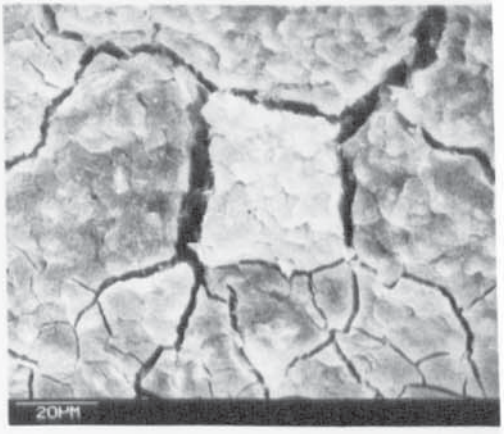

External
$T_a = 130^{o}C$

Plate 9.6

Electron Microphotographs Showing the Effect
Of Solid Nature on the Crust Structure.

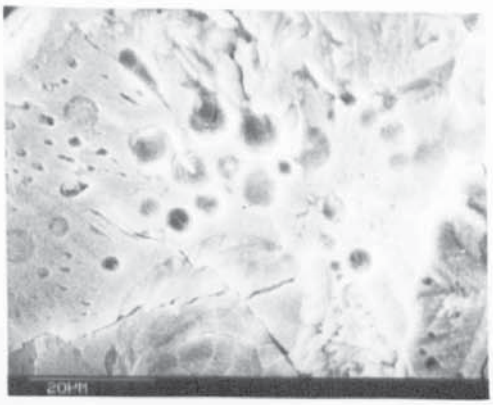

a. Crust of Inorganic Powder Formulation E

T_a = 200°C

θ = 300s

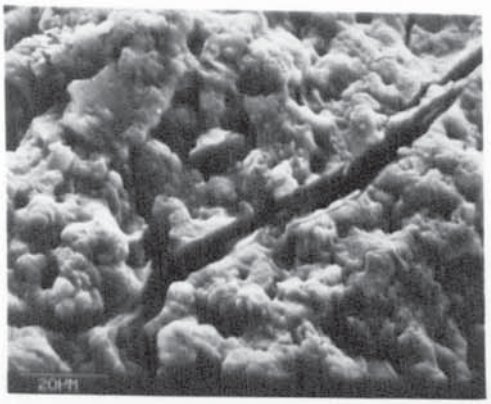

b. Crust of Inorganic Powder Formulation D

T_a = 200°C

θ = 300s

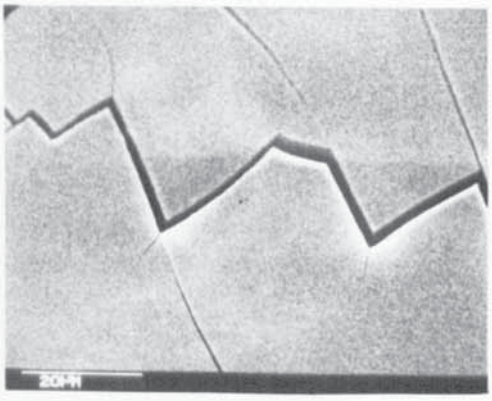

c. Crust of Organic Pigment B

T_a = 130°C

θ = 2400s

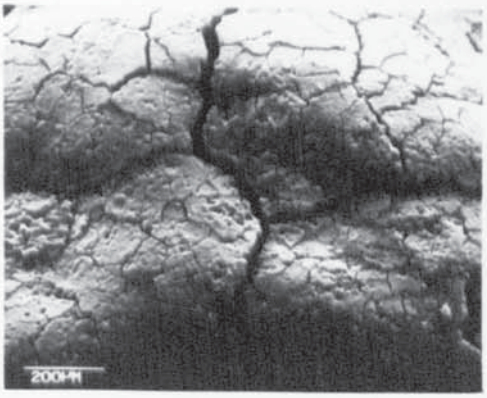

d. Crust of Organic Pigment A

T_a = 130°C

θ = 480s

Plate 9.7

Electron Microphotographs Showing the Effect of Solid Content On The Crust Structure of Inorganic Powder Formulation C.

$T_a = 130^{o}C$; $\theta = 1800s$

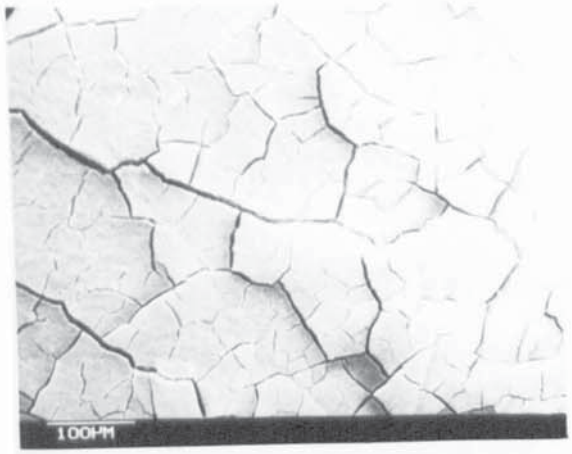

a. C_1 = 60% wt/wt

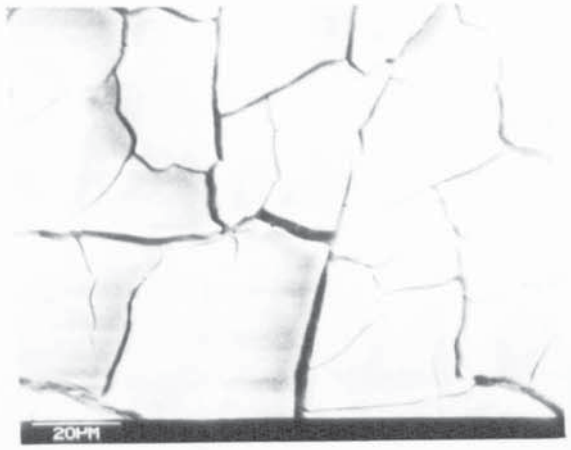

b. C_1 = 60% wt/wt

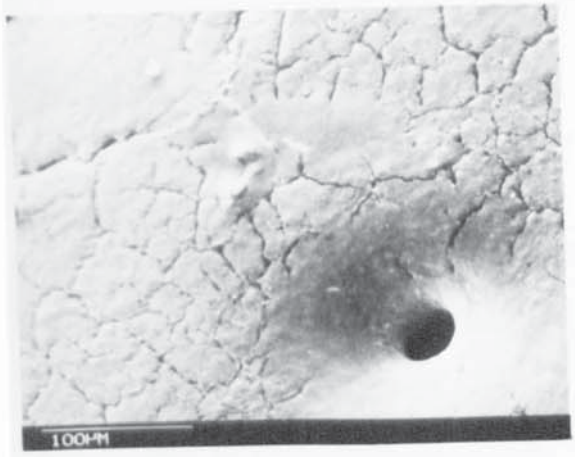

c. C_1 = 70% wt/wt

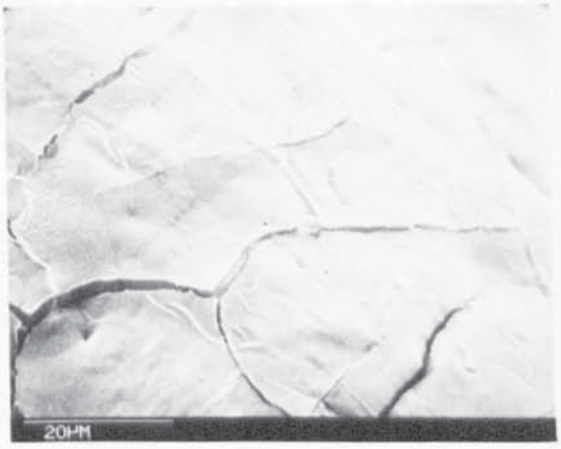

d. C_1 = 70% wt/wt

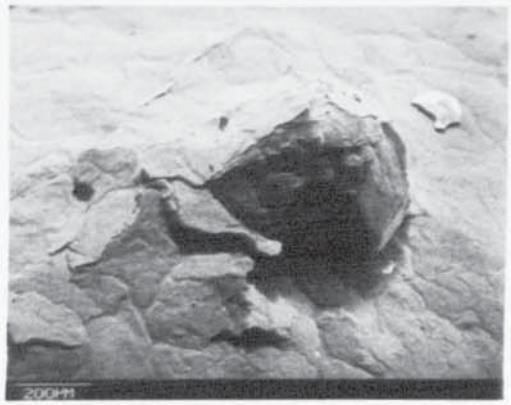

Plate 9.9

Crust of Inorganic Powder Formulation E Showing initiation of a Blow Hole Prior to 'Exploding'.

$T_a = 93^{\circ}C$

$\theta = 600s$

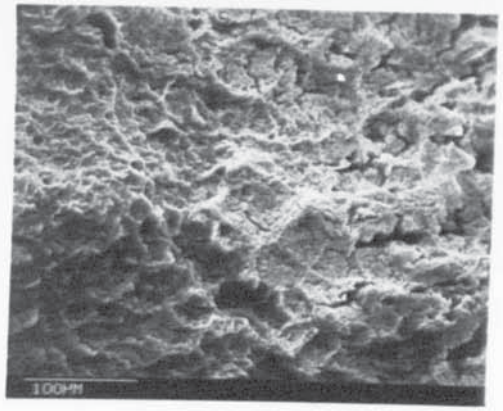

b

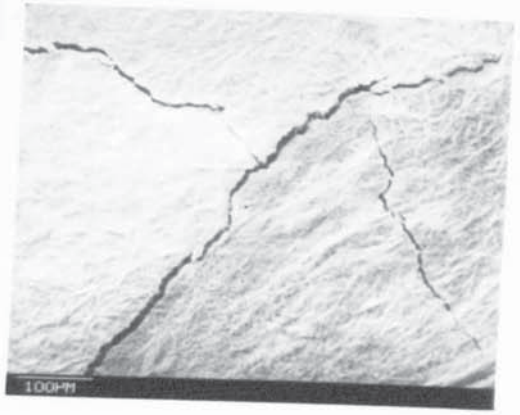

a

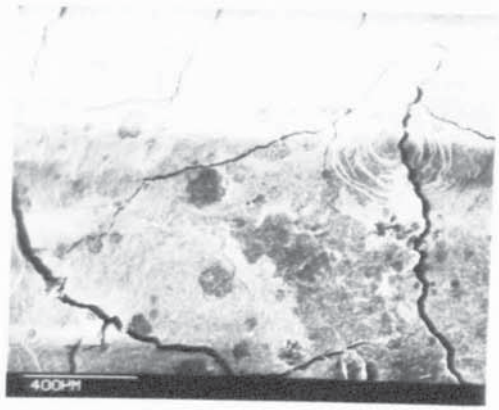

c

Plate 9.8

Electron microphotographs Showing the Effect of Additives on Crust Structure of Organic Paste A Slurry Drop Containing 12% wt/wt.

$T_a = 200^{\circ}C$; $\theta = 900s$.

a - No additive
b - 13% Dispersol Additive
c - 13% NaCl Solution.

Plate 9.10

Photographs of Drops of Organic Pigment A. $T_a = 200^{\circ}C$

Deformation Involving Two Protrusions Followed By Reformation After 'Exploding'

θ = 140s

θ = 190s

θ = 250s

θ = 300s

θ = 330s

θ = 390s

they joined together following 'explosion'. The crust then reformed and further 'explosions' followed. The crust rebuilt after explosions finally expanded and produced a 'rough' crust. Such crusts were thinner than usual (e.g. by a factor of 8) due to expansion and solids loss in explosions.

Another mechanism of expansion of the crust was observed when a drop of Organic Pigment B dried at 165°C; the drop deformation profile is illustrated in Plate 9.11. The drop deformed within 30 seconds of introduction into the tunnel; the longitudinal expansion increased with time and was followed by 'exploding'. This phenomenon was obviously related to the film-formation already discussed.

An aerated drop of Organic Pigment B was also followed photographically as shown in Plate 9.12. The same type of expansion was demonstrated as for a non-aerated drop (Plate 9.11) except that the aerated drop expanded symmetrically. However, the final shapes of the exploded crusts (Plates 9.11 and 9.12) was similar after a drying time of 15 minutes.

Plate 9.13 illustrates the profile of suspended drop of Inorganic Powder D at 200°C. In this case a drop formed a hemispherical crust with an elongated branch from the side. These visual observations were sometimes repeated 3 or 4 times for each specific drop, and good reproducibility was obtained.

To sum up, several different modes of solid formation were observed,

1. Formation of a porous crust with cracks;
2. Formation of a crystalline crust;
3. Formation of an expanded, or contracted, crust with either longitudinal-deformation or protrusions-formation; or
4. In specific cases as soon as a drop was introduced into the drying gas a skin, or membrane, formed. This acted to resist mass transfer.

Unlike in modes 1 to 3 crust growth formation appeared not to be localised. The consequence of film formation and the different crust growth mechanism was a relatively slow drying rate.

Due to crust, or skin, formation the resistance to mass transfer increases

Plate 9.11

Photographs of Drops of Organic Pigment B. $T_a = 165^{\circ}C$

Longitudinal Deformation

θ = 30s

θ = 180s

θ = 360s

θ = 420s

θ = 720s

θ = 900s

Plate 9.12

Photographs of Aerated Drop of Organic Pigment B

$T_a = 135^{o}C$

Symmetrical Expansion Prior to Elongation.

θ = 300s

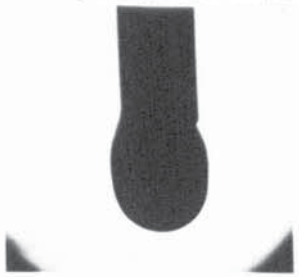

θ = 480s

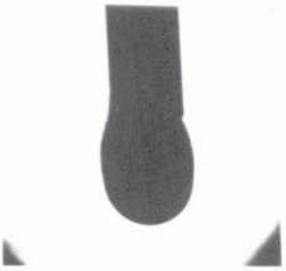

θ = 600s

θ = 900s

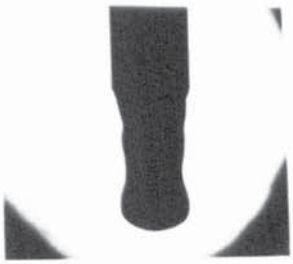

Plate 9.13

Photographs Showing Profile of Drop of Inorganic Powder D

$T_a = 200^{o}C$

θ = 185s

θ = 104s

θ = 137s

θ = 190s

with time. Pressure build-up inside the drop may then result in either cracks or hole-blowing, or sometimes in drop expansion. In a few cases crust contraction was observed when a brittle crust formed containing many cracks.

In the case of free-flight drops, and for pure liquid drops, the shape of each drop tended to be spheroidal rather than spherical. That is, the bottom was flattened due to the force of the rising air-flow whilst the top face was under reduced pressure and therefore maintained its spherical shape.

9.6.2 Free-Flight Drops

For drops in free-flight the equivalent diameters were measured by the techniques already described in Chapter 7

All drops containing solids behaved like pure liquid drops before crust formation, i.e they were stable and remained in a specific zone in the working section. Once the crust started to form there was a high degree of oscillation and deformation and it became difficult to retain the drop in the working-section. It tended to either hit the wall or be carried away with the air. However, after the crust had been formed completely the particle exhibited a high degree of stability. There was no deformation but some were spinning whilst others simply 'floated'. Two types of phenomena were observed during crust formation;

(1) A crust was not completely formed on the top part of the drop; hence crust formation started from the underside, spread upwards, and resulted in a saucer-shape. Some of these drops floated without spinning, others spun about a vertical axis. Sodium sulphate decahydrate and Inorganic Powder Formulation C drops followed this mechanism.

(2) A similar mechanism to that above was observed but once the crust was completed the flying saucer inverted by 'flipping-over', e.g. with calcium carbonate. In this case the crust was thinner (by a factor of 1/3rd), presumably due to the effect of air pressure inside the inverted, still-plastic, crust. This plasticity arose because of the wetness of the crust, i.e. the free-moisture acted as a plasticiser.

Conversely in case (1) the flying saucer had a dry crust still facing the high pressure region on the lower face; hence any movement was restricted to the upper, still-wet, side.

Plate 9.15 illustrates Stereoscan microphotographs of free-flight drops of Inorganic Powder Formulation C at two different air temperatures of 35°C and 97°C. The top-side was found to be rougher than the underside, confirming the two different surface-formation mechanisms suggested in (1) above.

The free-flight experiments enabled air velocity in the tunnel to be monitored to determine the minimum air flow to keep the drop suspended i.e. just in excess of the drop terminal velocity. The minimum air velocity, corresponding to the minimum drop size of 1.5 mm, to keep the drop suspended in the working section was found to be 4.8 ms^{-1}. The free-flight drop was analogous to the case of drops in a spray in a counter-current spray dryer. However for the same size drop in a dryer the droplet's terminal velocity should exceed 4.8 ms^{-1} to enable the dried particles to reach the bottom of the chamber and not stay suspended in the up-coming air. By calculation the terminal velocity for a drop (i.e. the largest encountered in a dryer) of 1000μm (1) would be 2.4 ms^{-1}. For a 10μm drop (the smallest likely to be acceptable) this would reduce to 0.24 ms^{-1}.

9.6.3 Spray-Dried Products

Plate 9.16 presents Scanning Electron Microscope Photographs of spray-dried Inorganic Powder Formulation C and sodium carbonate. Examination of the photographs shows that the particles of Inorganic Powder C are spherical in the size range 30μm to 150 μm. However some are adhering together; some are shells containing small particles inside. There are cracks and holes in the surface. In all cases this could be explained as;

(1) As drop drying proceeds cracks or holes which are formed allow liquid to escape and hence a wet surface is formed. Fine particles or 'dust' can

Plate 9.14

Photograph of a Water Drop in Free-Flight

$T_a \simeq 35^{\circ}C$

Increased Tendency to Sphericity with Increasing θ

θ = 5s

θ = 120s

Plate 9.15

Scanning Electron Microscope Microphotographs of Free-Flight Drops of Inorganic Powder Formulation C. C_1 = 40% wt/wt.

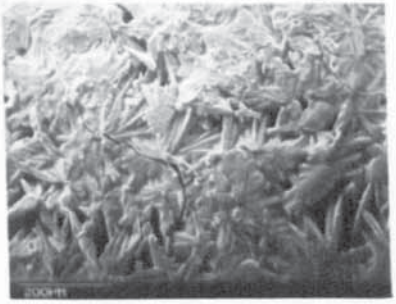

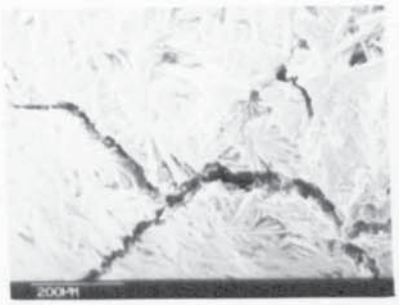

Underside

a. $T_a = 97^{\circ}C$

Underside

b. $T_a = 35^{\circ}C$

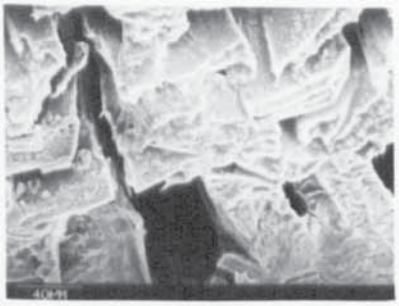

Topside

c. $T_a = 97^{\circ}C$

Topside

d. $T_a = 35^{\circ}C$

Plate 9.16

Spray-Dried Products of Inorganic Powders

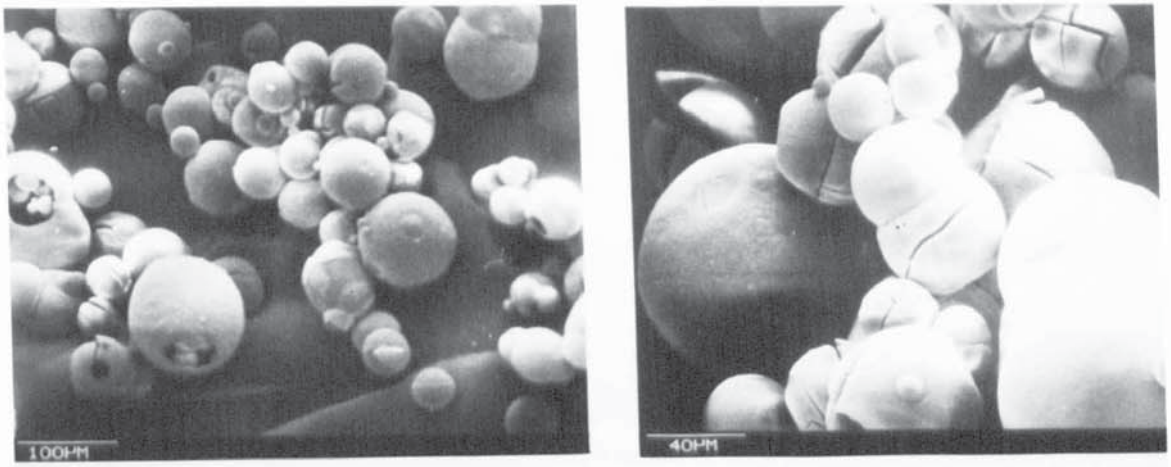

Inorganic Powder Fromulation C

T_a = 250°C

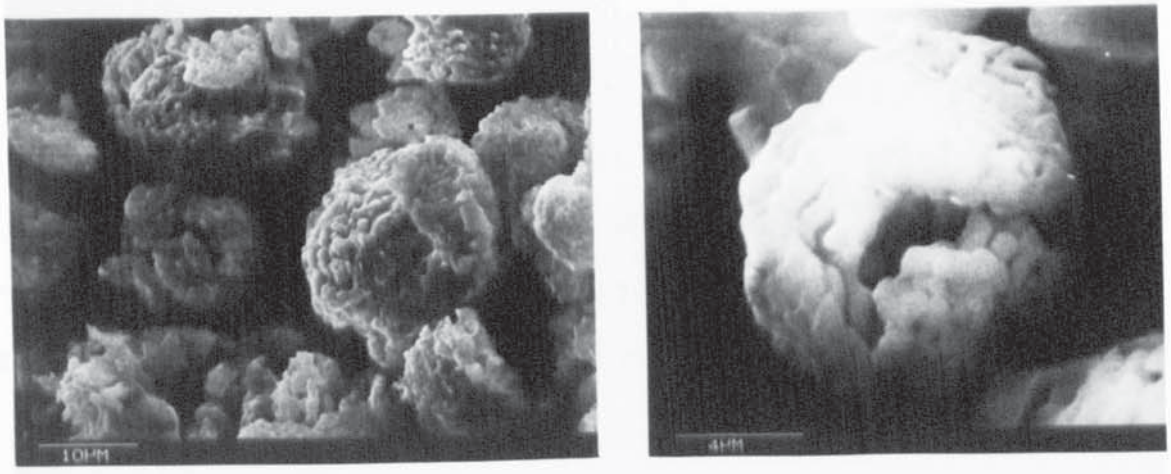

Sodium Carbonate

T_a = 250°C

adhere on this wet surface.

(2) Adherance of large particles could result from the products not being sufficiently dried; hence particles on collision in the drier, or even on collection, adhere together. Products which are hygroscopic will, if exposed to atmosphere following collection, absorb moisture which may result in particles joining and forming a chain. Sometimes two or three particles form an integrated agglometrate.

(3) This product formed hollow spherical particles and in some cases dust can be clearly seen inside them. Accumulation of dust inside the hollow particles only occurs in broken shells during collection and not before particles settle in the base of the tower.

Conversely sodium carbonate did not produce smooth spherical particles; they were much smaller in size than the Inorganic Powder C particles and there was significant agglomeration. Table 9.17 lists characteristics of spray-dried products depending upon whether they are spherical and smooth, or non-spherical and rough.

For one operating condition a mixture of particle forms was also present in the final product. As explained above this would be expected, since not every single drop or particle meets absolutely the same drying condition; hence drops undergo, to some extent, different moisture evaporation and follow a different drying mode. In summary microscopic studies and visual observation confirm the production of heterogeneous dried products due to local variations in drying chamber conditions (i.e. drop size, temperature and residence time). High temperature could lead to drop 'explosions' and hence shell formation, or liquid transfer out through holes or cracks possibly allowing dust to stick on the wetted solid surface . Small particles (i.e. < 10 μm) and dust were also observed in the products. This was attributable to the spray from the nozzle being non-uniform. This was related to the mechanism of atomisation. Small solid spheres of sodium carbonate were also obtained indicative of a drop dried slowly.

Whatever the mode of atomisation each droplet in the resulting spray is

Table 9.17

Comparison of Finished Particle Characteristics

Assumptions - identical products
- identical d_{32}

Characteristics	Smooth Spherical	Rough Non-Spherical
Resistance to fragmentation	Preferable	—
Solubility, 'Dispersibility'	—	Preferable (Larger surface area)
Free-Flowing	Preferable	—
Moisutre Absorption (wettability)	—	Preferable
High Bulk Density	Preferable	—
Particle Density	Preferable	(More likely to be porous)
'Sinkability'	Preferable	—

ejected at a velocity greatly in excess of the air velocities within the chamber. However, droplet kinetic energy is soon dissipated by air friction and direct penetration is limited to short distances from the atomiser. The droplets become influenced by the surrounding air flow and movement is governed by the design of the air disperser. No published work was found on drop aerodynamics, i.e whether or not they spin in a spray drier. Droplet movement in the drying chamber consists of, droplet release from the atomiser, droplet deceleration and finally free fall.

The drying of an aerated drop involves internal mass transfer to the air inside the drop in addition to the surface mass transfer. This may lead to drop expansion and hence formation of a hollow sphere. The main effect however is that the drop dries faster due to the internal and external evaporation.

In conclusion circulation, oscillation and rotation were all observed with free-flight pure liquid drops. Drops containing solid were less deformed and as the crust started to form circulation and oscillation were damped out. Drop deformation was unavoidable at high temperatures.

Under some circumstances there was shrinkage of the drop crust. Such shrinkage would probably cause some expression of liquid to the surface. Hence in a restricted region there would be a more efficient means of moisture transport within the drop; furthermore release of this liquid on part of the surface could yield a higher local evaporation rate than elsewhere. Expansion, or contraction, of a drop also increased, or decreased, the diffusion path. When large cracks penetrated right through the crust they provided a large flow area for vapour diffusion i.e. an increased evaporation rate. Cracks which did not penetrate completely provided for rapid transfer from some planes to the surface. The above suggests that, in some cases, combined drying mechanisms are involved. Exploding/fragmented drops were also seen which might be accompanied by liquid transfer in this region whilst transfer in other regions is by diffusion. These new observations on single drops expose the limitations of the theoretical models proposed in this field. Consideration of the complete behaviour, and their inclusion in

theoretical models will describe the drying process better.

9.7 Applicability of Single Drop Studies to Spray Drying

For modelling purposes, single drops should ideally be undeformed and of similar size to those in an actual spray drier i.e. < 1000 μm. However unless the technique of electrostatic suspension (58, 57) was adaptable, the minimum drop sizes which can be investigated are:

By nozzle suspension > 2 mm

By filament suspension (after 115) > 1.4 mm

In free-flight > 1.5 mm.

Therefore it is necessary to extrapolate results from these by a factor of approximately 1/10 on drop diameter. The justification for doing this is that the rate controlling features are in all cases crust formation and the process of moisture movement, and the mechanisms are therefore comparable.

Section 9.6 highlighted the minimum temperature at which single drops started to deform. In practical spray drying with co-current flow the inlet air temperature should be lower than this temperature to avoid 'explosions', shrinkage, over-heating, or ballooning phenomena; therefore this temperature represents an optimum for a spray drier. A higher air temperature is permissible with counter-current air flow provided it does not result in product-degradation.

How best to contact the spray with drying air is dependent upon the nature of both the spray and product involved. For example, in the counter-current arrangement, the hottest drying air contacts the dried particles as they are about to leave the chamber. If the dried product can withstand a very hot environment, and a coarse product is required, this layout is suitable. However if the particle cannot withstand such high-temperature conditions, alternative contacting methods must be employed and the co-current system may be suitable. In this the hottest drying air contacts droplets at their maximum moisture content and the evaporation process prevents high droplet temperatures.

The temperature to which droplets and particles are subjected in co-current, counter-current and mixed-flow drying chambers can be readily-appreciated from the air temperature profile characteristics (135). Ade-John (135) undertook experiments to confirm his model of the air-flow pattern in a pilot plant, 9ft high x 4ft diameter counter-current, perspex drying tower. He proposed that the flow model consists of two, well-stirred tanks at the top and the conical bottom end of the drier. In between there is a plug flow zone and in parallel with these three there is an inert by-pass stream. This hypothesis was confirmed by smoke experiments on the tower, by injecting white smoke at the air inlet port of the drier and measuring the residence times.

The initial solids content has been shown in Section 9.1 to have a considerable effect on the evaporation from droplets. Hence for any commercial drying process, a study of the evaporation rates from individual droplets gives some indication of the droplet drying characteristics and the drying mechanisms. A substantial amount of evaporation takes place when the droplet surfaces are saturated and cool. Drying chamber design and air flow rate provide a droplet residence time in the chamber, so that the desired droplet moisture removed is completed, and product is removed from the dryer, before product temperatures can rise to the outlet drying air temperature of the chamber (for counter-current), or the inlet air temperature (for co-current). Hence there is little chance of heat damage to the product. Sufficient residence time is essential to permit completion of drying to meet product specification; means of prediction is important to avoid the under or over sizing of the drying chamber.

As the drying chamber can represent a large cost item in any spray-drying installation, correct sizing is essential for minimising installation costs while maximising performance by producing high-quality dried powders at minimum operating cost. Thus chambers are designed to handle an air volume containing sufficient heat for drying the spray droplets, and to provide a residence time sufficient to yield particles of the desired moisture content. Hence measurements of the evaporation rates of single drops, as in Section 9.1, give an estimate of the drop moisture content at any specific time.

Application of the same parameters to a practical spray drying tower assists in avoiding either particles overheating or solids build-up following particle impingment on the chamber walls due to in-sufficient drying (an example of the estimating procedure is given at the end of this Section). In the latter case impingment of particles still containing high moisture contents causes them to adhere and to form a layer on the walls. Deposits which fall off may have been overheated, and changed its specification, or may still be wet and contaminate the products. Wall build-up of combustible material may also result in fires, or if dispersed, dust - explosions (1).

Example - Calculation of Drying within 10s residence time.

For drying of Inorganic Powder Formulation C of 40% wt/wt at Ta = 130°C, the steady rate of evaporation is 1.46×10^{-3} gm. cm^{-2}. s^{-1}

$$\text{mass} = \frac{\pi}{6} (0.6)^3 (1.13)$$

$$= 1.3 \times 10^{-1} \text{gm}$$

Therefore initial moisture content $= 7.8 \times 10^{-2}$gm

Hence in 10s, moisture removal = $1.65 \times 10^{-3} \times 10 = 1.65 \times 10^{-2}$gm.

This implies that after 10 seconds the drop will have lost about 80% of its initial moisture content i.e. it should not adhere on wall impingement.

9.8 Droplet Sprays and Spray-Dried Product Size Distribution Study

The nozzle used to study droplet spray size distribution was a Delavan centrifugal pressure nozzle with organic paste slurry as feed. It consisted of a nozzle, washer, orifice, swirl insert, end plate of distributor, liquid distributor, washer and nozzle body. The signal from a Malvern Laser Particle Size Analyser sent to a microcomputer which analysed the results and out put the weight percent in each size band. The latter was converted into a number percent assuming a constant density and spherical droplets. The number percent in each band was expressed as,

$$N = \frac{\Delta W/d^3}{\sum_{1}^{n} \Delta W/d^3_n} \qquad (9.5)$$

where N = number percent in band

w = weight percent in band

d = mean diameter in band

n = number of size band.

The Sauter mean diameter, d_{32}, was expressed as,

$$d_{32} = \frac{\Sigma \Delta W}{\Sigma \Delta W/d} \qquad (9.6)$$

A program written to calculate the experimental d_{32} is listed in Appendix E.1. The results are listed in Tables E1 - E6. In addition this program was converted to another form for use on FORTRAN 77; this is also given in Appendix E.2.

The data provided an opportunity to test the model developed by Ashton (136). The program given there was simplified for nozzles with straight sided outlets of constant slope and therefore not requiring the Runge-Kutta 4th order integration routine to evaluate nozzle outlet gradient. This modified program (137) is given in Appendix E.3.

Figures 9.24 and 9.25 are plots of mean droplet diameter versus solids content for Organic Paste Slurries A and B respectively. With Organic Paste A the Sauter mean diameter increased with solid content, from 66 μm to 84 μm at an inlet feed pressure of 180 psi and from 54 μm to 67 μm at a feed pressure of 270 psi for an increase from 12 to 18% wt/wt solids content. This trend would be expected since the higher the solids content the higher the proportion of energy required to overcome the increased drag forces. As shown in Figure 9.25 the Sauter mean diameter d_{32} for Organic Paste B also increased with solids content in the range 20 to 24% wt/wt;

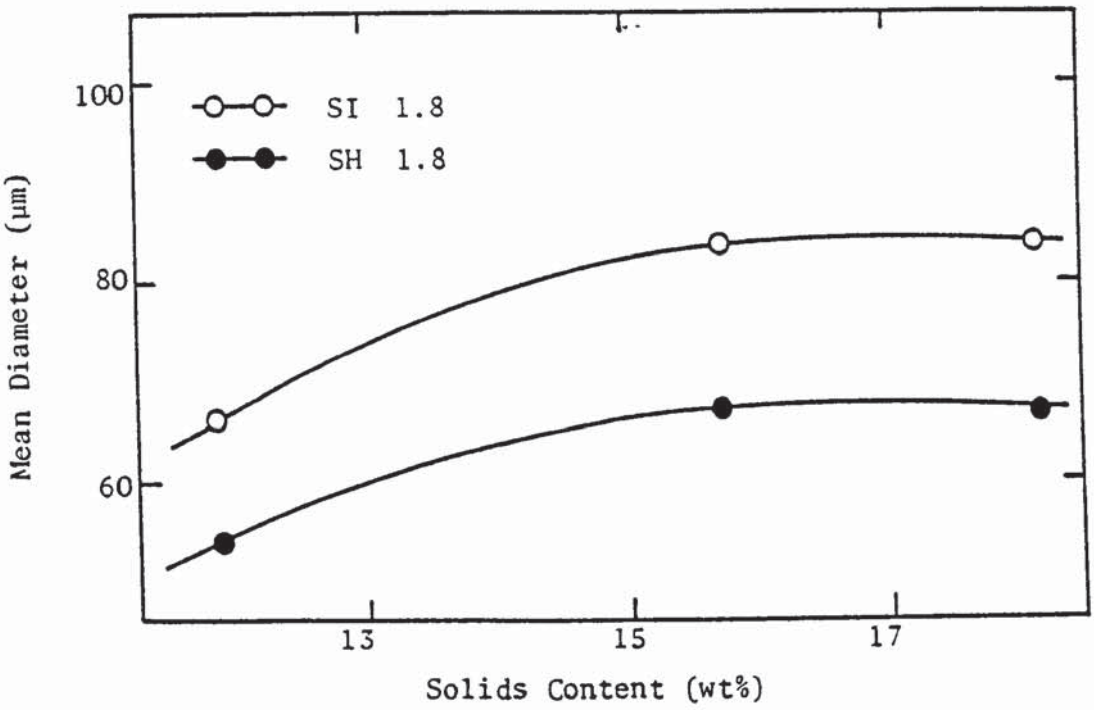

Figure 9.24 Organic Paste Formulation A

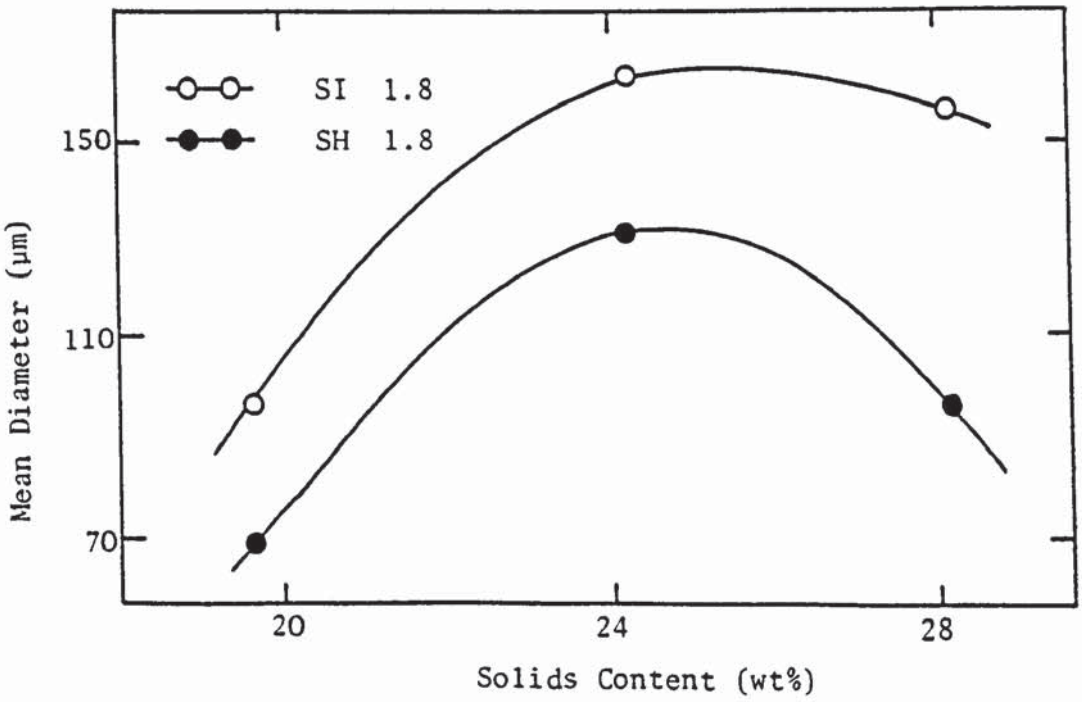

Figure 9.25 Organic Paste Formulation B

however between solids contents of 24 to 28% wt/wt d_{32} decreased. This apparent inconsistency was due to the variation in viscosity effect, since the slurries were non-Newtonian and thus the shear stress versus shear rate curves were non-linear as shown in Figure 9.27. The results of d_{32} increase almost linearly with viscosity which would be expected from consideration of the energy required for atomisation as illustrated in Figure 9.26.

A comparison between experimental d_{32} values, calculated from program E.1 or E.2, a selection of which are listed in Tables E1 - E6, covering a range of operating conditions and the theoretical d_{32}, predicted from applying program E.3, is tabulated in Table 9.18. [A complete set of experimental d_{32} data over the range of pressure, nozzle types and dimensions, and viscosities studied accompanies this Thesis as Unbound Material]. The model failed to give good agreement between experimental and predicted d_{32} values for nozzle SG1.2 at low inlet feed pressure (170 psi) i.e. the % deviation was 33 to 48%. As feed pressure increased the model tended to underestimate d_{32} by approximately 30%. Viscosity appeared to have no significant effect on the size of the deviation of the predicted d_{32} values.

The model also failed to predict reasonable d_{32} values for nozzle SG 1.4 at low inlet feed pressures and underestimated the values, albeit by only approximately 23%, at higher pressures. Good agreement was found when the inlet feed pressure was > 350 psi at feed viscosity 35 cp. Figures 9.28 and 9.29 are typical of the better plots of d_{32} (experimental) versus d_{32} (predicted), and d_{32} (predicted) against feed inlet pressure respectively and demonstrate good agreement. The deviations at low pressure suggest that the flow patterns on which the model is based are not stable under these conditions. Further work would be useful in this area of operation.

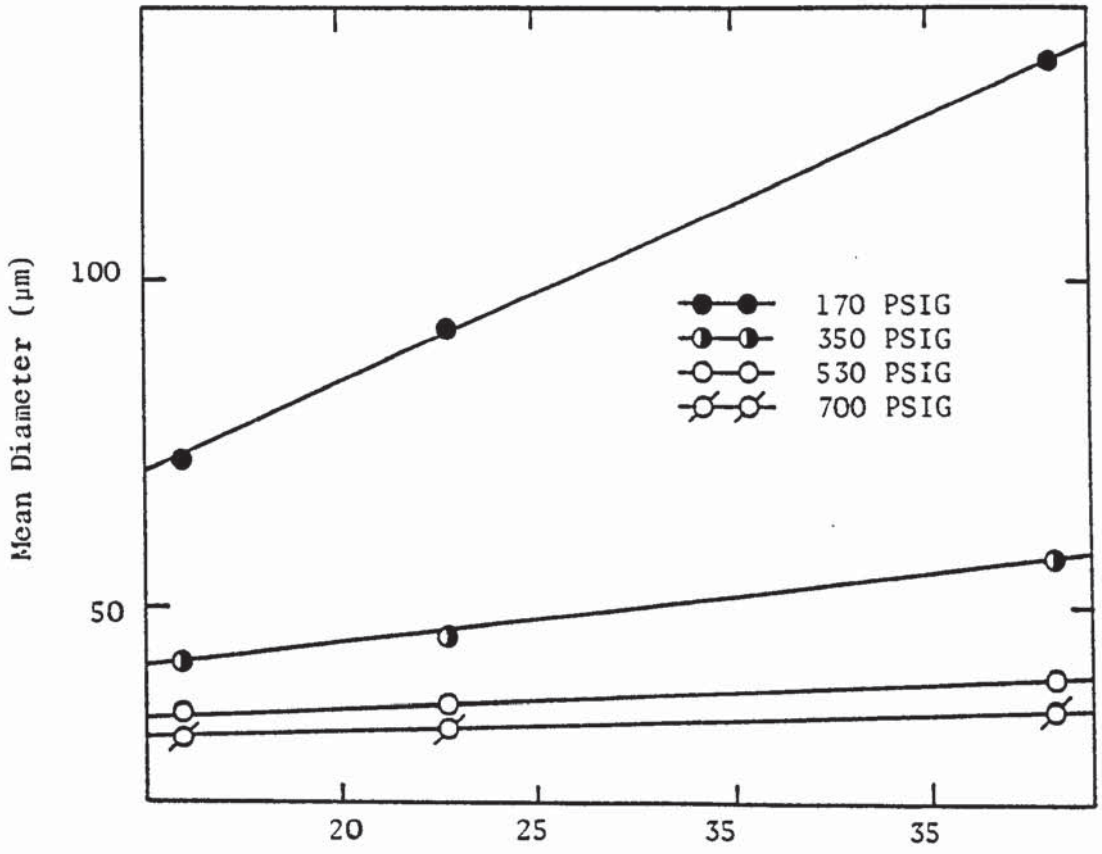

Figure 9.26 Apparent Viscosity (Cp) of Organic Paste B
Nozzle SF 1.2

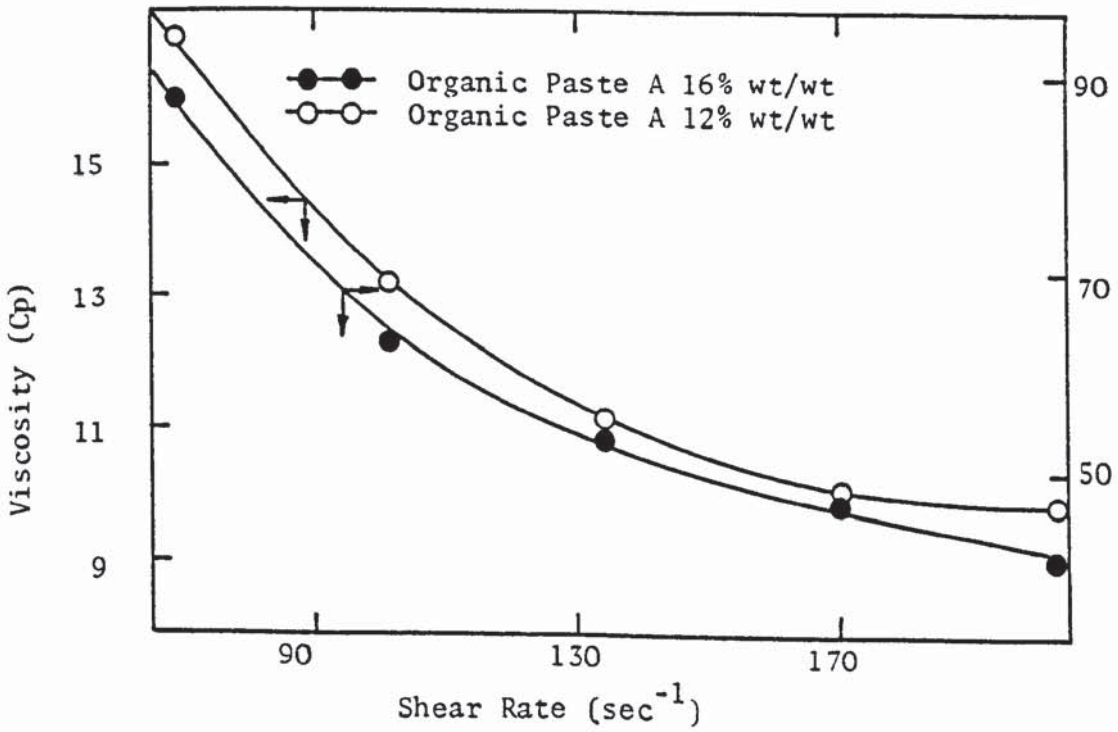

Figure 9.27 Viscosity -v- Shear Rate

Table 9.18 Comparison Between Experimental d_{32} and Predicted d_{32}

A. Nozzle Dimensions SG 1.2

μ_{feed} cp	P_{inlet} psi	Q_{feed} $cm^3.s^{-1}$	d_{32} Calculated µm	d_{32} Predicted µm
6.6	170	48	67	40
	310	55	47	29
	530	65	40	22
	680	72	33	20
16.5	170	45	80	38
	350	56	49	27
	530	64	36	22
	700	72	31	21

B. Nozzle Dimensions SG 1.4

μ_{feed} cp	P_{inlet} psi	Q_{feed} $cm^3.s^{-1}$	d_{32} Calculated µm	d_{32} Predicted µm
22	170	45	72	38
	350	55	48	26
	530	67	41	23
	730	84	35	22
35.1	175	43	65	37
	350	70	41	33
	530	83	33	26
	710	96	29	24
41.5	170	43	88	35
	350	58	50	26
	500	78	42	26
	700	88	35	23
52	180	49	106	38
	350	66	50	30
	530	78	41	25
	660	90	34	24

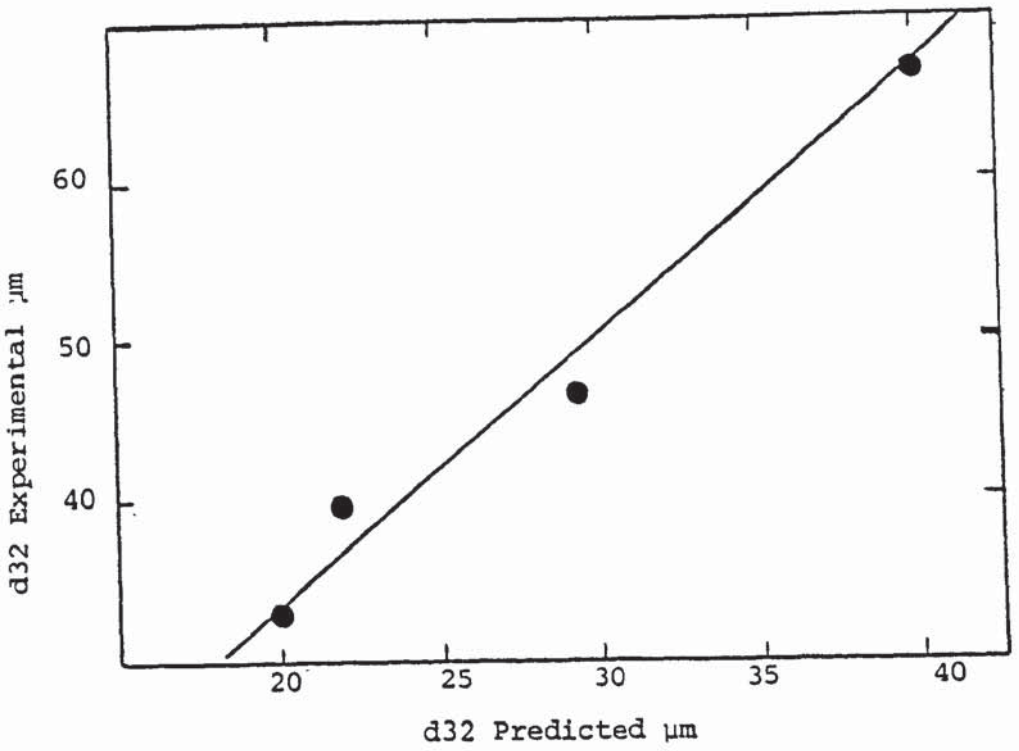

Figure 9.28 d32 Exp. -v- d32 Pred.
Nozzle SG 1.2 and µ = 6.6 Cp

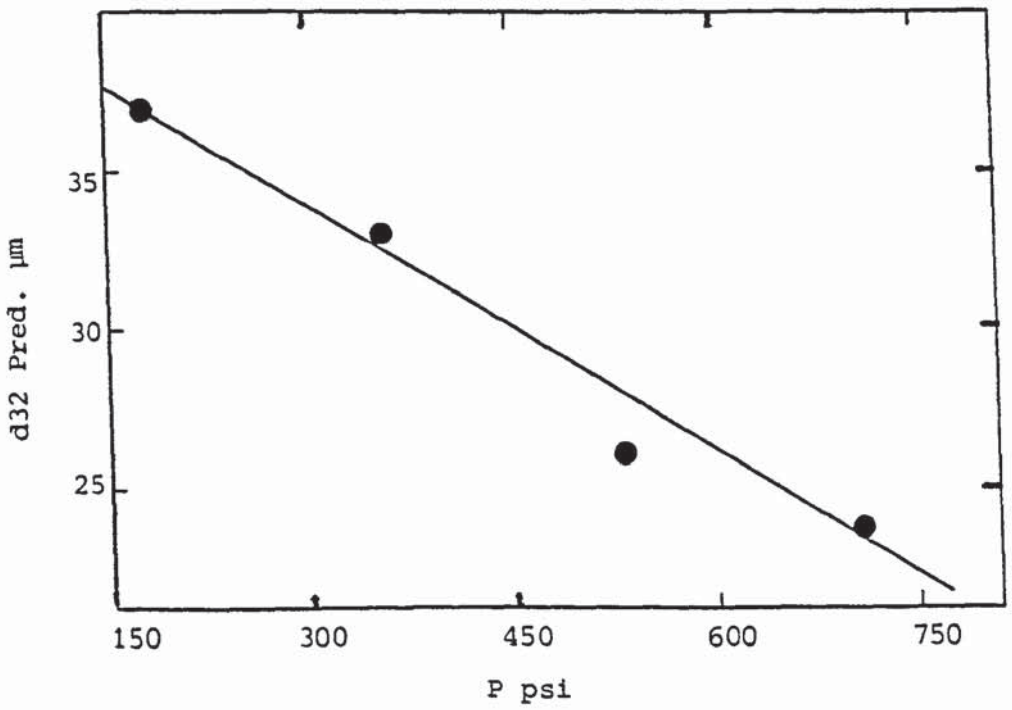

Figure 9.29 d32 Pred. -v- Pressure
Nozzle SG 1.4 and µ = 35 Cp

Cone angles from a range of Delavan nozzles (SE, SH, SI and SF swirl chambers with orifice diameters varying from 1.1mm to 1.8mm) were investigated. In general the angle varied (either upwards or downwards) only slightly with change in delivery pressure or feed concentration. By way of example Table 9.19 shows the cone angles for one specific nozzle (S.G. 1.4); here the variation in angle was only 0.03^{o} per psi. The remaining data, showing similar minor variations, is included in the Unbound Material since it is of no great significance. Therefore in practical application the nozzle dimensions, and not the inlet pressure, could be expected to determine spray angle.

Particle size distributions from the Niro dryer were studied briefly. The results are tabulated in Table 9.20. The mean particle diameter of Inorganic Powder Formulation C products revealed a significant increase in size with increase in feed solution concentration. For example the particle size increased from 70 μm to 130 μm when solids content increased from 40% to 70% wt/wt. No great change in particle size occurred with changing inlet air temperature or the pressure (speed) of the rotary atomiser.

Table 9.19

Spray Cone Angles

Nozzle = SG 1.4

Feed = Organic Paste B

Viscosity = 27 Cp

Pressure (PSIG)	170	350	530	700
Cone Angle (O)	45	49	50.5	56

Table 9.20

Mean Particle Diameters of Inorganic Powder Products

Feed % Solids Content wt/wt	Inlet Air Temperature °C	Nozzle Pressure $kg.cm^{-2}$	Mean Particle Diameter $cm \times 10^{-2}$
40	180	4.4	7
60			6
70			13
60	180	2.2	7.5
70			12
60	250	4.4	5.3
60	250	2.2	8

CHAPTER 10

FURTHER ANALYSIS OF RESULTS AND THEIR SIGNIFICANCE

The primary objective of this investigation was to study the drying behaviour of single drops with different operating parameters to assist in the prediction of spray drying performance related to drop residence time, inlet temperature and feed concentration. The controlling steps in drying are the mechanisms of the transport processes through the crusts which are formed and the study concentrated on these aspects.

The review of the literature identified the different designs of wind tunnel and different evaporation rate measurement techniques applied by numerous investigators. The general design of wind tunnel is based on supplying drying air at a constant velocity and temperature to simulate, as closely as possible, condition within a spray dryer. The present designs covered a range of air temperature from 20°C to 300°C for the horizontal wind - tunnel and from 35°C to 125°C for the vertical wind - tunnel; those temperatures were chosen because the minimum working temperature in the horizontal tunnel was 20°C (i.e. ambient temperature) and this was logically increased in increments of 20°C. In the free-flight experiments the minimum temperature was 35°C and the maximum 125°C; hence the temperature range in both rigs was comparable. The range of drop sizes covered was from 2mm to 8mm.

The results will be analysed in subsequent sections according to the method of drop suspension and whether or not it contained solids.

10.1 Suspended Water Drops

Evaporation of pure liquid drops was studied at air temperatures ranging from 20°C to 120°C at air flowrates between 0.2×10^{-3} m^3s^{-1} to 1.7 m^3s^{-1}. The value of ß in the mass transfer correlation, equation 8.1, was found to be 0.516, in good agreement with the value of 0.6 reported by Ranz and Marshall (26) and 0.552 by Frossling (11). This agreement served to confirm the reliability of the present design. At elevated temperatures, the value of ß varied from 0.471 to 0.374 for air temperatures between 50°C to 120°C.

Similarly the value of ϕ in equation 8.2 was found to be 0.668 but at

elevated temperatures its value varied from 0.65 to 0.529.

Audu (103) proposed a temperature correction term $(T_a - T_d)/T_{amb}$ with an index of -0.008 to fit his results. Downing (97) has proposed that at elevated temperatures,

$$Nu = \frac{1}{B} \ln (1 + B) (2.0 + 0.6\, Re^{0.5}\, Pr^{0.33}) \qquad (10.1)$$

It has been shown by Spalding (138) that heat transferred to the outward diffusing vapour at high temperatures could be accounted for by the dimensionless transfer number B. Consequently the temperature correction term and transfer number were included in equations 8.1 and 8.2 to correlate the results at the stated temperatures. The following modified correlations were obtained:

$$Sh = 2.0 + 0.501 \left(\frac{T_a - T_d}{T_{amb}}\right)^{-0.03} Re^{0.5}\, Sc^{0.33} \qquad (10.2)$$

and,

$$Nu = 2.0 + 0.228 \left(\frac{1}{B}\right)^{0.2} Re^{0.5}\, Pr^{0.33} \qquad (10.3)$$

The importance of the correlations can be demonstrated; for example at air temperature of 84°C approximately 27.6% of the total heat transferred is conductive heat from the nozzle and radiative heat from the surroundings. This supports the earlier statement of Fuchs (45) that this additional heat input should not be ignored.

10.2 Free-Flight Water Drops

The value of ß in equation 8.1 in this case varied between 0.7 and 0.575 for temperatures ranging from 35°C to 125°C. Correspondingly for the same temperature range the value of ϕ in equation 8.2 was in the range 0.736 to 0.583.

Each free-flight liquid drop was observed to oscillate vigorously and its shape was always deformed. The degree of drop stability and its uniformity increased

with decrease in initial drop size. This was obviously due to reduction in surface (surface tension) force with increasing diameter.

As described in Section 8.2 the results were well correlated by the modified equations 8.7 and 8.8. With a free-flight drop there is obviously no conductive heat transfer since it is suspended freely in the drying media; however there is still a radiative heat transfer contribution. Obviously a drop suspended on a nozzle as a hemisphere has only approximately half the interfacial area of a drop of similar diameter in free-flight, a difference increased further by the tendency for the latter to form a shperoid. However comparison on an area-free basis between the heat and mass transfer coefficients in equations 8.5, 8.7 and 8.6, 8.8 respectively shows that the values for free-flight drops were always somewhat greater, presumably due to the enhancement from oscillation and increased local gas velocities.

In general results of both, free-flight and suspended drop experiments, gave excellent agreement with those of Ranz and Marshall (26) and Frossling (11) confirming the reliability of the instruments and the techniques. This was particularly important for the free-flight studies since this was the first time this technique had been applied to drying investigations.

10.3 Suspended Drops Containing Solids

Drying Rates

The drying curves for drops of aqueous sodium sulphate decahydrate, organic pigments, inorganic powder solutions and organic paste slurries were presented in Figures 9.1 - 9.14 as rate of evaporation against time for different initial moisture contents, air velocities and temperatures and nature of solids. The effect of additives was also investigated.

The drying curves show good agreement with those published by Charlesworth and Marshall (25) but the present investigation extended to higher initial concentrations, i.e. up to 70% wt/wt solids. Use of such a high concentration commercially would have numerous advantages for spray drying, e.g. to obtain a higher

solids throughput and more economical use of thermal energy. During the first period of drying the rates of both heat and mass transfer were controlled by the water-vapour film resistance; this is characteristic of evaporation from a free-liquid surface. The solid concentration would be expected to rise from the initial concentration towards a saturation value corresponding with the 'critical moisture content'. Drying rates in the second drying period, i.e. after crust formation showed a great deal of variation, a phenomenon also experienced by Charlesworth and Marshall (25) and Trommelen and Crosby (27). In this the crust resistance to moisture diffusion becomes predominant so that the precise structure of the crust, particularly the porosity, strongly affects the subsequent evaporation rate.

Crust Formation

Crust formation presents an extra resistance to mass transfer; Therefore the rate of drying would be expected to vary with,

i - crust thickness

ii - porous, crystalline or impervious crust formation

iii - formation of a skin, or membrane if any

Examination of Figure 9.16 shows that the crust thickness growth rate increased with increase in the air flow rate. Ranz and Marshall (26) and Charlesworth and Marshall (25) showed that once the crust started to form parts of it may be redissolved and then reformed at a different rate from the rest of the crust. This phenomenon is likely to increase with increase in the air flow rate, since this increases variation between local mass transfer rates. As the air flow rate is further increased, drying takes place more rapidly and the effects of the above phenomenon will be minimal. Consequently, the crust thickness growth rate increases with increase in air flow rate; however a thick crust increases the resistance to mass transfer, therefore the rate of drying decreases. Also a high initial solids content resulted in a thicker crust which in turn increased the resistance to moisture diffusion. As mentioned in Section 9.6 at an initial concentration of 50% wt/wt sodium sulphate decahydrate the drop crust formed at an air temperature of 60^{o}C and a velocity of 0.2 ms^{-1} hardly exhibited any

pores even at a magnification of 5000 and the crust appeared relatively smooth. However as air velocity was increased crust roughness became noticeable and the pores could be clearly distinguished (Plate 9.2). At higher temperatures large crystals and pores were visible as is evident (Plate 9.3). Therefore a critical state appeared to exist whereby a crust, from a relatively smooth and non-porous structure reverted to a rough and jagged surface with significantly large pores. This observation agreed with the results of Cheong's (115) study of drops of sodium sulphate decahydrate and will be discussed later in this chapter.

Significant differences were observed (in droplet behaviour, evaporation rates, and final crust structure) between Organic Pigment A and Organic Pigment B under identical drying conditions. Organic Pigment A with a typical, cracked and porous crust, had higher evaporation rates, (Plate 9.6 c and d). Dried drops of Organic Pigment A possessed crusts with large pores from the inside and large fissures from the outside. The dried material was hard but these crust features could also arise from 'shell-shattering' in practical spray drying even at moderate air temperatures. On the other hand drops of Organic Pigment B appeared to form a semi-permeable skin, or membrane, surrounding the wet core early in the drying process which would reduce the evaporation rate prior to crust formation. Furthermore in the later stages of drying the surface fissures did not appear to extend right through the crust; this was confirmed by the negligible crust porosity - a phenomenon not observed with any of the other organic and inorganic chemicals investigated. Drops of both organic pigments demonstrated 'boiling' and internal 'steam explosion' phenomena at higher temperatures i.e. > 165°C, which would be undersirable in practical spray drying resulting in fines generation. Therefore for the same particle size of product, any improvement in drying rates for Organic Pigment B would depend on the use of additives as demonstrated in this section. The formation of a film/skin in the early stages of drying could also be modified to give improved evaporation rates.

Crust Porosity

The porosity of a crust of Organic Pigment A dried at 100°C was

estimated to be 8.4×10^{-2} and, at 135°C, 2.1×10^{-2}. Comparison of the electron microphotograph of the external crust structures shows that those at 100°C were rougher with many fine cracks between the major fissures; the internal structure was also highly porous. These observable differences are confirmed by the estimated porosities. Electron micrographs of the external and internal crust structures are reproduced at Plate 9.6d. Plate 9.6 c, illustrates an unusual smooth crust without pores; this crust was rigid and lacked the myriad of surface cracks typical of Pigment A.

Examination of Plates 9.4 and 9.7 shows that crust produced at 40 to 70% wt/wt initial solution concentration of Inorganic Powder Formulation C, and 130°C air temperature had a smooth external surface with cracks in but few distinguishable blow holes. Drops of 40% wt/wt initial solution of the same material dried at 110°C tended to form crusts with fewer cracks; at 70% wt/wt initial concentration and 130°C many holes were visible in the crust when viewed at low magnification. All this is indicative of surface evaporation and crust formation at an early stage when drying > 60% wt/wt solutions. The test described in Table 9.15 showed that 200°C was the maximum practical temperature for operation; in spray drying the critical air temperature giving a fast evaporation rate but a tendency for drops to explode, producing fragments, would be of a similar order.

As described in Table 9.16, based on visual and photographic observations, a uniform crust could not be obtained in repeated tests with Inorganic Powder Formulation E at 130°C air temperature. However they were obtained at the next lower (93°C) and higher (165°C) temperatures. The explanation for this could be that relatively slow evaporation takes place at 93°C leading to uniform, porous crust formation; conversely at 165°C rapid evaporation from the surface causes a crust to be formed quickly but containing holes or cracks (e.g. Plate 9.6) from which internal pressure can be released so that the crust geometry remains uniform. An air temperature of 200°C was excessive for both products D and E and in an operating spray drier would result in a tendency for drops to 'explode'. The optimum operating temperatures therefore appeared to be between 93°C and 130°C for Inorganic Powder Formulation E

and 130°C + for Inorganic Powder Formulation D.

Confirmation that evaporation rates depend on the crust structure and porosity is shown at the same condition in Tables 9.1 and 9.2 for Organic Pastes A and B.

Effect of Additives

Presence of an additive remarkably changed the crust structure. The change depends on the nature of the additive, e.g. addition of Dispersol produced a completely different crust structure to the same material with sodium chloride as additive as shown in Plate 9.8. Obviously addition of an additive may inhibit the drying rate if it tends to reduce the porosity of the crust or vice versa. In this case Dispersol apparently migrated to the surface and, being amorphous, increased the porosity (Plate 9.8b). Sodium Chloride crystallisation at the surface (Plate 9.8c) resulted in the most porous crust. These effects would clearly be concentration-dependent. Due to expansion of the droplets during drying it was observed, using an optical microscope, that the crust thickness decreased with time. However the scatter of the data was unavoidable since fracture of a crust, or crust shrinkage and blow holes, could result in a sudden increase in evaporation from the drop. This phenomena was also noted by Cheong with sodium sulphate decahydrate (115). Elongation also increased the evaporation area.

Generally crusts formed from drops of high solids concentration and, or, at high air temperature were more prone to fracture and 'blow holes'. When fracture occurred the resistance to moisture diffusion suddenly diminished and evaporation proceeded at a high rate. However, the fractures were rapidly re-filled by further deposition of crust and the process repeated. This resulted in dried particles that were distorted in shape with fractures and sometimes large 'blow holes'. Repetition of the processes could also result in pieces of crust falling-away. This may be one of the causes of fine dust in spray - dried products which in commercial practice must either be re-cycled, or agglomerated in a subsequent stage (e.g. a fluidized bed). Clearly therefore, as mentioned earlier, there is an optimum operating condition for any product for maximum throughput with the minimum of fines.

10.4 Free-Flight Drops Containing Solids

When a drop was first injected into the working - section of the vertical wind tunnel evaporation proceeded as for pure liquid drops. It also exhibited oscillation and internal circulation and the stability and sphericity depended upon the drop size. Crust formation would tend to reduce internal circulation so the drop is not well-mixed; hence a variation in solids content in the drop leads to non-uniform mass transfer from the drop surface i.e. a crust forms randomly around the drop which affects drop balance. However, as discussed in the previous section, crust dissolution and re-formation causes the crust to be formed non-uniformly around the drop. A consequent variation in local mass transfer rates will also affect the drop stability in this stage. This instability in drops does not persist once the crust has completely formed; the drop then ceases to rotate around its axis, stop oscillating and forms a saucer - shape. The final dried crust shape resembled a deep saucer. As described earlier the saucer - shaped crust formed with calcium carbonate only flipped over and continued to rotate around the axis. The aerodynamics causing flip - over relate to the different saucer - shape with a thicker crust having a lip around the rim and to the 'plasticity' of dried calcium carbonate. The differences are illustrated in Figure 10.1.

Saucer - shaped crusts, the underside of one of which is shown in Plate 9.15, resulted from the maximum evaporation rate from the underside of the drop i.e. facing the air-flow. The evaporation rate decreases moving around the drop reaching a minimum value at the top (11, 26). Then the action on the upper liquid zone of surface tension tending to minimise the surface area and of gravity produces the concave suface. Plate 9.15 of Inorganic Powder Formulation C shows that the undersides were smooth but the tops became concave and rougher; this could arise since when the crust completely covers the underside its resistance to mass transfer is considerably greater than the more liquid saturated top side so that in the last stage of drying there is a significant increase in evaporation from the top causing fissures. This is probably characteristic of drying a non-spinning, drop with air flow from beneath, i.e. greater evaporation from the underside; a phenomenon not present in a well-mixed tower.

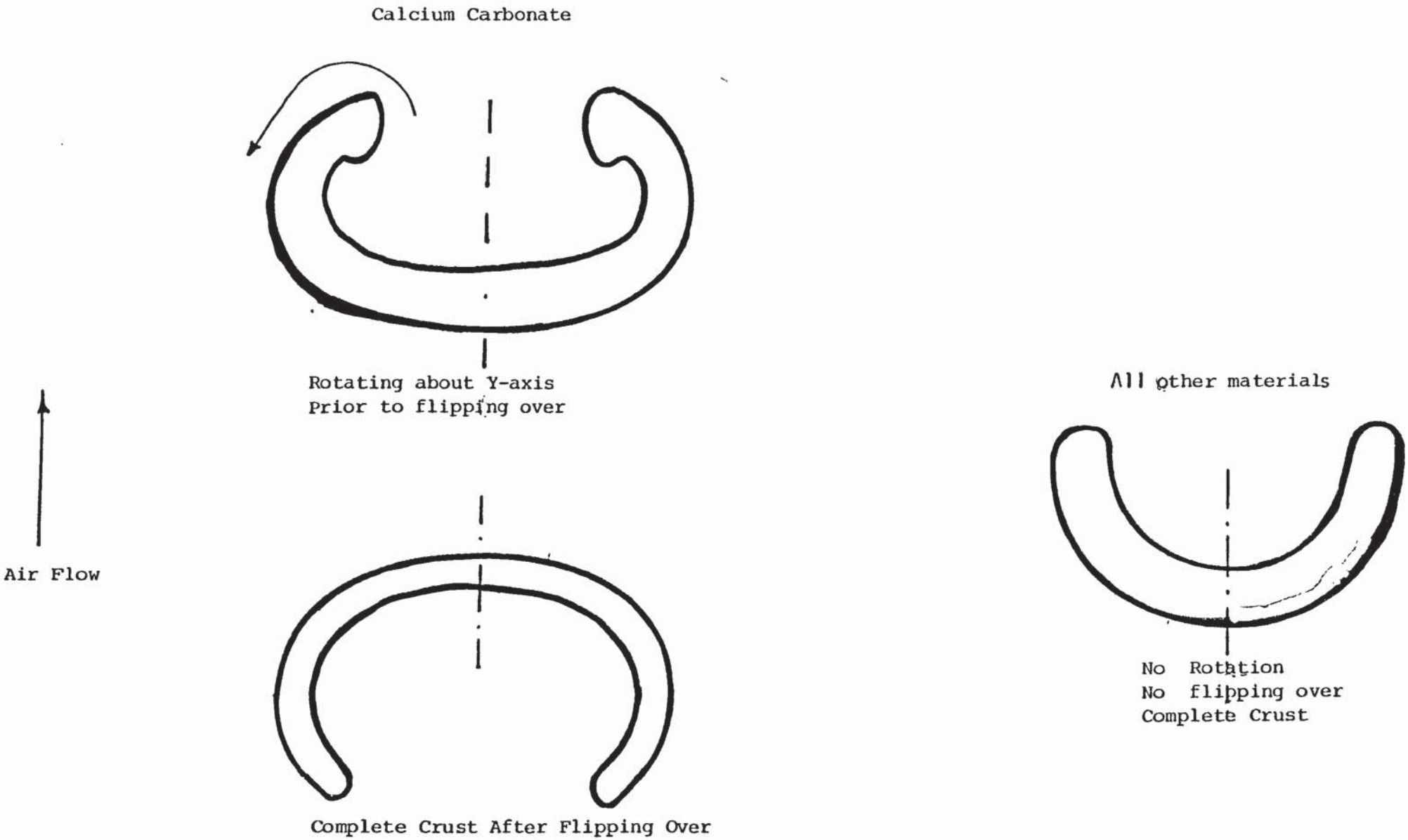

Figure 10.1 Saucer-Shaped Drop Formation and Flip-Over Phenomena 5mm Initial Slurry Drops in Free-Flight.

To obtain a spherical drop, with a non-flattened underside, would require a drop < 1mm diameter when released into the working section. Drops < 1mm could not however be retained in freely-flight in the present equipment i.e. 1.5mm was a minimum.

In conclusion crust structure was found to be similar in terms of cracks, holes or fractures whether the material was from a suspended drop or spray-dried. This implies that under the same conditions of solids content, air velocity and temperature crust structure was similar and hence the mechanisms of moisture movement were identical. Hence, despite the unavoidable difference in drop size, single drop studies have proved to be useful for predicting and optimising spray drier performance.

10.5 Droplet Sprays and Spray - Dried Products

The mean particle diameter d_{32} of Inorganic Powder Formulation C dried in the Niro unit was independent of inlet air temperature in the range 180°C to 250°C. However there was a significant increase by a factor of 1/3rd, in particle size with increase in feed solution concentration from 60 to 70%. A sample of spray-dried Inorganic Powder Formulation C (Plate 9.16) comprised characteristic spherical particles in the size range 30μm to 150μm some of which were adhering together. Some were shells containing smaller particles inside; there were cracks and holes in the surface. Conversely the sodium carbonate (also in Plate 9.16) tended to be agglomerated. (n.b. the sodium carbonate microphotograph is magnified and 10 times larger than that for Inorganic Powder Formulation C). The sodium carbonate particle was made up from smaller particles i.e. 15 μm, agglomerated together. This would result from smaller particles being wet enough to stick together, probably mainly on the walls of the drying chamber or in the bottom of the chamber but also to a limited extent in the cyclone and the collecting jar.

The Sauter mean diameter of the particle distribution produced with Organic Paste Formulation A slurries increased with solids content of 12 to 18% wt/wt.

However Organic Paste B showed an increase in d_{32} as solid content increased to 24% wt/wt but d_{32} then started to decrease when the solids content increased to 28% wt/wt. This was explained by the non-Newtonian behaviour referred to in Section 9.8.

The shape of the product particle depends upon droplet formation during atomisation and upon droplet/particle behaviour during drying. An agglomerate can be formed through two or more droplets coalescing in the proximity of the atomiser and drying in this state or through partially - dried droplets adhering to each other in the lower regions of the chamber, due to their sticky surfaces, (Plate 9.16).

Droplets and particles comprising sprays and dried products are not uniform in size; therefore they have different Reynolds numbers and their residence times and final moisture contents also vary. The atomiser cannot form totally homogeous sprays and droplets are also subjected to different shape distortions depending upon their drying characteristics and travel within the dryer. In this work it was found that some droplets contracted to a smaller shape when they dried and others tended to expand. Thus the relationship between the spray produced initally from an atomiser (which is itself dependent on atomiser design and operating parameters), and the particle size distribution, and variation in moisture content between individual dried particles, is extremely complex. It is unlikely to be describable by any one model and a range of different solids, including skin-forming and organic materials require further study.

10.6 Drop Core Temperature Measurements

Core temperature - profile measurements were carried out on suspended drops of sodium sulphate decahydrate and Inorganic Powder Formulation C solutions. A comparison between drop core temperature behaviour is shown in Figures 9.21 to 9.23.

The behaviour of sodium sulphate decahydrate during drying at air temperatures above 33°C is unusual in that it forms different hydrates with incongruent

melting points (134). Below the transition temperature of 32.4, the monoclinic decahydrate crystals are in equilibrium with the liquid phase. At the transition point, the rhombic crystals of anhydrous sulphate commence to separate and exist in equilibrium with the decahydrate and the saturated solution.

Figure 9.21 shows the shape of core temperature curves of sodium sulphate decahydrate solution. At an air temperature of 20°C a depression in core temperature occurs initially due to evaporation from the free surface as it approaches the wet-bulb temperature; the core temperature then starts to rise again. This lowering in temperature was not observed at higher drying temperatures as shown in Figures 9.21 to 9.23. The values of the constant core temperatures attained depended on the temperature of the drying media.

This behaviour is strong evidence of a phase change in sodium sulphate decahydrate. Therefore dry crust samples were prepared from drops of sodium sulphate decahydrate dried at air temperatures ranging from 22°C to 120°C. Thermogravimetry undertaken in a Linseis Thermobalance L81 showed that the crust of a drop dried at 22°C contained 7 to 9 crystalling hydrated water molecules; one dried at 35°C contained 4 to 6 molecules; one dried at 65°C contained 1 to 3 molecules the last sample dried at 120°C contained no hydrated water molecules. This was clear confirmation of the phase change occurring during drying.

The shape of core temperature curve for a drop of Inorganic Powder Formulation C at an air temperature of 20°C showed a similar trend to sodium sulphate decahydrate at the same temperature. The lowering in the drop core temperature is due to evaporation from the free surface before the crust starts to form and reaches a minimum which is the wet-bulb temperature. Once the crust starts to form the temperature gradually increases. Core temperature curves for drops at 40°C, 61°C and 79°C did not exhibit the constant temperature period, which is clear evidence that there was no phase change. At these temperatures core temperatures started to increase gradually but remained less than the surrounding temperature even after a residence time of 1 hour.

10.7 Experimental Techniques

No parallel studies of the drying of free-flight solution or slurry droplets, or the use of a Laser Particle Size Analyser for particle size distribution, have been reported in the literature. Audu (103) studied slurry droplets suspended on a rotated nozzle but did not take into account the heat transfer to the drop by conduction through the nozzle or the heat transfer by radiation from the surroundings to the drop. Previously Frossling (11), Ranz and Marshall (26), and Charlesworth and Marshall (25) studied the evaporation from single stationary droplets suspended from a glass filament or thermocouple, and Pei et. al. (96) used single stationary spheres constructed from Celite with known porosities. Such techniques, though permitting measurement of the droplet weight as drying proceeds, are limited in application since the relative velocity of the drop present in a spray drying chamber, is non-existent. The porosity of spray-dried particles varies with the composition of the formulation, so that conclusive results on mass transfer in spray driers cannot be obtained from the evaporation of liquids from Celite spheres of fixed porosity. Furthermore drying from fixed stationary droplets is from one side only, the drying rate being greatest on the side facing the air flow, and smallest in the wake region. This situation exists whenever a drop is simply suspended in a horizontal or a vertical wind tunnel. It was easily overcome in the case of a suspended drop in a horizontal tunnel by rotating the drop. In the case of a drop suspended in a vertical wind tunnel one side faces the incident air but the other inevitably remains in the wake region. Consequently, a rotated suspended drop in a horizontal wind tunnel with side flowing air was designed and adapted for the present investigation. The major disadvantage of the technique was the difficulty of measuring the droplet weight, as well as the heat conducted to the drop through the nozzle. The free-flight drops bear a closer resemblance to the situation in a spray dryer. However evaporation from the drop is still not uniform because the air impinges on the under-side first whereas in a spray-drier the air flow is less-directional and the velocity is less than the terminal velocity of smaller drops.

CHAPTER 11

CONCLUSIONS AND RECOMMENDATIONS

11.1 CONCLUSIONS

The major conclusions from this study are presented below.

11.1.1 Pure Liquid Drops

1. The literature review revealed some disagreement as to the form of the Nusselt equation for heat transfer to drops. Furthermore the majority of previous investigators who measured evaporation rates from suspended drops ignored heat transfer by conduction along the drop suspension filament and by radiation from the surroundings.

For pure liquid drops the experimental data in this work were well correlated by the modified equations,

$$Sh = 2.0 + 0.5 \left(\frac{T_a - T_d}{T_{amb}}\right)^{-0.03} Re^{0.5} Sc^{0.33} \qquad (8.5)$$

$$Nu = 2.0 + 0.23 \left(\frac{\lambda}{Cp\Delta T}\right)^{0.2} Re^{0.5} Pr^{0.33} \qquad (8.6)$$

for suspended drops of 2 mm to 8 mm; and

$$Sh = 2.0 + 0.62 \left(\frac{T_a - T_d}{T_{amb}}\right)^{-0.01} Re^{0.5} Sc^{0.33} \qquad (8.7)$$

$$Nu = 2.0 + 0.3 \left(\frac{\lambda}{Cp\Delta T}\right)^{0.17} Re^{0.5} Pr^{0.33} \qquad (8.8)$$

for free-flight drops of 1.5 mm to 6 mm. The wind factors, ß, in equation 8.3 were 24 to 36% larger than in a previous investigation (103) because corrections were included for heat gain other than by forced convection.

Equations 8.7 and 8.8 are the first to be presented to correlate heat and mass transfer coefficients for free-flight drops. The correlation coefficients were 0.97 and 0.98 respectively and furthermore the wind factors show reasonable agreement with the suspended drop correlations equations 8.5 and 8.6 and with those of Frossling

(11) and Ranz and Marshall (26).

2. Free-flight drops tended to oscillate but became more stable as the size decreased below 3 mm and hence more spherical in shape. Oscillation of a drop was completely damped - out as the drop size decreased below 2 mm. (Under such condtions evaporation rate per unit area would be more uniform over the drop surface since additional local turbulence created by oscillations would affect k_g).

11.1.2 Drops Containing Dissolved or Undissolved Solids

This research covered drops of aqueous sodium sulphate decahydrate, Inorganic Powders, Organic Pigment solutions and Organic Paste slurries.

3. When drops of the above materials were dried a hollow crust was eventually formed. Thus models based on a receding interface (115) apply only to e.g. a drop solids - content of 80% at which vapour, escape of which is retarded by the thick crust, must form part of the core. The crust thickness growth rate increased with increase in air mass flowrate, air temperature and the initial moisture content. The crusts varied in structure; some were crystalline porous, rough non-crystalline, or like a skin/membrane i.e. very smooth and non-porous. Hence the drying rate after crust formation was, and in practical drying will always be, product specific.

4. Very good agreement was obtained between experimental overall mass transfer coefficients and those predicted from:

$$\frac{1}{K_o} = \frac{1}{H_1 k_g} + \frac{1}{k_c} \qquad (5.26)$$

where k_g was predicted from equations 8.5 and 8.7

k_c the controlling crust coefficient was predicted from,

$$k_c = \frac{D_v \varepsilon^{1.5}}{\psi}$$

porosity, ε, was predicted using a modified Kozeny equation using crust pressure drop data, equation 5.28. ψ, the crust thickness, was measured by using an electron microscope or optical microscope.

5. With suspended droplets at higher temperatures, crusts tended to deform. Some deformation was characterised by longitudinal expansion or formation of a 'protrusion' from the side; sometimes two protrusions formed, followed either by an explosion or repetitive re-building of the crust giving a final product with a rough surface. Some of the crusts cracked to release the internal pressure and formed blow holes.

6. In accordance with previous observations (Chapter 9), drying of drops was characterised by two distinct drying periods; an initial constant rate period and a falling rate period as soon as the crust was formed. After crust formation fractures occurred randomly but were more frequent at higher temperatures. The optimum air temperature for an industrial spray tower was considered predictable from that allowing retention of uniform crusts on single droplets.

7. Core temperature measurements for drops of sodium sulphate decahydrate solution were characterised by a distinct constant temperature period during crust formation. This was confirmed by Thermalgravimetry to be due to a solid phase change.

8. Presence of additive (either Dispersol or sodium chloride) increased the drying rate. Electron Scanning Microscopy showed that this was due to changing the structure and the porosity of the crust.

9. Drop size distribution from centrifugal pressure nozzles were correlated with the simplified form of Ashton's (136) model. Reasonable agreement was found between the experimental and theoretical results at operating pressures >350 psi. The predicted d_{32} values were in general 30% smaller. However at lower pressures (e.g. 170 psi) the predicted values were sometimes > 50% smaller.

11.2 Recommendations for Further Work

General

1. The effect of additives, such as sodium chloride solution, on the drying characteristics for certain products was inconclusive, although some improvements were observed. These effects should therefore be included in future investigations.

2. Investigation of the drying characteristics of aerated drops is recommended for further work. Drops containing an air bubble have been predicted theoretically to give a uniform crust and a faster drying rate [111] than that for a similar non-aerated drop. Again however limited experimental results were inconclusive [112].

3. No work has been published on the drying rates and drying characteristics of natural products (e.g. coffee extract, milk) using the suspended drop and free-flight drop techniques. The potential film-forming, and product-specific crusts, make them particularly suited for further study.

4. The occurrence of fracture in individual particles is not predicted from published theoretical models. Detailed studies could be undertaken to further understanding of this phenomenon, i.e. conditions under which the rate of vapour release inside the drop exceeds the loss through diffusion until eventually the crust ruptures.

5. On the limited observations in Section 9.4 film-forming materials should result in smooth surfaced, particles but would require a longer residence time for equivalent dryness. A study of film forming materials and methods of increasing their drying rates is recommended. The film may have a further advantage in 'sealing-in' odour or flavour in food products during the early period prior to crust formation.

6. There is scope for investigation of the change in drop, and subsequently particle, size distribution along the spray drying chamber as particles travel, i.e. from atomisation to finished product. Comparison between spray size distribution and the particle size distribution at different heights using the Malvern Analyser will provide valuable information on drop drying mechanisms.

7. There is scope for studying single droplets drying under vacuum

conditions.

8. The model proposed for droplet d_{32} values from centrifugal pressure nozzles by Ashton (136), and later simplified (137), shows promise but could be refined for lower pressure operation (i.e. < 170 psi).

Suspended Drops Experimentation

Improvements and extensions to this work could include:-

9. Applying another drying media, e.g. superheated steam, since the arrangement did include a superheated steam generation unit.

10. The nozzle design did not facilitate measurements of the change in droplet weight as drying proceeded. Such direct measurement is preferable and therefore modification of the nozzle design should be considered. Fixing the drop suspension device into a sensitive, calibrated, spring-type scale balance would provide for direct drop-weight measurements after any time interval.

11. For nozzle rotation, a D.C. motor would be preferable so that a variable rotation speed could be tested.

12. Drop temperature measurement experiments could be extended to cover different drops of different materials. For this purpose a thinner thermocouple, e.g. as developed by Cheong (115), would be useful since it would minimise heat gain by conduction.

13. To minimise the conductive heat transfer to the drop the nozzle should be constructed from material of low thermal conductivity, e.g. glass or composite nozzles could be used. The latter could be designed by incorporating a non-conductive insert, e.g. of asbestos - substitute.

Free - Flight Drop Experimentation

14. The following modifications are recommended: Installation of wire gauze above the working section, to protect the fan and testing elements from any item dropped into the working section accidently. The control valve should ideally be replaced by one giving close control over air flow rate. Calibration of this valve, i.e. position when open -vs- corresponding velocity in the working section, would then be helpful. The

drop-forming unit should be modified to reduce nozzle vibration during injection. This unit could give the exact injected drop volume by observing the difference in liquid volume inside the syringe i.e. a microburete nozzle design.

APPENDICES

APPENDIX A

Least Square Technique for Data Correlation.
Tables A1 - A31 Data for Evaporation From Suspended and Free-Flight Pure Water Droplets.

The data listed are, for convenience, as calculated i.e. without rounding-up. It is not intended to imply a greater accuracy that is indicated on page 118.

A.1 Least Square Technique for Data Correlation

A.1.1 Constant Air Temperature

From Equation 8.1

$$Sh = 2 + \beta Re^{0.5} Sc^{0.33}$$

By rearrangement and taking logarithms to the base e,

$$\log_e (Sh-2) = \log_e \beta + \log_e (Re^{0.5} Sc^{0.33}) \qquad (A.1)$$

Let, $X1 = \log_e (Sh-2)$

$X2 = \log_e (Re^{0.5} Sc^{0.33})$

$X3 = \log_e \beta$

The error between the given data and the approximating function at $X2_i$ can be expressed by,

$$e(X1_i) = X1_i - X2_i - X3 \qquad (A.2)$$

The objective function is to minimise the sum of the errors squared, expressed as,

$$e(X1_i)^2 = S = \sum_{i=1}^{n} (X1_i - X2_i - X3)^3 \qquad (A.3)$$

Differentiating S with respect to X3, and setting the differential equation to zero,

$$\frac{dS}{dX3} = -2 \sum_{i=1}^{n} (X1_i - X2_i - X3) = 0 \qquad (A.4)$$

Thus,

$$\sum X1_i - \sum X2_i - \sum nX3 = 0 \qquad (A.5)$$

Therefore,

$$X3 = \frac{1}{n} \left(\sum X1_i - \sum X2_i \right) \qquad (A.6)$$

The value of β can then be evaluated from equation (A.6) by taking the exponential of X3, that is:

$$\beta = \exp(X3) \qquad (A.7)$$

The correlation coefficient C is represented by,

$$C = \left[1 - \frac{\sum (X1_i - X2_i - X3)^2}{\sum (X1_i - \bar{X}1)^2} \right]^{\frac{1}{2}} \qquad (A.8)$$

where, $\bar{X}1 = \frac{1}{n} \sum X1_i$

Equations (A.6), (A.7) and (A.8) were used for suspended drop data and again for free-flight drop data. However, the same analytical procedure was followed to find the values of ϕ in equation (8.2) for both suspended and free-flight drop data, and hence equation (A.7) becomes,

$$\phi = \exp (X3) \qquad (A.9)$$

and let $X1 = \log_e (NU-2)$

$X2 = \log_e (Re^{0.5} Pr^{0.33})$

$X3 = \log_e \phi$

A computer program listed in Appendix A.1.1.1 was used for data analysis at constant temperature.

A.1.2 Variable Air Temperature

From the applied proposed correlation (8.3),

$$Sh = 2 + \beta \left| \frac{\bar{T}_a - \bar{T}_s}{T_{amb}} \right|^n Re^{0.5} Sc^{0.33}$$

Rearranging and taking logarithms to the base e,

$$\log_e(Sh-2) = \log_e \beta + n\log_e \left| \frac{\bar{T}_a - \bar{T}_s}{T_{amb}} \right| + \log_e Re^{0.5} Sc^{0.33} \qquad (A.10)$$

Let,

$$X1 = \log_e (Sh-2)$$

$$X2 = \log_e (Re^{0.5} Sc^{0.33})$$

$$X3 = \log_e \beta$$

$$X4 = \log_e \left| \frac{\bar{T}_a - \bar{T}_s}{T_{amb}} \right|$$

The errors squared e $(X1_i)^2$, is thus expressed as,

$$e(X1_i)^2 = S = \sum_{i=1}^{n} (X1_i - X2_i - X3 - nX4_i)^2 \qquad (A.11)$$

Differentiating S with respect to X3 and n respectively, and equating both equations to zero,

$$\frac{\partial s}{\partial X3} = -2 \sum_{i=1}^{n} (X1_i - X2_i - X3 - nX4_i) = 0 \qquad (A.12)$$

and

$$\frac{\partial s}{\partial n} = -2 \sum_{i=1}^{n} X4_i (X1_i - X2_i - X3 - nX4_i) = 0 \qquad (A.13)$$

Equation A.12 can be written as,

$$\sum X1_i - \sum X2_i - nX3 - n \sum X4_i = 0 \qquad (A.14)$$

Thus,

$$X3 = \frac{1}{n} \sum X1_i - \sum X2_i - n \sum X4_i \qquad (A.15)$$

Expanding equation (A.13),

$$\sum(X4_i.X1_i) - \sum(X4_i.X2_i) - X3 \sum X4_i - n \sum(X4_i)^2 = 0 \qquad (A.16)$$

Substituting equation (A.15) into (A.16) and rearranging,

$$n = \frac{n \sum(X4_i.X1_i).n \sum(X4_i.X2_i)-(\sum X4_i)(\sum X1_i)+(\sum X4_i)(\sum X2_i)}{n \sum(X4_i)^2 - (\sum X4_i)^2} \qquad (A.17)$$

The value of n can then be used in equation (A.15) to evaluate X3, and

$$\beta = \exp(X3) \qquad (A.18)$$

The same procedure was used for equation (8.4), whre

$$X1 = \log_e (NU-2)$$

$$X2 = \log_e (Re^{0.5} Pr^{0.33})$$

$$X3 = \log_e \phi$$

$$X4 = \log_e (1/B)$$

The correlation coefficient is expressed as,

$$C = \left[1 - \frac{\sum(X1_i - X2_i - X3 - nX4_i)^2}{\sum(X1_i - \bar{X}1)^2} \right]^{\frac{1}{2}} \qquad (A.19)$$

Equations (A.15), (A.17) and (A.18) were used for data of both suspended and free-flight drop. A computer progam listed in Appendix A.1.2.1 was used to correlate the results according to the above equations.

```
 10 **A.1.1.1**CONSTANT AIR TEMPERATURE**
 20 ***************EQUATIONS 8.1&8.2
 25 I
 30 DIMENSION  Y(20),X(20)
 40 B=2.0
 50 N=20
 60 M=3
 70 S1=0.0
 80 S2=0.0
 90 S3=0.0
 100 S4=0.0
 110 READ*,Z
 120 READ*,(X(I),Y(I),I=1,N)
 130 DO 2 I=1,N
 140 S1=S1+(Y(I)-B)*X(I)**0.5*Z**0.33
 150 S2=S2+X(I)*X**0.67
 160 A2 CONTINUE
 170 A=S1/S2
 180 PRINT*,' RE         SH'
 190 PRINT*,'---------------'
 200 S=0.0
 210 S2=0.0
 220 DO 4 J=1,N
 230 Y1=B+A*X(J)**0.5*Z**0.33
 240 S=S+Y(J)
 250 S2=S2+(Y1-Y(J))**2
 260 PRINT,X(J),Y(J),Y1
 270 A4 CONTINUE
 280 S=S/N
 290 S1=0.0
 300 DO 6 K=1,N
 310 S1=S1+(Y(K)-S)**2.0
 320 A6 CONTINUE
 330 S1=S1/N
 340 C1=(1-S2/(N*S1))**0.5
 350 PRINT*,'CORRELARTION COEFFICIENT=',C1
 360 STOP
 370 END
READY.
```

```
 10 **A.1.2.1****VARIABLE AIR  TEMPERATURE****
 20 **************EQUATIONS 8.3 & 8.4
 25 I
 30 DIMENTION Y(100),Z(100),W(100)
 40 N=80
 50 S1=0.0
 60 S2=0.0
 70 S3=0.0
 80 S4=0.0
 90 S5=0.0
 100 S6=0.0
 110 READ*(Y(I),Z(I),W(I),I=1,N)
 120 DO 3 I=1,N
 130 S1=S1+LOG(Y(I)-2.0)
 140 S2=S2+LOG(Z(I))
 150 S3=S3+LOG(W(I))
 160 S4=S4+(LOG(W(I)))*(LOG(Y(I)-2))
 170 S5=S5+(LOG(Z(I)))*LOG(W(I)))
 180 S6=S6+(LOG(W(I)))**2.0
 190 A 3 CONTINUE
 200 B=(N*S5+S1*S3-N*S4-S2*S3)/(S3*2.0-N*S6)
 210 X=(S1-S2-B*S3)/N
 220 X=EXP(X)
 230 PRINT*,"  SH    "
 240 PRINT*,"------"
 250 S1=0.0
 260 S2=0.0
 270 DO 5 J=1,N
 280 U=W(J)**B*Z(J)
 290 C1=2+X*U
 300 S1=S1+Y(J)
 310 S2=S2+(Y(I)-Y(J))**2.0
 320 PRINT*,Y(J),Y1
 330 A 5 CONTINUE
 340 S1=S1/N
 350 S3=0.0
 360 DO 7 K=1,N
 370 S3=S3+(Y(K)-S1)**2.0
 380 A 7 CONTINUE
 390 S3=S3/N
 400 C1=(1-S2/(N*S3))**0.5
 410 PRINT*,"CORRELATION COEFFICIENT=",C1
 420 STOP
 430 END
READY.
```

A.2 Data for Evaporation Characteristics of Suspended Water Drops

Table A1

Air Temperature = 21°C
Drop Temperature = 7°C
Drop Diameter = 2×10^{-3}m

Air Flowrate $kg.s^{-1} \times 10^{-4}$	Inlet Air Humidity $kg/kg \times 10^{-3}$	Outlet Air Humidity $kg/kg \times 10^{-3}$
2.4	2.2	2.8
4.1	2.2	2.6
6.7	2.2	2.5
9.2	2.3	2.5
12.1	2.3	2.4
15.2	2.3	2.4
18.5	2.3	2.4

Table A2

Air Temperature = 21°C
Drop Temperature = 7°C
Drop Diameter = 5×10^{-3} m

Air Flowrate $kg.s^{-1} \times 10^{-4}$	Inlet Air Humidity $kg/kg \times 10^{-3}$	Outlet Air Humidity $kg/kg \times 10^{-3}$
2.4	2.2	2.5
4.1	2.3	2.5
6.7	2.3	2.5
9.2	2.3	2.5
12.1	2.3	2.4
15.2	2.3	2.4
18.5	2.4	2 4

Table A3

Air Temperature = 21°C
Drop Temeprature = 7°C
Drop Diameter = 8×10^{-3} m

Air Flowrate $kg.s^{-1} \times 10^{-4}$	Inlet Air Humidity $kg/kg \times 10^{-3}$	Outlet Air Humidity $kg/kg \times 10^{-3}$
2.4	2.3	2.6
4.1	2.3	2.5
6.7	2.3	2.5
9.2	2.3	2.5
12.1	2.3	2.4
15.2	2.3	2.4
18.5	2.3	2.4

Table A4

Air Temperature = 50°C
Drop Temperature = 18.1°C
Drop Diameter = 2×10^{-3}m

Air Flowrate $kg.s^{-1} \times 10^{-4}$	Inlet Air Humidity $kg/kg \times 10^{-3}$	Outlet Air Humidity $kg/kg \times 10^{-3}$
2.4	4.7	5.4
4.1	4.7	5.2
6.7	4.8	5.1
9.2	4.8	5.1
12.1	4.9	5.1
15.2	4.9	5.1
18.5	4.9	5.0

Table A5

Air Temperature = 50°C
Drop Temperature = 18.1°C
Drop Diameter = 5×10^{-3}m

Air Flowrate $kg.s^{-1} \times 10^{-4}$	Inlet Air Humidity $kg/kg \times 10^{-3}$	Outlet Air Humidity $kg/kg \times 10^{-3}$
2.4	4.7	5.3
4.1	4.7	5.2
6.7	4.7	5.0
9.2	4.8	5.0
12.1	4.8	5.0
15.2	4.9	5.0
18.5	4.9	5.0

Table A6

Air Temperature = 50°C
Drop Temperature = 18.1°C
Drop Diameter = 8×10^{-3}m

Air Flowrate $kg.s^{-1} \times 10^{-4}$	Inlet Air Humidity $kg/kg \times 10^{-3}$	Outlet Air Humidity $kg/kg \times 10^{-3}$
2.4	4.7	5.4
4.1	4.7	5.2
6.7	4.8	5.1
9.2	4.8	5.1
12.1	4.8	5.0
15.2	4.8	5.0
18.5	4.8	5.0

Table A7

Air Temperature = 84°C
Drop Temperature = 27.4°C
Drop Diameter = 2×10^{-3}m

Air Flowrate $kg.s^{-1} \times 10^{-4}$	Inlet Air Humidity $kg/kg \times 10^{-3}$	Outlet Air Humidity $kg/kg \times 10^{-3}$
2.4	8.7	9.6
4.1	8.7	9.4
6.7	8.7	9.2
9.2	8.8	9.1
12.1	8.8	9.1
15.2	8.8	9.1
18.5	9.0	9.0

Table A8

Air Temperature = 84°C
Drop Temperature = 27.4°C
Drop Diameter = 5×10^{-3}m

Air Flowrate $kg.s^{-1} \times 10^{-4}$	Inlet Air Humidity $kg/kg \times 10^{-3}$	Outlet Air Humidity $kg/kg \times 10^{-3}$
2.4	8.7	9.5
4.1	8.7	9.3
6.7	8.7	9.1
9.2	8.7	9.0
12.1	8.8	9.0
15.2	8.8	9.0
18.5	8.8	9.0

Table A9

Air Temperature = 84°C
Drop Temperature = 27.4°C
Drop Diameter = 8 x 10^{-3}m

Air Flowrate $kg.s^{-1} \times 10^{-4}$	Inlet Air Humidity kg/kg x 10^{-3}	Outlet Air Humidity kg/kg x 10^{-3}
2.4	8.7	9.8
4.1	8.7	9.5
6.7	8.7	9.2
9.2	8.7	9.1
12.1	8.8	9.1
15.2	8.8	9.1
18.5	8.8	9.0

Table A10

Air Temperature = 120°C
Drop Temperature = 34.8°C
Drop Diameter = 2 x 10^{-3}m

Air Flowrate $kg.s^{-1} \times 10^{-4}$	Inlet Air Humidity kg/kg x 10^{-3}	Outlet Air Humidity kg/kg x 10^{-3}
2.4	8.2	9.3
4.1	8.2	9.0
6.7	8.2	8.8
9.2	8.2	8.6
12.1	8.2	8.6
15.2	8.3	8.6
18.5	8.3	8.5

Table A11

Air Temperature = 120°C
Drop Temperature = 34.8°C
Drop Diameter = 5 x 10^{-3}m

Air Flowrate $kg.s^{-1} \times 10^{-4}$	Inlet Air Humidity $kg/kg \times 10^{-3}$	Outlet Air Humidity $kg/kg \times 10^{-3}$
2.4	8.2	9.3
4.1	8.2	9.0
6.7	8.2	8.7
9.2	8.2	8.6
12.1	8.3	8.6
15.2	8.3	8.6
18.5	8.3	8.5

Table A12

Air Temperature = 120°C
Drop Temperature = 34.8°C
Drop Diameter = 8 x 10^{-3}m

Air Flowrate $kg.s^{-1} \times 10^{-4}$	Inlet Air Humidity $kg/kg \times 10^{-3}$	Outlet Air Humidity $kg/kg \times 10^{-3}$
2.4	8.2	9.3
4.1	8.2	9.0
6.7	8.3	8.8
9.2	8.3	8.7
12.1	8.3	8.6
15.2	8.3	8.5
18.5	8.3	8.5

Table A13

Air Temperature = 21°C
Drop Temperature = 7°C
Air Velocity = 2.694 $m.s^{-1}$

Time Sec	Drop Diameter mm	(Drop Diameter)^2 mm^2
10	4.1	17.1
20	4.0	16.5
40	3.9	15.5
60	3.8	14.5
80	3.6	13.5
100	3.5	12.5
120	3.4	11.5
140	3.2	10.5
160	3.0	9.5
180	2.9	8.5
200	2.7	7.6
220	2.6	6.7
240	2.4	5.8
260	2.2	4.9
280	2.0	4.0

Table A14

Air Temperature = 30°C
Drop Temperature = 10.6°C
Air Velocity = 2.694 $m.s^{-1}$

Time Sec	Drop Diameter mm	(Drop Diameter)^2 mm^2
10	5.5	31.2
20	5.4	30.0
30	5.3	28.8
40	5.2	27.6
50	5.1	26.4
60	5.0	25.3
70	4.9	24.2
80	4.7	22.9
90	4.6	21.8
100	4.5	20.7
110	4.4	19.6
120	4.3	18.6

Table A15

Air Temperature = 40°C
Drop Temperature = 15.8°C
Air Velocity = 2.694 $m.s^{-1}$

Time Sec	Drop Diameter mm	(Drop Diameter)^2 mm^2
20	3.8	14.5
40	3.6	13.1
60	3.4	11.6
80	3.2	10.2
100	2.9	8.8
120	2.7	7.5
140	2.4	6.1
160	2.2	4.8
180	1.8	5.5

Table A16

Air Temperature = 50°C
Drop Temperature = 18.1°C
Air Velocity = 2.694 $m.s^{-1}$

Time Sec	Drop Diameter mm	(Drop Diameter)^2 mm^2
20	5.0	25.2
40	4.8	23.3
60	4.6	21.7
80	4.5	20.2
100	4.2	18.1
120	4.0	16.4
140	3.8	14.7
160	3.6	13.0
180	3.3	12.2
200	3.1	9.6
220	2.8	8.0
240	2.5	6.3
260	2.1	4.7

Table A17

Air Temperature = 65°C
Drop Temperature = 23.3°C
Air Velocity = 2.694 $m.s^{-1}$

Time Sec	Drop Diameter mm	(Drop Diameter)^2 mm^2
15	4.8	23.1
30	4.6	21.2
45	4.4	19.3
60	4.2	17.7
75	3.9	15.9
90	3.7	14.1
105	3.5	12.4
120	3.2	10.7
135	3.0	9.1
150	2.7	7.5
165	2.4	5.8
180	2.0	4.2

Table A.18

Air Temperature = 80°C
Drop Temperature = 27.0°C
Air Velocity = 2.694 $m.s^{-1}$

Time Sec	Drop Diameter mm	(Drop Diameter)^2 mm^2
15	5.0	25.0
30	4.7	22.7
45	4.5	20.6
60	4.2	18.4
75	4.0	16.3
90	3.7	14.2
105	3.4	12.0
120	3.1	10.1
135	2.8	8.2
150	2.5	6.3
165	2.1	4.4

Table A.19

Air Temperature = 95°C
Drop Temperature = 29.0°C
Air Velocity = 2.694 $m.s^{-1}$

Time Sec	Drop Diameter mm	(Drop Diameter)^2 mm^2
15	5.0	25.0
30	4.7	22.5
45	4.5	20.3
60	4.2	17.9
75	3.9	15.6
90	3.6	13.3
105	3.3	11.0
120	2.9	8.8
135	2.5	6.5
150	2.0	4.0

A.3 Data for Evaluation Characteristics of Free-Flight Drops

Table A20

Air Temperature = 35°C
Drop Temperature = 13.2°C
Nozzle Size = 2.0 mm

Time Sec	Equivalent Drop Diameter m x 10^{-3}	Air Velocity $m.s^{-1}$	Mass kgx10^{-6}
60	3.2	5.5	34.4
120	3.1	5.4	31.1
180	3.0	5.4	29.4
240	2.9	5.3	24.2
300	2.7	5.3	20.7
360	2.6	5.2	16.6
420	1.7	5.1	13.0
480	1.7	5.0	12.2
540	1.5	4.8	10.4
600	1.5	4.8	6.0

Table A21

Air Temperature = 35°C
Drop Temperature = 13.2°C
Nozzle Size = 3.00 mm

Time Sec	Equivalent Drop Diameter m x 10^{-3}	Air Velocity $m.s^{-1}$	Mass kgx10^{-6}
60	4.8	5.7	47.3
120	4.3	5.6	45.5
180	4.2	5.6	40.4
240	4.2	5.5	33.2
300	4.1	5.3	24.1
360	3.3	5.3	21.5
420	2.7	5.2	17.9
480	1.9	5.2	16.8
540	1.8	5.1	14.3
600	1.6	4.9	8.2

Table A22

Air Temperature = 35°C
Drop Temperature = 13.2°C
Nozzle Size = 4.00 mm

Time Sec	Equivalent Drop Diameter m x 10^{-3}	Air Velocity $m.s^{-1}$	Mass kgx10^{-6}
60	6.2	5.9	61.1
120	6.1	5.8	54.7
180	6.0	5.7	48.0
240	5.3	5.6	44.3
300	5.2	5.5	38.1
360	4.2	5.5	32.9
420	4.0	5.4	26.5
480	3.1	5.3	22.4
540	2.5	5.3	19.6
600	2.4	5.0	11.1

Table A23

Air Temperature = 68°C
Drop Temperature = 25.9°C
Nozzle Size = 2 mm

Time Sec	Equivalent Drop Diameter m x 10^{-3}	Air Velocity $m.s^{-1}$	Mass kgx10^{-6}
45	3.4	5.4	31.5
90	2.8	5.4	30.4
135	2.8	5.4	25.9
180	2.0	5.3	24.0
225	1.8	5.3	20.6
270	1.7	5.2	17.5
315	1.5	5.1	15.2
360	1.4	5.0	12.7
405	1.4	4.8	9.5
450	1.3	4.8	6.2

Table A24

Air Temperature = 68°C
Drop Temperature = 25.9°C
Nozzle Size = 3mm

Time Sec	Equivalent Drop Diameter m x 10^{-3}	Air Velocity $m.s^{-1}$	Mass kgx10^{-6}
45	4.6	5.6	44.5
90	4.4	5.6	40.0
135	3.2	5.5	36.6
180	3.1	5.4	31.1
225	2.8	5.4	27.3
270	2.6	5.3	25.6
315	1.8	5.3	22.4
360	1.4	5.2	17.3
405	1.4	5.0	12.2
450	1.3	4.7	8.8

Table A25

Air Temperature = 68°C
Drop Temperature = 25.9°C
Nozzle Size = 4mm

Time Sec	Equivalent Drop Diameter m x 10^{-3}	Air Velocity $m.s^{-1}$	Mass kgx10^{-6}
45	5.7	5.9	64.8
90	5.4	5.9	60.6
135	5.3	5.8	54.9
180	5.2	5.7	46.1
225	4.0	5.6	42.4
270	3.8	5.5	36.9
315	3.4	5.4	31.2
360	2.3	5.4	28.5
405	2.2	5.3	21.7
450	2.0	5.2	17.3

Table A26

Air Temperature = 97°C
Drop Temperature = 32.8°C
Nozzle Size = 2 mm

Time Sec	Equivalent Drop Diameter m x 10^{-3}	Air Velocity $m.s^{-1}$	Mass kgx10^{-6}
30	3.3	5.4	32.1
60	2.8	5.4	30.8
90	2.7	5.4	28.0
120	2.4	5.3	25.1
150	2.0	5.3	23.5
180	1.9	5.3	21.4
210	1.7	5.3	19.7
240	1.5	5.3	17.0
270	1.4	5.1	15.6
300	1.1	5.1	14.5

Table A27

Air Temperature = 97°C
Drop Temperature = 32.8°C
Nozzle Size = 3mm

Time Sec	Equivalent Drop Diameter m x 10^{-3}	Air Velocity $m.s^{-1}$	Mass kgx10^{-6}
30	4.4	5.7	47.3
60	3.7	5.6	45.7
90	3.0	5.6	44.2
120	2.8	5.6	41.8
150	2.4	5.6	39.5
180	2.1	5.5	37.8
210	1.9	5.5	35.0
240	1.7	5.5	32.4
270	1.6	5.4	30.9
300	1.4	5.4	27.4

Table A28

Air Temperature = 97°C
Drop Temperature = 32.8°C
Nozzle Size = 4 mm

Time Sec	Equivalent Drop Diameter m x 10^{-3}	Air Velocity $m.s^{-1}$	Mass kgx10^{-6}
30	5.8	5.9	63.6
60	5.3	5.8	59.2
90	4.4	5.8	56.1
120	3.5	5.8	54.2
150	3.4	5.7	50.7
180	3.1	5.7	46.8
210	2.7	5.6	42.6
240	2.0	5.6	40.5
270	1.8	5.5	38.6
300	1.6	5.5	34.5

Table A29

Air Temperature = 125°C
Drop Temperature = 35.9°C
Nozzle Size = 2 mm

Time Sec	Equivalent Drop Diameter m x 10^{-3}	Air Velocity $m.s^{-1}$	Mass kgx10^{-6}
15	3.4	5.5	33.6
30	3.1	5.5	32.2
45	2.9	5.4	27.2
60	2.5	5.4	26.5
75	2.3	5.3	24.4
90	2.1	5.3	22.3
105	2.0	5.3	20.1
120	1.8	5.2	16.7
135	1.4	5.2	16.3
150	1.1	5.1	15.2

Table A30

Air Temperature = 125°C
Drop Temperature = 35.9°C
Nozzle Size = 3 mm

Time Sec	Equivalent Drop Diameter m x 10^{-3}	Air Velocity $m.s^{-1}$	Mass kgx10^{-6}
15	4.5	5.7	49.2
30	4.1	5.7	46.9
45	3.9	5.7	43.2
60	3.6	5.6	39.4
75	3.3	5.5	35.1
90	2.8	5.5	32.2
105	2.4	5.4	30.7
120	2.0	5.4	27.0
135	1.8	5.3	25.5
150	1.5	5.3	22.0

Table A31

Air Temperature = 125°C
Drop Temperature = 35.9°C
Nozzle Size = 4 mm

Time Sec	Equivalent Drop Diameter m x 10^{-3}	Air Velocity $m.s^{-1}$	Mass kgx10^{-6}
15	5.6	5.9	60.0
30	5.4	5.8	56.5
45	4.8	5.8	53.6
60	4.4	5.7	50.3
75	4.0	5.6	45.6
90	3.5	5.6	42.1
105	3.1	5.5	37.9
120	2.8	5.3	34.7
135	2.3	5.4	30.8
150	2.0	5.3	23.7

APPENDIX B

Tables B1 - B26
Data for Evaluation of Drying Characteristics of Drops of Sodium Sulphate Decahydrate Solutions, and Different Inorganic Powders Solutions.

The data listed are, for convenience, as calculated i.e. without rounding-up. It is not intended to imply a greater accuracy that is indicated on page 118.

B.1 Drying Characteristics of Sodium Sulphate Decahydrate Solution Drops

Table B1

Sodium Sulphate Decahydrate solution = 60% wt/wt
Drop Diameter = 4×10^{-3} m
Air Temperature = 120°C
Air Velocity = 0.9 $m.s^{-1}$
Inlet Air Humidity = 7.8×10^{-3} kg/kg

Time Min.	Outlet Air Humidity kg/kg x 10^{-3}
0.1	8.1
1	8.2
2	8.0
3	7.9
4	7.9
5	7.9
6	7.9
7	7.9
8	7.9
9	7.9
10	7.9
15	7.9
20	7.9
25	7.9
30	7.9

Table B2

Sodium Sulphate Decahydrate solution = 50% wt/wt
Drop Diameter = 6×10^{-3} m
Air Temperature = 100°C
Air Velocity = 0.1 $m.s^{-1}$
Inlet Air Humidity = 7.9×10^{-3} kg/kg

Time Min.	Outlet Air Humidity kg/kg x 10^{-3}
0.1	8.2
1	8.3
2	8.5
3	8.6
4	8.3
5	8.3
6	8.1
7	8.1
8	8.1
9	8.0
10	8.0
15	8.0
20	7.9
25	7.9
30	7.9

Table B3

Sodium Sulphate Decahydrate solution = 50% wt/wt
Drop Diameter = 4×10^{-3} m
Air Temperature = 120°C
Air Velocity = 0.9 $m.s^{-1}$
Inlet Air Humidity = 8.3×10^{-3} kg/kg

Time Min.	Outlet Air Humidity kg/kg x 10^{-3}
0.1	9.0
1	9.2
2	9.0
3	9.0
4	8.9
5	8.9
6	8.9
7	8.9
8	8.91
9	8.91
10	8.8
15	8.8
20	8.8
25	8.8
30	8.8

Table B4

Sodium Sulphate Decahydrate solution = 50% wt/wt
Drop Diameter = 4×10^{-3} m
Air Temperature = 100°C
Air Velocity = 0.9 $m.s^{-1}$
Inlet Air Humidity = 8.3×10^{-3} kg/kg

Time Min.	Outlet Air Humidity kg/kg x 10^{-3}
0.1	8.7
1	8.9
2	9.0
3	8.6
4	8.5
5	8.5
6	8.5
7	8.5
8	8.5
9	8.5
10	8.5
15	8.5
20	8.5
25	8.5
30	8.5

Table B5

Sodium Sulphate Decahydrate solution = 50% wt/wt
Drop Diameter = 4×10^{-3} m
Air Temperature = 100°C
Air Velocity = 0.1 $m.s^{-1}$
Inlet Air Humidity = 8.3×10^{-3} kg/kg

Time Min.	Outlet Air Humidity kg/kg x 10^{-3}
0.1	9.0
1	9.2
2	9.2
3	9.0
4	9.0
5	8.8
6	8.8
7	8.8
8	8.8
9	8.8
10	8.8
15	8.8
20	8.8
25	8.8
30	8.8

Table B6

Sodium Sulphate Decahydrate solution = 60% wt/wt
Drop Diameter = 4×10^{-3} m
Air Temperature = 100°C
Air Velocity = 1.1 $m.s^{-1}$
Inlet Air Humidity = 8.1×10^{-3} kg/kg
Outlet Air Humidity = 8.6×10^{-3} kg/kg

Time Min.	Crust Thickness (mm) x 10^{-2}
5	4.8
10	6.4
15	9.1
20	10.1
25	11.0
30	11.6

Table B7

Sodium Sulphate Decahydrate solution = 60% wt/wt
Drop Diameter = 4×10^{-3} m
Air Temperature = 120°C
Air Velocity = 1.1 $m.s^{-1}$
Inlet Air Humidity = 8.7×10^{-3} kg/kg
Outlet Air Humidity = 9.1×10^{-3} kg/kg

Time Min.	Crust Thickness (mm) $\times 10^{-2}$
5	6.2
10	9.1
15	10.8
20	12.5
25	13.2
30	14.6

Table B8

Sodium Sulphate Decahydrate solution = 50% wt/wt
Drop Diameter = 4×10^{-3} m
Air Temperature = 120°C
Air Velocity = 1.1 $m.s^{-1}$
Inlet Air Humidity = 8.6×10^{-3} kg/kg
Outlet Air Humidity = 9.1×10^{-3} kg/kg

Time Min.	Crust Thickness (mm) $\times 10^{-2}$
5	5.2
10	7.8
15	10.0
20	11.7
25	12.6
30	13.9

Table B9

Sodium Sulphate Decahydrate solution = 50% wt/wt
Drop Diameter = 4×10^{-3} m
Air Temperature = 120°C
Air Velocity = 0.6 $m.s^{-1}$
Inlet Air Humidity = 8.1×10^{-3} kg/kg
Outlet Air Humidity = 8.6×10^{-3} kg/kg

Time Min.	Crust Thickness (mm) $\times 10^{-2}$
5	4.7
10	7.3
15	9.5
20	10.9
25	11.6
30	12.7

B.2 Drying Characteristics of Drops of Inorganic Powder Solutions

Table B10

Inorganic Powder Formulation C
Solution Solids Content = 40% wt/wt
Density = 1.257×10^{3} kg.m^{-3}
Drop Diameter = 6×10^{-3} m
Air Temperature = 110°C
Air Velocity = 0.8 m.s^{-1}
Inlet Air Humidity = 6.4×10^{-3} kg/kg

Time Sec	Outlet Air Humidity kg/kg x 10^{-3}
10	6.6
20	6.9
30	7.1
40	7.2
50	7.3
60	7.3
70	7.3
80	7.3
90	7.3
100	7.3
110	7.3
120	7.3
130	7.2
140	7.2
150	7.2
160	7.2
170	7.2
180	7.1

Time Sec	Outlet Air Humidity kg/kg x 10^{-3}
190	7.1
200	7.1
210	7.1
220	7.1
230	7.0
240	7.0
250	7.0
260	7.0
270	7.0
280	7.0
290	7.0
300	7.0
360	7.0
420	6.9
600	6.9
660	6.8
900	6.7

Table B11

Inorganic Powder Formulation C
Solution Solids Content = 40% wt/wt
Density = 1.257×10^{3} kg.m^{-3}
Drop Diameter = 6×10^{-3} m
Air Temperature = 130°C
Air Velocity = 0.8 m.s^{-1}
Inlet Air Humidity = 6.4×10^{-3} kg/kg

Time Sec	Outlet Air Humidity kg/kg x 10^{-3}
10	7.0
20	7.1
30	7.2
40	7.3
50	7.4
60	7.4
70	7.4
80	7.4
90	7.4
100	7.4
110	7.4
120	7.4
130	7.4
140	7.4
150	7.4
160	7.4
170	7.3
180	7.3

Time Sec	Outlet Air Humidity kg/kg x 10^{-3}
190	7.3
200	7.3
210	7.2
220	7.2
230	7.2
240	7.2
250	7.2
260	7.2
270	7.2
280	7.2
290	7.2
300	7.2
360	7.1
420	7.1
600	7.1
660	7.1
900	7.1

Table B12

Inorganic Powder Formulation C
Solution Solids Content = 50% wt/wt
Density = 1.383 x 10^3 $kg.m^{-3}$
Drop Diameter = 6 x 10^{-3} m
Air Temperature = 130°C
Air Velocity = 0.8 $m.s^{-1}$
Inlet Air Humidity = 6.2 x 10^{-3} kg/kg

Time Sec	Outlet Air Humidity kg/kg x 10^{-3}
10	6.7
20	6.9
30	6.9
40	7.0
50	7.0
60	7.0
70	7.0
80	7.0
90	7.0
100	7.0
110	7.0
120	7.0
130	6.9
140	6.9
150	6.9
160	6.9
170	6.9
180	6.9

Time Sec	Outlet Air Humidity kg/kg x 10^{-3}
190	6.9
200	6.9
210	6.9
220	6.9
230	6.9
240	6.9
250	6.9
260	6.9
270	6.9
280	6.9
290	6.9
300	6.9
360	6.9
420	6.8
600	6.8
660	6.8
900	6.8

Table B13

Inorganic Powder Formulation C
Solution Solids Content = 60% wt/wt
Density = 1.42×10^{3} kg.m^{-3}
Drop Diameter = 6×10^{-3} m
Air Temperature = 130°C
Air Velocity = 0.8 m.s^{-1}
Inlet Air Humidity = 6.4×10^{-3} kg/kg

Time Sec	Outlet Air Humidity kg/kg x 10^{-3}
10	6.6
20	6.7
30	6.9
40	7.0
50	7.1
60	7.1
70	7.1
80	7.1
90	7.1
100	7.1
110	7.1
120	7.1
130	7.1
140	7.1
150	7.1
160	7.1
170	7.1
180	7.1

Time Sec	Outlet Air Humidity kg/kg x 10^{-3}
190	7.1
200	7.1
210	7.1
220	7.1
230	7.1
240	7.1
250	7.1
260	7.1
270	7.1
280	7.1
290	7.1
300	7.1
360	7.1
420	7.1
600	7.0
660	7.0
900	7.0

Table B14

Inorganic Powder Formulation C
Solution Solids Content = 70% wt/wt
Density = 1.55 x 10^3 kg.m^{-3}
Drop Diameter = 6 x 10^{-3} m
Air Temperature = 130°C
Air Velocity = 0.8 m.s^{-1}
Inlet Air Humidity = 6.3 x 10^{-3} kg/kg

Time Sec	Outlet Air Humidity kg/kg x 10^{-3}
10	6.5
20	6.6
30	6.6
40	6.6
50	6.6
60	6.6
70	6.6
80	6.6
90	6.6
100	6.6
110	6.6
120	6.6
130	6.6
140	6.6
150	6.6
160	6.6
170	6.6
180	6.6

Time Sec	Outlet Air Humidity kg/kg x 10^{-3}
190	6.6
200	6.6
210	6.6
220	6.6
230	6.6
240	6.6
250	6.6
260	6.6
270	6.6
280	6.6
290	6.6
300	6.6
360	6.6
420	6.6
600	6.5
660	6.5
900	6.5

Table B15

Inorganic Powder Formulation D
Solution Solids Content = 25% wt/wt
Density 1.152 x 10^3 $kg.m^{-3}$
Drop Diameter = 4 x 10^{-3} m
Air Temperature = 34°C
Air Velocity = 0.7 $m.s^{-1}$
Inlet Air Humidity = 7.0 x 10^{-3} kg/kg

Time Sec	Outlet Air Humidity kg/kg x 10^{-3}	Time Sec	Outlet Air Humidity kg/kg x 10^{-3}
10	7.1	100	7.1
20	7.1	110	7.1
30	7.1	120	7.1
40	7.1	130	7.1
50	7.1	140	7.1
60	7.1	150	7.1
70	7.1	160	7.1
80	7.1	170	7.1
90	7.1	180	7.1

Table B16

Inorganic Powder Formulation D
Solution Solids Content = 25% wt/wt
Density 1.152 x 10^3 $kg.m^{-3}$
Drop Diameter = 4. x 10^{-3} m
Air Temperature = 64°C
Air Velocity = 0.7 $m.s^{-1}$
Inlet Air Humidity = 7.0 x 10^{-3} kg/kg

Time Sec	Outlet Air Humidity kg/kg x 10^{-3}	Time Sec	Outlet Air Humidity kg/kg x 10^{-3}
10	7.3	100	7.4
20	7.4	110	7.4
30	7.6	120	7.4
40	7.7	130	7.4
50	7.8	140	7.4
60	7.7	150	7.4
70	7.7	160	7.4
80	7.6	170	7.4
90	7.5	180	7.4

Table B17

Inorganic Powder Formulation D
Solution Solids Content = 25% wt/wt
Density 1.152 x 10^3 $kg.m^{-3}$
Drop Diameter = 4. x 10^{-3} m
Air Temperature = 93°C
Air Velocity = 0.8 $m.s^{-1}$
Inlet Air Humidity = 6.5 x 10^{-3} kg/kg

Time Sec	Outlet Air Humidity kg/kg x 10^{-3}	Time Sec	Outlet Air Humidity kg/kg x 10^{-3}
10	6.9	100	7.3
20	7.0	110	7.3
30	7.2	120	7.3
40	7.2	130	7.2
50	7.2	140	7.2
60	7.2	150	7.2
70	7.2	160	7.0
80	7.2	170	7.0
90	7.3	180	7.0

Table B18

Inorganic Powder Formulation D
Solution Solids Content = 25% wt/wt
Density 1.152 x 10^3 $kg.m^{-3}$
Drop Diameter = 4. x 10^{-3} m
Air Temperature = 130°C
Air Velocity = 0.9 $m.s^{-1}$
Inlet Air Humidity = 6.2 x 10^{-3} kg/kg

Time Sec	Outlet Air Humidity kg/kg x 10^{-3}	Time Sec	Outlet Air Humidity kg/kg x 10^{-3}
10	6.7	100	7.7
20	7.5	110	7.6
30	7.5	120	7.5
40	7.6	130	7.5
50	7.7	140	7.4
60	7.9	150	7.4
70	7.9	160	7.4
80	7.9	170	7.3
90	7.9	180	7.3

Table B19

Inorganic Powder Formulation D
Solution Solids Content = 25% wt/wt
Density 1.152 x 10^3 $kg.m^{-3}$
Drop Diameter = 4 x 10^{-3} m
Air Temperature = 165°C
Air Velocity = 1.0 $m.s^{-1}$
Inlet Air Humidity = 7.0 x 10^{-3} kg/kg

Time Sec	Outlet Air Humidity kg/kg x 10^{-3}
10	8.7
20	8.9
30	9.1
40	9.1
50	9.2
60	9.1
70	8.7
80	8.7
90	8.7

Time Sec	Outlet Air Humidity kg/kg x 10^{-3}
100	8.7
110	8.7
120	8.7
130	8.7
140	8.7
150	8.7
160	8.6
170	8.6
180	8.6

Table B20

Inorganic Powder Formulation D
Solution Solids Content = 25% wt/wt
Density 1.152 x 10^3 $kg.m^{-3}$
Drop Diameter = 4 x 10^{-3} m
Air Temperature = 200°C
Air Velocity = 1.1 $m.s^{-1}$
Inlet Air Humidity = 6.9 x 10^{-3} kg/kg

Time Sec	Outlet Air Humidity kg/kg x 10^{-3}
10	8.4
20	8.8
30	9.0
40	9.2
50	9.2
60	9.0
70	9.4
80	10.2
90	12.1
100	12.1
110	11.7
120	10.8
130	9.7
140	10.8
150	11.1

Time Sec	Outlet Air Humidity kg/kg x 10^{-3}
160	10.3
170	10.8
180	9.9
190	10.0
200	9.4
210	8.8
220	8.7
230	8.8
240	8.8
250	8.4
260	8.0
270	7.9
280	7.9
290	7.9
300	7.9

Table B21

Inorganic Powder Formulation E
Solution Solids Content = 25% wt/wt
Density 1.13 x 10^3 $kg.m^{-3}$
Drop Diameter = 4 x 10^{-3} m
Air Temperature = 34°C
Air Velocity = 0.7 $m.s^{-1}$
Inlet Air Humidity = 7.0 x 10^{-3} kg/kg

Time Sec	Outlet Air Humidity kg/kg x 10^{-3}
10	7.1
20	7.1
30	7.1
40	7.2
50	7.2
60	7.2
70	7.1
80	7.1
90	7.1

Time Sec	Outlet Air Humidity kg/kg x 10^{-3}
100	7.1
110	7.1
120	7.1
130	7.2
140	7.2
150	7.1
160	7.1
170	7.1
180	7.1

Table B22

Inorganic Powder Formulation E
Solution Solids Content = 25% wt/wt
Density 1.13 x 10^3 $kg.m^{-3}$
Drop Diameter = 4 x 10^{-3} m
Air Temperature = 64°C
Air Velocity = 0.7 $m.s^{-1}$
Inlet Air Humidity = 7.0 x 10^{-3} kg/kg

Time Sec	Outlet Air Humidity kg/kg x 10^{-3}
10	7.3
20	7.4
30	7.6
40	7.6
50	7.6
60	7.5
70	7.5
80	7.5
90	7.4
100	7.4
110	7.4

Time Sec	Outlet Air Humidity kg/kg x 10^{-3}
120	7.4
130	7.4
140	7.4
150	7.4
160	7.4
170	7.4
180	7.4
190	7.4
200	7.4
210	7.4

Table B23

Inorganic Powder Formulation E
Solution Solids Content = 25% wt/wt
Density 1.13 x 10^3 $kg.m^{-3}$
Drop Diameter = 4 x 10^{-3} m
Air Temperature = 93°C
Air Velocity = 0.8 $m.s^{-1}$
Inlet Air Humidity = 6.3 x 10^{-3} kg/kg

Time Sec	Outlet Air Humidity kg/kg x 10^{-3}	Time Sec	Outlet Air Humidity kg/kg x 10^{-3}
10	7.0	130	7.5
20	7.2	140	7.5
30	7.5	150	7.5
40	7.5	160	7.5
50	7.5	170	7.5
60	7.5	180	7.4
70	7.5	190	7.3
80	7.5	200	7.3
90	7.5	210	7.2
100	7.5	220	7.2
110	7.5	230	7.1
120	7.5		

Table B24

Inorganic Powder Formulation E
Solution Solids Content = 25% wt/wt
Density 1.13 x 10^3 $kg.m^{-3}$
Drop Diameter = 4 x 10^{-3} m
Air Temperature = 130°C
Air Velocity = 0.9 $m.s^{-1}$
Inlet Air Humidity = 6.1 x 10^{-3} kg/kg

Time Sec	Outlet Air Humidity kg/kg x 10^{-3}	Time Sec	Outlet Air Humidity kg/kg x 10^{-3}
10	7.7	100	7.8
20	8.1	110	7.8
30	8.2	120	7.8
40	8.2	230	7.8
50	8.2	140	7.7
60	8.1	150	7.6
70	8.1	160	7.6
80	7.9	170	7.6
90	7.8	180	7.6

Table B25

Inorganic Powder Formulation E
Solution Solids Content = 25% wt/wt
Density 1.13 x 10^3 $kg.m^{-3}$
Drop Diameter = 4 x 10^{-3} m
Air Temperature = 165°C
Air Velocity = 1.0 $m.s^{-1}$
Inlet Air Humidity = 7.1 x 10^{-3} kg/kg

Time Sec	Outlet Air Humidity kg/kg x 10^{-3}
10	8.0
20	9.7
30	9.9
40	10.3
50	10.3
60	10.3
70	9.7
80	9.7
90	9.7

Time Sec	Outlet Air Humidity kg/kg x 10^{-3}
100	9.7
110	9.7
120	9.7
230	9.7
140	9.7
150	9.7
160	9.7
170	9.7
180	9.7

Table B26

Inorganic Powder Formulation E
Solution Solids Content = 25% wt/wt
Density 1.13 x 10^3 $kg.m^{-3}$
Drop Diameter = 4 x 10^{-3} m
Air Temperature = 200°C
Air Velocity = 1.1 $m.s^{-1}$
Inlet Air Humidity = 6.9 x 10^{-3} kg/kg

Time Sec	Outlet Air Humidity kg/kg x 10^{-3}
10	8.9
20	9.2
30	10.4
40	10.4
50	10.8
60	10.8
70	10.8

Time Sec	Outlet Air Humidity kg/kg x 10^{-3}
80	10.7
90	10.8
100	10.6
110	10.6
120	10.6
130	10.6
140	12.4

APPENDIX C

Tables C1 - C17
Data for Evaluation of Drying Characteristics of Drops of Different Organic Paste Slurries and Organic Pigment Solutions

The data listed are, for convenience, as calculated i.e. without rounding-up. It is not intended to imply a greater accuracy that is indicated on page 118

C.1 Drying Characteristics of Drops of Organic Paste Slurries

Table C1

Organic Paste Formulation A
Slurry Solids Content = 12%
Density = 1.070×10^3 kg.m^{-3}
Air Temperature = 300°C
Drop Temperature = 75°C
Drop Diameter = 7×10^{-3}m
Air Velocity = 2.1 m.s^{-1}
Inlet Air Humidity = 8.1×10^{-3} kg/kg

Time Min.	Outlet Air Humidity kg/kg x 10^{-3}
10	10.9
20	11.1
30	11.3
40	11.4
50	11.7
60	11.7
70	11.8
80	11.9
90	11.9

Time Min.	Outlet Air Humidity kg/kg x 10^{-3}
100	12.0
110	12.0
120	12.1
130	13.3
140	12.7
150	12.1
160	11.8
170	11.7
180	11.7

Table C2

Organic Paste Formulation A
Slurry Solids Content = 12%
Dispersol Solution = 13%
Density = 1.065×10^3 kg.m^{-3}
Air Temperature = 300°C
Drop Temperature = 72.8°C
Drop Diameter = 7×10^{-3}m
Air Velocity = 2.1 m.s^{-1}
Inlet Air Humidity = 7.3×10^{-3} kg/kg

Time Min.	Outlet Air Humidity kg/kg x 10^{-3}
10	10.4
15	10.4
20	10.4
25	10.3
30	10.8
35	10.9
40	11.2
50	11.4
60	11.5

Time Min.	Outlet Air Humidity kg/kg x 10^{-3}
70	11.3
80	11.2
95	11.3
100	11.4
110	11.4
120	11.4
130	11.2
140	11.3

Table C3

Organic Paste Formulation A
Slurry Solids Content = 12%
Sodium Chloride Solution = 13%
Density = 1.068 x 10^3 kg.m^{-3}
Air Temperature = 300°C
Drop Temperature = 71.2°C
Drop Diameter = 7 x 10^{-3}m
Air Velocity = 2.1 m.s^{-1}
Inlet Air Humidity = 7.3 x 10^{-3} kg/kg

Time Min.	Outlet Air Humidity kg/kg x 10^{-3}
10	10.6
20	10.8
30	11.0
40	11.1
50	11.7
60	11.9
70	12.1
80	12.1
90	12.0
100	12.0
110	12.1
120	12.2
140	12.2
150	12.1
160	12.0

Table C4

Organic Paste Formulation A
Slurry Solids Content = 12%
Dispersol solution = 13%
Density = 1.095 x 10^3 kg.m^{-3}
Air Temperature = 300°C
Drop Temperature = 78.3°C
Drop Diameter = 7 x 10^{-3}m
Air Velocity = 2.1 m.s^{-1}
Inlet Air Humidity = 7.3 x 10^{-3} kg/kg

Time Min.	Outlet Air Humidity kg/kg x 10^{-3}
10	9.0
15	9.3
20	9.4
25	9.5
30	9.8
35	9.8
40	10.5
45	10.0
50	9.8
55	10.0
60	9.5
66	9.5
70	9.8
80	9.5
90	9.8
100	10.0
110	9.8

Table C5

Organic Paste Formulation A
Slurry Solids Content = 12%
Dispersol Solution = 13%
Density = 1.065×10^3 kg.m^{-3}
Air Temperature = 200°C
Drop Temperature = 51.8°C
Drop Diameter = 7×10^{-3}m
Air Velocity = 1.7 m.s^{-1}
Inlet Air Humidity = 8.4×10^{-3} kg/kg

Time (Sec)	Outlet Air Humidity kg/kg x 10^{-3}
10	9.5
15	10.1
20	10.0
25	10.1
30	10.1
35	10.3
40	10.3
45	10.3
50	10.4
55	10.7
60	10.5

Time (Sec)	Outlet Air Humidity kg/kg x 10^{-3}
65	10.5
70	10.6
75	10.5
80	10.8
85	10.5
90	10.4
100	10.5
110	10.5
120	10.5
130	10.5

Table C6

Organic Paste Formulation A
Slurry Solids Content = 15%
Dispersol Solution = 13%
Density = 1.076×10^3 kg.m^{-3}
Air Temperature = 200°C
Drop Temperature = 56.5°C
Drop Diameter = 7×10^{-3}m
Air Velocity = 1.7 m.s^{-1}
Inlet Air Humidity = 7.9×10^{-3} kg/kg

Time (Sec)	Outlet Air Humidity kg/kg x 10^{-3}
10	8.9
15	9.1
20	9.1
25	9.0
30	9.2
35	9.3
40	9.7
45	9.9
50	9.6
60	9.8

Time (Sec)	Outlet Air Humidity kg/kg x 10^{-3}
65	9.7
70	10.0
75	9.7
80	9.7
85	9.7
90	9.6
95	9.6
100	9.6
120	9.5
135	9.7

Table C7

Organic Paste Formulation A
Slurry Solids Content = 15%
Dispersol Solution = 13%
Density = 1.08×10^3 kg.m^{-3}
Air Temperature = 200°C
Drop Temperature = 54.7°C
Drop Diameter = 7×10^{-3}m
Air Velocity = 1.7 m.s^{-1}
Inlet Air Humidity = 7.9×10^{-3} kg/kg

Time (Sec)	Outlet Air Humidity kg/kg x 10^{-3}
10	9.0
15	9.1
20	9.2
30	9.4
35	9.3
40	9.4
45	9.6
50	9.7
55	9.7
60	9.7
70	9.7
80	9.8
85	9.8

Time (Sec)	Outlet Air Humidity kg/kg x 10^{-3}
90	9.9
100	9.3
105	9.8
110	9.7
115	9.8
120	9.9
135	9.8
140	10.0
150	9.8
160	9.8
170	9.7
180	9.7
190	9.6

Table C8

Organic Paste Formulation A
Slurry Solids Content = 18%
Dispersol Solution = 13%
Density = 1.095×10^3 kg.m^{-3}
Air Temperature = 200°C
Drop Temperature = 59.1°C
Drop Diameter = 7×10^{-3}m
Air Velocity = 1.7 m.s^{-1}
Inlet Air Humidity = 8.9×10^{-3} kg/kg

Time (Sec)	Outlet Air Humidity kg/kg x 10^{-3}
10	9.0
15	9.1
20	9.2
30	9.4
35	9.3
40	9.4
45	9.6
50	9.7
55	9.7
60	9.7
70	9.7

Time (Sec)	Outlet Air Humidity kg/kg x 10^{-3}
75	9.9
80	9.3
90	9.8
95	9.7
100	9.8
110	9.9
120	9.8
130	10.0
140	9.8
145	9.8
150	9.7

Table C9

Organic Paste Formulation B
Slurry Solids Content = 12%
Dispersol Solution = 13%
Density = 0.994 x 10^3 kg.m^{-3}
Air Temperature = 200°C
Drop Temperature = 49.6°C
Drop Diameter = 7 x 10^{-3}m
Air Velocity = 1.7 m.s^{-1}
Inlet Air Humidity = 9.2 x 10^{-3} kg/kg

Time (Sec)	Outlet Air Humidity kg/kg x 10^{-3}
10	10.9
20	11.2
30	11.7
40	11.8
50	11.8
60	11.8
70	11.7
80	11.6
90	11.6

Time (Sec)	Outlet Air Humidity kg/kg x 10^{-3}
100	11.6
110	11.5
120	11.5
130	11.7
140	11.3
150	11.2
160	11.1
170	10.9
180	10.7

Table C10

Organic Paste Formulation B
Slurry Solids Content = 15%
Dispersol Solution = 13%
Density = 1.1 x 10^3 kg.m^{-3}
Air Temperature = 200°C
Drop Temperature = 54°C
Drop Diameter = 7 x 10^{-3}m
Air Velocity = 1.7 m.s^{-1}
Inlet Air Humidity = 9.3 x 10^{-3} kg/kg

Time (Sec)	Outlet Air Humidity kg/kg x 10^{-3}
10	10.6
20	10.9
30	11.5
40	11.5
50	11.5
60	11.6
70	11.5
80	11.5
90	11.5
100	11.5

Time (Sec)	Outlet Air Humidity kg/kg x 10^{-3}
110	11.6
120	11.7
130	11.7
140	11.6
150	11.6
160	11.5
170	11.6
180	11.4
190	11.2
200	10.8

Table C11

Organic Paste Formulation B
Slurry Solids Content = 15%
Dispersol Solution = 13%
Density = 1.12×10^3 kg.m^{-3}
Air Temperature = 200°C
Drop Temperature = 52.3°C
Drop Diameter = 7×10^{-3}m
Air Velocity = 1.7 m.s^{-1}
Inlet Air Humidity = 9.3×10^{-3} kg/kg

Time (Sec)	Outlet Air Humidity kg/kg x 10^{-3}
10	10.9
20	11.1
30	11.6
40	11.6
50	11.7
60	11.7
70	11.7
80	11.7
90	11.6
100	11.6

Time (Sec)	Outlet Air Humidity kg/kg x 10^{-3}
110	11.7
120	11.6
130	11.5
140	11.6
150	11.4
160	11.4
170	11.2
180	11.3
190	10.6

Table C12

Organic Paste Formulation B
Slurry Solids Content = 18%
Dispersol Solution = 13%
Density = 1.13×10^3 kg.m^{-3}
Air Temperature = 200°C
Drop Temperature = 61°C
Drop Diameter = 7×10^{-3}m
Air Velocity = 1.7 m.s^{-1}
Inlet Air Humidity = 9.3×10^{-3} kg/kg

Time (Sec)	Outlet Air Humidity kg/kg x 10^{-3}
10	10.1
20	10.6
30	10.8
40	10.8
50	10.7
60	10.7
70	10.7

Time (Sec)	Outlet Air Humidity kg/kg x 10^{-3}
80	10.7
90	10.6
100	10.6
110	10.6
120	10.6
130	10.6
140	10.6

C.2 Drying Characteristics of Drops of Organic Pigment Solutions

C.2 Drying

Table C13

Organic Pigment A
Solution Solids Content = 22%
Air Temperature = 100°C
Drop Temperature = 38°C
Drop Diameter = 7×10^{-3}m
Air Velocity = 0.8 $m.s^{-1}$
Inlet Air Humidity = 6.73×10^{-3} kg/kg

Time (Sec)	Outlet Air Humidity kg/kg x 10^{-3}	Time (Sec)	Outlet Air Humidity kg/kg x 10^{-3}
10	7.0	70	7.1
20	7.0	80	7.1
30	7.1	90	7.1
40	7.1	100	7.0
50	7.1	110	7.0
60	7.1	120	7.0

Table C14

Organic Pigment A
Solution Solids Content = 22%
Air Temperature = 135°C
Drop Temperature = 43.2°C
Drop Diameter = 7×10^{-3}m
Air Velocity = 0.9 $m.s^{-1}$
Inlet Air Humidity = 6.7×10^{-3} kg/kg

Time (Sec)	Outlet Air Humidity kg/kg x 10^{-3}	Time (Sec)	Outlet Air Humidity kg/kg x 10^{-3}
10	7.2	70	7.3
20	7.3	80	7.3
30	7.3	90	7.3
40	7.3	100	7.2
50	7.3	110	7.2
60	7.3	120	7.2

Table C15

Organic Pigment B
Solution Solids Content = 22%
Air Temperature = 100°C
Drop Temperature = 40.7°C
Drop Diameter = 7×10^{-3}m
Air Velocity = 0.8 $m.s^{-1}$
Inlet Air Humidity = 6.7×10^{-3} kg/kg

Time (Sec)	Outlet Air Humidity kg/kg x 10^{-3}
10	6.9
20	6.9
30	7.0
40	7.0
50	7.0
60	7.0
70	6.9
80	6.9
90	6.9
100	6.9
110	6.9
120	6.9
130	6.9
140	6.9
150	6.2
160	6.2
170	6.9

Time (Sec)	Outlet Air Humidity kg/kg x 10^{-3}
180	6.9
190	6.9
200	6.9
210	6.9
220	6.9
230	6.9
240	6.9
250	6.9
260	6.9
270	6.9
280	6.9
290	6.9
300	6.9
310	6.9
320	6.9
330	6.9
340	6.9

Table C16

Organic Pigment B
Solution Solids Content = 22%
Air Temperature = 135°C
Drop Temperature = 48.1°C
Drop Diameter = 7×10^{-3}m
Air Velocity = 0.9 $m.s^{-1}$
Inlet Air Humidity = 6.7×10^{-3} kg/kg

Time (Sec)	Outlet Air Humidity kg/kg x 10^{-3}
10	6.9
20	7.0
30	7.0
40	7.0
50	7.0
60	7.1
70	7.2
80	7.2
90	7.2
100	7.2
110	7.2
120	7.2

Time (Sec)	Outlet Air Humidity kg/kg x 10^{-3}
130	7.2
140	7.1
150	7.1
160	7.1
170	7.1
180	7.1
190	7.0
200	7.0
210	7.0
220	7.062
230	7.062
240	7.062

Table C17

Organic Paste Formulation A
Slurry Solids Content = 18% wt/wt
Drop Diameter = 4×10^{-3} m
Air Temperature = 200°C
Air Velocity = 1.7 m.s^{-1}
Inlet Air Humidity = 8.9×10^{-3} kg/kg
Outlet Air Humidity = 9.8×10^{-3} kg/kg

Time (Sec)	Crust Thickness (mm) $\times 10^{-2}$
120	18.8
240	15.7
360	13.5
480	10.9
600	10.0
900	10.0

```
 10 **C.2
 20 **EVAPORATION FROM DROPLETS**
 25 *
 30 DIMENSION V(50),RHI(50),RHO(50),G(50),HI(50)
 35 DIMENSION HO(50),NA(50),KG(50),SH(50),KGP(50)
 40 REAL M,NA,KG
 50 REAL A,HI,HO
 60 READ*,N
 70 READ*,TA,TS,RD,PV,PP,R,M,T
 80 READ*,(V(I),RHI(I),RHO(I),I=1,N)
 90 PRINT*,"G     HI     HO     NA     KG     SH     KGP"
 100 PRINT*,"-------------------------------------"
 110 P=760.0
 120 A=18.0/29.0
 130 DE=1.2929*(273.16)/(273.16+TA)
 140 VIS=1.72E-5*(TA+273.16)/273.16
 150 DV=0.22((TA+273.16)/273.16)**1.75
 160 DO 5 J=1,N
 170 RE=DE*RD*V(J)/VIS
 180 SC=VIS/(DE*DV)
 190 HI(J)=A*RHI(J)*PV/((100P)-(RHI(J)*PV))
 200 HO(J)=A*RHO(J)*PV/((100P)-(RHO(J)*PV))
 210 G(J)=V(J)*DE/(1.0+HI(J))
 220 AA=22.0*RD**2.0/14.0
 230 NA(J)=(G(J)*(HO(J)-HI(J)))/AA
 240 KG(J)=(R/M)*NA(J)*(TA+273.16)/(PV-PP)
 250 SH(J)=KG(J)*RD/DV
 260 KGP(J)=DV*(2.0+0.501*RE**0.5*SC**0.33*((TA-TS)/T)**(-0.03))/RD
 270 PRINT*,G(J),HI(J),HO(J),NA(J),KG(J),SH(J),KGP(J)
 280 A 5 CONTINUE
 290 STOP
 300 END
READY.
```

APPENDIX D

Core Temperature Profile Measurements for Sodium Sulphate Decahydrate Solution and Inorganic Powder Solution.

Data for Crust Thermal Conductivity Evaluation

D.1 Core Temperature Measurements

Table D1

Sodium Sulphate Decahydrate Solution = 40% wt/wt
Air Velccity = 1 $m.s^{-1}$
Air Temperature = 20°C

Time (Sec)	Core Temperature °C
0	20.0
10	18.8
20	18.0
30	18.0
40	18.0
50	18.0
60	18.0
70	18.0
80	18.0
90	18.0
100	18.0
110	18.0
120	18.0
130	18.0
140	18.0
150	18.0
160	18.0
170	18.1
180	18.1
190	18.1
200	18.1
210	18.1
220	18.1
230	18.1
240	18.0
250	18.0
260	18.0
270	18.1
280	18.1
290	18.1
300	18.1
310	18.1

Time (Sec)	Core Temperature °C
320	18.1
330	18.1
340	18.1
350	18.2
360	18.2
390	18.2
420	18.2
450	18.3
480	18.3
510	18.3
540	18.3
570	18.1
600	18.1
630	18.0
660	18.0
690	18.0
720	18.1
750	18.1
780	18.2
810	18.2
840	18.2
900	18.2
960	18.4
1020	18.7
1080	19.0
1140	19.0
1200	19.2
1500	19.9
1980	20.0
2400	20.0
3600	20.0

Table D2

Inorganic Powder Formulation C solution = 40% wt/wt
Air Velocity = 1 $m.s^{-1}$
Air Temperature = 20°C

Time (Sec)	Core Temperature °C
0	20.0
10	18.0
20	17.9
30	17.5
40	17.3
50	17.2
60	17.2
70	17.5
80	17.6
90	17.8
100	17.9
110	18.0
120	18.0
130	18.0
140	18.0
150	18.1
160	18.2
170	18.5
180	18.6
190	18.7
200	18.8
210	18.9
220	19.0
230	19.0
240	19.0

Time (Sec)	Core Temperature °C
250	19.0
260	19.0
270	19.0
280	19.0
290	19.1
300	19.1
310	19.2
320	19.2
330	19.4
340	19.5
350	19.5
360	19.7
390	19.8
420	19.9
450	20.0
480	20.0
510	20.0
540	20.0
570	20.0
600	20.0
1200	20.0
1500	20.0
1800	20.0
3600	20.0

Table D3

Sodium Sulphate Decahydrate Solution = 40% wt/wt
Air Velocity = 1 $m.s^{-1}$
Air Temperature = 40°C

Time (Sec)	Core Temperature °C
0	25.0
10	25.7
20	26.0
30	26.8
40	27.2
50	27.9
60	28.1
70	28.5
80	28.9
90	29.0
100	29.1
110	29.1
120	29.5
130	29.6
140	29.7
150	29.8
160	29.9
170	29.9
180	30.0
190	30.0
200	30.0
210	30.0
220	30.0
230	30.0
240	30.0
250	30.1
260	30.1
270	30.2
280	30.2
290	30.2
300	30.4
310	30.5
320	30.6
330	30.6
340	30.6
350	30.8
360	30.9
390	31.0
420	31.2
450	31.8
480	32.2
510	33.0
540	33.9
570	34.2
600	35.0
660	36.0
720	36.2
780	36.6
840	36.9
900	37.0
1800	39.0

Table D4

Inorganic Powder Formulation C Solution = 40% wt/wt
Air Velocity = 1 $m.s^{-1}$
Air Temperature = 40°C

Time (Sec)	Core Temperature °C
0	22.0
10	24.3
20	25.0
30	25.5
40	26.0
50	26.5
60	27.0
70	27.3
80	27.9
90	28.0
100	28.2
110	28.7
120	29.0
130	29.1
140	29.2
150	29.5
160	29.8
170	29.8
180	30.0
190	30.0
200	30.0
210	30.1
220	30.2
230	30.3
240	30.4
250	30.6
260	30.8
270	30.9
280	30.9
290	31.0
300	31.0

Time (Sec)	Core Temperature °C
310	31.0
320	31.0
330	31.0
240	31.1
250	31.1
360	31.2
390	31.5
420	31.8
450	31.9
480	32.0
510	32.0
540	32.1
570	32.2
600	32.5
630	32.8
660	32.9
720	33.0
750	33.0
780	33.0
810	33.1
840	33.1
870	33.3
900	33.6
960	33.8
1020	34.0
1080	34.0
1140	34.2
1200	34.8
1500	35.2
1800	38.5
3600	38.5

Table D5

Sodium Sulphate Decahydrate Solution = 40% wt/wt
Air Velocity = 1 $m.s^{-1}$
Air Temperature = 60°C

Time (Sec)	Core Temperature °C
0	27.0
10	29.0
20	30.0
30	31.2
40	32.1
50	33.0
60	33.3
70	33.8
80	34.0
90	34.0
100	34.2
110	34.6
120	34.8
130	34.9
140	35.0
150	35.0
160	35.1
170	35.2
180	35.8
190	36.2
200	37.0
210	37.8
220	38.8
230	39.2
240	40.0
250	40.6
260	41.5

Time (Sec)	Core Temperature °C
270	42.0
280	43.0
290	43.3
300	44.0
360	45.2
390	46.2
420	47.0
450	47.9
480	48.1
510	48.7
540	48.5
570	49.0
600	49.1
630	49.3
660	49.7
690	49.9
720	50.0
750	50.0
780	50.0
810	50.0
840	50.0
870	50.0
900	50.0
1200	50.1
1500	50.8
1800	51.0
3600	53.3

Table D6

Inorganic Powder Formulation C Solution = 40% wt/wt
Air Velocity = 1 $m.s^{-1}$
Air Temperature = 61°C

Time (Sec)	Core Temperature °C
0	26.0
10	29.0
20	30.5
30	31.5
40	32.4
50	33.2
60	34.0
70	34.7
80	35.2
90	35.9
100	36.2
110	37.0
120	37.4
130	38.0
140	38.9
150	39.2
160	40.0
170	40.1
180	40.7
190	41.0
200	41.2
210	41.6
220	41.9
230	42.0
240	42.1
250	42.6
260	42.8

Time (Sec)	Core Temperature °C
270	43.0
280	43.0
290	43.1
300	43.2
330	43.9
360	44.2
390	44.8
420	45.0
450	45.2
480	45.7
510	45.9
540	46.0
570	46.1
600	46.4
630	46.6
660	46.8
690	46.9
720	47.0
780	47.0
840	47.0
900	47.1
960	47.5
1020	47.8
1080	47.9
1500	49.0
1800	49.8
3600	51.0

Table D7

Sodium Sulphate Decahydrate Solution = 40% wt/wt
Air Velocity = 1 $m.s^{-1}$
Air Temperature = 79°C

Time (Sec)	Core Temperature °C
0	30.0
10	32.0
20	34.2
30	36.5
40	38.0
50	39.1
60	40.1
70	41.0
80	41.2
90	41.7
100	42.0
110	42.0
120	42.1
130	42.2
140	42.7
150	42.9
160	43.0
170	43.2
180	43.8
190	44.5
200	46.0
210	47.5
220	49.5
230	51.0
240	52.9
250	54.0

Time (Sec)	Core Temperature °C
260	54.9
270	55.0
280	55.0
290	55.2
300	55.8
310	56.0
320	56.0
330	56.0
340	56.0
350	56.2
360	56.7
390	57.0
420	57.2
450	57.9
480	58.0
510	58.0
540	58.0
570	58.2
600	58.5
900	60.0
1200	61.5
1500	62.0
1800	63.0
3600	68.0

Table D8

Inorganic Powder Formulation C Solution = 40% wt/wt
Air Velocity = 1 $m.s^{-1}$
Air Temperature = 79°C

Time (Sec)	Core Temperature °C
0	33.0
10	35.5
20	37.5
30	39.2
40	40.8
50	42.0
60	43.0
70	44.5
80	45.5
90	46.7
100	47.5
110	48.1
120	49.0
130	50.0
140	50.9
150	51.3
160	52.0
170	52.3
180	53.0
190	53.2
200	53.8
210	54.0
220	54.7
230	55.0
240	55.2

Time (Sec)	Core Temperature °C
250	55.8
260	56.0
270	56.0
280	56.4
290	56.8
300	57.0
310	57.0
320	57.2
330	57.4
240	57.7
350	57.8
360	58.0
390	58.1
420	58.6
450	58.9
480	59.0
510	59.1
540	59.3
570	59.5
600	59.9
900	61.0
1200	61.2
1500	62.0
1800	62.0
3600	66.0

D.2 Crust Thermal Conductivity Evaluations

Calculation involved (a) determination of the heat transfer rate ($J.m^{-2}.s^{-1}.°C^{-1}$) characteristics of the apparatus, (b) use of this to determine conductivity.

Let A_1, A_2, A_3, A_X = Emissive areas of discs and sample respectively.

θ_1, θ_2, θ_3 = Respective thermocouple readings

θ = Laboratory temperature

V_o = Voltage across the heater

I = Current in amperes

t = Thickness of sample

e = Heat transfer rate

k_{tc} = Thermal conductivity

Then,

$$\frac{V_o I}{4.2} = e \left[A_1(\theta_1-\theta)+A_2(\theta_2-\theta)+A_X\left(\frac{\theta_2+\theta_3}{2}-\theta\right)+A_3(\theta_3-\theta) \right] \quad (D.1)$$

Whence e,

$$k_{tc}A_X \frac{(\theta_2-\theta_3)}{t} = e \left[\frac{A_X}{2}\left(\frac{\theta_2+\theta_3}{2}-\theta\right)+A_3(\theta_3-\theta) \right] \quad (D.2)$$

Whence k_{tc},

Table D9

Room Temperature = 25°C
Thickness of Inorganic Powder = 9×10^{-3} m

Time (Min)	Current (Amp)	Voltage (Volt)	Temperature of Disc 1 °C	Temperature of Disc 2 °C	Temperature of Disc 3 °C
0	0	0	23	23	23
10	0.5	40.8	24	33	33.2
20	0.5	41	27.2	43	45
30	0.5	41.2	32	51.5	53.7
40	0.5	41.7	36.3	58.1	59.9
50	0.5	41.2	40.2	63.8	66
60	0.5	41.2	44	68.1	69
70	0.5	41.2	47	70/6	71.3
80	0.5	41.2	51.7	76	74.2
90	0.5	41.1	53	77	75.4
100	0.5	40.8	54.4	78.1	76.8
110	0.5	41.0	55.8	79	77.5
120	0.5	40.8	56	79.5	77.5
130	0.5	40.8	56.7	79.9	78

Table D10

Room Temperature = 22°C
Thickness of Sodium Sulphate Decahydrate = 9×10^{-3} m

Time (Min)	Current (Amp)	Voltage (Volt)	Temperature of Disc 1 °C	Temperature of Disc 2 °C	Temperature of Disc 3 °C
0	0	0	21.0	21.0	21.0
20	0.1	8.8	21.1	21.9	22.1
40	0.1	8.8	21.9	22.5	23.1
60	0.1	8.8	22.0	23.0	23.9
80	0.1	8.8	22.5	23.5	24.6
100	0.1	8.8	23.0	24.0	25.05
120	0.1	8.8	23.7	24.9	26.0
140	0.1	8.8	24.1	25.3	26.5
160	0.1	8.8	24.8	26.0	27.0
180	0.1	8.8	25	26.2	27.2

APPENDIX E

Computer Programs for Calculation of Experimental And Predicted Droplet Mean Diameter d32.

```
20 E.1
30
40
50 REM  DROP SIZE DISTRIBUTION
52 REM  ORGANIC PASTE SLURRIES
54 REM     ATOMISATION PROJECT                                DATA STORE
55 REM
90 DIM D$(20),L(20),K$(20),S(20),D(20)
95 DIM B(20,15),N(20,15),D1(15),C(15),S1(16)
96 DIM P(20),F(20),SM(20),W(20)
100 FORI=1TO20
110 READL(I),K$(I),S(I),D$(I),W(I)
120 NEXTI
130 FORK=1TO15
140 READD1(K)
150 NEXTK
190 FORK=1TO16
195 READS1(K)
197 NEXTK
198 REM
202 OPEN1,4:OPEN5,4,1:OPEN3,4,2
205 FORI=1TO20
220 READ P(I),F(I)
230 FORK=1TO15
240 READB(I,K)
250 NEXTK
251 IFI=10THEN275
252 GOTO340
270 REM
275 GOSUB10000
280 REM
290 GOSUB15000
295 REM
300 GOSUB16000
340 NEXTI
350 END
1000 REM DATA STORE FOR NOZZLE SIZE AND          SOLIDS CONTENT
1001 REM
1005 DATA 8,SH2.0,11.87,13 %,55.5
1010 DATA 7,SH2.0,11.87,13 %,53
1020 DATA 2,SH2.0,15.74,13 %,50.5
1025 DATA 1,SH2.0,15.74,13 %,52.5
1030 DATA 6,SH2.0,18.15,13 %,50.5
1040 DATA 5,SH2.0,18.15,13 %,57.5
1042 DATA 18,SH2.0,15.49,13 %,50
1050 DATA 3,SG2.0,15.74,13 %,68
1060 DATA 4,SH2.4,15.74,13 %,66.5
1070 DATA 19,SI1.8,15.49,13 %,42.5
1080 DATA 20,SH1.8,15.49,13 %,55
1085 REM
1090 DATA 14,SH2.0,19.66,26 %,49
1095 DATA 13,SH2.0,19.66,26 %,59
```

```
1102 DATA 10,SH2.0,24.23,26 %,53
1105 DATA 9,SH2.0,24.23,26 %,53.5
1120 DATA 16,SH2.0,28.09,26 %,50
1130 DATA 15,SH2.0,28.09,26 %,52.5
1140 DATA 17,SH2.0,24.2,26 %,43
1150 DATA 11,SI1.8,24.23,26 %,32
1155 DATA 12,SH1.8,24.23,26 %,46
1205 REM
1325 REM
1345 REM
1460 DATA412.88,211,136.6,98.55,74.45
1462 DATA 57.4,44.6,34.65,27,21,16,13
1465 DATA10.25,8.15,6.5
1500 REM
1510 DATA564,261.6,160.4,112.8,84.3,64.6,50.2
1515 DATA 39,30.3,23.7,18.5,14.5,11.4
1520 DATA9.1,7.2,5.8
1530 REM
2000 REM SIZE DISTRIBUTION DATA AND                    FLOWRATES
2010 REM    PROCION YELLOW P-3R
2020 DATA 12,.08,20.4,22.6,12,9.3,7.2,6.5,4.4
2025 DATA 5.7,3.2,2.5,.3,0,.5,,.9,.6
2030 DATA 18,.104,14.9,19.8,13.8,9.5,8.4,6.4,5.4
2035 DATA 4.5,4.9,3.5,3.5,1,1,1.2,.9
2040 DATA12,.075,31.3,27,9.8,7.5,4.5,4.9,2.7,3
2045 DATA 2.3,1.6,3.1,0,0,.8,.6
2050 DATA 18,.097,20.5,27.4,13.7,8.8,6.5,4.7
2055 DATA 3,3,1.6,3.6,1.5,1.8,.7,1.1,.8
2060 DATA 12,.049,33.4,21.2,12.4,6.2,6.2,4.2
2065 DATA 2.1,4.3,3.6,1.8,2.3,0,0,.7,.5
2070 DATA 18,.082,23.7,25.8,12.4,7.9,5.7,4.9
2075 DATA 3.4,4.3,2.5,2.9,2.4,1.9,.6,.9,.6
2080 DATA 12,.088,28.9,26.4,13.9,6.4,4.4,6.8
2085 DATA 4.2,1.9,2.3,1.5,1.3,1.4,0,0,0
2090 DATA 12,.073,26.5,24.8,11.2,9,5.5,3.7,3.8
2095 DATA 3.7,3.8,2.3,3.5,0,0,.9,.6
2100 DATA 12,.096,26.4,26.8,11.3,8.2,5.9,4.1
2105 DATA 2.3,4.1,4.3,1,2.4,1.7,0,.8,0
2110 DATA 12,.085,30.8,20.8,9.5,8,7.5,7.1,6.5
2115 DATA 3.2,2,1.2,1.1,0,0,.8,.6
2120 DATA 12,.079,22.1,26,14.3,6.6,6.6,5.8,2.6
2125 DATA 5.3,1.9,3,2.4,.9,0,.9,.6
2130 REM
2140 DATA 12,.082,15.1,36.5,17.2,11.1,4.8,3.6
2145 DATA 4.2,0,3.5,0,2,0,1.1,0,0
2150 DATA 18,.108,7.7,22.5,22.8,12.9,7.8,9.9
2155 DATA 2.6,3.3,3.4,2.5,.2,1.5,1.1,.8,0
2160 DATA 12,.077,36.7,37.8,7.3,8.2,3.7,2.1,0
2165 DATA 3.8,0,.1,.1,0,0,0,0,
2170 DATA 18,.103,27.3,36.1,14.7,7,7.2,2.8,1.4
```

```
2180 DATA 12,.079,29.6,35.3,15,8,5,3.3,0,0,2,0,0,0,0,0,0
2190 DATA 10,.085,15.5,30.8,20.1,11.5,8.1,4.6
2195 DATA 3.8,1,1.3,0,1.4,0,.8,0,.5
2200 DATA 12,.057,29.2,39.8,12.2,9.3,4.2,4,.8,.3,.1,0,0,0,0,0,0
2210 DATA 12,.085,38.6,30.2,10,7,5.3,3,2.1,3.4,0,.1,.1,0,0,0,0
2220 DATA 12,.057,33.1,38.7,7.3,8.7,4.4,2.6
2225 DATA 1.3,0,3.5,0,.1,0,0,0,0
10000 REM   SUBROUTINE TO CALC NO %
10010 CT=0
10020 FORK=1TO15
10030 C(K)=B(I,K)/100/D1(K)↑3
10040 CT=CT+C(K)
10050 NEXTK
10060 FORK=1TO15.
10070 N(I,K)=C(K)/CT*100
10080 NEXTK
10100 RETURN
15000 REM  SUBROUTINE TO CALC SAUTER                    MEAN DIAMETERS
15010 SA=0:ET=0
15030 FORK=1TO15
15040 SA=SA+B(I,K)
15050 ET=ET+B(I,K)/D1(K)
15060 NEXTK
15070 SM(I)=SA/ET
15100 RETURN
15102 REM
16000 REM  PRINTING RESULTS
16005 PRINT#1,"       TABLE :";I
16006 PRINT#1,"       ————————"
16007 PRINT#1
16010 F$="        999.9        999.9            99.9            99.9"
16012 PRINT#3,F$
16015 IFI>11 THEN16018
16016 PRINT#1,CHR$(1)"   ORGANIC PASTE FORMULATION A"
16017 PRINT#1,CHR$(1)"   ————————————————————":PRINT#1:GOTO16022
16018 PRINT#1,CHR$(1)"   ORGANIC PASTE FORMULATION B"
16019 PRINT#1,CHR$(1)"   ————————————————————":PRINT#1
16020 PRINT#3,F$
16022 PRINT#1,CHR$(1)"       RUN NO.                  : C";L(I)
16024 PRINT#1,CHR$(1)"       NOZZLE DIMENSIONS        : ";K$(I)
16025 PRINT#1,CHR$(1)"       SOLIDS CONTENT (WT.%):";S(I)
16026 PRINT#1,CHR$(1)"       CONE ANGLE (DEG.)        :";W(I)
16027 IFI=7ORI=18THEN16030
16028 PRINT#1,CHR$(1)"       DISPERSOL                : ";D$(I)
16029 GOTO16038
16030 PRINT#1,CHR$(1)"       SODIUM CHLORIDE (SAT): ";D$(I)
16038 SM(I)=INT(SM(I)*100+.5)/100
16040 FORK=1TO15
16045 N(I,K)=INT(N(I,K)*100+.5)/100
```

```
16046 NEXTK
16050 PRINT#1:PRINT#1:PRINT#1
16058 PRINT#1,TAB(28)"*   PRESS (BAR)           =";P(I)
16060 PRINT#1,TAB(28)"*   FLOW (LT/S)           =";F(I)
16062 PRINT#1,TAB(28)"*   MEAN DIA. (MICRONS)   =";SM(I)
16065 PRINT#1,TAB(28)"————————————————————————————————————————"
16070 PRINT#1,TAB(15)"SIZE          *      WT % IN      NO.% OF MEAN"
16080 PRINT#1,TAB(15)"BAND          *       BAND          SIZE"
16090 PRINT#1,"         UPPER       LOWER   *"
16100 PRINT#1,"      ————————————————————————————————————————————————————";
16110 PRINT#1,"_____"
16120 FORK=1TO15
16130 PRINT#5,S1(K),S1(K+1),B(I,K),N(I,K)
16140 NEXTK
16165 PRINT#1:PRINT#1:PRINT#1:PRINT#1:PRINT#1:PRINT#1:PRINT#1:PRINT#1
16166 PRINT#1:PRINT#1:PRINT#1
16170 RETURN
20000 REM PRINTING SAUTER MEAN DIA.
20005 PRINT#1,"RUN NO.";L(I)
20010 PRINT#1,"NOZ   .";K$(I)
20020 PRINT#1,"S.C   .";S(I)
20025 PRINT#1
20050 PRINT#1,"PRESS =";P(I);"MEAN DIA =";SM(I)
20070 PRINT#1:PRINT#1
20080 RETURN
20500 REM
30000 REM
30010 REM
30020 REM
```

```
 1 E.2
 3 **CALCULATION OF DROP SIZE D32
 4 *******EXPERIMENTALL  D32
 10 READ*,N
 30 READ*,M
 80 DO 5 I=1,M
 90 READ*,(D(J),W(J),J=1,N)
 100 SUM(0)=0.0
 110 DO 10 J=1,N
 120 SUM(J)=SUM(J-1)+W(J)
 130 A10 CONTINUE
 140 SUMW(0)=0.0
 150 SUMDWW(0)=0.0
 160 DO 15 K=1,N
 170 SUMW(K)=W(K)/D(K)
 180 SUMDW(K)=SUMDW(K-1)+SUMW(K)
 190 A15 CONTINUE
 200 D32(I)=SUM(N)/SUMDW(N)
 210 PRINT 100,I,D32(I)
 220 A100 FORMAT(10,'D32',12,')=',F10.3)
 230 A5 CONTINUE
 240 STOP
 250 END
READY.
```

```
LI EREHASN
1   ===> AS 7=HDAT
2   ===> XE
3              D32( 1)=     61.016
4              D32( 2)=     60.554
5              D32( 3)=     71.428
6              D32( 4)=     63.666
7              D32( 5)=     71.656
8              D32( 6)=     85.133
9              D32( 7)=     85.453
10              D32( 8)=     48.120
11              D32( 9)=     52.744
12              D32(10)=     50.508
13              D32(11)=     46.751
EOT..
```

```
1 E.3
2 CALCULATION OF THEORETICAL
3 *******DROP SIZE D32*******
5 REM FLOW RATE,Q,M↑3/S
6 INPUT "INPUT FLOWRATE",Q
10 REM SWRIL CHAMBER RADIUS ,RS,M
20 RS=0.005
30 REM SURFACE TENSION ,ST
50 REM SLURRY DENSITY,D,KG/M↑3
60 D=1220
70 REM OPERATING PRESSURE,P
80 INPUT "INPUT OPERATING PRESSURE",P1
82 P=P1*6895
85 REM OROFICE RADIUS ,RO,M
90 RO=0.0007
100 REM VISCOSITY ,MU,KG/M.S
110 MU=0.035
120 REM AREA OF SWIRL CHAMBER ,AS
130 AS=3.14159*(RS↑2)
140 REM CIRCULATION CONSTANT ,S
150 S=Q*RS/AS
160 REM ESTIMATE RAC↑2
170 R2=(D/S*P))*((S↑2)+((S↑4)+SQR(16*(RO↑2)*(S↑2) *P/D)))
180 REM ESTIMATE VZ
190 VZ=Q/(.14159*(RS↑2-R2))
200 REM ESTIMATE V(THETA)
210 RT=(RO+SQR(R2))/2
220 VO=S/RT
230 REM EVALUATE ATAN(VO/VZ)
240 OP=ATAN(VO/VZ)
250 N1=(2*RO*D*VZ/MU)
260 N2=(2*RO*D*VZ/ST)
270 N3=S/9.81
272 PRINT"N1="N1
274 PRINT"N2="N2
276 PRINT"N3="N3
278 PRINT"OP="OP
280 OM=(3.14159*N1↑0.027)*(N3↑0.2)*(OP↑0.872)/(N2↑0.5)
290 REM CHECK SHEET VELOCITY
300 VS1=0.7*SQR(2*P/D)
310 PRINT "SHEET VELOCITY 1",VS1
320 PRINT "SHEET VELOCITY 1",VS1
340 REM CALCULATE SHEET LENGTH ,L
350 L=1871.35*RO*2*(N1)↑-0.117*(N2)↑-0.449*(OM)↑-0.434
360 REM DROP SIZE ,DS
370 DS=0.46*(Q/((VS1)↑3.0*L*SIN(OM)))↑0.5
380 PRINT "DROP SIZE ",DS"M"
390 END
READY.
```

```
>RUN
N1 =  43.55627
N2 =27.7176264
N3 =4.54265257E-4
OP =1.48198251
SHEET VELOCITY 1      44.653089
DROP SIZE 3.28906391E-5M
```

TABLE E1

RUN NO.	: B 43
NOZZLE DIMENSIONS	: SG1.2
DENSITY (GMS/CC)	: 1.09
VISCOSITY (CP)	: 6.6

SIZE BAND UPPER	SIZE BAND LOWER	*PRESS(PSIG)= 170 *FLOW(LT/S) = .048 *MEAN DIA. = 67.12 WT% IN BAND	NO.% OF MEAN SIZE	*PRESS(PSIG)= 310 *FLOW(LT/S) = .055 *MEAN DIA. = 47.62 WT% IN BAND	NO.% OF MEAN SIZE
564.0	261.6	13.6	.0	10.1	.0
261.6	160.4	25.3	.0	17.9	.0
160.4	112.8	11.1	.1	12.7	.0
112.8	84.3	11.7	.3	10.4	.1
84.3	64.6	9.2	.7	7.9	.2
64.6	50.2	6.6	1.0	7.8	.5
50.2	39.0	6.8	2.3	5.7	.8
39.0	30.3	4.7	3.5	5.9	1.9
30.3	23.7	3.4	5.3	5.1	3.4
23.7	18.5	2.4	7.9	4.9	7.0
18.5	14.5	3.4	23.6	4.7	14.0
14.5	11.4	1.0	14.3	2.8	17.2
11.4	9.1	.0	.0	1.6	19.9
9.1	7.2	.7	40.3	.8	19.8
7.2	5.8	.0	.0	.3	14.6

SIZE BAND UPPER	SIZE BAND LOWER	*PRESS(PSIG)= 530 *FLOW(LT/S) = .065 *MEAN DIA. = 39.8 WT% IN BAND	NO.% OF MEAN SIZE	*PRESS(PSIG)= 680 *FLOW(LT/S) = .072 *MEAN DIA. = 32.92 WT% IN BAND	NO.% OF MEAN SIZE
564.0	261.6	3.8	.0	1.7	.0
261.6	160.4	12.7	.0	6.9	.0
160.4	112.8	14.2	.0	11.1	.0
112.8	84.3	12.6	.1	12.3	.0
84.3	64.6	9.3	.2	13.0	.1
64.6	50.2	7.8	.3	7.8	.2
50.2	39.0	6.7	.7	8.0	.5
39.0	30.3	6.7	1.5	6.6	.9
30.3	23.7	4.9	2.3	7.2	2.2
23.7	18.5	6.3	6.2	6.2	4.0
18.5	14.5	5.5	11.4	7.4	10.0
14.5	11.4	4.0	17.2	4.2	11.7
11.4	9.1	2.1	18.3	3.1	17.5
9.1	7.2	1.2	20.8	1.7	19.1
7.2	5.8	.6	20.5	1.5	33.2

TABLE E2

RUN NO. : B 28
NOZZLE DIMENSIONS : SG1.2
DENSITY (GMS/CC) : 1.14
VISCOSITY (CP) : 16.5

SIZE BAND UPPER	SIZE BAND LOWER	*PRESS(PSIG)= 170 *FLOW(LT/S) = .045 *MEAN DIA. = 79.75 WT% IN BAND	NO.% OF MEAN SIZE	*PRESS(PSIG)= 350 *FLOW(LT/S) = .056 *MEAN DIA. = 49.09 WT% IN BAND	NO.% OF MEAN SIZE
564.0	261.6	16.4	.0	5.2	.0
261.6	160.4	21.9	.2	12.5	.0
160.4	112.8	13.3	.4	11.7	.1
112.8	84.3	11.6	1.1	11.7	.2
84.3	64.6	8.9	2.0	11.4	.6
64.6	50.2	8.5	4.1	10.4	1.3
50.2	39.0	6.7	7.0	9.5	2.5
39.0	30.3	5.8	12.9	8.6	4.9
30.3	23.7	2.5	11.8	6.6	8.0
23.7	18.5	1.9	18.8	5.2	13.2
18.5	14.5	2.0	41.3	3.4	18.0
14.5	11.4	.0	.0	1.6	17.6
11.4	9.1	.0	.0	.9	19.9
9.1	7.2	.0	.0	.3	13.2
7.2	5.8	.0	.0	.0	.0

SIZE BAND UPPER	SIZE BAND LOWER	*PRESS(PSIG)= 530 *FLOW(LT/S) = .064 *MEAN DIA. = 35.77 WT% IN BAND	NO.% OF MEAN SIZE	*PRESS(PSIG)= 700 *FLOW(LT/S) = .078 *MEAN DIA. = 31.58 WT% IN BAND	NO.% OF MEAN SIZE
564.0	261.6	2.3	.0	.0	.0
261.6	160.4	5.5	.0	2.5	.0
160.4	112.8	12.2	.0	8.7	.0
112.8	84.3	11.1	.1	13.6	.1
84.3	64.6	10.3	.2	11.2	.2
64.6	50.2	10.2	.5	9.5	.4
50.2	39.0	8.5	.8	9.8	.8
39.0	30.3	9.9	2.2	8.8	1.6
30.3	23.7	8.1	3.8	7.6	3.0
23.7	18.5	7.7	7.6	10.0	8.4
18.5	14.5	6.4	13.2	6.6	11.7
14.5	11.4	3.2	13.7	5.7	20.9
11.4	9.1	2.5	21.6	2.7	20.0
9.1	7.2	1.1	18.9	2.2	32.4
7.2	5.8	.5	16.9	.0	.0

TABLE E3

RUN NO.	: B 1
NOZZLE DIMENSIONS	: SG1.4
DENSITY (GMS/CC)	: 1.16
VISCOSITY (CP)	: 22

SIZE BAND UPPER	SIZE BAND LOWER	*PRESS(PSIG)= 170 *FLOW(LT/S) = .045 *MEAN DIA. = 72.45 * WT% IN BAND	NO.% OF MEAN SIZE	*PRESS(PSIG)= 350 *FLOW(LT/S) = .055 *MEAN DIA. = 48.02 * WT% IN BAND	NO.% OF MEAN SIZE
564.0	261.6	14.1	.0	1.0	.0
261.6	160.4	21.7	.0	19.3	.0
160.4	112.8	12.7	.1	13.5	.0
112.8	84.3	10.8	.3	11.4	.1
84.3	64.6	10.9	.7	10.6	.3
64.6	50.2	10.6	1.6	10.1	.6
50.2	39.0	6.4	2.0	8.1	1.1
39.0	30.3	5.5	3.8	7.4	2.3
30.3	23.7	2.2	3.2	5.7	3.7
23.7	18.5	2.6	7.9	4.9	6.7
18.5	14.5	1.0	6.3	2.7	7.8
14.5	11.4	.0	.0	1.7	10.1
11.4	9.1	.0	.0	1.0	12.0
9.1	7.2	.6	31.8	.5	12.0
7.2	5.8	.4	41.8	.9	42.6

SIZE BAND UPPER	SIZE BAND LOWER	*PRESS(PSIG)= 530 *FLOW(LT/S) = .067 *MEAN DIA. = 41.53 * WT% IN BAND	NO.% OF MEAN SIZE	*PRESS(PSIG)= 730 *FLOW(LT/S) = .084 *MEAN DIA. = 35.41 * WT% IN BAND	NO.% OF MEAN SIZE
564.0	261.6	.0	.0	.0	.0
261.6	160.4	11.1	.0	2.5	.0
160.4	112.8	15.7	.0	12.7	.0
112.8	84.3	12.1	.1	15.2	.1
84.3	64.6	12.0	.2	12.9	.2
64.6	50.2	9.8	.5	10.8	.4
50.2	39.0	7.9	.8	8.8	.7
39.0	30.3	8.4	1.9	8.0	1.4
30.3	23.7	6.0	2.9	7.5	2.7
23.7	18.5	5.5	5.7	6.9	5.3
18.5	14.5	3.9	8.4	4.7	7.6
14.5	11.4	2.3	10.3	3.0	10.0
11.4	9.1	1.5	13.5	2.1	14.1
9.1	7.2	.9	16.1	1.3	17.4
7.2	5.8	1.1	39.0	1.5	39.7

TABLE E4

RUN NO. : B 51
NOZZLE DIMENSIONS : SG1.4
DENSITY <GMS/CC> : 1.15
VISCOSITY <CP> : 35.1

SIZE BAND UPPER	SIZE BAND LOWER	*PRESS(PSIG)= 175 *FLOW(LT/S) = .043 *MEAN DIA. = 65.48 WT% IN BAND	NO.% OF MEAN SIZE	*PRESS(PSIG)= 350 *FLOW(LT/S) = .07 *MEAN DIA. = 41.69 WT% IN BAND	NO.% OF MEAN SIZE
564.0	261.6	14.5	.0	4.8	.0
261.6	160.4	19.7	.0	19.0	.0
160.4	112.8	12.2	.1	10.9	.0
112.8	84.3	11.6	.3	9.5	.1
84.3	64.6	9.5	.7	8.7	.2
64.6	50.2	8.6	1.3	7.5	.4
50.2	39.0	6.9	2.3	7.6	.8
39.0	30.3	5.7	4.1	6.9	1.6
30.3	23.7	3.6	5.5	6.1	3.0
23.7	18.5	3.3	10.6	5.6	5.9
18.5	14.5	1.5	10.1	4.8	10.6
14.5	11.4	1.0	13.9	3.0	13.7
11.4	9.1	.4	11.2	2.3	21.2
9.1	7.2	.7	39.2	1.1	20.2
7.2	5.8	.0	.0	.6	21.7

SIZE BAND UPPER	SIZE BAND LOWER	*PRESS(PSIG)= 530 *FLOW(LT/S) = .083 *MEAN DIA. = 33.62 WT% IN BAND	NO.% OF MEAN SIZE	*PRESS(PSIG)= 710 *FLOW(LT/S) = .096 *MEAN DIA. = 29.14 WT% IN BAND	NO.% OF MEAN SIZE
564.0	261.6	1.6	.0	1.7	.0
261.6	160.4	11.8	.0	5.3	.0
160.4	112.8	11.8	.0	10.6	.0
112.8	84.3	11.7	.0	12.4	.0
84.3	64.6	7.4	.1	8.5	.1
64.6	50.2	8.3	.2	8.6	.2
50.2	39.0	8.2	.5	7.5	.4
39.0	30.3	6.5	.9	7.3	.8
30.3	23.7	6.2	2.0	6.6	1.5
23.7	18.5	6.6	4.4	7.1	3.5
18.5	14.5	6.3	8.9	7.1	7.3
14.5	11.4	4.7	13.7	5.2	11.1
11.4	9.1	3.2	18.8	4.2	18.2
9.1	7.2	1.9	22.2	2.4	20.7
7.2	5.8	1.2	27.7	2.1	35.7

TABLE E5

RUN NO. : B 45
NOZZLE DIMENSIONS : SG1.4
DENSITY (GMS/CC) : 1.16
VISCOSITY (CP) : 41.5

SIZE BAND UPPER	SIZE BAND LOWER	*PRESS(PSIG)= 170 *FLOW(LT/S) = .043 *MEAN DIA. = 88.17 WT% IN BAND	NO.% OF MEAN SIZE	*PRESS(PSIG)= 350 *FLOW(LT/S) = .058 *MEAN DIA. = 50.28 WT% IN BAND	NO.% OF MEAN SIZE
564.0	261.6	19.9	.0	10.2	.0
261.6	160.4	23.4	.2	14.4	.0
160.4	112.8	12.9	.5	14.0	.1
112.8	84.3	11.6	1.3	8.6	.1
84.3	64.6	7.8	2.1	9.7	.5
64.6	50.2	9.7	5.7	8.7	.9
50.2	39.0	4.4	5.5	7.4	1.7
39.0	30.3	5.1	13.6	7.4	3.7
30.3	23.7	1.3	7.3	5.8	6.2
23.7	18.5	2.0	23.7	5.4	12.1
18.5	14.5	1.6	39.6	4.4	20.6
14.5	11.4	.0	.0	1.9	18.4
11.4	9.1	.0	.0	1.0	19.6
9.1	7.2	.0	.0	.4	15.5
7.2	5.8	.0	.0	.0	.0

SIZE BAND UPPER	SIZE BAND LOWER	*PRESS(PSIG)= 500 *FLOW(LT/S) = .078 *MEAN DIA. = 42.67 WT% IN BAND	NO.% OF MEAN SIZE	*PRESS(PSIG)= 700 *FLOW(LT/S) = .088 *MEAN DIA. = 34.91 WT% IN BAND	NO.% OF MEAN SIZE
564.0	261.6	2.9	.0	2.2	.0
261.6	160.4	14.4	.0	7.2	.0
160.4	112.8	12.6	.0	12.2	.0
112.8	84.3	10.5	.1	11.3	.1
84.3	64.6	10.4	.3	9.6	.2
64.6	50.2	9.1	.7	10.0	.4
50.2	39.0	7.5	1.2	7.7	.7
39.0	30.3	8.3	2.9	7.3	1.5
30.3	23.7	6.6	4.9	8.3	3.8
23.7	18.5	6.7	10.5	7.7	7.4
18.5	14.5	4.7	15.4	6.6	13.3
14.5	11.4	3.5	23.8	5.2	21.7
11.4	9.1	1.5	20.5	2.0	16.8
9.1	7.2	.7	19.1	2.0	33.5
7.2	5.8	.0	.0	.0	.0

TABLE E6

RUN NO.	: B 48
NOZZLE DIMENSIONS	: SG1.4
DENSITY (GMS/CC)	: 1.17
VISCOSITY (CP)	: 52.4

SIZE BAND UPPER	SIZE BAND LOWER	*PRESS(PSIG)= 180 *FLOW(LT/S) = .049 *MEAN DIA. = 106.7 * WT% IN BAND	NO.% OF MEAN SIZE	*PRESS(PSIG)= 350 *FLOW(LT/S) = .066 *MEAN DIA. = 49.8 * WT% IN BAND	NO.% OF MEAN SIZE
564.0	261.6	29.3	.0	12.5	.0
261.6	160.4	23.4	.4	18.7	.0
160.4	112.8	11.2	.7	8.4	.0
112.8	84.3	12.6	2.2	7.8	.1
84.3	64.6	5.4	2.2	10.1	.3
64.6	50.2	6.4	5.7	8.3	.5
50.2	39.0	5.6	10.7	8.3	1.2
39.0	30.3	2.0	8.2	7.2	2.2
30.3	23.7	1.0	8.6	5.7	3.7
23.7	18.5	2.5	45.4	4.6	6.4
18.5	14.5	.2	7.6	3.1	9.0
14.5	11.4	.1	7.8	1.7	10.2
11.4	9.1	.0	.0	1.1	13.3
9.1	7.2	.0	.0	.6	14.5
7.2	5.8	.0	.0	.8	38.1

SIZE BAND UPPER	SIZE BAND LOWER	*PRESS(PSIG)= 530 *FLOW(LT/S) = .078 *MEAN DIA. = 40.95 * WT% IN BAND	NO.% OF MEAN SIZE	*PRESS(PSIG)= 660 *FLOW(LT/S) = .089 *MEAN DIA. = 33.8 * WT% IN BAND	NO.% OF MEAN SIZE
564.0	261.6	8.3	.0	3.2	.0
261.6	160.4	13.8	.0	10.6	.0
160.4	112.8	11.0	.0	11.3	.0
112.8	84.3	9.3	.0	9.9	.0
84.3	64.6	8.1	.1	9.7	.1
64.6	50.2	7.9	.4	7.9	.2
50.2	39.0	8.4	.9	8.7	.5
39.0	30.3	7.3	1.7	7.1	1.0
30.3	23.7	6.4	3.1	7.3	2.2
23.7	18.5	6.0	6.1	6.8	4.3
18.5	14.5	5.0	10.7	5.8	7.7
14.5	11.4	2.6	11.5	3.9	10.7
11.4	9.1	2.3	20.6	2.5	13.8
9.1	7.2	1.1	19.6	2.2	24.2
7.2	5.8	.7	24.6	1.6	34.8

NOMENCLATURE

The symbols have the meaning listed below, unless otherwise stated in the text.

A	Surface area of hemispherical drops (m^2)
A_e	Equivalent surface area of a spheroid droplet (m^2)
A_m	Mass transfer area
A_h	Heat transfer area
a	Constant in Table 4.1
b	Constant in Table 4.1
C	Concentration
C_A	Molar concentration of component A
C_o	Initial concentration
C_1	Solids content
C_S	Concentration on droplet surface
C_∞	Concentration at infinite distance
C_{pv}	Heat capacity of diffusing vapour ($J.kg^{-1}.K^{-1}$)
C_p	Heat capacity of air ($J.kg^{-1}.K^{-1}$)
C_c	Heat of crystallisation per unit mass of water evaporated ($J.kg^{-1}$)
D_m	Molecular diffusivity ($m^2.s^{-1}$)
D_{AB}	Diffusion coefficient of A in a mixture of A and B.
D_V	Effective diffusivity ($m^2.s^{-1}$)
d	diameter (m)
d_p	Drop diameter (m)
$\bar{d}_p$	Mean droplet diameter (m)
$d_{(N)}$	Number of droplets in size increment
d_c	Crust external diameter (m)
d_g	Glass bed diameter (m)

d_{gm}	Geometric mean droplet diameter
d_{max}	Maximum droplet diameter
d_n	Diameter of nozzle
d_R	Rosin - Rammler mean droplet diameter
d_e	Equivalent drop diameter
d_h	Horizontal drop diameter
d_v	Vertical drop diameter
E	Sphericity
e	Emissivity
e_n	Emissivity of nozzle
f	Dispersion coefficient in Table 4.1
F_a	Geometry factor
g	Acceleration due to gravity ($m.s^{-1}$)
G	Dry air mass flowrate ($kg.s^{-1}$)
H	Humidity kg/kg
H_i	Inlet air humidity kg/kg
H_o	Outlet air humidity kg/kg
H_d	Downstream humidity kg/kg
H_u	Upstream humidity kg/kg
H_S	Saturation humidity at drop temperature
h_g	Gas film heat transfer coefficient ($W.m^{-2}.K^{-1}$)
I	Current (amp.)
K_o	Overall mass transfer coefficient ($m.s^{-1}$)
k_g	Gas film mass transfer coefficient ($m.s^{-1}$)
k_c	Crust mass transfer coefficient ($m.s^{-1}$)
k_p	Mass transfer coefficient ($kg.m^{-2}.s^{-1}.atm^{-1}$)
k	Thermal conductivity of air ($W.m^{-1}.K^{-1}$)
k_t	Thermal conductivity of stainless steel ($W.m^{-1}.K^{-1}$)

k_V	Thermal conductivity of diffusing vapour ($W.m^{-1}.k^{-1}$)
k_{tc}	Thermal conductivity of crust ($W.m^{-1}.k^{-1}$)
M_W	Molecular weight (kg/kgmole)
$\dot{m}$	Evaporation rate ($kg.m^{-2}.s^{-1}$)
$\dot{m}_o$	Evaporation rate in stagnant medium
$\dot{m}'_o$	Evaporation rate in stagnant medium neglecting radiation
N_A	Rate of mass transfer per unit area ($kg.m^{-2}.s^{-1}$)
P	Total pressure (atm)
p	Partial pressure of water vapour (atm)
p_c	Vapour pressure on surface of core
ΔP	Pressure drop through crust ($kg.m^{-1}.s^{-2}$)
p_s	Saturation vapour pressure (atm)
p_g	Partial pressure of air
p_v	Vapour pressure
q_e	Rate of heat transfer by radiation
q_n	Rate of heat transfer to a drop through the nozzle
r	Radius
r_o	Initial radius of evaporating drops
R	External drop radius
R_C	Universal gas constant ($Atm.m^3.kgmol^{-1}.K^{-1}$)
S_b	Specific surface area (m^{-1})
S_N	Number standard deviation
S_G	Geometric standard deviation
T	Temperature
T_i	Inlet air temperature
T_g, T'_g	Gas temperature in °C and K respectively
T_s, T'_s	Drop temperature in °C and K respectively
T_{amb}	Ambient temperature

T_C	Core temperature
v	Velocity ($m.s^{-1}$)
V	Volume
V_o	Voltage (volt)
X	Interface between crust and core
X_w	Mass fraction of water
y	Distance in the direction of diffusion

DIMENSIONLESS GROUPS

B	Transfer No. = $C_p \Delta T/\lambda$
Gr	Grashof No. = $d_p^3 \rho^2 g \beta_1 \Delta T/\mu^2$
Nu	Nusselt No. = $d_p h_g/k$
Nu_o	Nusselt No. under stagnant conditions
Nu_R	Nusselt No. without neighbouring particles
Pr	Prandtl No. = $Cp\mu/k$
Pe	Peclet No. = Re.Pr = $Cp\ v\ d_p\ \rho/k$
Re	Reynolds No. = $vd_p\rho/\mu$
Sc	Schmidt No. = $\mu/D_v\rho$
Sh	Sherwood No. = $k_g\ d_p/D_v$
Sh_o	Sherwood No. under stagnant conditions
Sh_R	Sherwood No. without neighbouring particles
St	Stanton No. $hg/C_p\rho v$

GREEK SYMBOLS

β	Coefficient in Frössling's equation
β_1	Coefficient of expansion in equation 3.7
ϕ	Crust thickness (m)
ε	Porosity of crust
$\Delta\theta$	Time interval
θ_c	Time for completion of solid crust formation
θ	Drying time (sec.)
γ	Dimensionless ratio in Equation (4.7)
ϕ_Y	Positive root of $\tan hy = \frac{Y}{\gamma+1}$
λ	Latent heat of vaporisation ($J.kg^{-1}$)
σ_1	Surface tension dyne/cm
σ	Stefan-Boltzman constant
ϕ	Constant
ρ	Density ($kg.m^{-3}$)
ρ_c	Core density
μ	Viscosity ($kg.m^{-1}.s^{-1}$)
ν	Kinematic viscosity ($m^2.s^{-1}$)
η	Index constant
π	Constant = 3.1416

REFERENCES

1. Keey, R.B., Drying Principles and Practice, lst ed., Pergamon Press, Oxford (1972).

2. Masters, K., Spray Drying Handbook, 3rd ed., John Wiley and Sons, New York (1979).

3. Coulson, J.M. and Richardson, J.F., Chem. Eng., Vol 2, 2nd ed., Pergamon Press, Oxford (1976).

4. Fick, A., Ann. Phys., 94, 59 (1855).

5. Vaccarezza, L.M., Lombardi, J.L., Chirife, J., Can. J. Chem. Eng., 52, 576 (1974).

6. Coulson, J.M. and Richardson, J.F., Chem. Eng., Vol l, 2nd ed., Pergamon Press, Oxford (1970).

7. Whitman, W.G., Chem. Met. Eng., 29, 147 (1923).

8. Higbie, R., Trans. Am. Inst., Chem. Eng., 31, 365 (1935).

9. Danckwerts, P.V., Ind. Eng. Chem., 43, 1460 (1951).

10. Toor, H. L., Marchello, J. M., A. I. Ch. E. J., 4, 97 (1958).

11. Frossling, N., Gerlands Beitrage Zur Geophysik, 52, 170 (1938). (AERE Harwell Translation, August 1963).

12. Sano, Y., Keey, R.B., Chem. Eng. Sci., 37, 881 (1982).

13. Duffie, J. A., Marshall, W. R., Chem. Eng. Prog., 49, 417, 480 (1953).

14. Masters, K., The Chemical Engineer, March, 145-148 (1980).

15. Colbourn, A.P., Trans. Am. Inst. Chem. Eng., 29, 174 (1933).

16. Chilton, T.H., Colburn, A.P., Ind. Eng. Chem., 22, 967 (1930).

17. Chilton, T.H., Colburn, A.P., Ind. Eng. Chem., 26, 1183 (1934).

18. Gilliland, E. R., Sherwood, T.K., Ind. Eng. Chem., 26, 516 (1934).

19 Maisel, D.S., Sherwood, T.K., Chem. Ing. Prog., 46, 172, 131 (1950).

20. Sherwood, T.K., Pigford, R.L., Absorption and Extraction, McGraw-Hill, (1952).

21. Sherwood, T.K., Trans. Am. Inst. Chem. Eng., 36, 817 (1940).

22. Linton, W. H., Sherwood, T. K., Chem. Eng. Prog., 46, 258 (1950).

23. Audu, T.O.K., Jeffreys, G. V., Trans. Inst. Chem. Eng., 53, 165 (1975).

24. Maxwell, J. C., Collected Scientific Papers, Cambridge, 11, 625 (1890).

25. Charlesworth, D. H., Marshall, W. R., A.I.Ch.E.J., 6, 9 (1960).

26. Ranz, W. E., Marshall, W. R., Chem. Eng. Prog., 48, 141, 173 (1952).

27. Trommelen, A.M., Crosby, E. J., A.I.Ch.E.J., 16, 857 (1970).

28. Peck, R. E., Kauh, J. Y., A. I. Ch.E. J., 15, 85 (1969)

29. Lewis, W. K., Ind. Eng. Chem., 13, 427 (1921).

30. Newman, A. B., Trans. Am. Inst. Ch. Eng., 27, 203, 310 (1931).

31 Sherwood, T. K., Ind. Eng. Chem., 21, 12, 976 (1929).

32. Buckingham, E., U.S. Dept. Agr. Bur. Solids Bull., 38 (1907).

33. Hougen, O. A., McCauley, H. J., Marshall, W. R., Trans. Am. Inst. Ch. Eng., 36, 183 (1940).

34. Ceaglske, N. H., Hougen, O. A., Trans. Am. Inst. Ch. Eng., 33, 283 (1937).

35. Sherwood, T. K., Comings, E. W., Trans. Am. Inst. Ch. Eng., 28, 118 (1932).

36. Sherwood, T. K., Comings, E. W., Ind. Eng. Chem., 25, 311 (1933).

37. Gurr, C. G., Marshall, T.K., Hutton, J.T., Soil Sci., 74, 335 (1952).

38. Kuzmak, J. M., Sereda, P. J., Soil Sci., 84, 419 (1957).

39. Harmathy, T. Z., Ind. Eng. Chem. Fund., 8, 92 (1968).

40. Sherwood, T. K., Ind. Eng. Chem., 22, 132 (1930).

41. Sherwood, T. K., Ind. Eng. Chem., 24, 307 (1932).

42. Fuchs, N., Physikalische Zeitschrift der Sowjetunion, 6, 224 (1934). (NACA Technical Memorandum No. 1160).

43. Morse, H. W., Proc. Am. Acad. Arts and Sci., 45, 363 (1910).

44. Langmuir, I., Phy. Rev. Ser.II, 12, 368 (1918).

45. Fuchs, N., Evaporation and Droplet Growth in Gaseous Media, Pergamon Press, London (1959).

46. Topley, B., Whytlaw-Gray, R., Phil. Mag., 4, 873 (1927).

47. Houghton, H. G., Physics, 4, 419 (1933).

48. Langstroth, G. O., Diehl, C. H., Winhold, E.J., Cand. J. Res., 28A, 574 (1950).

49. Mathers, W. G., Madden, A. J., Edgar, L. P., Ind. Eng. Chem., 49, 961 (1957).

50. Yuge, T., Trans. A. S. M. E., 82, Series C, 214 (1960).

51. Steinberger, R. L., Treybal, R. E., A. I. Ch. E. J., 6, 227 (1960).

52. Adams, A.E.S., Pinder, K. L., Can. J. Chem. Eng., 50, 707 (1972).

53. Frazier, G. C., Change, H. W., Can. J. Chem. Eng., 55, 736 (1977).

54. Hoffman, T. W., Gauvin, W. H., Can. J. Chem. Eng., 38, 129 (1960).

55. Woodland, D. J., Mack, E., J. Am. Chem. Soc., 55, 3149 (1933).

56. Shereshefsky, J. L., Steckler, S., J. Chem. Phys., 4, 108 (1936).

57. Nestle, R. Z., Physics, 77, 174 (1932).

58. Schafer, K., Physics, 77, 198 (1932).

59 Gudris, N., Kulikova, L., Physics, 25, 121 (1924).

60. Pritchard, C. L., Biswas, S.K., British Chemical Engineering, 12, 879 (1967).

61. Majama, Togino, Bull. Inst. Phys. Chem. Res. (Tokyo), 9, 339 (1930).

62. Vyrubov, D. N., J. Tech. Phys. Moscow, 9, 1923 (1939). (Canadian Defence Research Board Translation, September 1949).

63. Kinzer, G. D., Gunn, R., J. Meteor., 81, 71 (1951).

64. Johnstone, H. F., Eades, D. K., Ind. Eng. Chem., 42, 2293 (1950).

65. Hsu, N. T., Sato, K., Sage, B. H., Ind. Eng. Chem., 46, 870 (1954).

66. Ingebo, R. D., Chem. Eng. Prog., 48, 403 (1952).

67. Sherwood, T. K., Trans. Am. Inst. Chem. Eng., 23, 28 (1929).

68. Garner, F. H., Suckling, R. D., A.I. Ch. E. J., 4, 114 (1958).

69. Garner, F. H., Hoffman, J. M., A. I. Ch. E. J., 6, 579 (1960).

70. Garner, F. H., Keey, R. B., Chem. Eng. Sci., 9, 119 (1958).

71. Evnochides, S., Thodos, G., A. I. Ch. E. J., 7, 78 (1961).

72. Pasternak, I. S., Gauvin, W. H., Can. J. Ch. Eng., 38, 35 (1960).

73. Pasternak, I. S., Gauvin, W. H., A. I.Ch. E.J., 7, 254 (1961).

74. Bowman, C. W., Ward, D. M., Johnson., A. I., Trass, O., Can. J. Chem. Eng., 39, 9 (1961).

75. Ward, D. M., Trass, O., Johnson, A. I., Can. J. Chem. Eng., 40, 164 (1962).

76. Jones, S.J. R., Smith, W., Proceedings of the Symposium on the Interaction Between Fluids and Particles, Int. Chem. Eng., London (1962).

77. Kinard, G. E., Manning, F. S., Mannaing, W. P., British Chem. Eng., 8, 326 (1963).

78. Garner, F. H., Skelland, A.H. P., Ind. Eng. chem, 46, 1255 (1954).

79. Finlay, B. A., PhD Thesis, University of Birmingham, England (1957).

80. Jarvis, J., PhD Thesis, University of Birmingham, England (1960).

81. Garner, F. H., Kendrick, P., Trans. Inst. Chem. Eng., 37, 155 (1959).

82. Lihou, D. A., PhD Thesis, University of Birmingham, England, (1963).

83. Avery, J. H., Ingram, A. W. K., Modern Laboratory Physics, lst ed., Pitman Press, (1971).

84. Lihou, D. A., Birmingham University, Chem. Eng., 17, 1 (1966).

85. Lihou, D. A., Trans. Inst. Chem. Eng., 50, 392 (1972).

86. Miura, K., Miura, T., Ohtani, S., A. I.Ch. E.Symp Series, 73, 95 (1977).

87. Sandoval-Robles, J. G., Riba, J. P., Couderc, J. P., Trans. Inst. Chem. Eng., 58, 132 (1980).

88. Sandoval-Robles, J. G., Delmas, H., Couderc, J. P., A.I.Ch.E.J., 27, 819 (1981).

89. Davis, E. J., Ray, A. K., Chang, R., A. I. Ch. E. Symp. Series, 74, 190 (1978).

90. Kramers, H., Physica, 12, 61 (1946).

91 Johnstone, H. F., Pigford, R. L., Chapin, J. H., Trans. Am. Inst. Ch. Eng., 37, 95 (1941).

92. Rowe, P. N., Claxton, K. T., Lewis, J. B., Trans. Inst. Chem. Eng., 43, T14 (1965).

93. Ranz, W. E., Trans. A. S. M. E., 78, 909 (1956).

94. Marshall, W. R., Trans. A. S. M. E., 77, 1377 (1955)

95. Pei, D. C. T., Gauvin, W. H., A. I. Ch. E. J., 9, 375 (1963).

96. Pei, D. C. T., Narasimhan, C., Gauvin, W. H., Proceedings of the Symposium on the Interaction Between Fluids and Particles., Inst. Chem. Eng., London, 243 (1952).

97. Downing, C. G., A.I. Ch. E. J., 12, 760 (1966).

98. Frazier, G. C., Hellier, W. W., Ind. Eng. Chem. Fund., 8, 807 (1969).

99. Crosby, E. J., Stewart, W. E., Ind. Eng. Chem. Fund., 9, 515 (1970).

100. Toei, R., Okazaki, M., Kubota, K., Ohashi, K., Mizata, K., Chem. Eng. (Japan) 30, 43 (1966).

101. Lee, K., Ryley, D. J., J. Heat Transfer, Trans. A. S. M. E., 90, 445 (1968).

102. Matlosz, R. L., Leipziger, S., Torda, T. P., J. Heat Mass Transfer, 15, 831 (1972).

103. Audu, T. O. K., PhD Thesis, University of Aston in Birmingham, England (1973).

104. Kadota, T., Hiroyasu., H., Bulletin J. S. M. E., 19, 1515 (1976).

105. Hiroyasu, H., Trans.J.S.M.S., 40, 3147 (1974).

106. Bell, J. R., Kaye, W. G., Nissan, A. H., A.I.Ch.E.J., 5, 103, 344 (1959).

107. Bolles, T. V., Nissan, A. H., George, H. H., A.I.Ch.E.J., 6, 406 (1960).

108. McCready, D. W., McCabe, W. L., Trans. Am. Inst. Chem. Eng., 29, 131 (1933).

109. Sherwood, T.K., Trans. Am. Inst. Chem. Eng., 32, 150 (1936).

110. Miura, K., Atarashiya, K., Ouchi, I., Ohtani, S., Kagaku Kogaku, 35, 643 (1971) - Translation :- Heat Transfer, Japan Research, 1, 11 (1972).

111. Wijlhuizen, A. E., Kerkhof, P.J.A.M., Bruin, S., Chem. Eng. Sci., 34, 651 (1979).

112. Van der Lijn, J., PhD Thesis, Agricultural University Wageningen, Netherlands, (1976).

113. Haertling, M., Drying 1980, Vol. 1., Hemisphere Publ. Corp., N.Y. (1980).

114. Esubiyi, A. O., PhD Thesis, University of Aston in Birmingham, England (1980).

115. Cheong, H. W,., PhD Thesis, University of Aston in Birmingham, England (1983).

116. Probert, R.P., Phil. Mag., 37, 94 (1946).

117. Rosin, P., Rammler, E., J. Inst. Fuel, 7, 29 (1933).

118. Fledderman, R. G., Hanson, A. R., University of Michigan Res. Dept., CM667 (1951).

119. Nukiyama, S., Tanasawa, Y., Trans. Soc. Mech. Eng., Japan, 4, 86 (1937).

120. Manning, W.P., Gauvin, W.H., A.I.Ch.E.J., 6, 184 (1960).

121. Bose, A.K., Pei, D.C.T., Can. J. Ch.Eng., 42, 259 (1964).

122. Dlouhy, J., Gauvin, W.H., A.I.Ch.E.J., 6, 29 (1960).

123. Dickinson, D.R., Marshall, W.R., A.I.Ch.E.J., 14, 541 (1968).

124. Niro Atomiser Manual (1980), Niro Atomiser , Copenhagen, Denmark.

125. Malvern 2200 Droplet and Spray Particle Sizer Manual (1982). Commodore, U. S. A.

126. Adrian, E.S., The Physics of Flow Through Porous Media, University of Toronto Press (1960).

127. Mugele, R. A., Evans, H.D., Ind. Eng. Chem., 43, 1317 (1951).

128. Baltas, L., Gauvin, W. H., A.I.Ch.E.J., 15, 764, 772 (1969).

129. Katta, S., Gauvin, W.H., A.I.Ch.E.J., 21, 143 (1975).

130. Miura, T., Ohtani, S., Maeda, S., Drying 1980, Vol. 1. Hemisphere Publ. Corp. New York (1980).

131. Williams, G.C., Schmitt, R.O., Ind. Eng. Chem. 38, 967 (1946).

132. Hinchley, J.W., Himus, G.W., Trans. I. Ch. Eng., 2, 57 (1924)

133. International Critical Tables, Vol. 5, 1st Ed., McGraw Hill Ltd., N.Y. (1933).

134. Glasstone, S., Text Book of Physical Chemistry, 1st Ed., Macmillan Ltd., London (1940).

135. Ade-John, A.O., PhD Thesis, University of Aston in Birmingham, England (1976).

136. Ashton, C., PhD Thesis, University of Aston in Birmingham, England (1980).

137. Knott, P., Unpublished Work, University of Aston in Birmingham, England, August (1985).

138. Spalding, D.B., 4th Int. Symp. on Combustion, 847, Williams and Williams, Baltimore, Maryland, (1953).

139. Tsubouchi, T., Sato, S., Chem. Eng. Prog. Symp. Ser., 56, 269, 285 (1960)

140. Miura, T., Ohtani, S., Kagaku Kogaku Ronbunshu, 5, 130 (1979)

141. Garner, F.H., Grafton, R.W., Proc. Roy. Soc., Ser. A, 224, 64 (1954)

142. Kendrick, P., PhD Thesis, University of Birmingham, England, (1955)